論文 / 著書情報
Article / Book Information

題目(和文)	様々な建物高さと減衰機構を有する免震構造における地震時性能の評価方法
Title(English)	Seismic Performance Evaluation Methodologies for Base-Isolated Buildings with Various Heights and Damping Mechanisms
著者(和文)	シムアンパン・サラン
Author(English)	Sarun Chimamphant
出典(和文)	学位:博士（工学）, 学位授与機関:東京工業大学, 報告番号:甲第9997号, 授与年月日:2015年9月25日, 学位の種別:課程博士, 審査員:笠井　和彦,元結　正次郎,坂田　弘安,山田　哲,佐藤　大樹
Citation(English)	Degree:Doctor (Engineering), Conferring organization: Tokyo Institute of Technology, Report number:甲第9997号, Conferred date:2015/9/25, Degree Type:Course doctor, Examiner:,,,,
学位種別(和文)	博士論文
Type(English)	Doctoral Thesis

Seismic Performance Evaluation Methodologies for Base-Isolated Buildings with Various Heights and Damping Mechanisms

By

Sarun Chimamphant

A Dissertation

Submitted to

Tokyo Institute of Technology

In partial fulfillment of

the requirements for the

degree of

Doctor of Engineering

ACKNOWLEDGEMENT

The author wishes to express his appreciation and wholehearted sense of gratitude to his advisor Professor Kazuhiko Kasai for his enthusiastic guidance, valuable suggestions, constructive criticisms, friendly discussions, and persistent supervision which are indispensable for completion of this thesis work.

In addition, the author would like to express his gratitude to the Japan Ministry of Education, Culture, Sports, Science and Technology (MEXT) for granting the scholarship for his study at Tokyo Institute of Technology.

Last but not least, the author gratefully acknowledges the continuing patience and vital sacrifices of his beloved father and mother, Mr. Somboon Chimamphant and Mrs. Kanya Chimamphant, whose love and supports are always a constant source of encouragement and guidance to him.

TABLE OF CONTENTS

CHAPTER 1

INTRODUCTION

1.1 Background and Problem Statements

Because of its excellent ability to protect buildings, their functions and their occupants, seismic isolation has been increasingly used in Japan, China, and other seismically active countries. The main feature of base isolation technology is that it introduces flexibility at the base story between the superstructure and the ground. This allows for extensive concentrated movement at the base story and reduces demands on the superstructure. In order to reduce this extensive movement at the base, isolators are often designed to absorb energy by adding devices with energy dissipation capacity, resulting in the addition of damping to the system. Energy dissipation can usually be achieved by fluid viscosity (velocity-dependent damper) or hysteresis of the force-displacement relationship (deformation-dependent damper).

To date, studies on seismic isolation have typically modeled buildings as two-degree-of-freedom (2DOF) system. The modeling, however, is not suitable for performance evaluation, since it does not simulate story-by-story responses such as inter-story drifts and floor accelerations, which can unevenly distribute throughout the building height. It is known that story responses can contain multiple modes and affect the structural and nonstructural story-by-story components, equipment, other contents, and occupants in various ways. Clearly, modeling seismically isolated buildings using a multi-degree-of-freedom (MDOF) system is essential for performance evaluation. Further, in order to provide comprehensive performance metrics, one must convert the story responses to the damage states of the specific items described above. Moreover, the superiority of isolation systems is effectively shown, and

thereby, their use can be justified to building owners by comparing their performance metrics with those of less costly and more common conventional structures.

Based on the above, the present research for the first time attempts performance evaluations of seismically isolated buildings by conducting time history analyses of their MDOF models. From among the numerous available evaluation methods, PEER Performance-Based Earthquake Engineering (PBEE) is selected, and the results are explained in comparison with conventional fixed-base buildings that are evaluated in the same manner. A key feature of the PEER methodology is the definition of performance metrics that are relevant to decision making for seismic risk mitigation. In brief, the PEER methodology estimates the mean annual frequency of exceeding a specific damage state for a specific structure in a given seismic environment. It is based on dynamic response time history analyses of a building that is subjected to a suite of earthquake ground motions that are scaled to intensities in accordance with the seismic hazard curve at the site. In original PEER PBEE framework, the schematic diagram is shown in the following Figure 1.1.

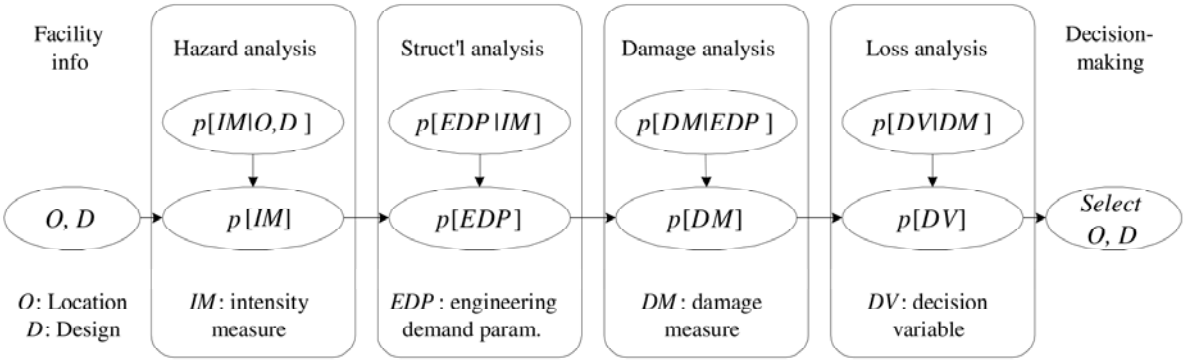

Figure 1.1 Underlying PEER PBEE probabilistic framework

As can be seen in the Figure, the framework is derived based by probabilistic approach which takes into account the probability of occurrence of ground motion (hazard analysis), the probability of the response demands under several ground motions (structural analysis), the probability of exceed damage states of structural/nonstructural components (damage analysis),

and the cost estimation (loss analysis). However, in this research, the loss analysis which concerns the cost repair will not be included. The result of the expected return period will be concluded. As examples for the performance evaluation, suspended ceilings and partition walls, which are sensitive to acceleration and deformation, respectively, will be used. Using the PEER methodology, the return periods of the sample nonstructural components are estimated based on their available fragility curves. In addition, the curves are varied hypothetically to understand the return period's sensitivity to curve features. Then, the medians and fragility function dispersions that are required to satisfy the desired failure return periods of these components are obtained for seismically isolated buildings.

Also, base-isolated buildings can also be categorized as response-controlled buildings. Previously, the so-called performance curves for vibration-controlled damped buildings have been proposed by Kasai et al. In a similar manner, by using only the properties of the buildings, superstructure period, superstructure damping ratio, isolation period, and isolation damping ratio, the performance curve for base-isolated building will be can be drawn. The performance curve is very meaningful such that it is possible to gain much more understanding of the response of the base-isolated buildings. By knowing the basic properties of the base-isolated building, the dynamic characteristics as well as the responses can be predicted.

For time history analyses, inelastic shear beam (stick) models are utilized to represent the MDOF systems. Stick models do not provide information on each component of the building, but they can produce the story-by-story responses that are necessary for performance evaluation. These models are considered appropriate, since they have small degrees of freedom and they considerably reduce computational effort, which otherwise could be excessive; they also exactly represent structural properties such as story stiffness and strength, which are closely associated with code requirements. Moreover, even though the performance of tall, flexible, base-isolated buildings is thought to be inefficient, they are frequently adopted in Japan. This research therefore also investigates performance including tall, flexible buildings.

Furthermore, a real existing tall base-isolated structure, so called J2 building, located in Suzukakedai campus, Tokyo Institute of Technology is selected for investigation since the monitoring system was installed, and several response data can be readily obtained. This building will be analyzed by using a 3D sophisticated nonlinear model. This sophisticated model and its results of the responses will be very useful. From the sophisticated model, simple shear model will be developed. The responses from the shear model are verified with those from the sophisticated model. Lastly, the performance evaluation methods developed in this research will be applied to this building. Applications of evaluation methods and their results are discussed.

1.2 Objectives and Scopes

The main objective are as follows:

1. To investigate the effects of isolation properties and hystereses on the response of multi-degree-of-freedom (MDOF) base-isolated buildings,
2. To examine the level of improvement of base-isolated buildings over conventional fixed-base buildings,
3. To evaluate the performance of buildings in a way that non-engineers could understand by using PEER methodology,
4. To develop a simplified and deterministic performance evaluation method for base-isolated buildings,
5. To examine the responses of a real existing base-isolated building, the efficiency of the isolation system, and to apply the performance evaluation methods on the building.

In summary, the scope for each chapter is described as follows.

Chapter 2 describes how analysis model used and the responses of the base-isolated buildings having various building, isolation properties, and isolation hysteresis.

Chapter 3 investigates the responses of conventional fixed-base buildings and compare the responses with those of the base-isolated buildings in Chapter 2.

Chapter 4 describes the PEER performance evaluation method which is used to evaluate the base-isolated buildings. The results are interpreted in terms of return periods which indicate how many years the building is expected to be continuously functional considering damage on nonstructural component. The result of the return period is easy to understand for non-engineers and can be used to design nonstructural component as explained more in this Chapter.

Chapter 5 proposes a simplified performance evaluation method for base-isolated buildings which is developed based on a single-mass two-layer model. This model is simple and the response spectrum analysis can be applied. Response of base-isolated buildings can be comprehensively understood from the developed performance curve.

Chapter 6 investigates the response of an existing tall base-isolated building. The building is called J2 building located in Suzukakedai campus, Tokyo Institute of Technology. Both 3-dimentional sophisticated frame model and simple shear beam model are developed and the responses from both models are verified with those from the recorded data. Performance evaluation methodologies described in Chapters 4 and 5 are then applied to this tall building.

CHAPTER 2

SEISMIC RESPONSES OF BASE-ISOLATED STRUCTURES

2.1 Base-Isolated Structures with ViscoElastic Isolation System

This section focuses on the responses of base-isolated structures having ViscoElastic isolation system. The effects of basic isolation properties which are isolation period T_b, isolation damping ratio ζ_b, and number of stories N are investigated. Modal contributions are examined by transfer functions.

2.1.1 Equivalent lateral static force

The American standard code ASCE 7-10 is adopted. The analytical model for a generic MDOF system is represented in this study by a shear beam (stick) model. An example model for 3-story base-isolated structure is shown in Figure 2.1.

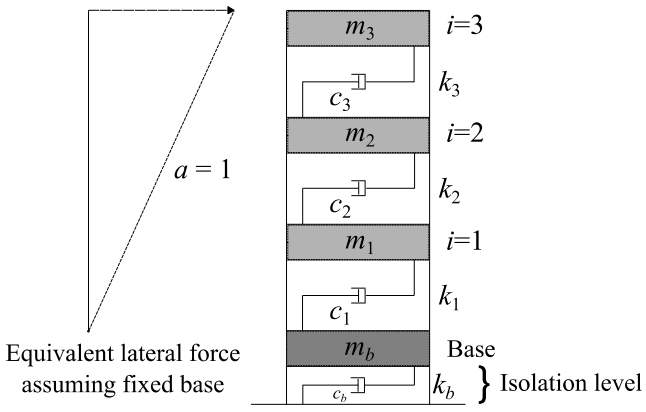

Figure 2.1 Equivalent lateral force profile and analytical model of base-isolated structures (Example of 3-Story)

The mass in each floor $m_i \left(i = 1 \text{ to } N\right)$ is assumed to be equal, and the mass of the base floor is defined as m_b. Story heights are assumed to be equal in all stories. The equivalent lateral seismic force is determined corresponding to the code as follows

$$F_x = \frac{w_x h_x^a}{\sum_{i=1}^{N} w_i h_i^a} V_s \tag{2.1}$$

where w_i and w_x are portion of the total effective seismic weight of the structure located or assigned to level i or x, h_i and h_x are height from the base to level i or x, a is an exponent related to the structure period T_s, and V_s is design base shear for the base-isolated structures.

According to the code, for base-isolated structures, a is always equal to one. Since the masses and story heights are the same in all stories, Equation (2.1) will always produce the triangular force profile as shown in Figure 2.1.

2.1.2 Stiffness, period, and damping of base-isolated structures

Since the code does not specifically limit the superstructure period, and there is no report regarding the typical superstructure period of base-isolated structure, such as 1.4 times the approximate fundamental period defined by the code. Therefore, we approach differently to obtain the stiffness matrix as follows.

First, the superstructure period is specified as $T_s = 0.1N$, where N is the number of stories above the isolation level. In this research, 3-, 9-, and 20-story, representing low, mid-rise, and tall buildings, are considered, hence, their corresponding superstructure periods T_s are 0.3, 0.9, and 2.0 seconds, respectively. The stiffness matrix $\underset{\sim}{K}_s$ can be obtained from the following Equation

$$\underset{\sim}{K}_s \underset{\sim}{\phi}_s = \left(\frac{2\pi}{T_s}\right)^2 \underset{\sim}{M}_s \underset{\sim}{\phi}_s \tag{2.2}$$

where $\underset{\sim}{M}_s$ is the diagonal uniform mass matrix and $\underset{\sim}{\phi}_s$ is the triangular shape, since the force profile from the code is triangular and displacement vector with desired uniform drift ratio will always produce triangular mode shape. This obtained $\underset{\sim}{K}_s$ is then checked against $C_d \underset{\sim}{F}$, where C_d is the deflection amplification factor equal to $R_I = 2$, and R_I shall be three-eighths of the R value for the fixed-base structure with an upper-bound value not to exceed 2.0 and lower-bound value not to be less than 1.0 (R for special moment resisting frame of fixed-base structure = 8.0) and $\underset{\sim}{F}$ is from Equation (2.1) to ensure that the displacement satisfies the maximum uniform drift ratio limit of 0.015 of the story height as specified by the code.

As for the damping, from the previous research studies, it has been found that the assumption of Rayleigh damping in the superstructure, the first mode damping ratio of the base-isolated structure tends to exceed the isolated damping ratio resulting in undesirable suppression of the first mode response. The stiffness proportional damping is recommended, hence, utilized in this study, i.e.,

$$C_s = \beta K_s \tag{2.3}$$

where C_s is the damping matrix and β is the stiffness-proportional damping coefficient that is to be set for the desired damping ratio at T_s. Superstructure damping ratio ζ_s = 0.02 is assumed in this study.

For the isolation system, base isolation periods $T_b = 2,\ 3,$ and 4 seconds and base isolation damping ratios ζ_b = 0.1 and 0.3 are considered to cover a wide range of base isolation properties. Note that T_b and ζ_b are defined by assuming a rigid superstructure, and the corresponding isolation stiffness $k_b = \left(2\pi/T_b\right)^2 m_{\text{total}}$ where m_{total} is the total mass of the base isolated structure, including the base story. The damping of the isolation system is idealized by linear viscous model, and corresponding isolation damping coefficient $c_b = \left(4\pi\zeta_b/T_b\right) m_{\text{total}}$.

Tables 2.1 and 2.2 list the natural periods and damping ratios of the considered base-isolated structures. Modal strain energy method is used to estimate the damping ratios for the

real value approach. Also note that complex eigenvalue analysis is also conducted and the results of natural periods and damping ratios are included in both tables.

Table 2.1 Natural periods of the base-isolated structures (seconds)

			T_b = 2 seconds			T_b = 3 seconds			T_b = 4 seconds		
Structure	**Eigenvalue**		T_1	T_2	T_3	T_1	T_2	T_3	T_1	T_2	T_3
3-story	$\zeta_b = 0.1$	Real	2.015	0.188	0.104	3.010	0.188	0.104	4.007	0.189	0.104
		Complex	2.014	0.188	0.104	3.010	0.188	0.104	4.007	0.189	0.104
	$\zeta_b = 0.3$	Real	2.015	0.188	0.104	3.010	0.188	0.104	4.007	0.189	0.104
		Complex	2.010	0.188	0.104	3.006	0.189	0.104	4.005	0.189	0.104
9-story	$\zeta_b = 0.1$	Real	2.149	0.514	0.290	3.099	0.526	0.292	4.074	0.531	0.293
		Complex	2.145	0.514	0.290	3.096	0.526	0.292	4.072	0.531	0.293
	$\zeta_b = 0.3$	Real	2.149	0.514	0.290	3.099	0.526	0.292	4.074	0.531	0.293
		Complex	2.108	0.511	0.291	3.068	0.526	0.293	4.049	0.531	0.293
20-story	$\zeta_b = 0.1$	Real	2.729	1.003	0.605	3.501	1.078	0.624	4.378	1.115	0.632
		Complex	2.724	1.000	0.604	3.493	1.076	0.624	4.369	1.114	0.632
	$\zeta_b = 0.3$	Real	2.729	1.003	0.605	3.501	1.078	0.624	4.378	1.115	0.632
		Complex	2.666	0.962	0.585	3.405	1.055	0.619	4.282	1.104	0.631

Table 2.2 Damping ratios of the base-isolated structures

			T_b = 2 seconds			T_b = 3 seconds			T_b = 4 seconds		
Structure	**Eigenvalue**		T_1	T_2	T_3	T_1	T_2	T_3	T_1	T_2	T_3
3-story	$\zeta_b = 0.1$	Real	0.098	0.043	0.063	0.099	0.039	0.061	0.099	0.038	0.060
		Complex	0.098	0.043	0.063	0.099	0.039	0.061	0.099	0.038	0.060
	$\zeta_b = 0.3$	Real	0.293	0.067	0.074	0.297	0.055	0.069	0.298	0.049	0.066
		Complex	0.294	0.067	0.074	0.297	0.055	0.069	0.299	0.049	0.066
9-story	$\zeta_b = 0.1$	Real	0.081	0.064	0.079	0.091	0.055	0.073	0.095	0.050	0.070
		Complex	0.081	0.064	0.079	0.091	0.055	0.073	0.095	0.050	0.070
	$\zeta_b = 0.3$	Real	0.241	0.127	0.116	0.272	0.099	0.098	0.284	0.083	0.089
		Complex	0.245	0.130	0.119	0.275	0.100	0.099	0.286	0.084	0.089
20-story	$\zeta_b = 0.1$	Real	0.044	0.073	0.093	0.065	0.071	0.086	0.077	0.066	0.081
		Complex	0.044	0.072	0.093	0.065	0.071	0.087	0.077	0.066	0.081
	$\zeta_b = 0.3$	Real	0.118	0.155	0.160	0.188	0.150	0.138	0.229	0.132	0.121
		Complex	0.115	0.148	0.163	0.189	0.154	0.144	0.231	0.135	0.124

Table 2.1 indicates that for short buildings, 3-story, the fundamental periods T_1 from complex-value approach are almost the same as those from real-value approach. For more flexible 9- and 20-story with $\zeta_b = 0.1$, T_1 are still very close to those from real-value approach. However when $\zeta_b = 0.3$, T_1 reduce to around 0.98 times due to the effect of non-proportional damping. Also for 3-story with $T_b = 2$, T_1 are almost equal to T_b. However, for 9- and 20-story, T_1 increase to 1.05 and 1.33 times, respectively, due to the flexibility in superstructures.

From Table 2.2, the damping ratios from complex-value approach are very close to those from real-value approach demonstrating reasonable accuracy of modal strain energy method for the short to tall base-isolated buildings considered. Also the actual 1st mode damping ratios ζ_1 indicated in the table are around 0.98, 0.8, and 0.4 times ζ_b for 3-, 9-, and 20-story structures, respectively. ζ_1 can be much lower than ζ_b assuming rigid superstructure. In the present paper, ζ_b will be used to categorize the base-isolated building, but this point must be kept in mind.

2.1.3 Strength of Base-Isolated Structures

The main difference of the design between fixed-base and base-isolated structures comes from the base shear. According to the code, the equivalent lateral force (ELF) procedure is not suitable for base-isolated buildings with greater than 4 stories. Although this is required, but in order to have consistent determination of stiffness distribution of structure, the ELF procedure is utilized. Dynamic analysis is then necessary to check with ELF procedure. This research also performs dynamic analysis. For the fixed-base structure, a special steel moment frame is considered, for which the code gives approximate structure period $T_s = 0.0724h^{0.8}$ where h is the building height in meter, typical story height is assumed to be 350 cm, the strength reduction factor $R = 8$, overstrength factor $\Omega_0 = 3$, and deflection amplification factor

$C_d' = 5.5$. However, for the superstructure of base-isolated structure, strength reduction factor $R_I = (3/8)R$ but not greater than 2.0, hence $R_I = 2$, deflection amplification factor C_d is equal to R_I, specified by the code, and over strength factor Ω_I is assumed equal to $\Omega_0 = 3$. From these information, the structures are designed and the required yield strengths both fixed-base and base-isolated structures are shown in Figure 2.2.

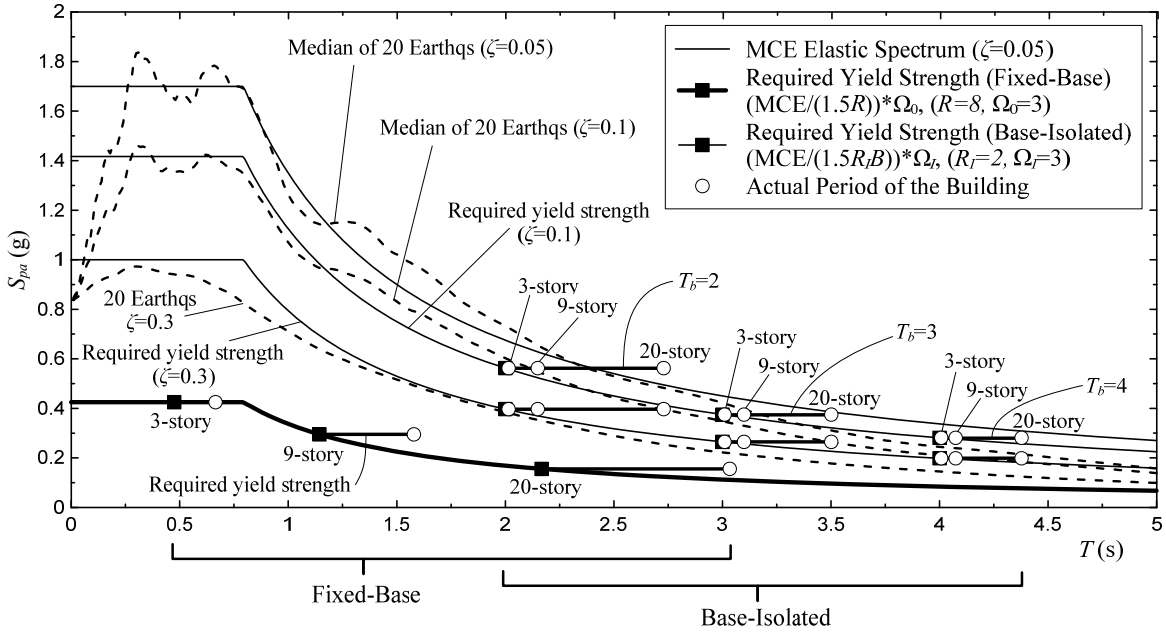

Figure 2.2 Required yield strength designed according to the ASCE code

It can be observed that the ratio of the median of the 20 ground motions to the required yield strength level of fixed-base structure is very large, and severe nonlinearity is expected for such buildings. However, for the base-isolated structures, the ratio is about 1.0 or less, much smaller than those of the fixed-base structures. Note that the required yield strengths for any superstructure (3-, 9-, or 20-story) of base-isolated structure will be the same, which are calculated at the isolation period T_b according to the code. Because of this, elastic behavior of superstructure of base-isolated building is assumed in this research.

2.1.4 Responses of Base-Isolated Structures

Twenty ground motions from Los Angeles SAC suite of ground motions for a 2% in 50 years seismic hazard (LA21--LA40), representing the MCE ground motions, are used in this study. Figure 2.3 shows the response spectra plots with 5% and 30% damping ratios for these ground accelerations together with the median and fitted elastic spectrum. The median peak ground acceleration (PGA) is approximately 0.84g.

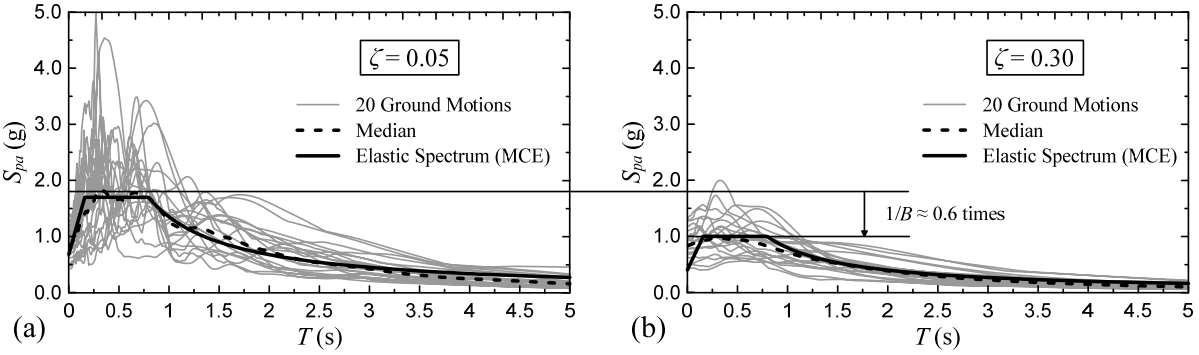

Figure 2.3 Pseudo acceleration spectra of SAC ground motions (ζ = 0.05 and 0.30)

This section focuses on drift ratio and floor acceleration responses which are keys to damage of both structural and nonstructural components. To interpret the response, these structures are subjected to the twenty ground motions. For each analysis and ground motion, drift ratio and peak floor acceleration are recorded at every story. The median and dispersion of drift ratio and floor acceleration for are determined from Equations (2.4) and (2.5):

$$x_m = \exp\left(\frac{1}{M}\sum_{j=1}^{M}\ln r_j\right), \tag{2.4}$$

$$\beta = \sqrt{\frac{1}{M-1}\sum_{j=1}^{M}\ln\left(\frac{r_j}{x_m}\right)^2} \tag{2.5}$$

where x_m is the median, β is the dispersion, M is the number of ground accelerations, and r_j is unique response for each ground motion. Equations (2.4) and (2.5) assume the data is sampled from a lognormal distribution. Median is a mathematical result that indicates that one half of the group is higher and one half lower. And dispersion indicates the degree of scatteredness of data about the median.

Figure 2.4 shows the results of the median drift ratios and median floor accelerations, respectively. Increase of isolation period T_b clearly reduces both the drift and acceleration demands in superstructures of both stiff and flexible buildings regardless of isolation damping ζ_b and number of stories N. This is not surprising because the reduced stiffness results in concentration of drift demand at the isolation level instead of the superstructure. Also large T_s/T_b leads to less effectiveness of the isolation in term of drift response.

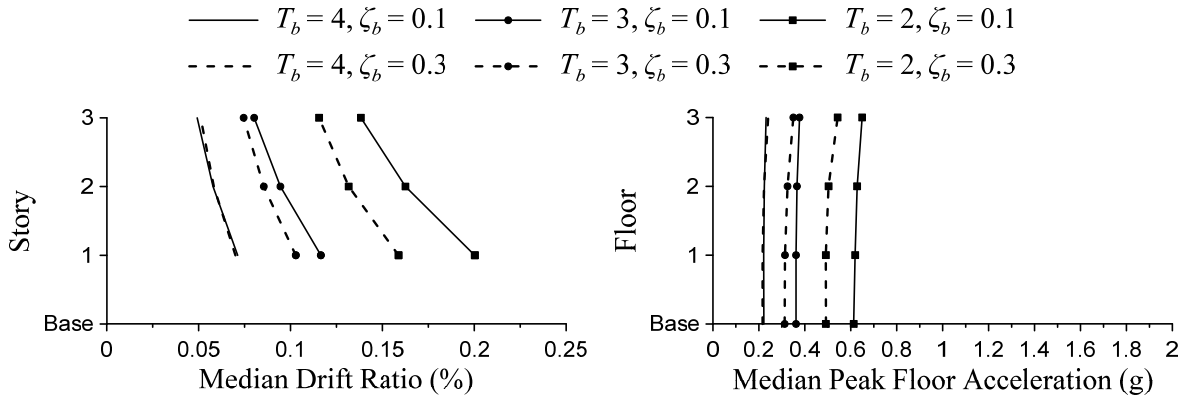

(a) 3-story

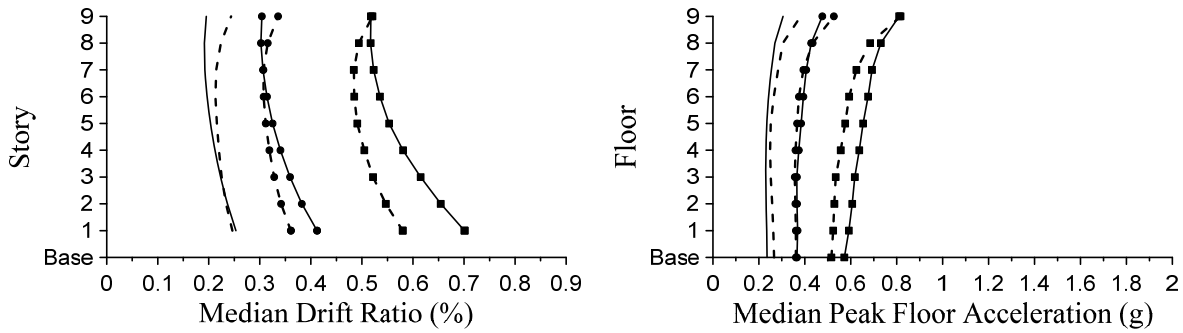

(b) 9-story

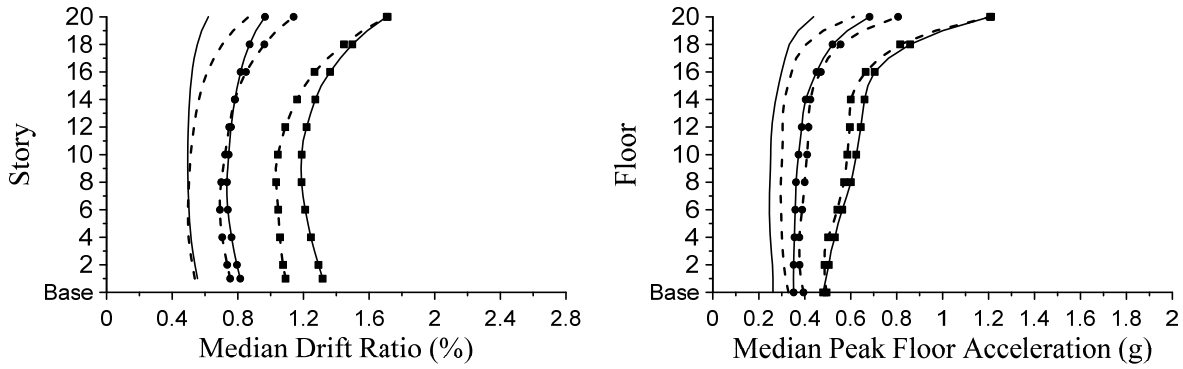

(c) 20-story

Figure 2.4 Median responses for (a) 3-story, (b) 9-story, and (c) 20-story

From these figures, it shows that the distributions of both drift and acceleration demands are sensitive to isolation damping (from solid lines to broken lines). Looking at the drift ratios, high isolation damping ratio ζ_b suppresses them in lower stories, but increases them in higher stories. For short buildings or stiff structures, the change in drift ratios is altered slightly, whereas for tall or flexible structures, the change is more dramatic. Because of this, adding more ζ_b reduces the displacement at the isolation level to prevent pounding but lessens effectiveness on the superstructure.

Also if isolation period T_b is small, added isolation damping ratio ζ_b helps reduce the drift ratio and acceleration demands. However, if T_b is higher (T_b = 4 seconds), added isolation damping ratio ζ_b could increase the demands in the superstructures. This is attributed to the excitation of higher mode effects due to the presence of non-proportional damping. These higher mode effects would change the distribution of the demands. This may arise from an increase in the base isolation damping ζ_b, while the superstructure damping ζ_s remains 2%. The equivalent damping ratio for the base-isolated structure is much lower than the target base isolation damping ratio ζ_b as can be seen in Table 2.2. As a result, added damping in the isolators may not have the benefit that would be assumed for a stiff superstructure.

Examining the effect of building height, or number of stories N, the results show that in short buildings (3-story with T_b = 4 and ζ_b = 0.1), the median drift ratio is around 0.05%,

while for taller 9- and 20-story base-isolated buildings, the median drift ratios are around 0.2% and 0.5%, which are 4 times and 10 times, respectively. When superstructure period T_s is longer, i.e. taller building, drift ratios and peak floor accelerations become more concentrated in the uppers stories, due to higher mode contribution. Also because of the code specified triangular force profile, apparently, the story shears in the upper stories are insufficient resulting in low stiffnesses. In practice, the design of the beam in the upper stories will govern and the strength and stiffness in the upper stories will be increased, which consequently reduces such high accelerations.

2.1.5 Transfer function

Since the base-isolated structures consist of two regions with significantly different levels of damping, ζ_b and ζ_s, non-proportional damping characteristics are expected. As a result, higher mode contribution is anticipated. To investigate the contribution from higher modes, transfer functions are estimated for each case of analysis by the following Equation

$$G(\omega) = \frac{A_{\text{floor}}(\omega)}{A_{\text{ground}}(\omega)} \tag{2.6}$$

where $A_{\text{floor}}(\omega)$ and $A_{\text{ground}}(\omega)$ are the Fourier spectra of the selected floor and ground, respectively. To investigate the mode contribution in this section, three cases are selected for investigation which are

(1) 3-story base isolated structure with T_b = 2 seconds

(2) 9-story base isolated structure with T_b = 3 seconds

(3) 20-story base isolated structure with T_b = 4 seconds

These base isolated structures are subjected to the same unscaled ground acceleration LA21 only. Figures 2.5 and 2.6 shows the results of the estimated transfer function for the roof acceleration (A_{floor} at the roof) and mid-floor accelerations (A_{floor} at the mid-floors),

respectively. The vibration periods are very close to those obtained from eigenvalue analyses shown in Table 2.1.

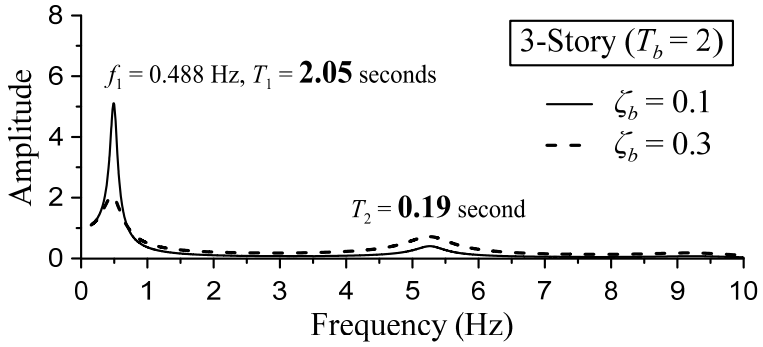

(a) 3-story base-isolated structures

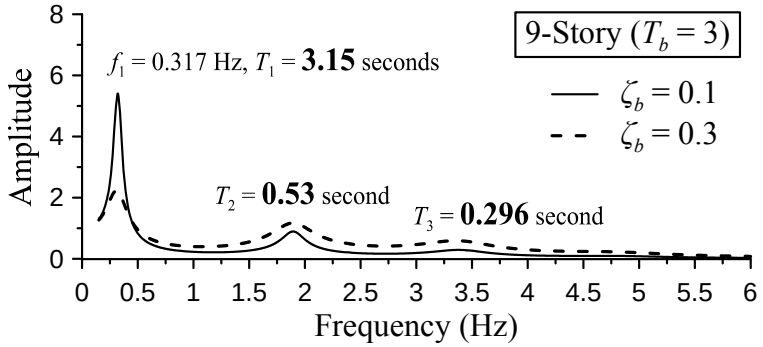

(b) 9-story base-isolated structures

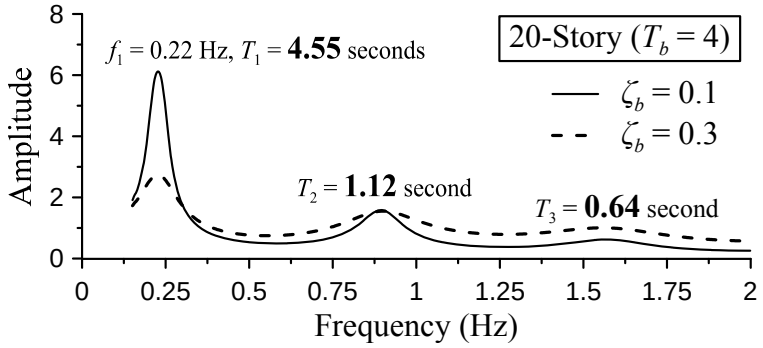

(c) 20-story base-isolated structures

Figure 2.5 Transfer functions for the floor accelerations (A_{floor} at the roof)

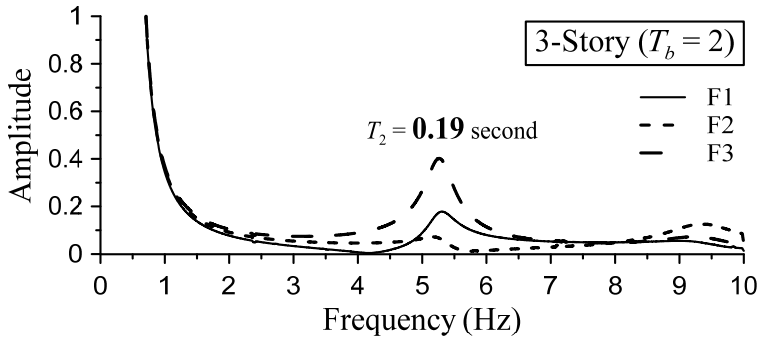

(a) 3-story base-isolated structures

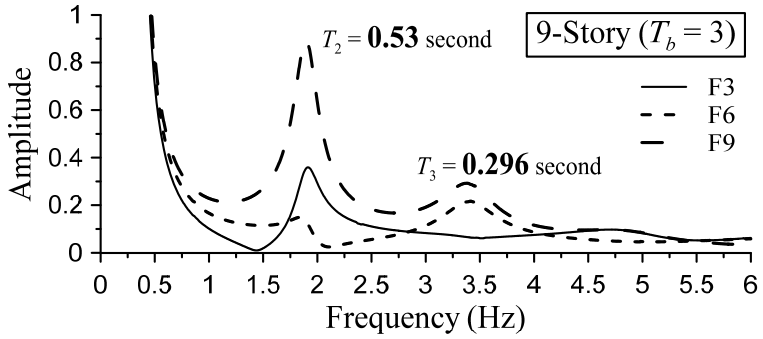

(b) 9-story base-isolated structures

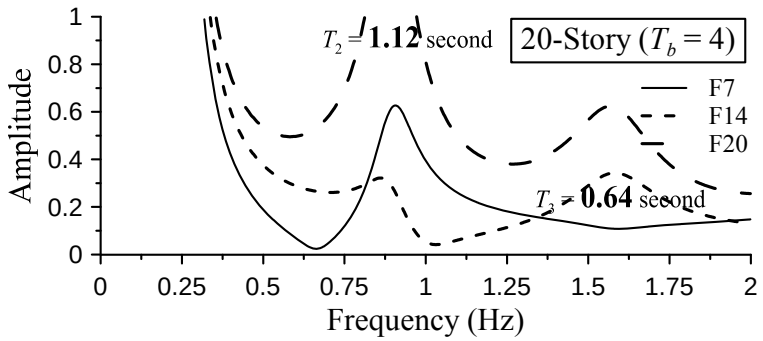

(c) 20-story base-isolated structures

Figure 2.6 Transfer functions for the floor accelerations (A_{floor} at the mid-floors)

Comparison of the transfer functions between different isolation damping ratios, ζ_b = 0.10 and ζ_b = 0.30, Figure 2.5(a,b,c), reveals that increasing the isolation damping reduces the amplitude of the transfer function at the 1st mode, however, at higher modes, the amplitudes become larger indicating that higher modes are anticipated due to highly non-proportional damping.

Figure 2.6 (b,d,f) shows the transfer functions when $A_{\text{floor}}(\omega)$ are the accelerations from the 1/3 building height, 2/3 building height, and top floors for the structures with $\zeta_b = 0.10$ only. Looking at the 1/3 building height floors, i.e. 1st (3-story), 3rd (9-story), and 7th (20-story) floors, the contributions from the 2nd and 3rd modes become lower. However, at the 2/3 building height, i.e. 2nd (3-story), 6th (9-story), and 14th floors, the 2nd mode is low, but the 3rd mode becomes higher. From this information, the building structure and the building contents, such as partition walls or suspended ceilings, should be designed with careful attention to the higher modes as well.

2.1.6 Modal analysis

In modal analysis a mathematical model of a structure's dynamic behavior is obtained. The mathematical model consists of a set of mode shapes each with an associated natural frequency and modal damping. These modal parameters provide a complete description of the structure's dynamic behavior. The strategy is that it decouples the structural MDOF problem into several uncoupled SDOF problems. There are several advantages to this. Modal analysis helps you understand how a structure vibrates (frequency, damping and mode shapes.) So it can also be used for investigating insight into the root cause of vibration problems. However, one of the main disadvantages is that it cannot account for higher mode contribution, since the analysis problem is solved independently for each mode. To account for higher mode effects, the problem needs to be solved simultaneously.

In order to confirm that non-proportional damping caused by large difference between isolation damping and superstructure results in higher mode participation, modal analysis of some cases of base-isolated structures are conducted which are

(1) 3-story base isolated structure with $T_b = 2$ seconds and $\zeta_b = 0.10$ and 0.30

(2) 9-story base isolated structure with $T_b = 3$ seconds and $\zeta_b = 0.10$ and 0.30

(3) 20-story base isolated structure with $T_b = 4$ seconds and $\zeta_b = 0.10$ and 0.30

Mode shapes are obtained from eigenvalue analysis, and are shown in Figure 2.7 for 3-, 9-, and 20-story base isolated structures.

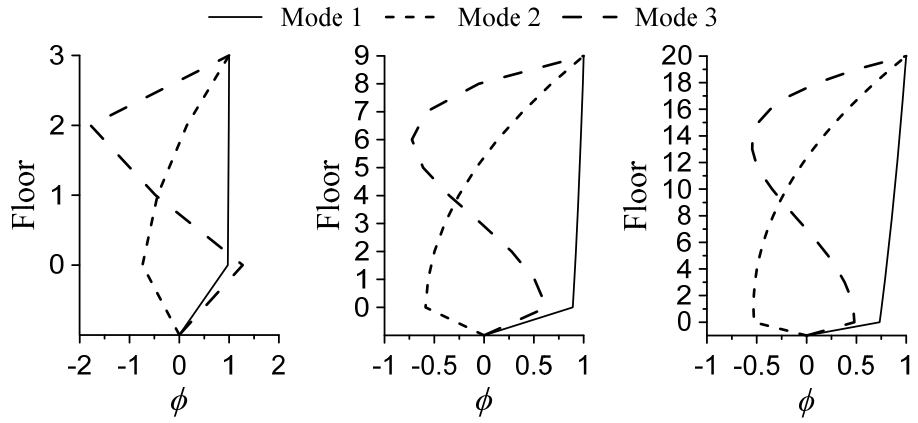

Figure 2.7 Mode shapes of 3-, 9-, and 20-story base-isolated structures

Here we neglect the complex part of the mode shapes, and apply modal strain energy theory to estimate the damping ratio in each mode from Equation (2.7):

$$\zeta_i = \frac{E_d}{4\pi E_s} = \frac{\omega_i \pi \underset{\sim}{\phi}_i^T \underset{\sim}{C} \underset{\sim}{\phi}_i}{4\pi \,½\, \underset{\sim}{\phi}_i^T \underset{\sim}{K} \underset{\sim}{\phi}_i} = \frac{\omega_i}{2} \frac{\underset{\sim}{\phi}_i^T \underset{\sim}{C} \underset{\sim}{\phi}_i}{\underset{\sim}{\phi}_i^T \underset{\sim}{K} \underset{\sim}{\phi}_i} \tag{2.7}$$

where ω_i is i^{th} mode natural circular frequency, $\underset{\sim}{\phi}_i$ is i^{th} mode shape, $\underset{\sim}{C}$ is damping matrix, and $\underset{\sim}{K}$ is stiffness matrix. Table 2.3 shows the modal damping ratios for 3-, 9-, and 20-story base isolated structures.

Table 2.3 Modal damping ratios

Mode	3-Story	9-Story	20-Story
1	0.098	0.091	0.077
2	0.043	0.055	0.066
3	0.063	0.073	0.081
4	0.085	0.097	0.104
5	-	0.122	0.128
6	-	0.148	0.154
7	-	0.174	0.181
8	-	0.200	0.208

9	-	0.226	0.235
10	-	0.252	0.262
11	-	-	0.289
12	-	-	0.316
13	-	-	0.344
14	-	-	0.371
15	-	-	0.399
16	-	-	0.426
17	-	-	0.453
18	-	-	0.481
19	-	-	0.508
20	-	-	0.535
21	-	-	0.562

The comparison between responses obtained from modal analysis and time history analysis from direction integration method is shown in Figures 2.8 and 2.9. These 3-, 9-, and 20-story base isolated structures are subjected to the ground acceleration LA21. Figures 2.8 and 2.9 show the responses for cases when ζ_b = 0.10 and 0.30 respectively.

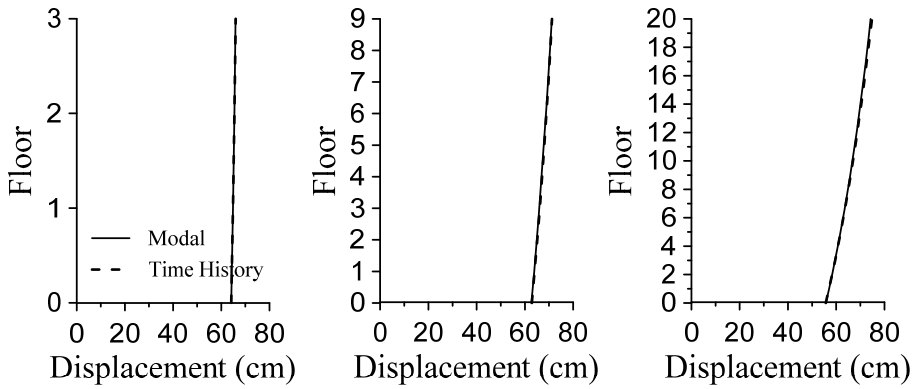

(a) Displacement (cm)

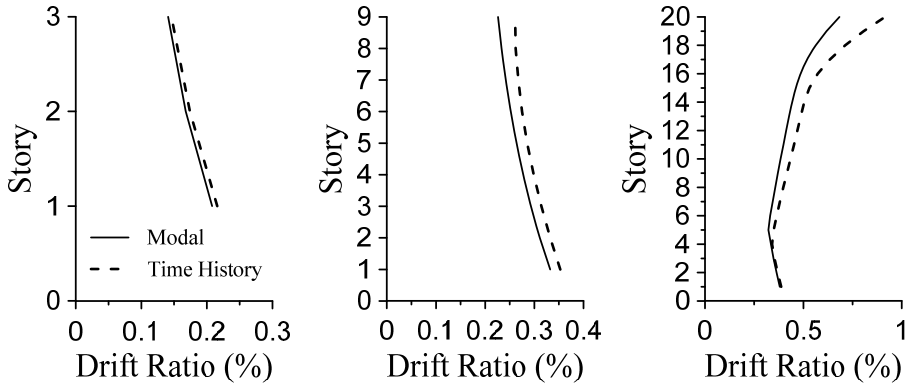

(b) Drift ratio (%)

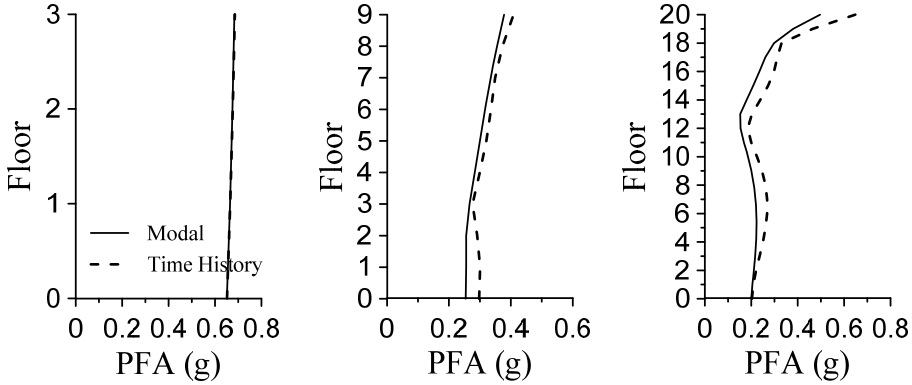

(c) Peak floor acceleration (g)

Figure 2.8 Comparison between responses from modal analysis and time history analysis from direct integration method ($\zeta_b = 0.10$)

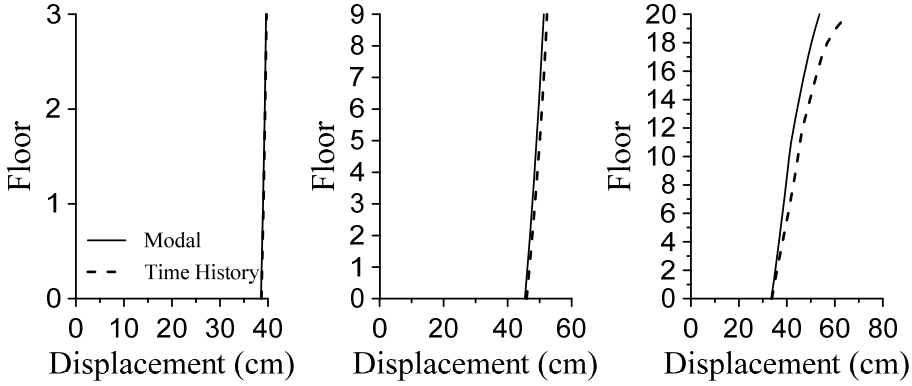

(a) Displacement (cm)

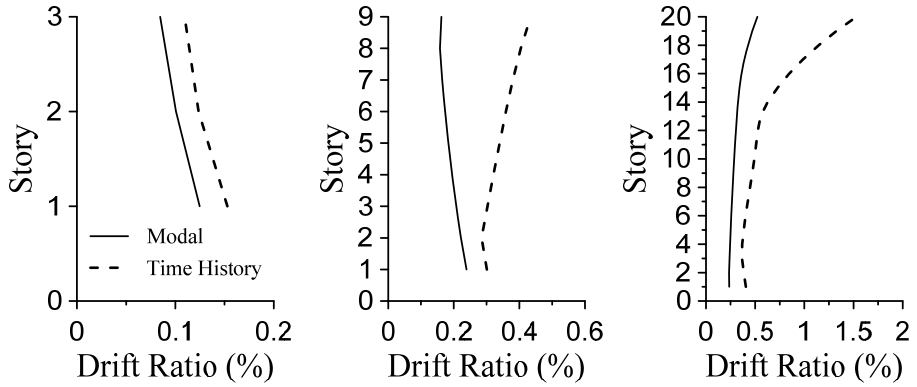

(b) Drift ratio (%)

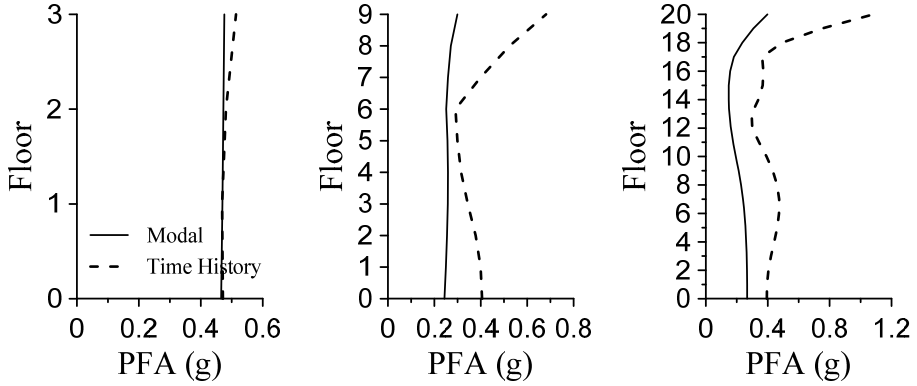

(c) Peak floor acceleration (g)

Figure 2.9 Comparison between responses from modal analysis and time history analysis from direct integration method ($\zeta_b = 0.30$)

Displacements are identical in Figure 2.8(a), and slightly different in Figure 2.9(a) for 9- and 20-story base isolated structures. Therefore, to compute maximum displacements, modal analysis shows sufficiently reliable results even when base isolation damping ratio ζ_b is as high as 30%. However maximum drift ratios and peak floor accelerations do not exhibit the same trends.

For 3-story base isolated structures, modal analysis for the case when the base isolation damping ratio $\zeta_b = 10\%$ (shown in Figure 2.8) appears to closely match time history response. However, when $\zeta_b = 30\%$ (shown in Figure 2.9), the response does not match very well. This could be attributed to the presence of non-proportional damping.

For 9- and 20-story base isolated structures, modal analysis appears to closely match time history response in both drift ratios and peak floor accelerations when base isolation damping ratio ζ_b = 10% as shown in Figure 2.8(b,c). However, when ζ_b = 30%, the response observed varies significantly, as shown in Figure 2.9(b,c). This is attributed to the presence of highly non-proportional damping.

2.2 Base-Isolated Structures with ElastoPlastic Isolation System

In the previous section, the isolation system was idealized as a ViscoElastic system. This section converts from the ViscoElastic (VE) system to ElastoPlastic (EP) system. In VE system, the isolation period and isolation damping ratio are defined as T_b and ζ_b, respectively. In this section, for EP system, the effective isolation period and effective isolation damping ratio are defined as T_{eff} and ζ_{eff} which are determined at a maximum displacement. The detail is described in subsequent sections.

2.2.1 Modelling of bilinear hysteretic damping isolator

Typical hysteresis behaviors are shown in Figure 2.1.

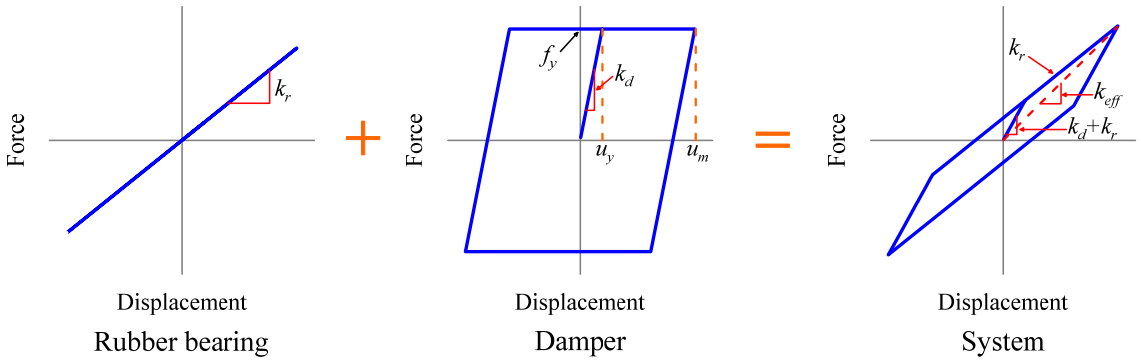

Figure 2.1 Typical bilinear hysteresis of base isolator

In Figure 2.1, all parameters are defined as follows: the rubber bearing stiffness k_r, the damper initial stiffness k_d, the yield displacement u_y, the yield strength of the damper f_y, the maximum displacement u_m, and the effective stiffness k_{eff}. From these parameters, the effective stiffness k_{eff} and the effective damping ratio ζ_{eff} can be obtained as follows

$$\begin{aligned} k_{eff}u_m &= \left(k_r + k_d\right)u_y + k_r\left(u_m - u_y\right) \\ &= k_r u_y + k_d u_y + k_r u_m - k_r u_y \\ &= k_d u_y + k_r u_m \end{aligned} \tag{2.1}$$

From Equation (2.1), k_{eff} will be

$$k_{eff} = \frac{k_d u_y}{u_m} + k_r \tag{2.2}$$

And the effective damping ζ_{eff} is determined as follows.

$$\zeta_{eff} = \frac{E_D}{4\pi E_{S0}} = \frac{4f_y\left(u_m - u_y\right)}{4\pi \,{}^1\!/_2\, k_{eff}u_m^2} = \frac{2f_y\left(u_m - u_y\right)}{\pi k_{eff}u_m^2} \tag{2.3}$$

By manipulating Equation (2.3), the energy dissipation per cycle ED can be interpreted as follows.

$$E_D = 2\pi\zeta_{eff}k_{eff}u_m^2 \tag{2.4}$$

Let p be the post-yield stiffness ratio shown in Equation (2.5)

$$p = \frac{k_r}{k_d + k_r} \tag{2.5}$$

By rearranging Equation (2.5), k_r becomes

$$k_r = \frac{pk_d}{1-p} \tag{2.6}$$

Substituting k_r from Equation (2.6) into Equation (2.2) and rearranging the equation produces k_d as follows.

$$k_d = \frac{k_{eff} u_m}{u_y + \frac{p u_m}{1-p}} \tag{2.7}$$

From Figure 2.1(middle), the dissipated energy E_D

$$E_D = 4 k_d u_y \left(u_m - u_y \right) \tag{2.8}$$

Substituting k_d from Equation (2.7) and E_D from Equation (2.4) into Equation (2.8), the Equation becomes

$$2\pi\zeta_{eff} k_{eff} u_m^2 = 4 \left(\frac{k_{eff} u_m}{u_y + p u_m / 1-p} \right) u_y \left(u_m - u_y \right) \tag{2.9}$$

Solving the above Equation for u_y, the result is

$$u_y = \frac{u_m}{2} - \frac{u_m \sqrt{1 + \pi\zeta_{eff} \left(\frac{\pi\zeta_{eff}}{4} - \left(\frac{1+p}{1-p} \right) \right)}}{2} - \frac{\pi\zeta_{eff} u_m}{4} \tag{2.10}$$

It can be seen that Equation (2.10) is constraint by the value in the square root to be greater than zero. Therefore, by finding the relationship between ζ_{eff} and p under the square root term, the result is shown Equation (2.11).

$$p \le \left(\frac{\pi\zeta_{eff} - 2}{\pi\zeta_{eff} + 2} \right)^2 \tag{2.11}$$

The plot of Equation (2.11) is shown in Figure 2.2.

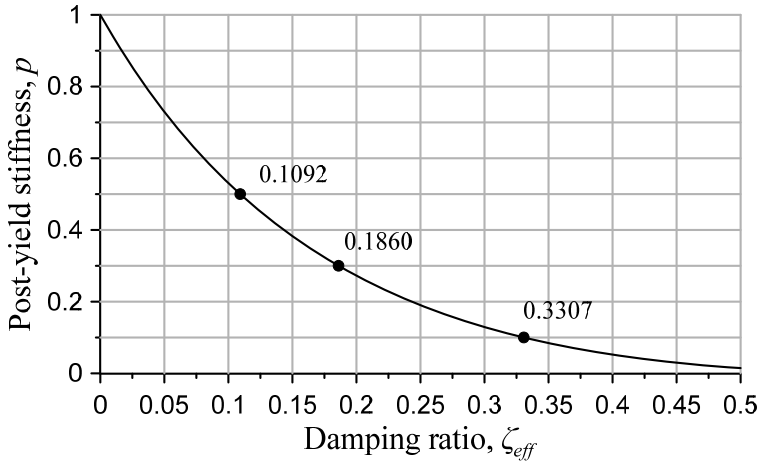

Figure 2.2 Relationship between effective damping ratio ζ_{eff} and post-yield stiffness p

From the figure, it can be interpreted that for the bilinear isolation system having the post-yield stiffness of 0.5, the maximum damping ratio that could be achieved is 0.1092. The values shown in the figure indicates that for the selected post-yield stiffness of 0.1, 0.3, and 0.5, the maximum damping ratio that can be produced is equal to 0.3307, 0.1860, and 0.1092 respectively. These values also correspond to the maximum values shown in Figure 2.3 which shows the relationship between the ductility and the effective damping ratio.

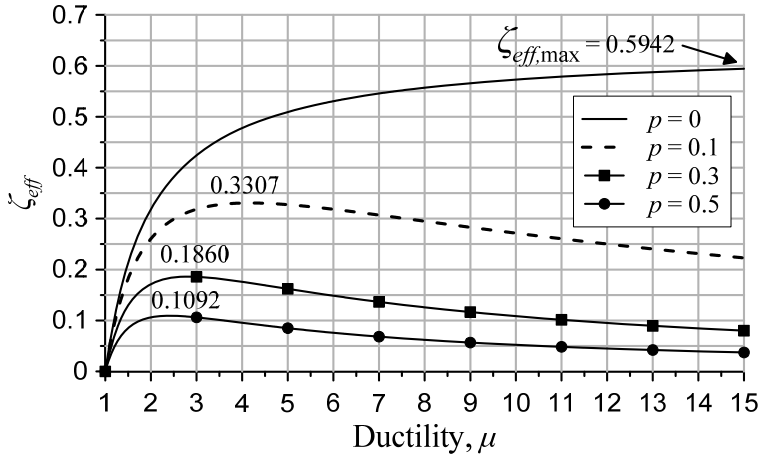

Figure 2.3 Relationship between ductility μ and effective damping ratio ζ_{eff}

The plots in Figure 2.3 are reproduced here from the following equations shown in the paper by Kasai et al, where $h_0 = 0$.

$$\zeta_{eff} = h_0 + \frac{2(1-p)(\mu-1)}{\pi\mu(1-p+p\mu)} \tag{2.12}$$

According to the ASCE 7-10 code, the displacement of the isolation system D_M is given as shown in the following Equation. This D_M will be used for u_m derived previously.

$$D_M = \frac{gS_{M1}T_{eff}}{4\pi^2 B} \tag{2.13}$$

where g is the gravitational acceleration, S_{M1} is the MCE 5% damped spectral acceleration at 1-sec period, in units of g-s (equals to 1.35 in this study), T_{eff} is the effective period, in seconds, of the seismic isolated structure, and B is the damping reduction factor which depends on the effective damping ratio ζ_{eff} tabulated in the ASCE code. The table for B is reproduced here as shown in Table 1. In this chapter, the same suite of ground motions (LA21 – LA40) will be used. And the location is Los Angeles area. So, S_{M1} equal to 1.35.

Effective Damping Ratio, ζ	***B***
≤ 0.02	0.80
0.05	1.00
0.10	1.20
0.20	1.50
0.30	1.70
0.40	1.90
≥ 0.50	2.00

As an example, for a selected base isolation property having the effective period T_{eff} and the effective damping ratio ζ_{eff} = 0.1 and given a post-yield stiffness p, we can obtain D_M from Equation (2.13). Then substituting D_M into u_m term in Equation (2.10) gives the yield displacement u_y. Then from u_y, k_d and k_r can then be obtained from Equations (2.7) and (2.6), respectively.

If 3-, 9-, and 20-story base isolated structures having effective isolation periods T_{eff} of 2, 3, and 4 seconds respectively and effective isolation damping ζ_{eff} = 0.10 are selected for investigation. And the post-yield stiffness ratios p considered are 0.1 and 0.3. To show the relationship between the displacement and the effective damping in the bilinear system, the equation is simply derived as shown below.

$$\zeta(u) = \frac{E_D}{4E_{S0}} = \frac{4k_d u_y (u - u_y)}{4\pi \frac{1}{2} k_{eff} u^2} = \frac{2k_d u_y (u - u_y)}{\pi \left(\frac{k_d u_y}{u} + k_r \right) u^2} \tag{2.14}$$

Figure 1 shows the results of Equation (2.14) corresponding to the selected case studies. T_{eff} = 2, 3, and 4 lines are for the 3-, 9-, and 20-story structures respectively.

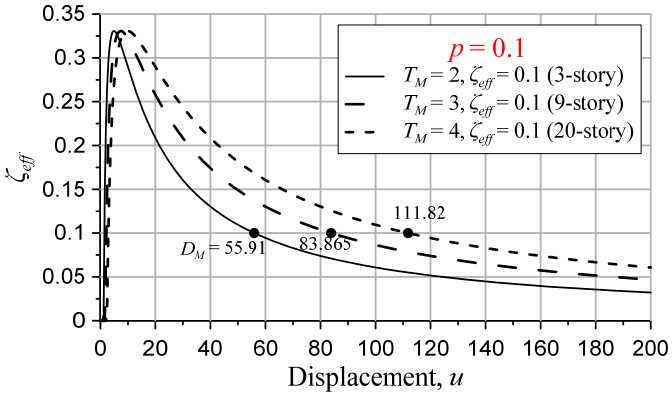

(a) Post-yield stiffness p = 0.1

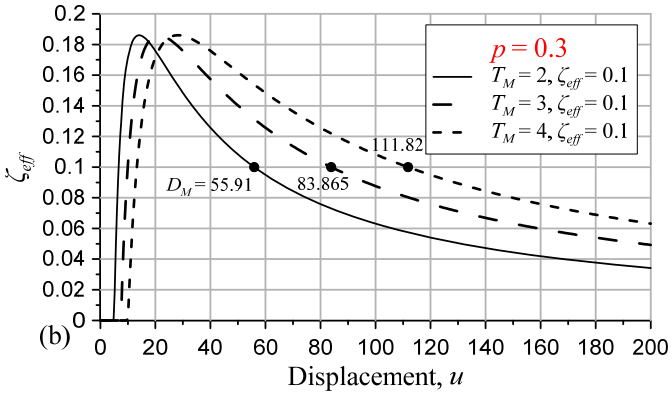

(b) Post-yield stiffness p = 0.3

Figure 2.4 Relationship between displacement u and effective damping ratio ζ_{eff}:

(a) p = 0.1 and (b) p = 0.3

D_M values in the figure are obtained from Equation (2.13) for each structure. It can be seen that the maximum effective damping ratio is limited to some level which is also corresponding to Figures 2.2 and 2.3. Before yielding of the isolator, the damping is zero, and increases rapidly at very small displacements, and then reduces as the displacement becomes larger. The rate of damping reduction after the peak in small post-yield stiffness ratio (p = 0.1) are greater than p = 0.3 as shown clearly. This shows that during the cyclic response of the isolation level, when the displacement reaches the design point, the effective damping ratio is equal to 10%. However, during smaller cyclic responses, the damping produced could be larger than 10%, especially in the p = 0.1 case, it could almost reach 35% of the damping ratio if the structure were subjected to small earthquake.

2.2.2 Responses of base-isolated structures

We want to compare the responses in this chapter with those obtained in the previous chapter. Hence, the response demands of interest will be drift ratio and floor acceleration. However, firstly, the comparison of the base displacement between the ViscoElastic (VE) in the previous chapter and the ElastoPlastic (EP) in this chapter will be made in order to preliminary verify the validity of the model. Also a simple SDOF model will also be made to compare. The analytical SDOF model is briefly described below.

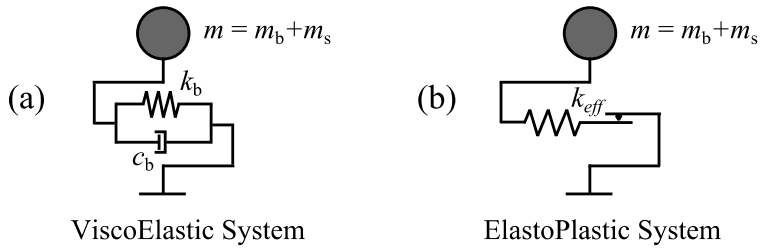

Figure 2.5 Single-degree-of-freedom (SDOF) models for
(a) ViscoElastic system and (b) ElastoPlastic system

Figure 2.5 shows the analytical model for a SDOF system for both ViscoElastic and ElastoPlastic systems. This system is associated with a rigid mass mounted on a single isolator. The mass m represents the total mass above the isolation system, including both structure mass m_s and base mass m_b. For the ViscoElastic system, Figure 2.5(a), the stiffness k_b and dashpot c_b are selected to represent the desired isolation period T_b and damping ratio ζ_b. The stiffness and dashpot are obtained from the Equations below. The mass m_b is equal to one and the mass m_s is equal to the summation of masses in all floors. Assume each floor mass is equal to one, then $m_s = N$ where N is the total number of stories above the isolation level.

$$k_b = \frac{4\pi^2}{T_b^2}\left(m_b + m_s\right) \tag{2.15}$$

$$c_b = \frac{4\pi}{T_b}\left(m_b + m_s\right)\zeta_b \tag{2.16}$$

For the ElastoPlastic system, since we want to compare with ViscoElastic system, then T_{eff} is set equal to T_b. Therefore k_{eff} can be obtained from Equation (2.17). The other parameters can be obtained as described in the previous section.

$$k_{eff} = \frac{4\pi^2}{T_{eff}^2}\left(m_b + m_s\right) \tag{2.17}$$

The case studies for this investigation is listed below.

1) 3-story ViscoElastic (VE) system ($T_b = 2$, $\zeta_b = 0.10$)
2) 9-story ViscoElastic (VE) system ($T_b = 3$, $\zeta_b = 0.10$)
3) 20-story ViscoElastic (VE) system ($T_b = 4$, $\zeta_b = 0.10$)
4) 3-story ElastoPlastic (EP) system ($T_{eff} = 2$, $\zeta_{eff} = 0.10$, $p = 0.1$)
5) 9-story ElastoPlastic (EP) system ($T_{eff} = 3$, $\zeta_{eff} = 0.10$, $p = 0.1$)
6) 20-story ElastoPlastic (EP) system ($T_{eff} = 4$, $\zeta_{eff} = 0.10$, $p = 0.1$)

7) 3-story ElastoPlastic (EP) system (T_{eff} = 2, ζ_{eff} = 0.10, p = 0.3)

8) 9-story ElastoPlastic (EP) system (T_{eff} = 3, ζ_{eff} = 0.10, p = 0.3)

9) 20-story ElastoPlastic (EP) system (T_{eff} = 4, ζ_{eff} = 0.10, p = 0.3)

10) 3-story ElastoPlastic (EP) system (T_{eff} = 2, ζ_{eff} = 0.10, p = 0.5)

11) 9-story ElastoPlastic (EP) system (T_{eff} = 3, ζ_{eff} = 0.10, p = 0.5)

12) 20-story ElastoPlastic (EP) system (T_{eff} = 4, ζ_{eff} = 0.10, p = 0.5)

The ground motions used are the same SAC suite of ground motions (LA21 – LA40) Each ground motion is scaled such that the acceleration S_{pa} is equal to the acceleration on the 5% damped elastic spectrum at the specified period as shown in Figure 2.6.

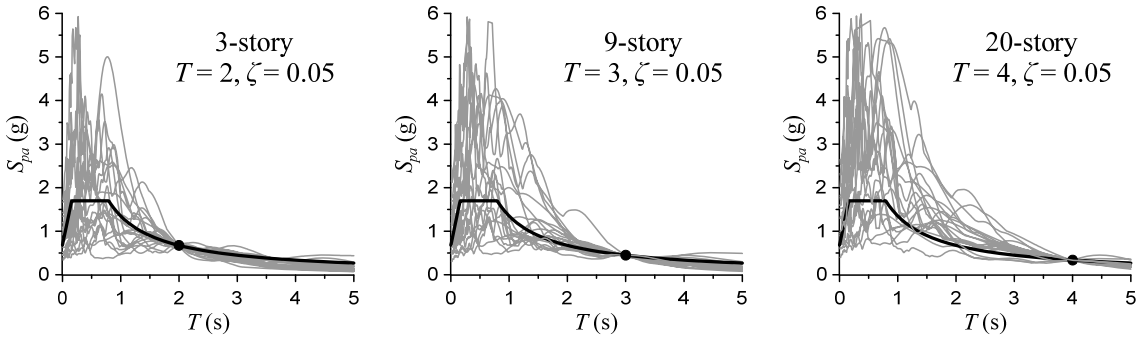

Figure 2.6 Scaled ground motions at $T = T_b = T_{eff}$

First, the comparisons between **SDOF** and **MDOF** base displacements are shown in Figures 2.7 – 2.9. Y-axis shows the ratio between the base displacement from the analysis and the maximum displacement u_m from the ASCE in Equation (2.13). (BaseDisp / u_m), indicating how much the responses are deviated from those predicted by the code.

For the case of 3-story structures, Figure 2.7(a) shows that the code-specified equation predicts quite well for short buildings. Also the responses obtained from SDOF and MDOF systems are almost identical. Figure 2.7(b–d)} also shows that the responses between and SDOF and MDOF are very similar. However, the deviation from the predicted values are larger than the VE case.

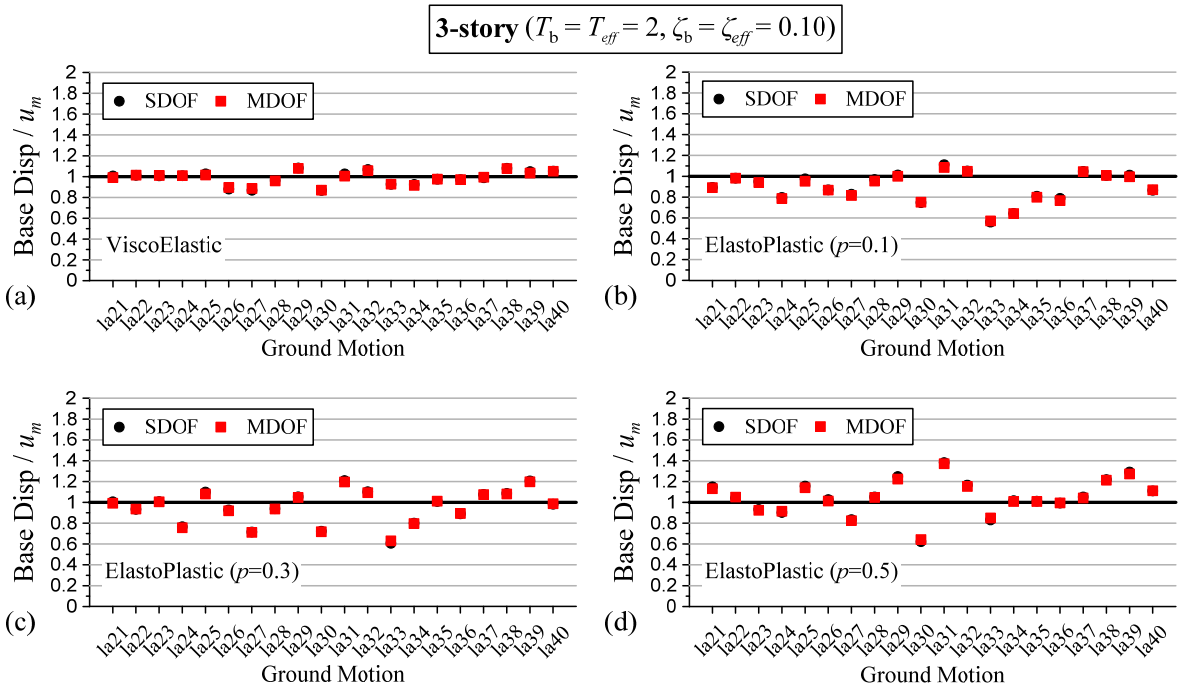

Figure 2.7 Comparison between SDOF and MDOF responses (3-story)

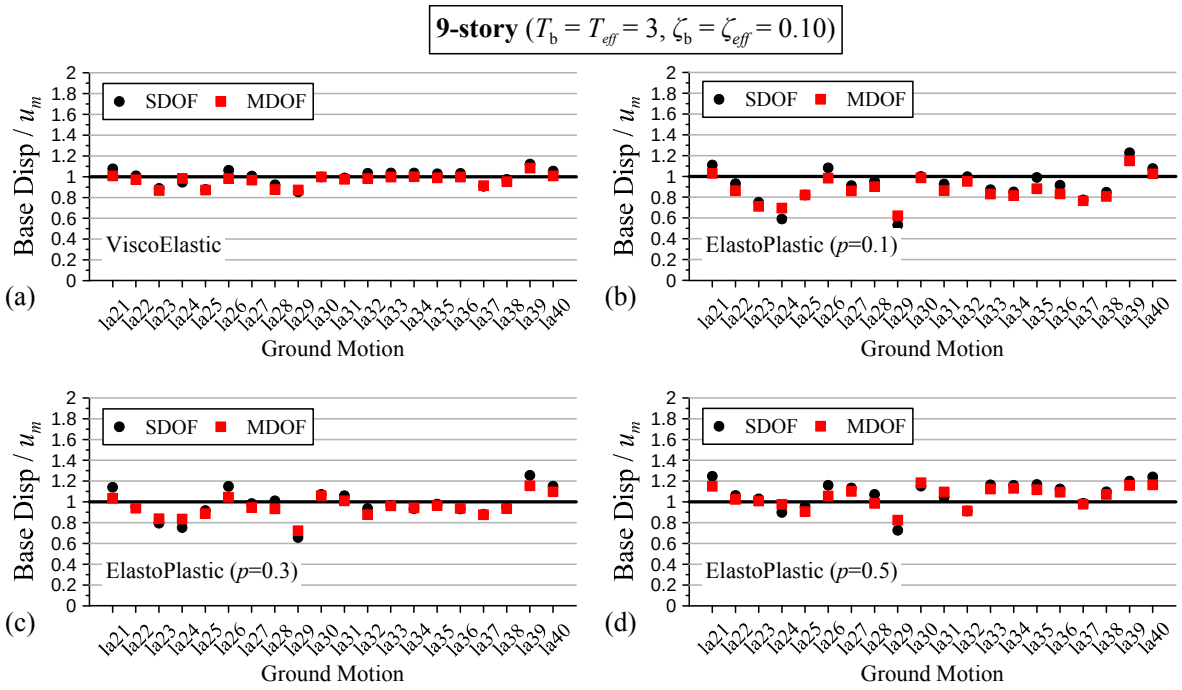

Figure 2.8 Comparison between SDOF and MDOF responses (20-story)

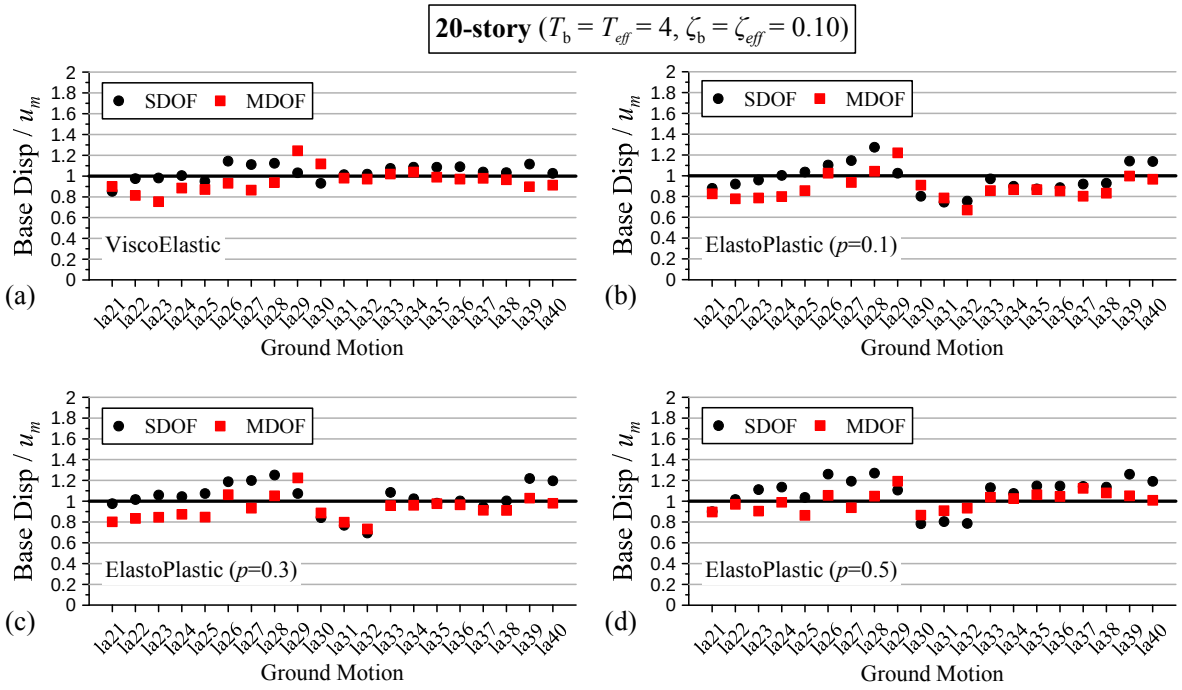

Figure 2.9 Comparison between SDOF and MDOF responses (20-story)

As the building gets taller, 9- and 20-story, the differences of the response between SDOF and MDOF systems appear more obviously, due to flexibility of the superstructure in tall buildings. It can also be observed that the responses from MDOF system are within 40% (0.6 – 1.4 in y-axis) from the code-specified value, even in tall buildings, where larger variation between SDOF and MDOF occurs. It also shows that the responses from MDOF system tend to be smaller than those of SDOF system. This indicates that with the assumption of rigid superstructure, the base displacement could be approximated reasonably well and is conservative.

Looking at the responses of the MDOF system in the ElastoPlastic (EP) cases, it can be observed that with small post-yield stiffness (p = 0.1), the predicted responses u_m from the code tend to be overestimated (Base Disp/u_m < 1.0), while for higher (p=0.5), the predicted responses tend to be underestimated (Base Disp/u_m > 1.0) as can be seen in Figures 2.7 – 2.9 (b-d).

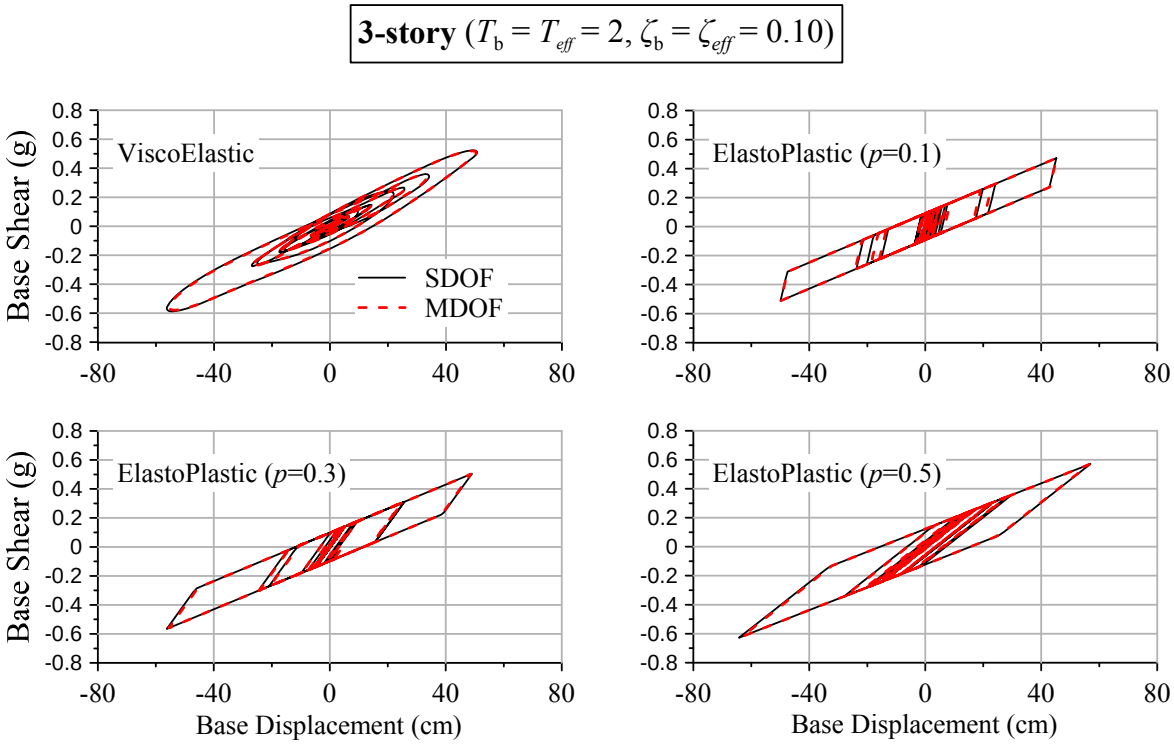

Figure 2.10 Hysteresis comparison between SDOF and MDOF (3-story)

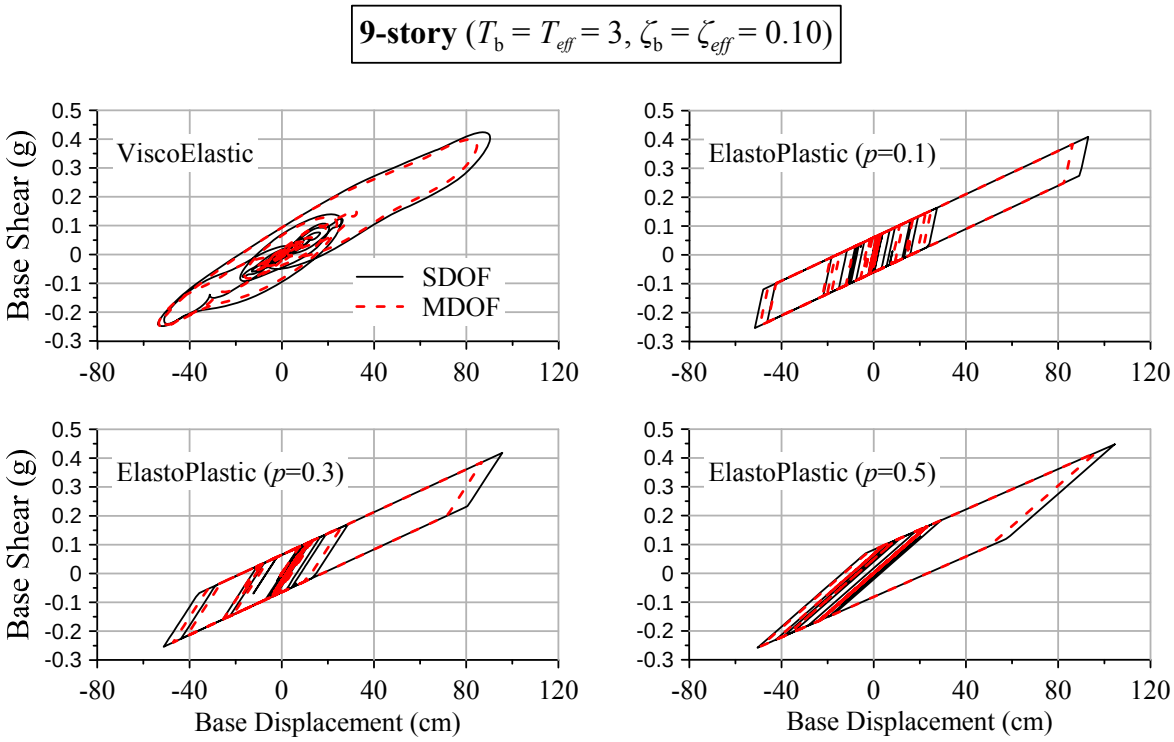

Figure 2.11 Hysteresis comparison between SDOF and MDOF (9-story)

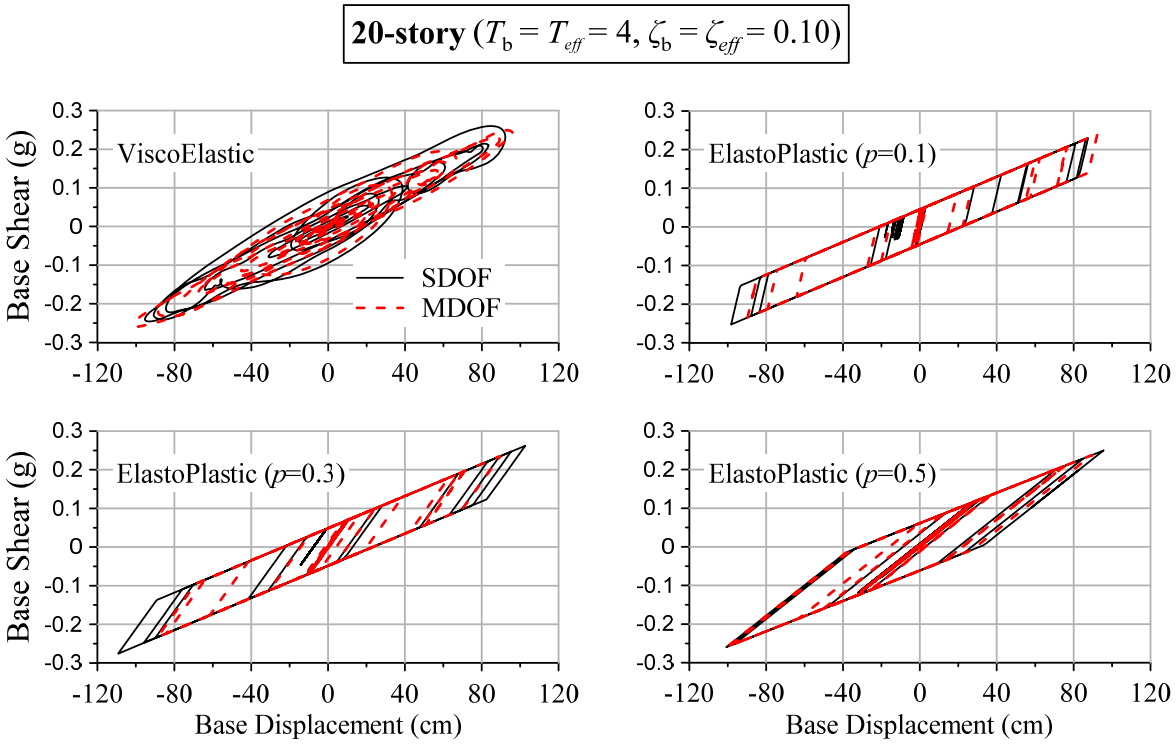

Figure 2.12 Hysteresis comparison between SDOF and MDOF (20-story)

Figures 2.10 – 2.12 show the hysteresis response comparison between SDOF and MDOF systems for the structures subjected to la21 ground motion.

For the 3-story isolated structures, the base displacements of MDOF system are almost identical to the SDOF system, not only the maximum displacement. For the 9-story isolated structures, the ViscoElastic and ElastoPlastic (p = 0.5) still seem to match well, while disagreements of the responses can be observed more in the ElastoPlastic with p = 0.1 and 0.3. It can be observed similarly for the 20-story isolated structures. These results show that the ElastoPlastic model derived in the previous section is accurate.

The comparison of MDOF building response will be made with the previous ViscoElastic case as well as the ElastoPlastic cases with different post-yield stiffness ratios p. Figures 2.13 – 2.15 show the drift ratio and acceleration median responses for the ElastoPlastic cases with p = 0.1, 0.3, and 0.5, respectively. Figure 2.16 shows the median responses for the cases of ζ_{eff} = 0.1 and p = 0.1, 0.3, and 0.5, altogether.

Compared with the median responses of the VE case in Figure 2.4, when $p = 0.1$ (Figure 2.13), the drift ratios for the 3-, 9-, and 20-story structures are slightly smaller at the lower stories but become much larger at the upper stories and for the 40-story structure, they are almost the same at the lower stories, but still much larger at the upper stories. Higher effective damping ratio ζ_{eff} tends to increase the drift ratios at the upper stories more. For the floor accelerations, they seem to concentrate in lower and upper floors, unlike the VE cases, where they are mostly concentrated at the upper floors only. Also the concentration at the upper floors appear to be more significant. Higher effective damping ratio ζ_{eff} also causes higher acceleration concentrations in the upper stories.

Comparison between different post-yield stiffness ratios p in Figure 2.16 shows that higher post-yield stiffness ratio p tends to increase the drift ratios in all cases as can be seen that red lines are almost always highest. However, it tends to reduce the acceleration concentration at the lower floors, but it could increase and also decrease the acceleration at the upper stories.

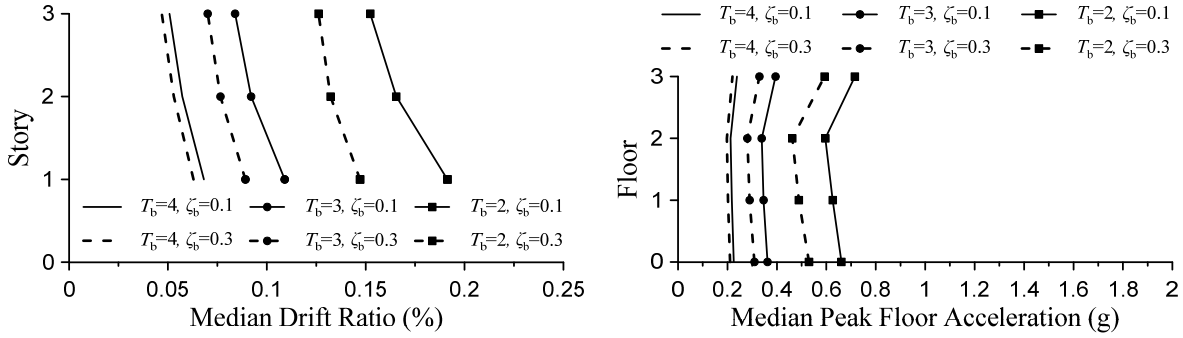

(a) 3-story

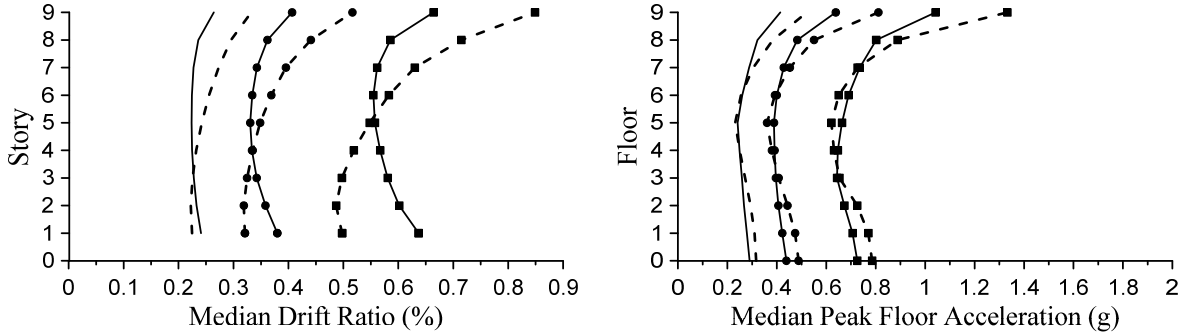

(b) 9-story

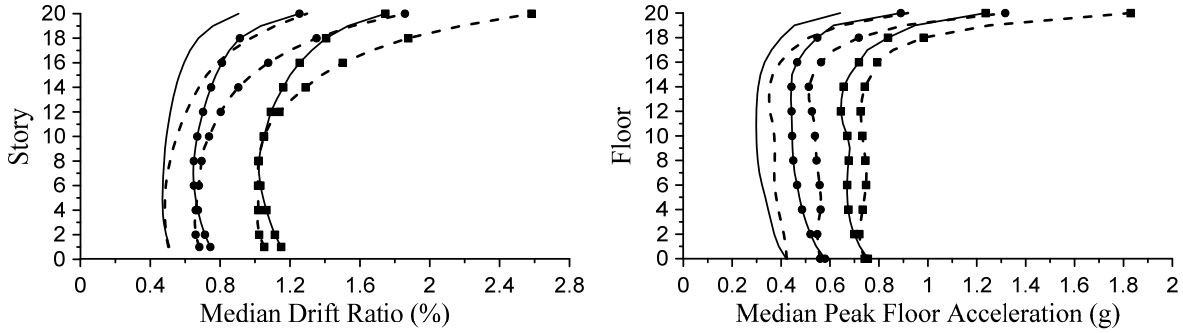

(c) 20-story

Figure 2.13 Median responses for

(a) 3-story, (b) 9-story, and (c) 20-story (p = 0.1)

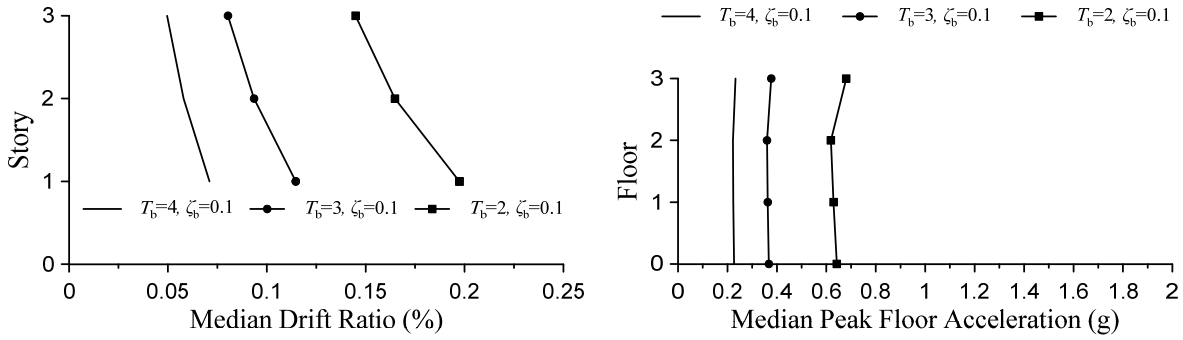

(a) 3-story

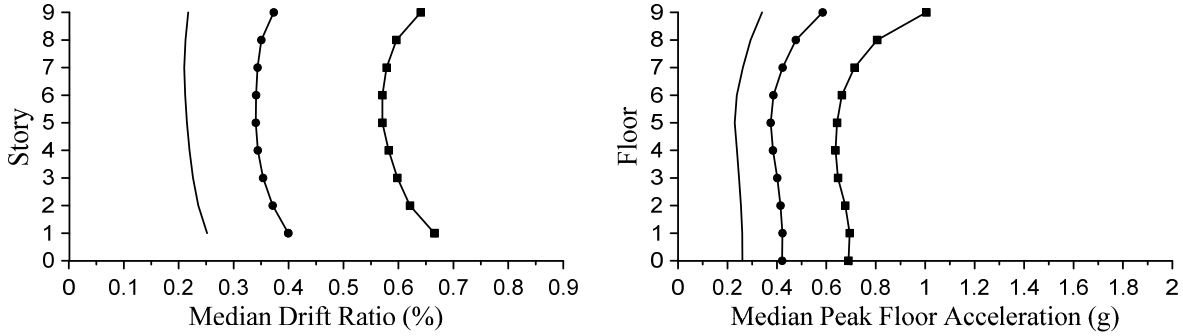

(b) 9-story

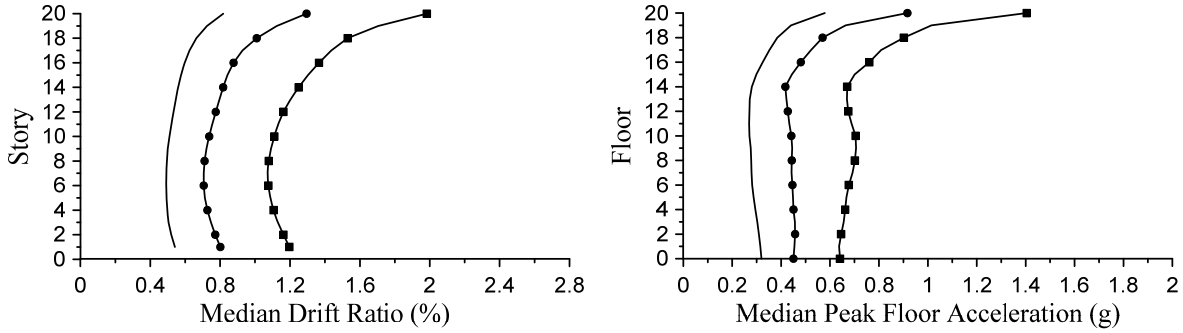

(c) 20-story

Figure 2.14 Median responses for

(a) 3-story, (b) 9-story, and (c) 20-story (p = 0.3)

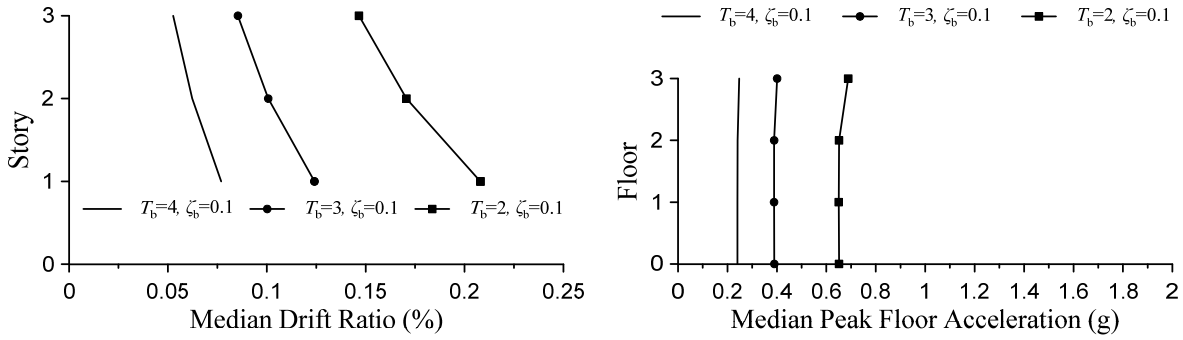

(a) 3-story

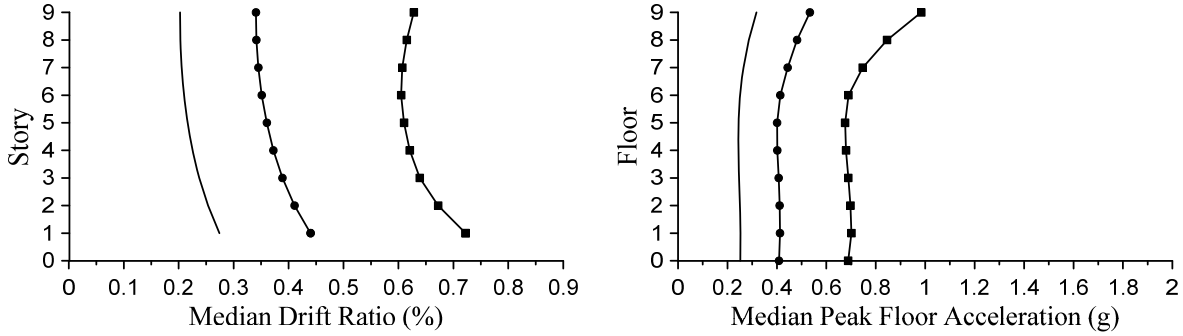

(b) 9-story

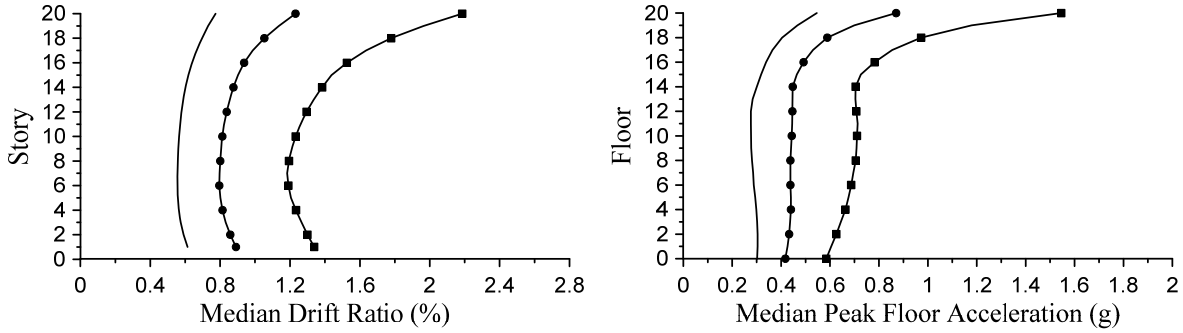

(c) 20-story

Figure 2.15 Median responses for

(a) 3-story, (b) 9-story, and (c) 20-story (p = 0.5)

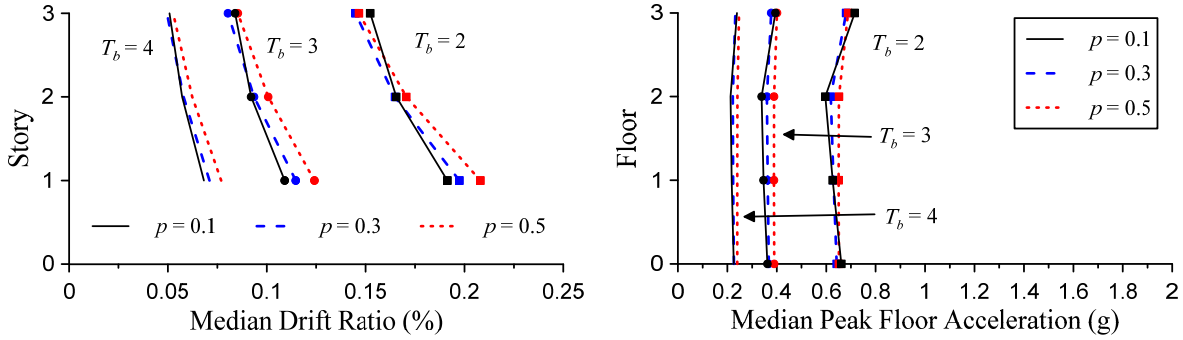

(a) 3-story

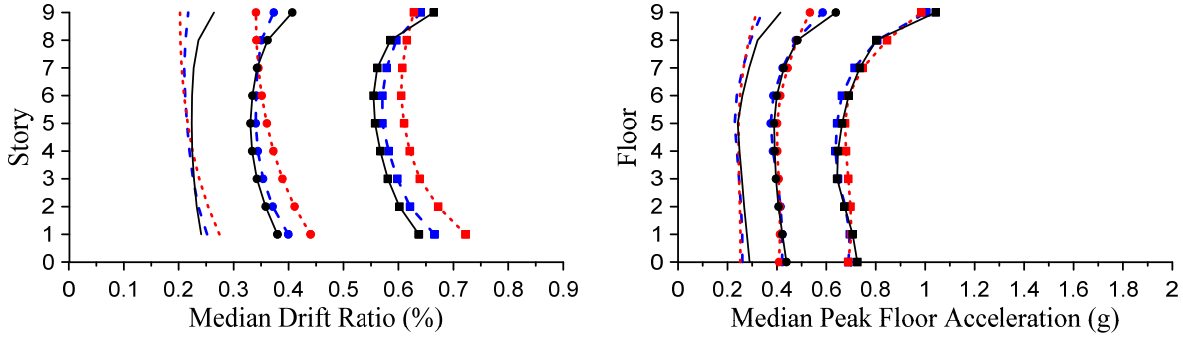

(b) 9-story

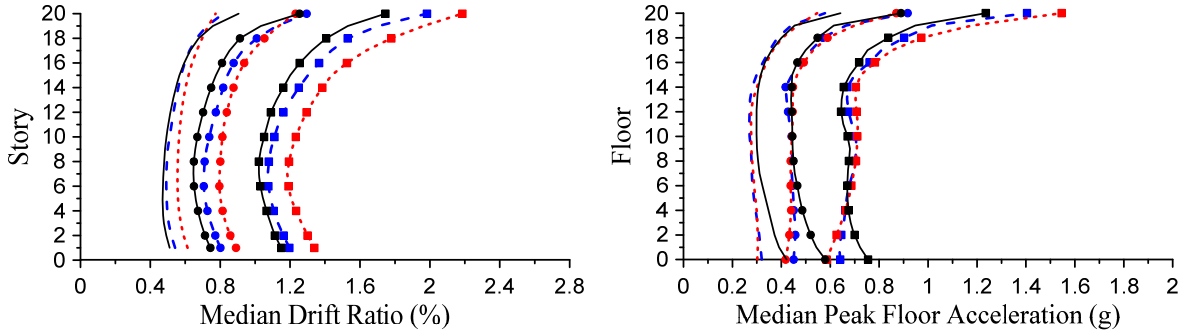

(c) 20-story

Figure 2.16 Median responses for (a) 3-story, (b) 9-story, and (c) 20-story base-isolated structures ($\zeta_{eff} = 0.1$ and $p = 0.1,0.3,0.5$)

2.2.3 Floor response spectra

Floor response spectra (FRS) with 3% damping ratio are produced by using the absolute floor acceleration at the roof of the structures. Figure 2.17 shows the floor response spectra (FRS) of the base-isolated structures with various post-yield stiffness ratios p together with those of the ViscoElastic system. These results represent the median values of the FRS from all of the floor accelerations.

Compared with the ViscoElastic isolation system cases, ElastoPlastic system cases with p = 0.1 shows that the acceleration response is reduced largely at the 1st mode period and increased at the 2nd mode for the 3-story, and 2nd and 3rd modes for the 9- and 20-story structures. When p is increased, the acceleration response becomes smaller at the 1st mode period, but larger at the higher mode periods. When p = 0.5, the acceleration is approximately equal to the VE case at the 1st mode period, but larger at the higher mode periods. These results indicate clearly that ElastoPlastic isolation system will always cause higher mode contribution more than ViscoElastic isolation system.

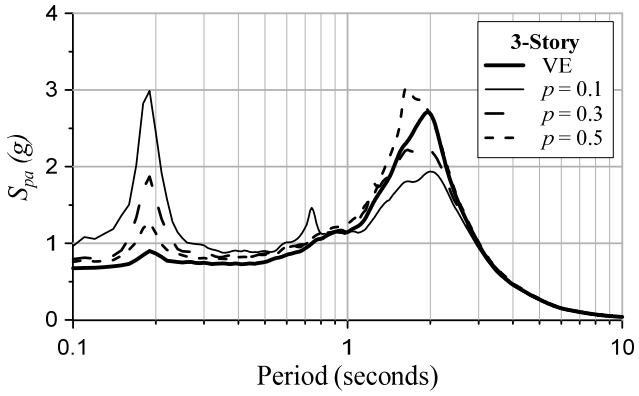

(a) 3-Story (T_{eff} = 2 seconds, ζ_b = 0.1)

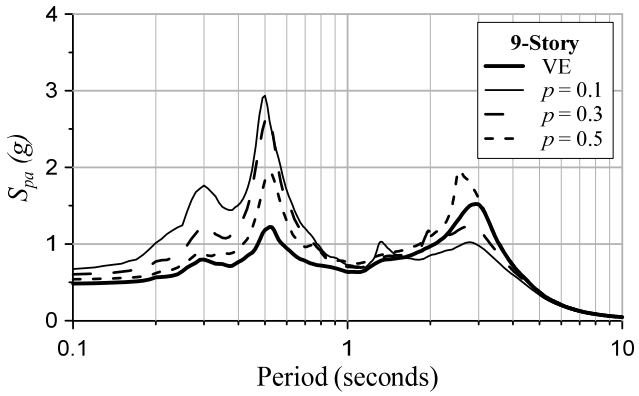

(b) 9-Story (T_{eff} = 3 seconds, ζ_b = 0.1)

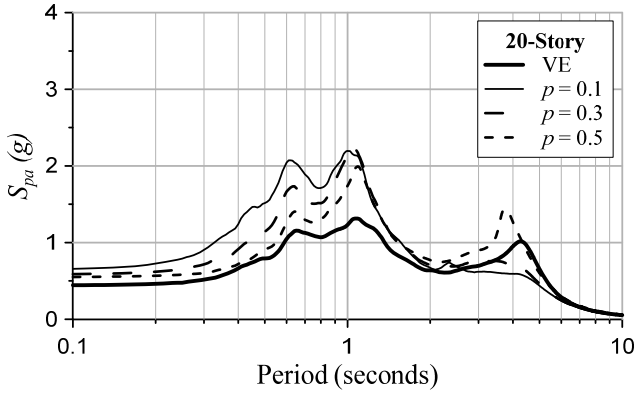

(b) 20-Story (T_{eff} = 4 seconds, ζ_b = 0.1)

Figure 2.17 Floor response spectra at the roof of the base-isolated structures having ViscoElastic system and ElastoPlastic system with various post-yield stiffness ratios p = 0.1, 0.3, and 0.5

CHAPTER 3

RESPONSE COMPARISON WITH CONVENTIONAL STRUCTURES

3.1 Modelling of Fixed-Base Structures

In order to observe how significant base-isolated structures are superior to those conventional fixed-base structures, the response comparisons are conducted in this chapter. Also, from the previous chapters, since the responses between the ViscoElastic and ElastoPlastic isolation system are not significant, from this chapter, only the base-isolated structures with ViscoElastic isolation systems will be used for comparison.

3.1.1 Equivalent lateral static force

Similar to the base-isolated structures, the analytical model for a generic MDOF system is represented in this study by a shear beam (stick) model. An example model for 3-story fixed-base structure is shown in Figure 3.1.

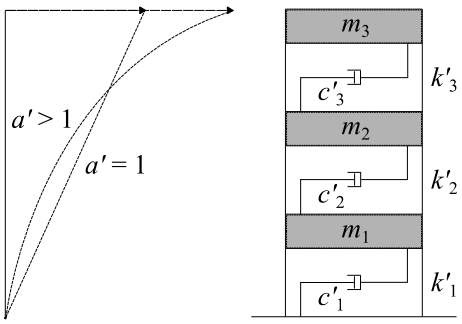

Figure 3.1 Equivalent lateral force profile and analytical model of fixed-base structures (Example of 3-Story)

The mass in each floor $m_i \left(i = 1 \text{ to } N\right)$ is assumed to be equal. Story heights are assumed to be equal in all stories. The equivalent lateral seismic force is determined corresponding to the code as follows

$$F'_x = \frac{w_x h_x^{a'}}{\sum_{i=1}^{N} w_i h_i^{a'}} V'_s \tag{3.1}$$

where w_i and w_x are portion of the total effective seismic weight of the structure located or assigned to level i or x, h_i and h_x are height from the base to level i or x, a' is an exponent related to the structure period T'_s, and V'_s is design base shear for the fixed-base structures.

According to the code, for fixed-base structures, $1 \le a \le 2$ varies according to the fundamental vibration period of the fixed-base structure, which will result in different lateral force profiles for different fixed-base structures.

3.1.2 Stiffness, period, and damping of fixed-base structures

According to the code, firstly the superstructure period is approximated. This period is used to determine the design base shear and force profile. The stiffness matrix is then obtained such that it satisfies uniform drift limit under the previously obtained force profile. The calculated period of the building is obtained from the stiffness matrix. However, the code specifies the limit of superstructure period. Therefore, if the calculated period violates this limit, the stiffness matrix is adjusted so that it satisfies the maximum limited period. The detail is described as follows.

The maximum drift ratio due to design lateral force shall not exceed 0.02 of the story height. Taken into account the deflection amplification factor $C'_d = 5.5$, the necessary stiffness for each story, in the stiffness matrix $\underset{\sim}{K}'_s$, which is of tri-diagonal form, can be determined by solving simultaneous equations below

$$\underset{\sim}{K}'_s \underset{\sim}{u} = C'_d \underset{\sim}{F}' \tag{3.2}$$

where $\underset{\sim}{F}'$ is the force vector from F'_x in Equation (3.1) and $\underset{\sim}{u}$ is the displacement vector indicating uniform story drift of 0.02 along the structure height. The calculated vibration period T'_{sj} and mode shape $\underset{\sim}{\phi}'_{sj}$ of the structure for the j^{th} mode are then obtained by solving eigenvalue problem in the following Equation:

$$\left[\underset{\sim}{K}'_s - \left(\frac{2\pi}{T'_{sj}} \right) \underset{\sim}{M}_s \right] \underset{\sim}{\phi}'_{sj} = \underset{\sim}{0} \tag{3.3}$$

where $\underset{\sim}{M}_s$ is the diagonal mass matrix known from the story mass explained earlier. Note that the mode shape $\underset{\sim}{\phi}'_{s1}$ will be not triangular if the force profile $\underset{\sim}{F}'$ is not triangular, that is $a' \neq 1$. Use of the calculated period T'_{s1} longer than the approximate period T'_s but smaller than $1.4T'_s$ is permitted by the code. Generally, the calculated period T'_{s1} will be longer than the approximate period T'_s. Hence, the reduction of design force is allowed, which will render the structure more flexible. However, this approach is not utilized. From previous study, most of the measured building periods for moment resisting steel frame structures fall in the range of T'_s and $1.6T'_s$. Therefore, in this study, the objective is to get the structure at the period of $1.4T'_s$ which is corresponding to limitation by the code. To achieve this, the stiffness matrix $\underset{\sim}{K}'_s$ is revised by using $\left(T'_{s1} / \min\left[T'_{s1}, 1.4T'_s \right] \right)^2$ to scale the stiffness entries. It can be seen that if $T'_{s1} < 1.4T'_s$, the scaling factor will be 1.0, while if $T'_{s1} \geq 1.4T'_s$, the scaling factor will be greater than 1.0, resulting in higher stiffness than the previously obtained stiffness, but still give period equal to $1.4T'_s$.

In this study, 3-, 9-, and 20-story fixed-base structures are considered. Considering each story height of 3.5m, the approximate formula gives $T'_s = 0.0724h^{0.8} =$ 0.475, 1.14, and 2.17 seconds, respectively. After apply the method described above, the actual periods of the fixed-

base structures are shown in Table 3.1. The structure is modeled to exhibit bilinear behavior with the post-yield stiffness 0.1 times the initial stiffness.

Table 3.1 Natural periods of the fixed-base structures (seconds)

	Mode						
Structure	**1**	**2**	**3**	**4**	**5**	**6**	**7**
3-Story	0.655	0.271	0.172	-	-	-	-
9-Story	1.579	0.633	0.400	0.293	0.232	0.192	0.164
20-Story	3.034	1.182	0.746	0.546	0.431	0.356	0.304

As for the damping, the viscous coefficients are determined considering Rayleigh damping model. i.e.,

$$\underset{\sim}{C}_s' = \alpha' \underset{\sim}{M}_s + \beta' \underset{\sim}{K}_s' \tag{3.4}$$

where $\underset{\sim}{C}_s'$ is the damping matrix, and α' and β' are the mass- and stiffness-proportional damping coefficients that are to be set for the desired damping ratios at two selected vibration periods, T_1 and T_2. Superstructure damping ratio $\zeta_s = 0.02$ is assumed. Table 3.2 lists the modal damping ratios of the considered fixed-base structures.

Table 3.2 Damping ratios of the fixed-base structures

	Mode						
Structure	**1**	**2**	**3**	**4**	**5**	**6**	**7**
3-Story	0.02	0.02	0.0261	-	-	-	-
9-Story	0.02	0.02	0.0262	0.0335	0.0410	0.0487	0.0564
20-Story	0.02	0.02	0.0264	0.0338	0.0415	0.0494	0.0574

3.1.3 Comparison of design base shears with the base-isolated structures

For the fixed-base structures, the design base shear V_s' is obtained from the following Equation,

$$V_s' = \min\left[\frac{S_{DS}}{R/I_e}W_s, \frac{S_{D1}}{T_s'\left(R/I_e\right)}W_s\right] \tag{3.5}$$

where S_{DS} is the design spectral response acceleration parameter in the short period range which is equal to 1.13g, S_{D1} is the design spectral response acceleration parameter at a period of 1.0s which is equal to 0.9g, R is the reduction factor which is equal to 8, I_e is the importance factor which is one, T_s' is the superstructure period, and W_s is the total weight of the superstructure.

For the base-isolated structure, the period of the superstructure above the isolation level is approximated as $T_s = 0.1N$, mentioned previously. However, unlike the fixed-base structure, the design superstructure shear is not determined by using T_s but instead using the stiffness and maximum force of the isolator at the design displacement from the code equation as follows

$$V_s = \frac{k_b D_D}{R_I} \tag{3.6}$$

where k_b is the lateral stiffness of the isolator, R_I is the reduction factor which is equal to 3/8 of the R for the fixed-base structure and must be less than 2, hence, $R_I = 2$, and D_D is the design displacement which is $gS_{D1}T_b/\left(4\pi^2 B\right)$. In this study, the isolation system is idealized by using a viscoelastic system, hence the isolation period T_b indicates the base isolation period linearized from nonlinearity at a certain displacement. Certainly the response will vary according to the hysteretic behavior of the isolation system. However, in order to study the fundamental trend of base isolated structure, the idealized viscoelastic system is utilized. Substituting D_D into Equation (3.6) and further manipulating by using $k_b = m\left(2\pi/T_b\right)^2$, where m is the total mass of the building including the isolation level, produce the following Equation:

$$V_s = \frac{k_b g S_{D1}\left(T_b / 4\pi^2\right)}{R_I}\frac{1}{B} = \frac{m\left(2\pi / T_b\right)^2}{R_I}\frac{g S_{D1} T_b}{\left(2\pi\right)^2}\frac{1}{B}\frac{W}{mg} = \frac{S_{D1}}{R_I T_b}\frac{1}{B}W \tag{3.7}$$

where W is the total weight of the building including the isolation level and B is the damping coefficient related to the isolation damping ratio ζ_b. Therefore, the relationship between V_s' and V_s is shown in the following Equation.

$$\frac{V_s}{V_s'} = \frac{R}{R_I}\cdot\frac{W}{W_s}\cdot\frac{1}{B}\cdot\max\left[\frac{S_{D1}}{S_{DS}}, \frac{1}{T_b}, \frac{T_s'}{T_b}\right] \tag{3.8}$$

In Equation (3.8), $R / R_I = 4$, $S_{D1} / S_{DS} = 0.794$, and $W / W_s = \left(N+1\right) / N$. Hence, it is possible to observe the trend which indicates when $V_s / V_s' > 1$ or vice versa by varying T_s' and T_b. Table 3.3 shows the values of V_s / V_s' for several cases of structures.

Table 3.3 V_s / V_s' for the 3-, 9-, and 20-story cases

	Isolation damping ratio = 10%, *B*=1.2			**Isolation damping ratio = 30%, *B*=1.7**		
	3-Story	**9-Story**	**20-Story**	**3-Story**	**9-Story**	**20-Story**
T_b	T_s' =0.475	T_s' =1.144	T_s' =2.167	T_s' =0.475	T_s' =1.144	T_s' =2.167
2	1.765	2.118	3.792	1.246	1.495	2.677
3	1.176	1.412	2.528	0.830	0.997	1.784
4	0.882	1.059	1.896	0.623	0.748	1.338

From Table 3.3, it is clearly shown that V_s / V_s' increases when structure becomes taller, damping is smaller, and T_b becomes shorter, and vice versa. This means that superstructure of base-isolated structure tend to be stronger than fixed base structure, while in fact when considering at the fundamental periods, it would be subjected to smaller acceleration. Therefore there is very high chance that the superstructure of base-isolated structure would remain elastic. Note that normally the effective modal mass is less than 1.0, but we assumed it to be 1.0 for comparison. This information assures the assumption of elastic superstructures of base-isolated structures used previously.

3.2 Response Comparison between Fixed-Base and Base-Isolated Structures

The same structures and SAC suite of ground motions (LA21 – LA40) defined earlier are used in this section. Both elastic and inelastic behaviors of the fixed-base structures are investigated and compared with the responses of the base-isolated structures. The responses of interest are median drift ratios and median floor accelerations.

Figure 3.2 shows that adding the isolation system to the fixed-base structure reduces the demands significantly. Comparison of the drift demands between the 3-story inelastic fixed-base and base-isolated (T_b = 2 seconds, ζ_b = 0.10) structures shows that the drift demands of the isolated structures are around 0.05 - 0.07 times those of the fixed-base structures at the top story. As the building gets taller, the reduction is small, but still exhibits much improvement. Drift concentrations at the top story of taller buildings, 9- and 20-story, are more pronounced in the inelastic fixed-base structures. Due to nonlinearity, the drift demands are much greater than those of the elastic fixed-base structures.

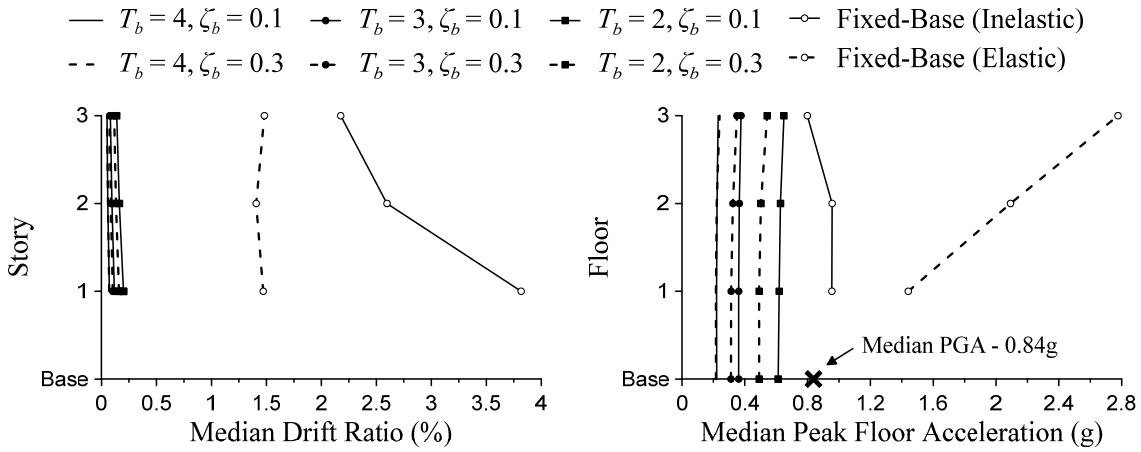

(a) 3-story base-isolated and fixed-base structures

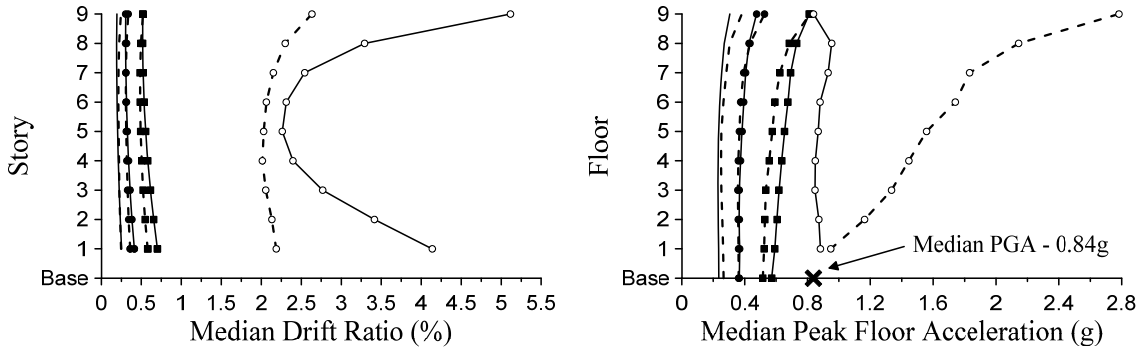

(b) 9-story base-isolated and fixed-base structures

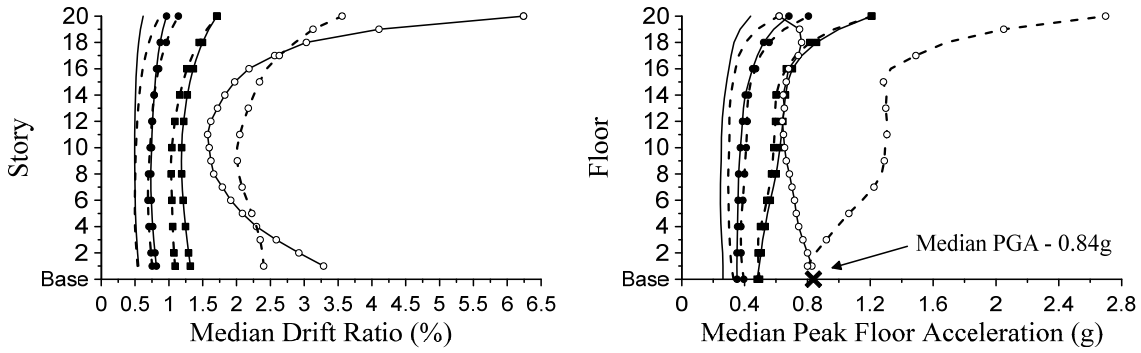

(c) 20-story base-isolated and fixed-base structures

Figure 3.2 Comparative responses of the base-isolated and fixed-base structures

Comparison of the peak floor accelerations between the fixed-base and base-isolated structures also exhibit the reduction of the acceleration demands on the superstructures. The accelerations in the upper stories of the inelastic fixed-base structures do not exhibit concentration due to nonlinearity of the structures. For the base-isolated structures, concentrations of accelerations appear in the upper stories, especially in the 20-story structures. Acceleration responses of the inelastic fixed-base structures appear to be slightly larger than the median peak ground accelerations. The responses of the isolated structures are smaller except for the case of 20-story isolated structures with $T_b = 2$ seconds. This is because T_b is the same as $T_s = 2$ seconds for the 20-story superstructure. Therefore, the effect of higher isolation period which lengthens the superstructure does not exhibit. Instead, it excited higher modes due to significant difference in the superstructure and isolation damping ratios.

In short buildings, the response could be reduced even more if the isolation system is more flexible by increasing the isolation period T_b. And for tall buildings, if the isolation period is appropriately larger than the superstructure period, the reduction of the response will be observed. This indicates that adding isolation system could always reduce the drift and acceleration responses on the superstructure, if T_b/T_s is larger than 1.

3.3 Floor Response Spectra

In the previous chapter, the knowledge of transfer function was introduced which was very useful in studying the property of the buildings which behave elastically. However, in this chapter, the fixed-base structures are nonlinear structures, using the estimated transfer function in the previous chapter will not produce the results correctly. Therefore, in this chapter, floor response spectra is utilized instead to examine the response contribution for each mode.

Floor response spectra (FRS) with 3% damping ratio are produced by using the absolute floor acceleration at the roof of the structures. Figure 3.3 shows the FRS of the inelastic fixed-base and base-isolated structures. These results represent the median values of the FRS from all of the floor accelerations.

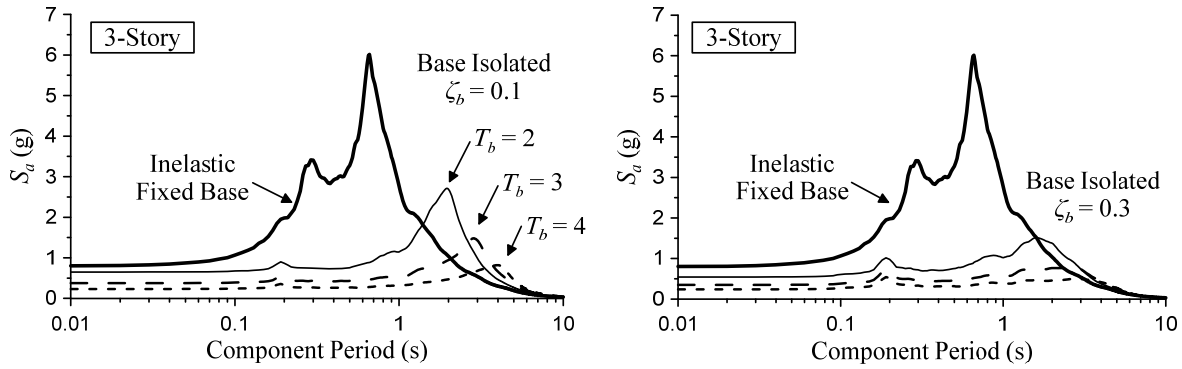

(a) 3-story fixed-base and base-isolated structures

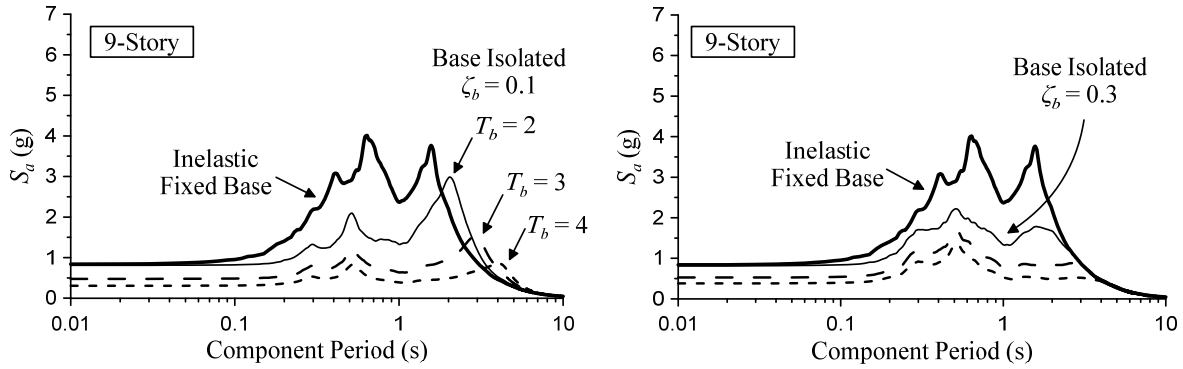

(b) 9-story fixed-base and base-isolated structures

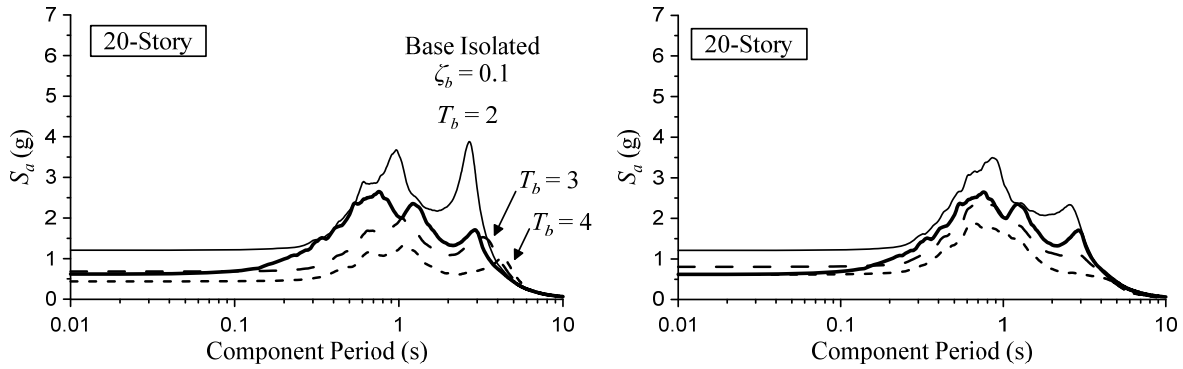

(c) 20-story fixed-base and base-isolated structures

Figure 3.3 Floor response spectra at the roof of the fixed-base and base-isolated structures: (Left) median acceleration ($\zeta_b = 0.1$) and (Right) median acceleration ($\zeta_b = 0.3$)

From Figure 3.3, increase of the isolation period T_b reduces the pseudo acceleration significantly. This is clear why increasing the isolation period T_b always improves the performance or reduces the demands induced on the superstructure. Increasing the isolation damping also decreases the first mode response, however, it tends to excite higher mode responses. This figure shows clearly the 2nd and 3rd mode response contributions are high, especially when isolation damping ratio ζ_b is increased.

Comparison between the fixed-base structures and base-isolated structures with $T_b = 2$ seconds and $\zeta_b = 0.10$ shows that the maximum acceleration reduces approximately by half at the 1st mode natural period for the 3-story structures, and reduces less significantly for the 9-story structures. And in the 20-story structures, the acceleration response of the base-isolated

structure becomes even greater than that of the fixed-base structure. For both 9- and 20-story isolated structures, responses from the 2nd mode becomes more apparent at the top story. The higher mode contribution could be attributed to the code assumption of triangular force profile used for base-isolated structures. The stiffnesses in the upper stories are not sufficiently provided.

The acceleration response results in smaller reduction or even greater amount for the 9- and 20-story structures because the isolation period T_b of 2 seconds is getting close to the superstructure period T_s of 0.9 and 2 seconds. Therefore, for taller buildings, the improvement is usually achieved by increasing the isolation period T_b such that it is far and practical to implement from the superstructure period T_s. The improvement would still be observed. Despite the slight improvement, this serves as a proof that adding a flexible isolated system always improves the superstructure resting on it, when appropriately isolation period T_b is assigned.

CHAPTER 4

PROBABILISTIC AND TIME-BASED PERFORMANCE EVALUATION METHODOLOGY

4.1 Performance Based Earthquake Engineering (PBEE)

The framework for performance-based earthquake engineering at the Pacific Earthquake Engineering Research Center (PEER) during the period 1997 – 2010. The PEER framework (Moehle and Deierlein, 2004) applies the total probability theorem to predict earthquake consequences in terms of the probability of incurring particular values of performance measures or outcomes including casualties, repair costs, and downtime. Figure 4.1 shows the underlying probabilistic framework.

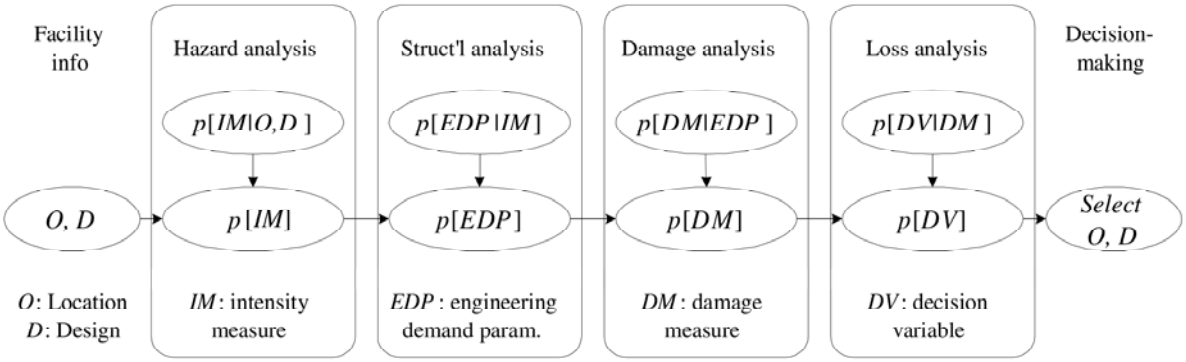

Figure 4.1 Underlying probabilistic framework

The framework can be used to develop three different types of performance assessment: intensity-based, scenario-based, and time-based assessments. In brief, intensity-based assessments evaluate a building's probable performance assuming that it is subjected to a specified earthquake shaking intensity. Scenario-based assessments evaluate a building's

probable performance assuming that it is subjected to a specified earthquake scenario consisting of a specific magnitude earthquake occurring at a specific location relative to the building site. Lastly, time-based assessments evaluate a building's probable performance over a specified period of time considering all the earthquakes that could occur in that time period, and the probability of occurrence associated with each earthquake. In this research, time-based approach will be utilized. Also, for base-isolated structures, the response demands occurred on the superstructures are generally small which do not cause collapse of the nonstructural components. Instead, minor damage state that disrupts the continued functionality of the building is more of concern. Therefore, in this research, the number of years (or return period) that the damage on the considered nonstructural component in the base-isolated building is expected to exceed continued functionality will be investigated. The derivation is shown in the following section.

4.1.1 Derivation of equation for performance evaluation

In this framework, seismic hazard analysis, structural analysis, and damage analysis are used concurrently. The hazard analysis is used to define the seismic intensity at a specific location and mean annual frequency of exceedance of the ground shaking intensity. Structural analysis is conducted by response history analysis using a suite of ground acceleration records to obtain various responses at multiple levels of seismic intensity. These responses are called engineering demand parameters (*EDP*). Damage analysis, obtained from experimental data and damage observations of structural components, nonstructural components, or building contents, describes the likelihood of exceeding predefined damage states (*DM*) as a function of engineering demand parameter (*EDP*). Brief derivation of the equation is described in the following.

Start by considering a site characterized by a seismic hazard curve $\lambda(s) = P\left[S > s \,\middle|\, 1 \text{ year}\right]$, where S is some random spectral acceleration at a natural period T. This function λ indicates the annual frequency of exceedance of the ground shaking intensity.

Suppose some event A is conditioned on a set of mutually exclusive events H_1, H_2, …, H_N, each with known probabilities of occurrence. Based on the total probability theorem, the likelihood of the event A can be expressed as

$$P[A] = \sum_{k=1}^{N} P\left[A \middle| H_k\right] P[H_k]. \tag{4.1}$$

Suppose the damage state DM is of interest and the response parameter that causes this damage is drift ratio δ. Then Equation (4.1) can be recast as the probability that the DM damage state is exceeded shown in Equation (4.2).

$$\lambda_{DM} = P\left[DM \,\middle|\, 1 \text{ year}\right] = \sum_{k=1}^{N} \underbrace{P\left[DM \middle| \delta = \delta_k\right]}_{\text{Fragility}} P[\delta = \delta_k] \tag{4.2}$$

The variable λ_{DM} is the mean annual frequency of exceeding DM. The probability $P[\delta = \delta_k]$ is the probability mass function (PMF) of the drift ratio δ over some one-year period, and will depend on the structural system and the seismic environment. Through IDA from a suite of ground motions, it is possible to estimate the drift ratio δ as a function of spectral acceleration s. Note that due to record-to-record variability of a suite of ground motions, two earthquakes with the same spectral acceleration s will not generally induce the same drift ratio δ, which means for a fixed spectral acceleration s, it is possible to estimate for cumulative distribution function (CDF) or probability distribution function (PDF) of the drift ratio δ. Combining the IDA and the hazard curves gives an expression for the PMF of the drift demand shown in Equation (4.3).

$$P\left[\delta=\delta_k\right]=\sum_{j=1}^{M}\underbrace{P\left[\delta=\delta_k\left|S=s_j\right.\right]}_{\text{IDA}}\underbrace{P\left[S=s_j\right]}_{d\lambda(s)} \tag{4.3}$$

Combining Equations (4.2) and (4.3) gives an expression for the annual probability of exceeding *DM* damage state as

$$\lambda_{DM}=\sum_{k=1}^{N}\left\{\underbrace{P\left[DM\left|\delta=\delta_k\right.\right]}_{\text{Fragility}}\cdot\sum_{j=1}^{M}\left\{\underbrace{P\left[\delta=\delta_k\left|S=s_j\right.\right]}_{\text{IDA}}\underbrace{P\left[S=s_j\right]}_{d\lambda(s)}\right\}\right\} \tag{4.4}$$

λ_{DM} in Equation (4.4) indicates the annual probability that a structure exceeds the damage state *DM*. The expected return period T_R^{DM} can be calculated by taking the reciprocal of λ_{DM} ($T_R^{DM}=1/\lambda_{DM}$).

4.1.2 Continued functionality damage state (*CF*)

In this study, the continued functionality (*CF*) damage state is of interest and it is the damage state in which the building remains usable without interruption after earthquake. Therefore, the response demand that triggers this *CF* damage state is very slight.

The fragility curves to represent this damage state can be obtained from available researches. FEMA P-58 which describes the PEER framework methodology also provides several fragility curves for use. However, we chose to use the fragility curves from the more recent available researches. And the damages to the partition wall (drift-sensitive component) and the suspended ceiling (acceleration-sensitive component) are considered. Therefore, Equation (4.4) can be modified to fit our criteria of using the continued functionality *CF* damage state as follows:

$$\lambda_{CF}=\frac{1}{T_R}=\sum_{k=1}^{N}\left\{P\left[CF\left|\delta=\delta_k\right.\right]\cdot\sum_{j=1}^{M}\left\{P\left[\delta=\delta_k\left|S=s_j\right.\right]P\left[S=s_j\right]\right\}\right\}\ \text{(drift-sensitive)} \tag{4.5}$$

$$\lambda_{CF}=\frac{1}{T_R}=\sum_{k=1}^{N}\left\{P\left[CF\left|a=a_k\right.\right]\cdot\sum_{j=1}^{M}\left\{P\left[a=a_k\left|S=s_j\right.\right]P\left[S=s_j\right]\right\}\right\}\ \text{(accel.-sensitive)} \tag{4.6}$$

$$\lambda_{CF} = \frac{1}{T_R} = \sum_{k=1}^{N} \left\{ P\left[CF \middle| a_c = a_{c,k} \right] \cdot \sum_{j=1}^{M} \left\{ P\left[a_c = a_{c,k} \middle| S = s_j \right] P\left[S = s_j \right] \right\} \right\} \quad \text{(accel.-sensitive)} \qquad (4.7)$$

Notice that there are two equations for acceleration-sensitive components. In Equation (4.6), *a* is the floor accelerations, however, in Equation (4.7), a_c is the component acceleration which is obtained by conducting time history analysis on the component using the floor acceleration. For rigid nonstructural component anchored to the floor, the floor acceleration may directly impose damage on the component. However, for flexible nonstructural components, such as suspended ceiling, the component acceleration is more appropriate to use for damage evaluation. Therefore, in this study, Equation (4.5) will be used for performance evaluation considering *CF* of the partition wall and Equation (4.7) for the suspended ceiling.

4.1.3 Damage analysis part

The first terms, $P\left[CF \middle| \delta = \delta_k \right]$ and $P\left[CF \middle| a_c = a_{c,k} \right]$ in Equations (4.5) and (4.7) are the fragility curves which indicate the probability of exceeding the *CF* damage state as a function of drift ratio and component acceleration and they are obtained from damage analysis based on experimental data and damage observations of the components. And it is called fragility curve or fragility function. In this study, the fragility functions for the partition wall and suspended ceiling from recent available researches are utilized as described in the following.

As for the partition wall, experiments on light gauge steel studded gypsum partition walls have been conducted recently at the University of Buffalo to assess their seismic fragility. A total of fifty partition wall specimens were constructed following standard construction techniques. The fragility functions reported in their study is adopted here. The damage description corresponding to *CF* is “slight damage to partition walls”. The median drift ratio and dispersion for this damage state are 0.35% and 0.56, respectively. Figure 4.1 shows the fragility function of the partition wall (Retamales et al., 2010).

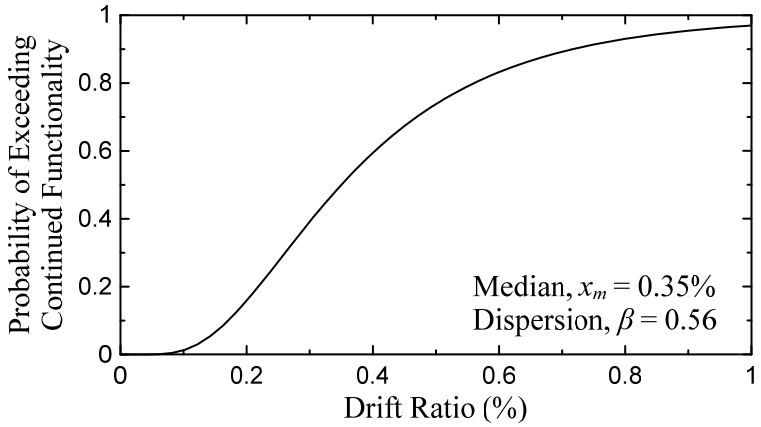

Figure 4.1 Fragility function of the considered partition wall

As for the suspended ceiling, fragility of Japanese ceiling systems is obtained through Monte Carlo analysis using 2D finite element analysis and assumed statistical variation of the strength of connections from experimental testing as a result of recent work by the Motoyui et al. The period T_c = 0.31 second and damping ratio ζ_c = 0.03 for the suspended ceiling are specified. The fragility function describing "failure of ceiling" reported in their study is used. The median acceleration and dispersion are 0.505*g* and 0.046, respectively. Figure 4.2 shows the fragility function of the suspended ceiling.

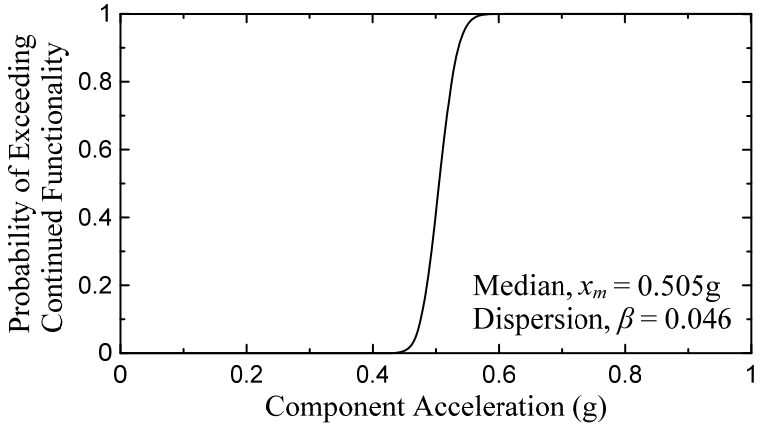

Figure 4.2 Fragility function of the considered suspended ceiling

4.1.4 Structural analysis part

The second terms, $P\left[\delta = \delta_k \middle| S = S_j\right]$ and $P\left[a_c = a_{c,k} \middle| S = S_j\right]$ in Equations (4.5) and (4.7) indicate the probability of occurrence of drift ratio and component acceleration under the ground motions for a specified intensity respectively. To cover various intensity levels, from very small to very large intensity, incremental dynamic analysis (IDA) is performed by gradually increasing the level of seismic intensity by scaling the ground motions at the fundamental period. The intensity range $\left(S_a^{\min} \le S_a \le S_a^{\max}\right)$ for the IDA are selected conforming to FEMA P-58. That is, $S_a^{\min}(T) = 0.05g$ for $T \le 1$ second and $0.05g/T$ otherwise, where T is the fundamental period of structure. And $S_a^{\max}$ is taken at λ = 0.0002 where λ is the annual frequency of exceedance of ground shaking intensity. A total of 300 intensity levels between $S_a^{\min}$ and $S_a^{\max}$ of the 20 ground motions defined earlier is used for the incremental dynamic analysis. The structures investigated are the same as those in the previous chapters.

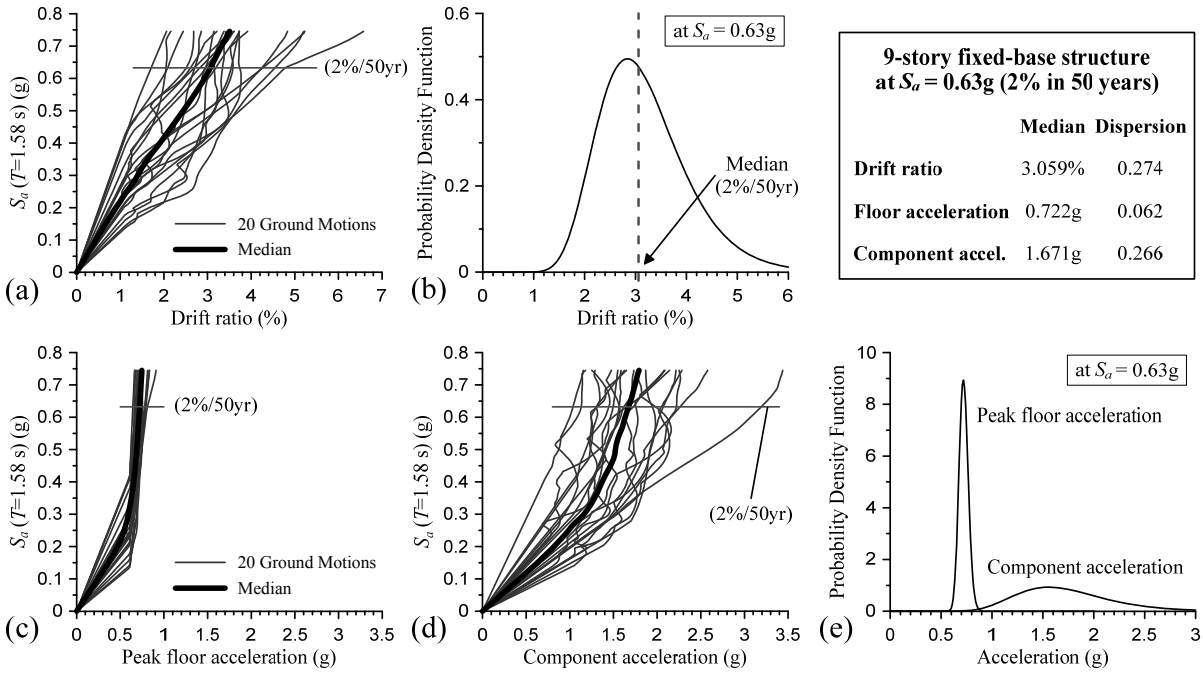

Figure 4.3 Incremental dynamic analyses results and probability density function of the 9-story fixed-base structure

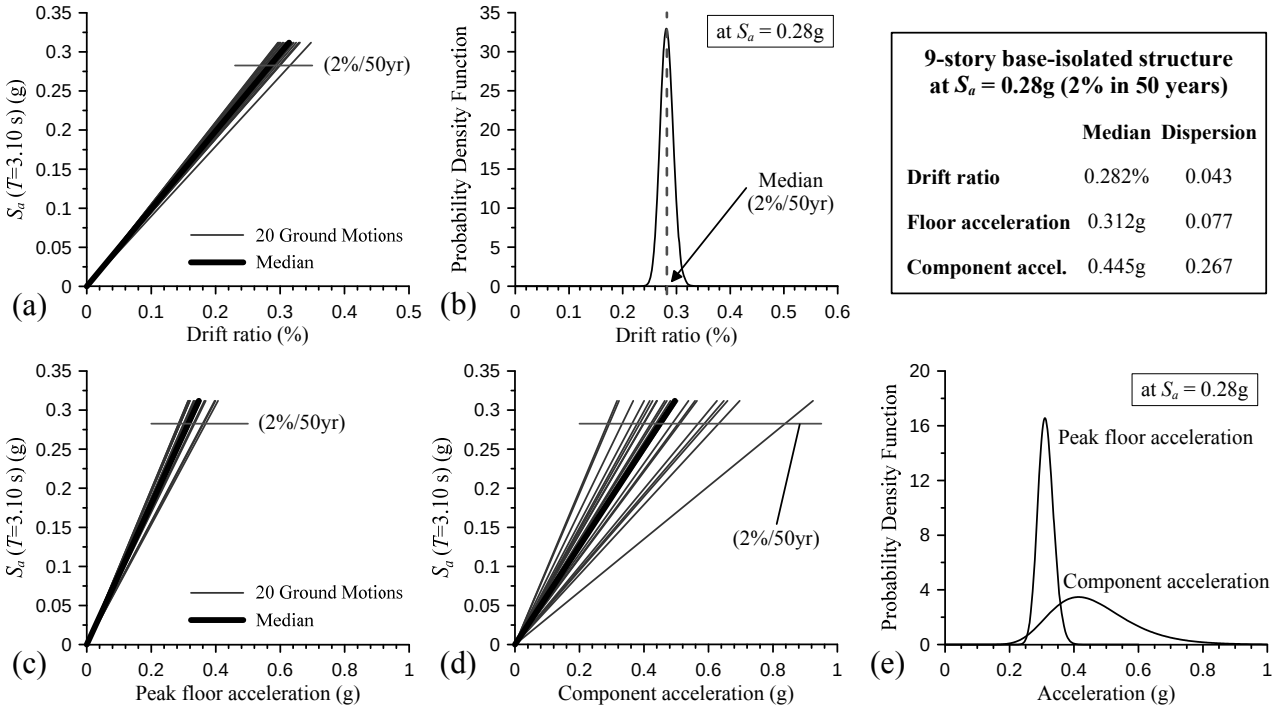

Figure 4.4 Incremental dynamic analyses results and probability density function of the 9-story base-isolated structure

Figure 4.3(a,c,d) shows the examples of IDA results of the 9-story fixed-base structure (T = 1.58 seconds) at the roof considering drift ratio, peak floor acceleration, and ceiling's response acceleration, respectively. Similarly, Figure 4.4(a,c,d) shows the results of the 9-story base-isolate structure with T_b = 3 seconds and ζ_b = 0.10 (T = 3.1 seconds). Each curve in the figures represents the response of the structure to a single ground motion whose intensity is increased until the specified $S_a^{\max}$. Considering the drift ratio at the intensity $S_a = 0.63g$ (Figure 4.3(a)) and $S_a = 0.28g$ (Figure 4.4(a)), corresponding to the 2% in 50 years ground motions for the fixed-base and base-isolated structures respectively, the probability density function can be obtained as shown in Figures 4.3(b) and 4.4(b) which will be used in the second term in Equation (4.5). It is shown clearly that the median drift ratio for the base-isolated structure is significantly smaller than that of the fixed-base structure. Considering the acceleration at the same intensity level (2%/50yr), it shows clearly that for such non-rigid

suspended ceiling, the component acceleration is higher than the peak floor acceleration, approximately 2.3 times at the median values shown in Figure 4.3(c,d) and 1.4 times in Figure 4.4(c,d). Because of higher median and dispersion in the component acceleration, acceleration-sensitive nonstructural components used in the building may need to be stronger to compensate for such large values of median and dispersion. The probability density functions can then be obtained as shown in Figures 4.3(e) and 4.4(e) which will be used in the second term in Equation (4.7). Note that area under each curve in Figures 4.3(b,e) and 4.4(b,e) is equal to one.

4.1.5 Seismic hazard analysis part

The last terms, $P\left[S = S_j\right]$, in both Equations (4.5) and (4.7) indicate the probability of occurrence of the ground shaking intensity obtained from hazard curve indicating its annual frequency of exceedance λ. The hazard curves are obtained by specifying the site's location (longitude and latitude) in OpenSHA. In this study, the site is assumed to be located in downtown Los Angeles area, where the latitude and longitude used to specify the location are 34.053 and -118.243 degrees, respectively. The attenuation model by Campbell and Borznia is used with $V_{S30} = 760$ m/s representing the boundary between B and C soil types, as defined in ASCE 7 (2010). Figure 4.5(a) shows the hazard curves for the periods of 2, 3, 4, and 5 seconds. The probability density function for these curves is approximated by the difference between the annual frequencies of exceedance of ground shaking intensities at each end of interval divided by its interval, $\left(\lambda\left(S_a^j\right) - \lambda\left(S_a^{j+1}\right)\right) / \left(S_a^{j+1} - S_a^j\right)$. The results are shown in Figure 4.5(b).

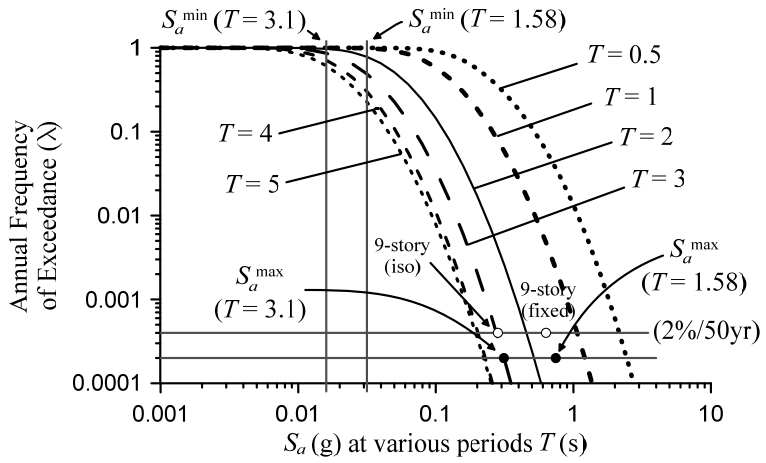

(a) Hazard curves for several periods at the Los Angeles area

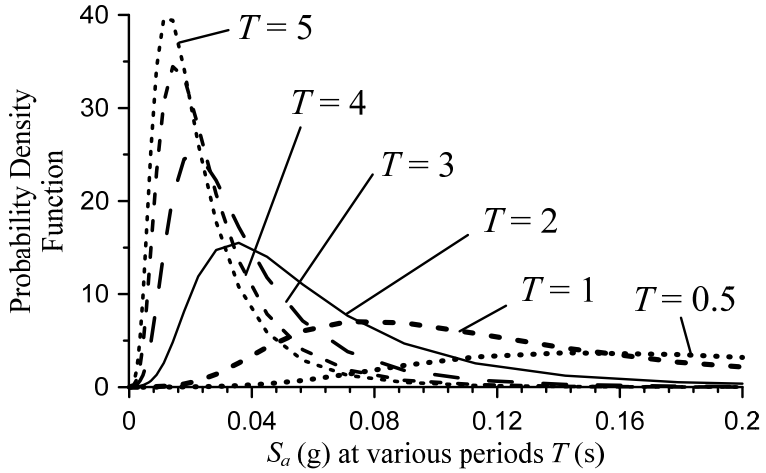

(b) Probability density function obtained from $\left(\lambda\left(S_a^j\right)-\lambda\left(S_a^{j+1}\right)\right)/\left(S_a^{j+1}-S_a^j\right)$

Figure 4.5 Seismic hazard curves for the Los Angeles area

4.2 Performance Evaluation Results

From now, $T_{R,p}$ and $T_{R,c}$ are defined which indicate the return period T_R considering the continued functionality *CF* of the partition wall and suspended ceiling, respectively. The higher return period T_R, the better the performance is. This chapter discusses T_R for both inelastic fixed-base and base-isolated structures.

4.2.1 Performance considering *CF* of partition wall

Figure 4.6 shows the results considering the *CF* of partition wall. For the base-isolated structures, the return period $T_{R,p}$ (years) in each story corresponds well to the drift demands shown previously in Figure 2.4. Higher drift demands result in poorer performance, whereas lower drift demands result in better performance. It is seen clearly that the $T_{R,p}$ in short buildings are significantly longer than tall buildings. On the other hand, for tall buildings, the return period $T_{R,p}$ could be as low as around 7 years in the top story of 20-story base-isolated structures, meaning that there is a high chance that some partition walls need to be fixed or replaced over the life of the building, resulting in the interruption of usage of this story due to wall repair or replacement. $T_{R,p}$ are below a thousand years except for the case (T_b = 4 seconds and ζ_b = 0.1) for the 9-story, below 80 years for the 20-story. It is also seen that increase of the isolation damping ratio could even cause lower performance in the upper stories as shown in Figure 4.6.

As for the fixed-base structures, all results show that the return periods $T_{R,p}$ are lower than 5 years. This is because the nonlinearity that occurs in the structures resulting large story drift ratios. Figure 3.2(a) shows rather large drift ratios, around more than 3%, while the continued functionality of the partition wall considered is only 0.35% at the median value. Another reason that this happens is because the evaluation method takes into account the probability of ground shaking intensity for the location as well. For large period structures, there is much lower chance of occurring. As a result, even though more drift ratios are observed in taller structures, but because of low probability of the ground motion, the return period may not be as short as one may think.

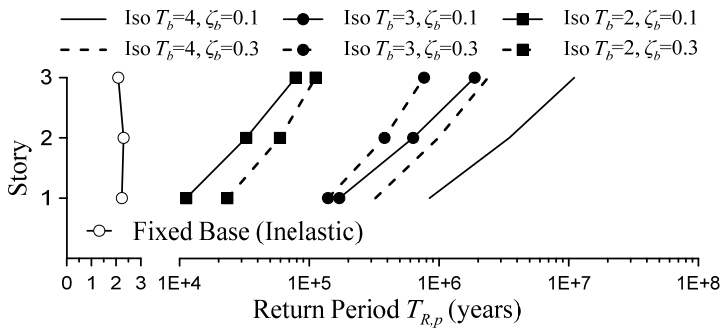

(a) 3-story structures

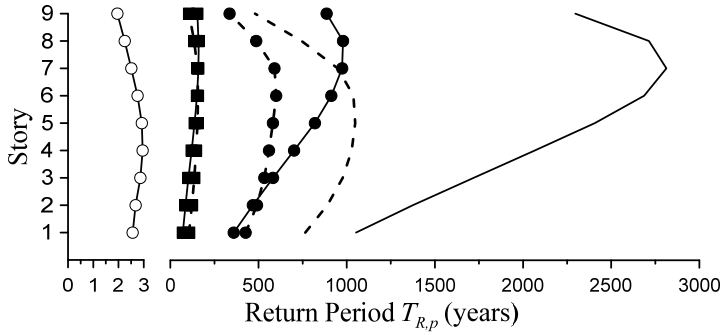

(b) 9-story structures

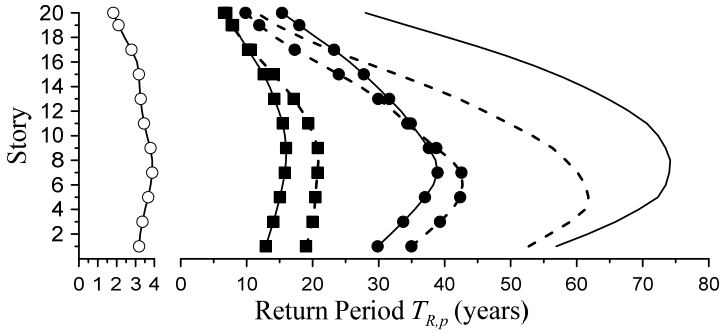

(c) 20-story structures

Figure 4.6 Return periods $T_{R,p}$ considering the *CF* of the partition wall

Comparison between the fixed-base and base-isolated structures shows that for short buildings, 3-story, the return periods increase from a few years to several thousand years and even much more if highly flexible isolation system is introduced (i.e. T_b = 4 seconds). For tall

buildings, 20-story, when T_b = 2 seconds, the return periods are around 2 times the return periods of the 20-story fixed-base structure. However, when T_b = 4 seconds, the return periods are around 8 times.

4.2.2 Performance considering *CF* of suspended ceiling

As mentioned earlier, component acceleration is important, thus the median component accelerations of the fixed-base and base-isolated structures subjected to the 20 ground motions are shown first in Figure 4.7. The result of return periods $T_{R,c}$ considering the *CF* of suspended ceiling is shown in Figure 4.8. For the base-isolated structures, the return period $T_{R,c}$ in each floor does not correspond well to the acceleration demands described earlier in Figure 2.4. This is because the performance calculated is based on the component acceleration evaluated at the ceiling's period, T_c = 0.31 second, not the peak floor acceleration. The component accelerations are higher and the distributions of them along the structure height are different from those of the peak floor accelerations as presented in Figure 2.4.

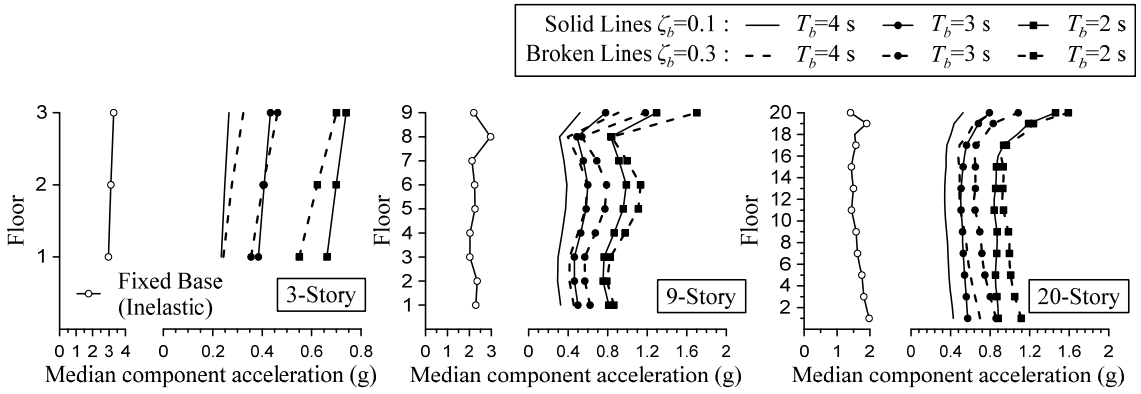

Figure 4.7 Median component acceleration of the fixed-base and base-isolated structures (3-, 9-, and 20-story structures)

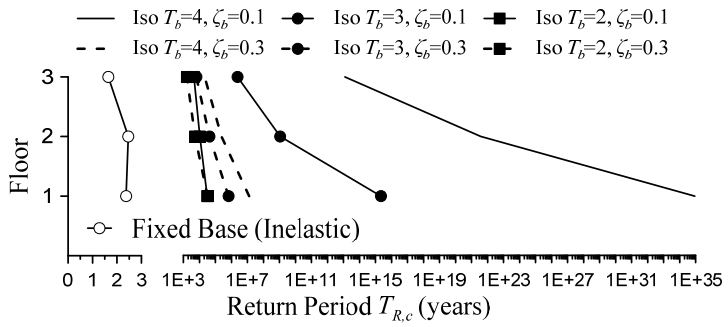

(a) 3-story structures

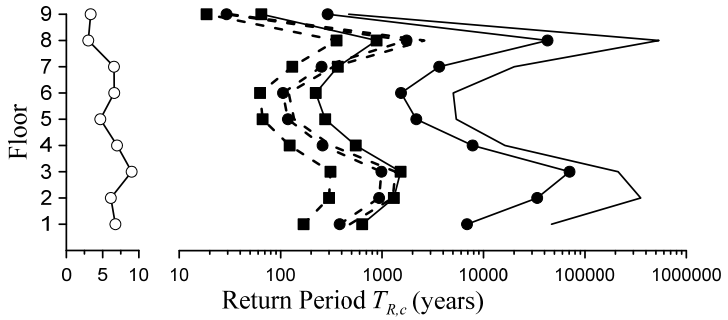

(b) 9-story structures

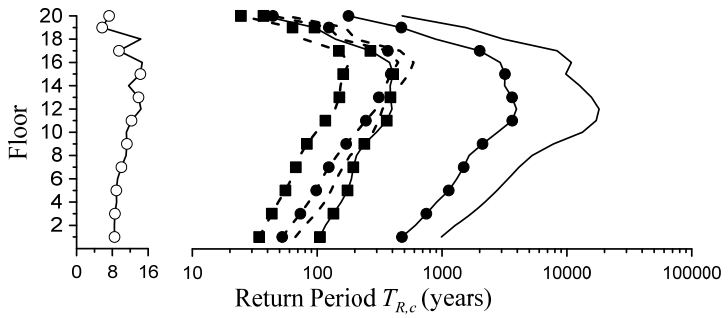

(c) 20-story structures

Figure 4.8 Return periods $T_{R,c}$ considering the *CF* of the suspended ceiling

The results of the component accelerations are compared for the 3-story (T_b = 2 seconds), 9-story (T_b = 3 seconds), and 20-story (T_b = 4 seconds) base-isolated structures with ζ_b = 0.1 commonly. Figure 2.4 shows that the roof accelerations are 0.65*g*, 0.48*g*, and 0.44*g*, respectively. However, Figure 4.7 shows that the component accelerations at the roofs are 0.74*g*, 0.78*g*, and 0.53*g* which are 1.14, 1.63, and 1.2 times the floors accelerations,

respectively. The highest increase is seen for the 9-story structure because its 3rd mode period is close to T_c = 0.31 second. In addition, as shown in Figure 2.6(b), for the floor acceleration, the 3rd mode contribution is also high at the 6th floor of 9-story structure. Since $T_{R,c}$ is directly affected by component acceleration, it becomes short as shown by irregular shape in Figure 4.8.

$T_{R,c}$ at the roofs are around 4500, 290, 480 years for the 3-, 9-, and 20-story structures, respectively, and they are shorter than the other floors. As the lognormal scale of the $T_{R,c}$ indicates, difference of component accelerations (Figure 4.7) between each floor appears to change the $T_{R,c}$ more than a hundred years (Figure 4.8). This is because the dispersion of the suspended ceiling is very small (β = 0.046). If the dispersion were greater, the change of $T_{R,c}$ might be less significant. Adding isolation damping ζ_b can worsen the performance, as shown in Figure 4.8 where $T_{R,c}$ reduces substantially when ζ_b = 0.3. This is not unusual since the highest considered isolation period is 4 seconds which is equal to the superstructure period of the structure.

If the ceiling's period T_c were 0.5 second, the component accelerations at the roofs for 3-, 9-, and 20-story base-isolated structures would be 0.75g, 1.18g, and 0.79g, respectively (Figure 3.3). The ratios of component acceleration, $S_a\left(T_c = 0.5\right) / S_a\left(T_c = 0.31\right)$, are 1.01, 1.51, and 1.49, respectively. These ratios indicate that, if the fragility function is the same, the return periods $T_{R,c}$ would increase very slightly for the 3-story, and more significantly for 9- and 20-story structures from the $T_{R,c}$ obtained for T_c = 0.31 second. From this, it can be interpreted that if the nonstructural component's period falls close to one of the modal vibration periods of the structure, the performance could be considerably worsened.

As for the fixed-base structures, the return periods $T_{R,c}$ are around 2, 8, and 12 years for the 3-, 9-, and 20-story structures, which are extremely shorter than those of the base-isolated structures. Especially for the 3-story structure, there is very high chance that in a few years, the suspended ceiling would fall and disrupt the continued functionality of the building.

4.3 Sensitivity of Performance to Fragility Functions

In the previous section, only a single fragility function was considered. However, there could be several fragility functions even for a single component due to a variety of types, sizes. Moreover, there are also uncertainties for fragility itself due to the limitation of the test condition to accurately represent the realistic behavior. Therefore, it is worth conducting sensitivity analysis to the fragility functions. Two main statistical parameters for both partition wall and suspended ceiling used in construction of a fragility function, median x_m and dispersion β, are examined for the 3-, 9-, and 20-story base-isolated structures with T_b = 2 seconds, ζ_b = 0.10. For the suspended ceiling, the same T_c = 0.31 second is used. The procedure below, however, will be applicable for any case of T_c if the corresponding fragility function is given. Also note that there is no need to perform any structural analysis at all since only the first term in Equations 4.5 and 4.7 are changed. Therefore, the results can be obtained quickly. Figures 4.9 and 4.10 show the fragility functions with varied medians and dispersions for the partition wall and suspended ceiling, respectively.

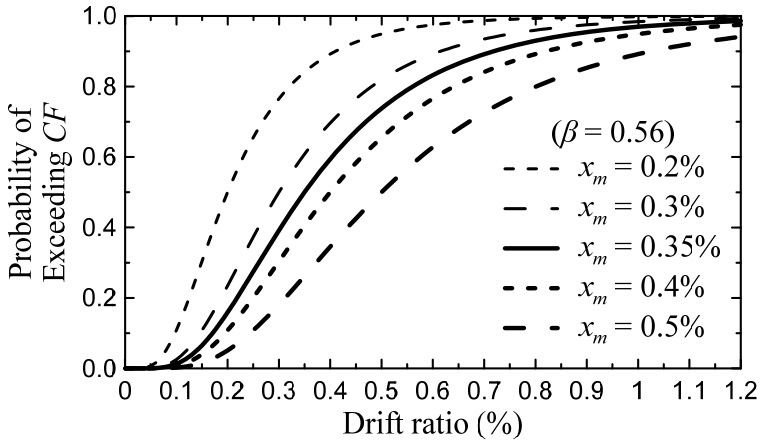

(a) Fixed dispersion β of 0.56 and various medians x_m

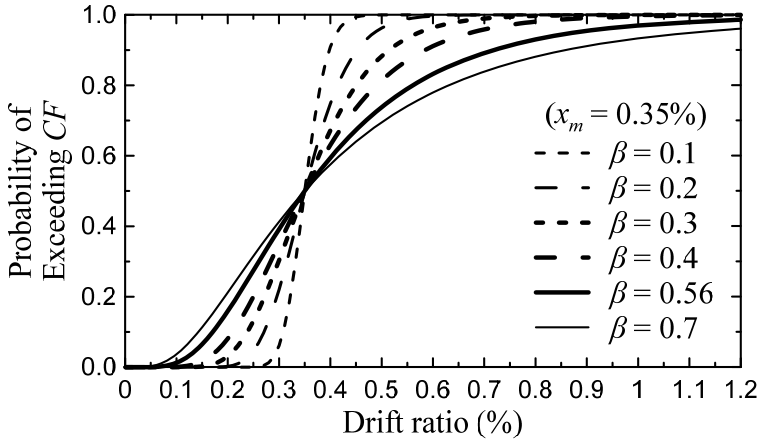

(a) Fixed median x_m of 0.35% and various dispersions β

Figure 4.9 Various fragility functions of partition walls

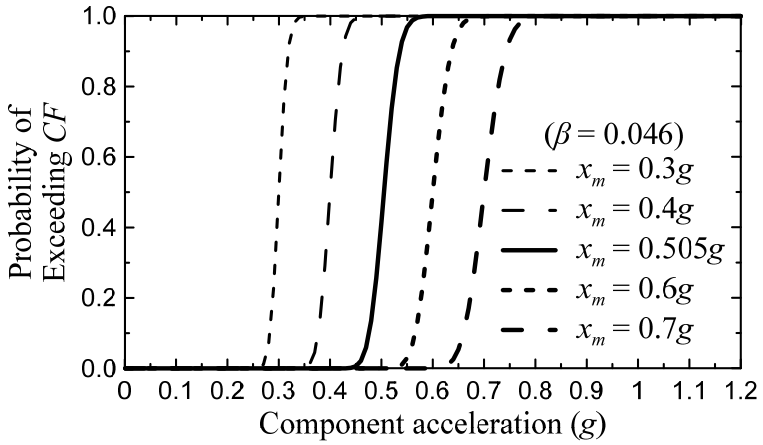

(a) Fixed dispersion β of 0.046 and various medians x_m

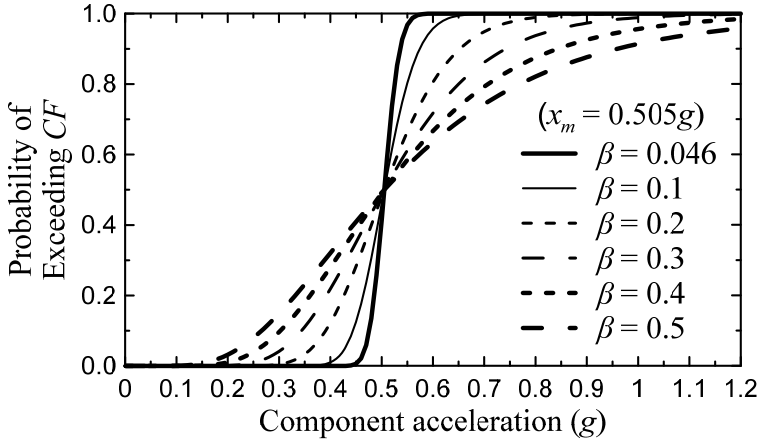

(a) Fixed median x_m of 0.505g and various dispersions β

Figure 4.10 Various fragility functions of suspended ceilings

4.3.1 Sensitivity of performance considering *CF* of partition wall

Figure 4.11(a) shows the case of varying the median x_m-values. For the 3-story base-isolated structure, compared with the $T_{R,p}$ of the original median x_m = 0.35%, the $T_{R,p}$ for x_m = 0.2% and 0.5% are approximately 0.07 times and 7.70 times, respectively. For the 9-story, they are 0.21 and 3.31 times, respectively. And for the 20-story, they are 0.37 and 2.24 times, respectively. Thus, $T_{R,p}$ for the 3-story structure is highly sensitive to x_m while for the 9- and 20-story structures, it is less sensitive, thereby limiting the effectiveness of increasing x_m.

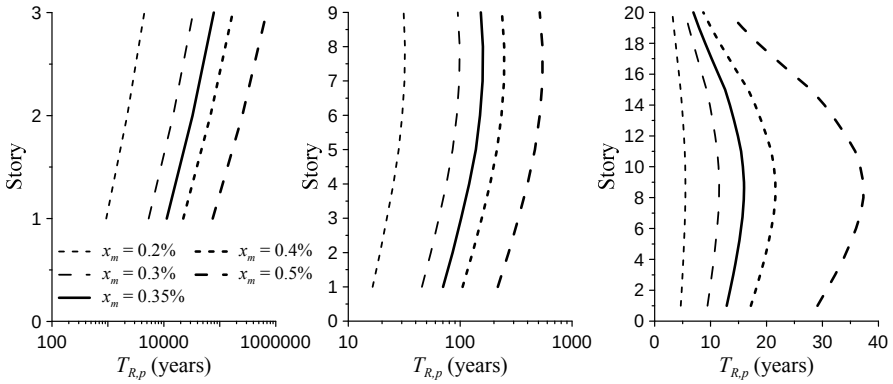

(a) Fixed dispersion β and various medians x_m

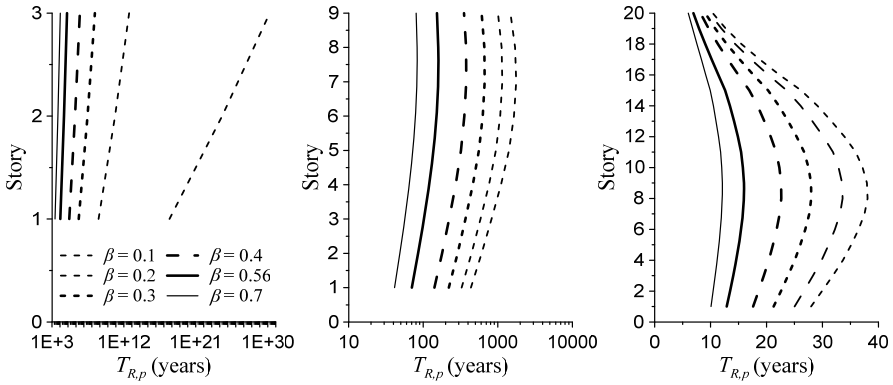

(b) Fixed median x_m and various dispersions β

Figure 4.11 Sensitivity of return period $T_{R,p}$ of 3-, 9-, and 20-story base-isolated structures to: (a) median x_m and (b) dispersion β

Figure 4.11(b) shows the case of varying the dispersion β-values. For the 3-story base-isolated structure, compared with the $T_{R,p}$ of the original dispersion $\beta = 0.56$, the $T_{R,p}$ for $\beta = 0.4$ and $\beta = 0.7$ are approximately 24.94 times and 0.18 time, respectively. For the 9-story, they are 2.26 and 0.54 times, respectively. And for the 20-story, they are 1.36 and 0.79 times. Thus, $T_{R,p}$ is highly sensitive to β for the 3-story structure and less sensitive for the 9- and 20-story structures.

4.3.2 Sensitivity of performance considering *CF* of suspended ceiling

Figure 4.12(a) shows the case of varying the median x_m-values. For the 3-story base-isolated structure, compared with the $T_{R,c}$ of the original median $x_m = 0.505g$, the $T_{R,c}$ for $x_m = 0.3g$ and $x_m = 0.7g$ are approximately 0.03 times and 51146.06 times, respectively. For the 9-story, they are 0.13 and 6.95 times, respectively. And for the 20-story, they are 0.18 and 4.04 times, respectively. Thus, $T_{R,c}$ for the 3-story structure is highly sensitive to x_m while for the 9- and 20-story structures, it is less sensitive, thereby limiting the effectiveness of increasing x_m.

Figure 4.12(b) shows the case of varying the dispersion β-values. Compared with the $T_{R,c}$ of the original dispersion $\beta = 0.046$, the $T_{R,c}$ for $\beta = 0.5$ are 0.04, 0.23, and 0.34 times for the 3-, 9-, and 20-story base-isolated structures, respectively. Note that the return period reduces with the increase of dispersion because the damage state *CF* will be exceeded earlier than those with less dispersion.

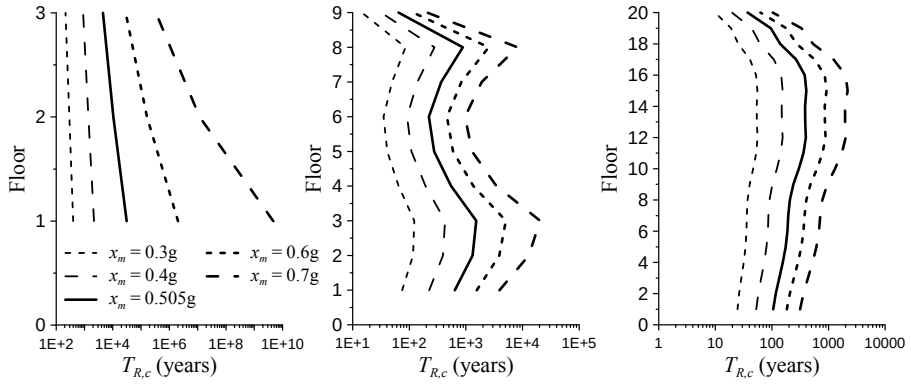

(a) Fixed dispersion β and various medians x_m

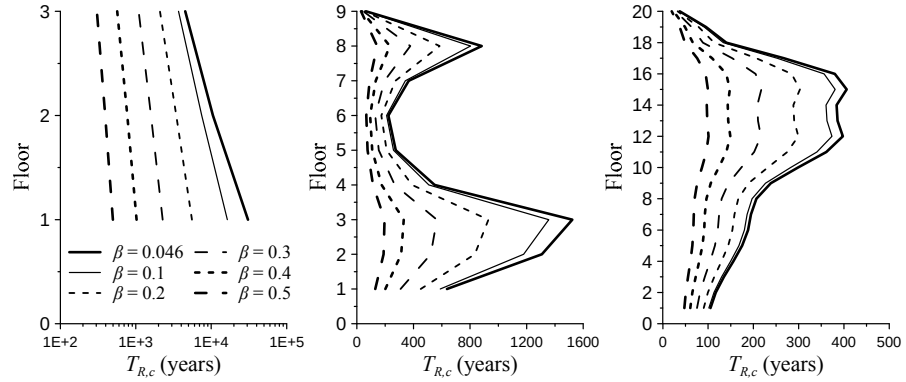

(b) Fixed median x_m and various dispersions β

Figure 4.12 Sensitivity of return period $T_{R,c}$ of 3-, 9-, and 20-story base-isolated structures to: (a) median x_m and (b) dispersion β

4.4 Required Response Demands for Target Performance

In the previous section, a method to evaluate the performance of a structure as a failure return period is demonstrated. Assuming the structures to be located in the Los Angeles area and considering the continued functionality of partition wall and suspended ceilings, the return periods of the structures were obtained. In this section, by utilizing this same methodology, it is possible to design nonstructural components such that it remains functional for the desired return period.

When designing a building, the owner may desire the building to remain functional without disruption of usage for a certain number of years T_R. By utilizing the procedures in the previous chapter, it is possible to find the necessary median x_m (i.e., drift ratio, floor acceleration, or component acceleration) and dispersion β to satisfy such condition. Knowing these required x_m and β is beneficial not only for achieving the desired T_R, but also for planning budget for partition wall or suspended ceiling or other drift-sensitive or acceleration-sensitive nonstructural components which will be useful during initial design phase. The following Figures 4.13 – 4.21 show the results of this application for the base-isolated structures, and Figures 4.22 – 4.24 for the fixed-base structures. The performance of the roof is investigated since poorest performance is often exhibited. Note that the capacity indicated in x-axis in these Figures means the required response demand that the nonstructural components need to be able to resist in order to achieve the desired return period T_R of interest.

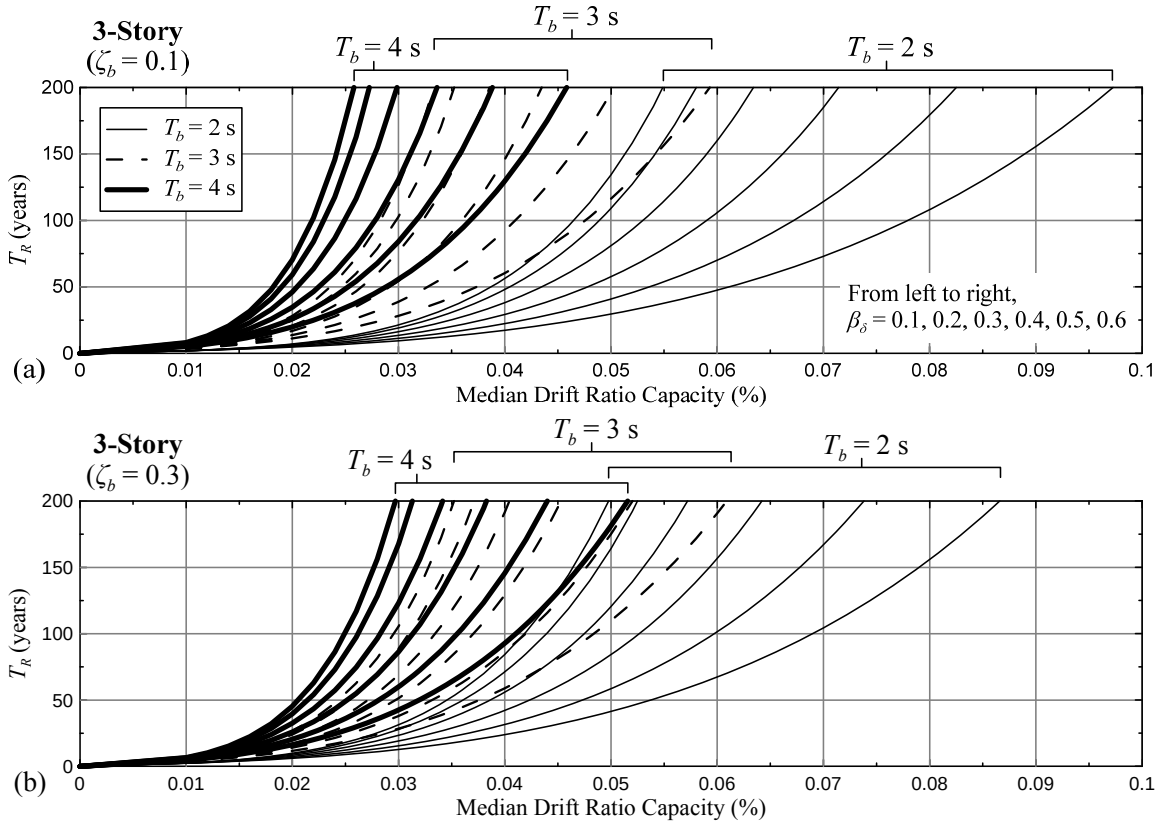

Figure 4.13 Performance curves for drift-sensitive components (3-story)

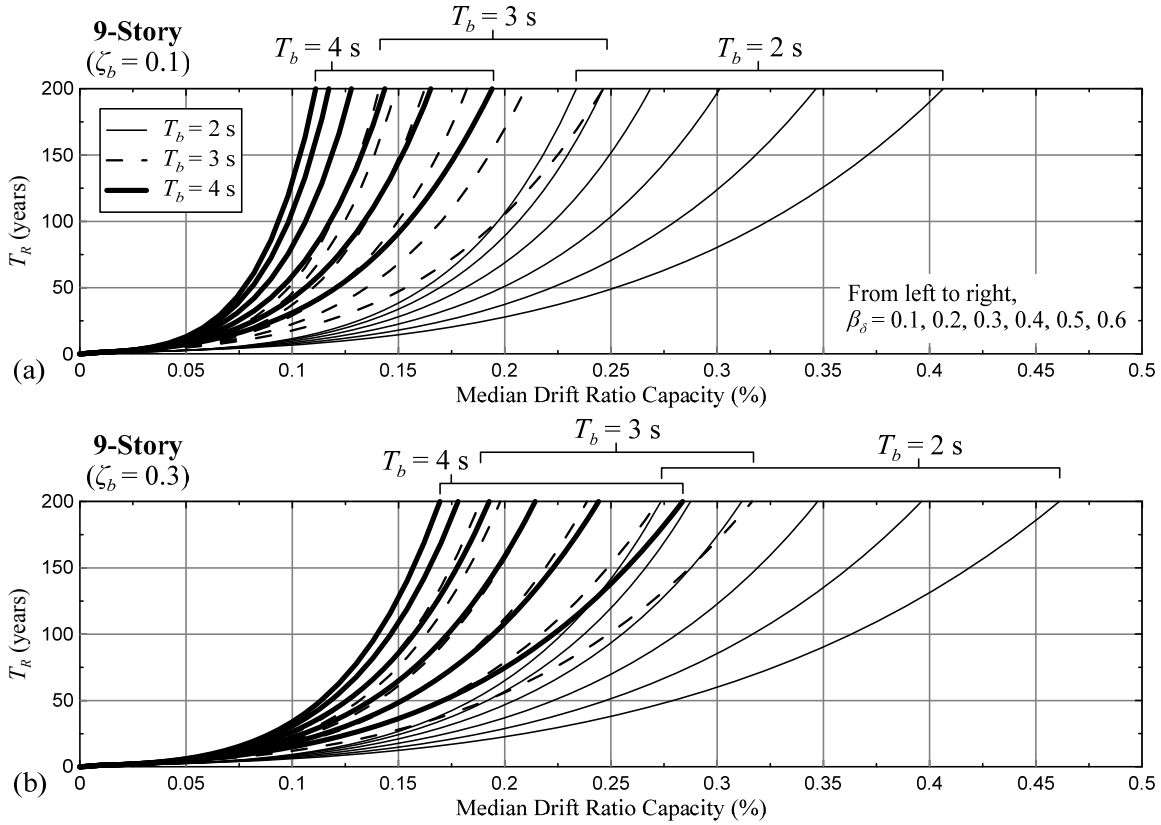

Figure 4.14 Performance curves for drift-sensitive components (9-story)

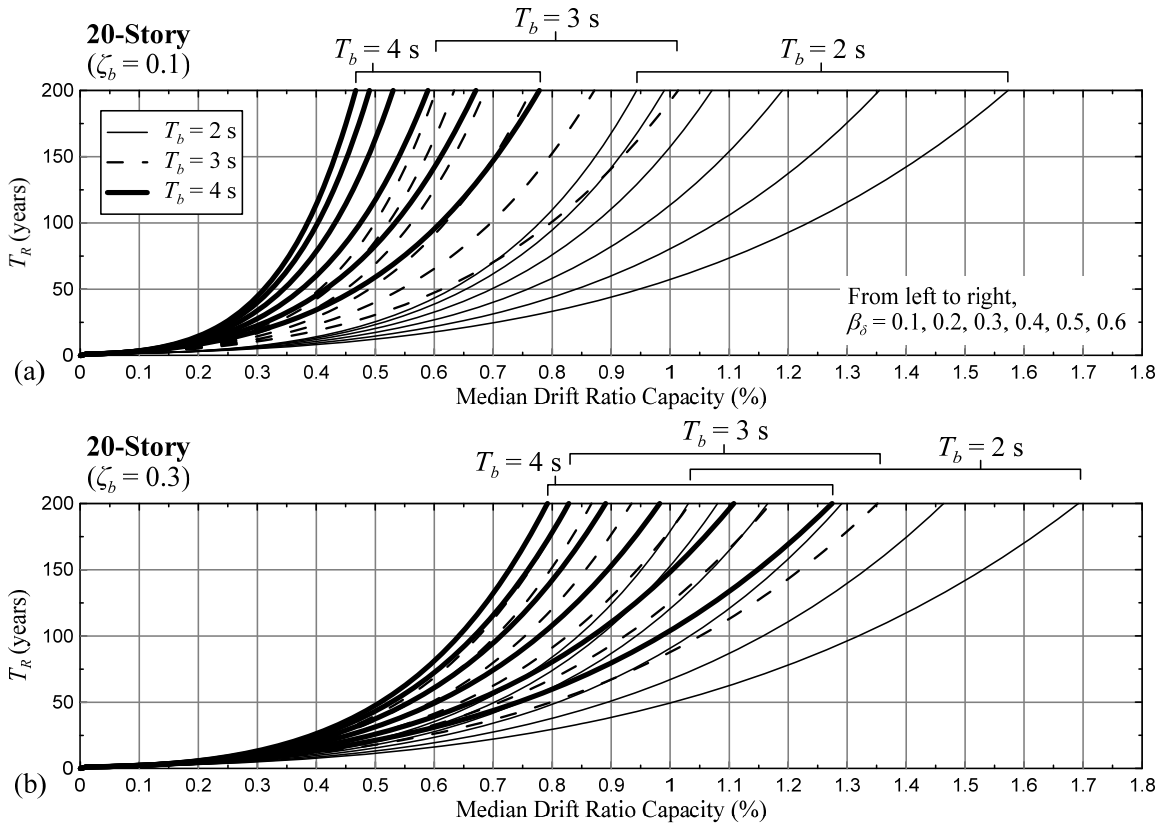

Figure 4.15 Performance curves for drift-sensitive components (20-story)

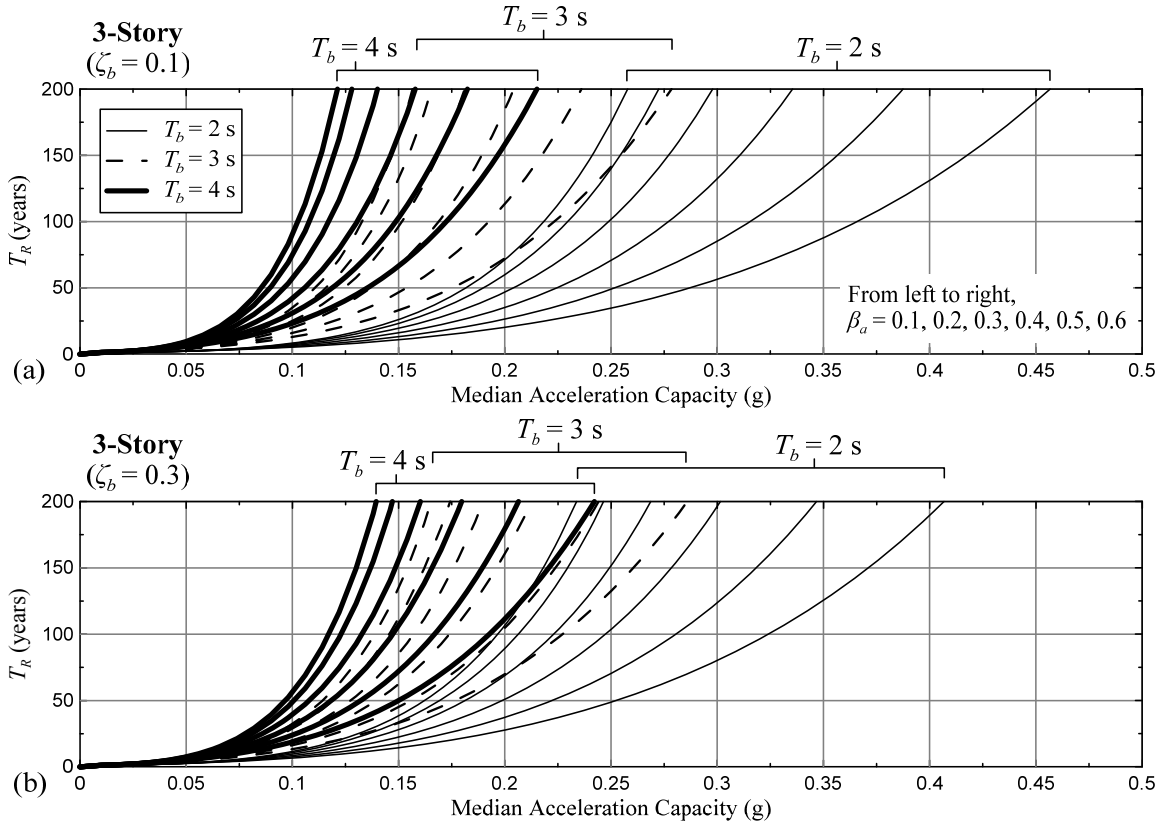

Figure 4.16 Performance curves for acceleration-sensitive components (3-story, T_c = 0 s)

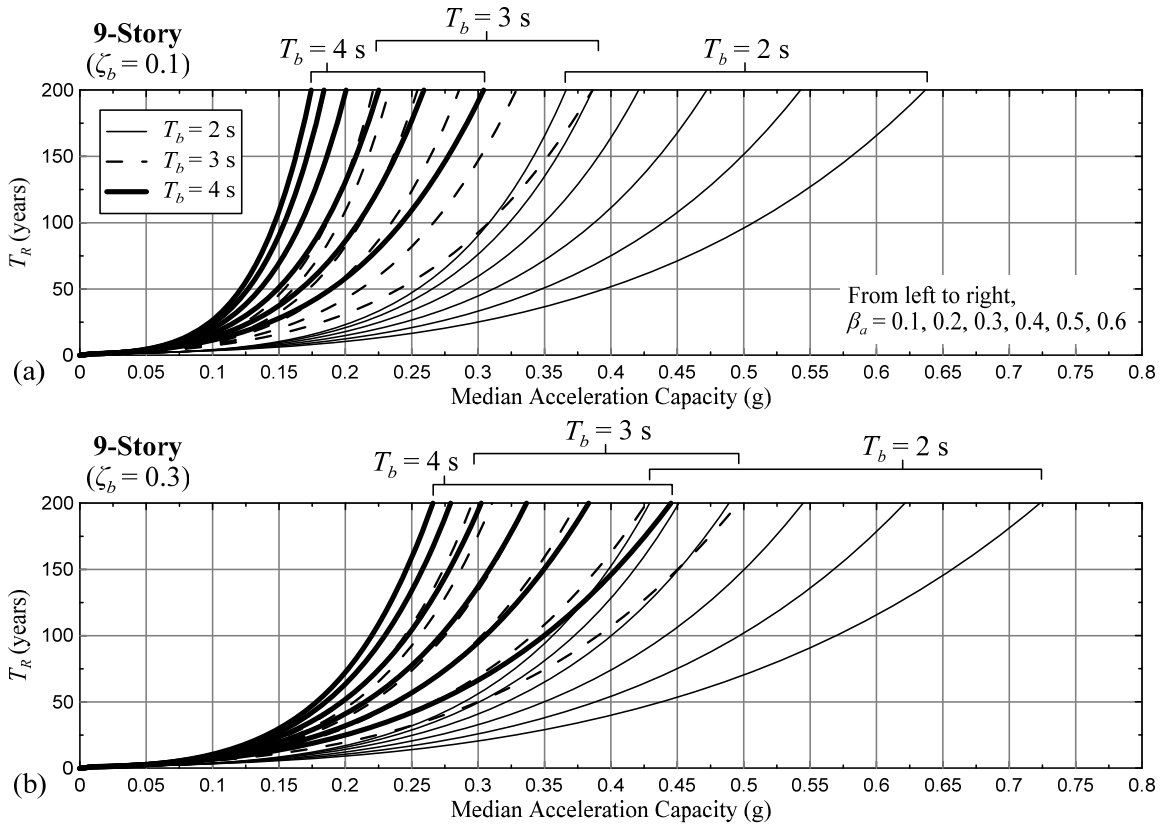

Figure 4.17 Performance curves for acceleration-sensitive components (9-story, T_c = 0 s)

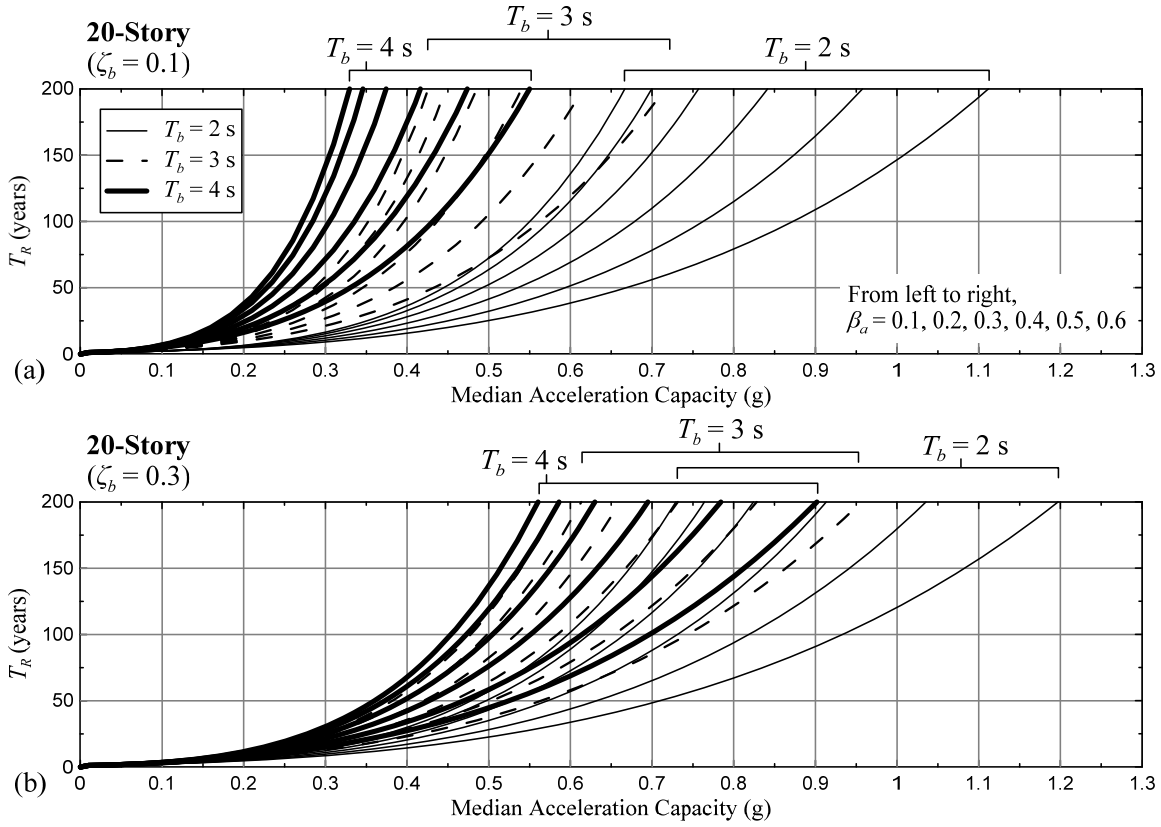

Figure 4.18 Performance curves for acceleration-sensitive components (20-story, T_c = 0 s)

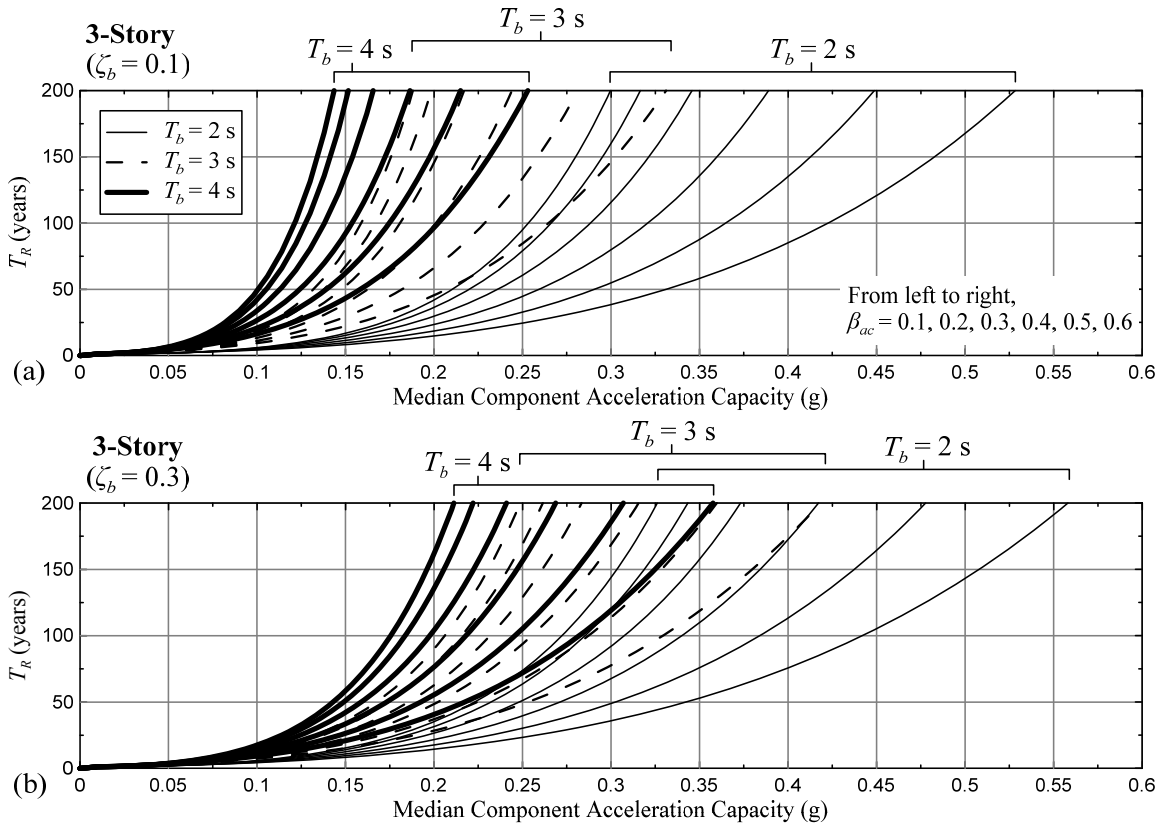

Figure 4.19 Performance curves for acceleration-sensitive components (3-story, T_c = 0.31 s)

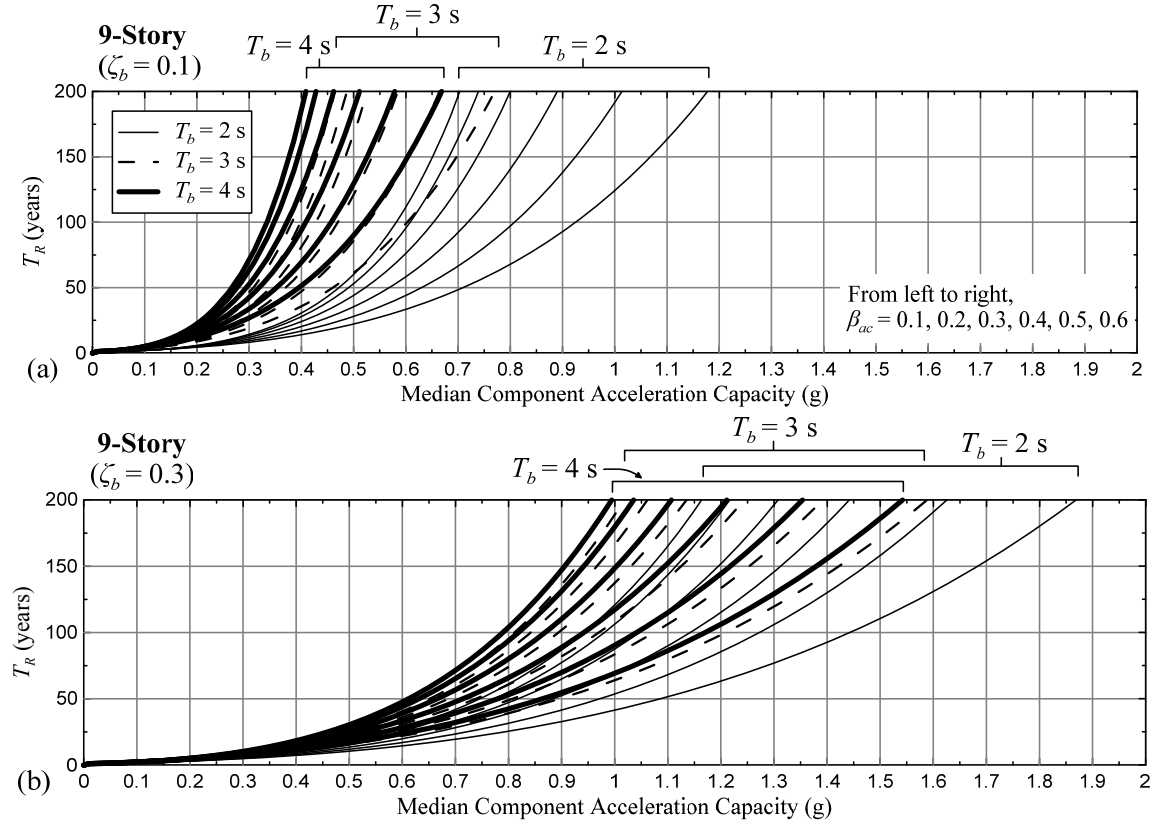

Figure 4.20 Performance curves for acceleration-sensitive components (9-story, T_c = 0.31 s)

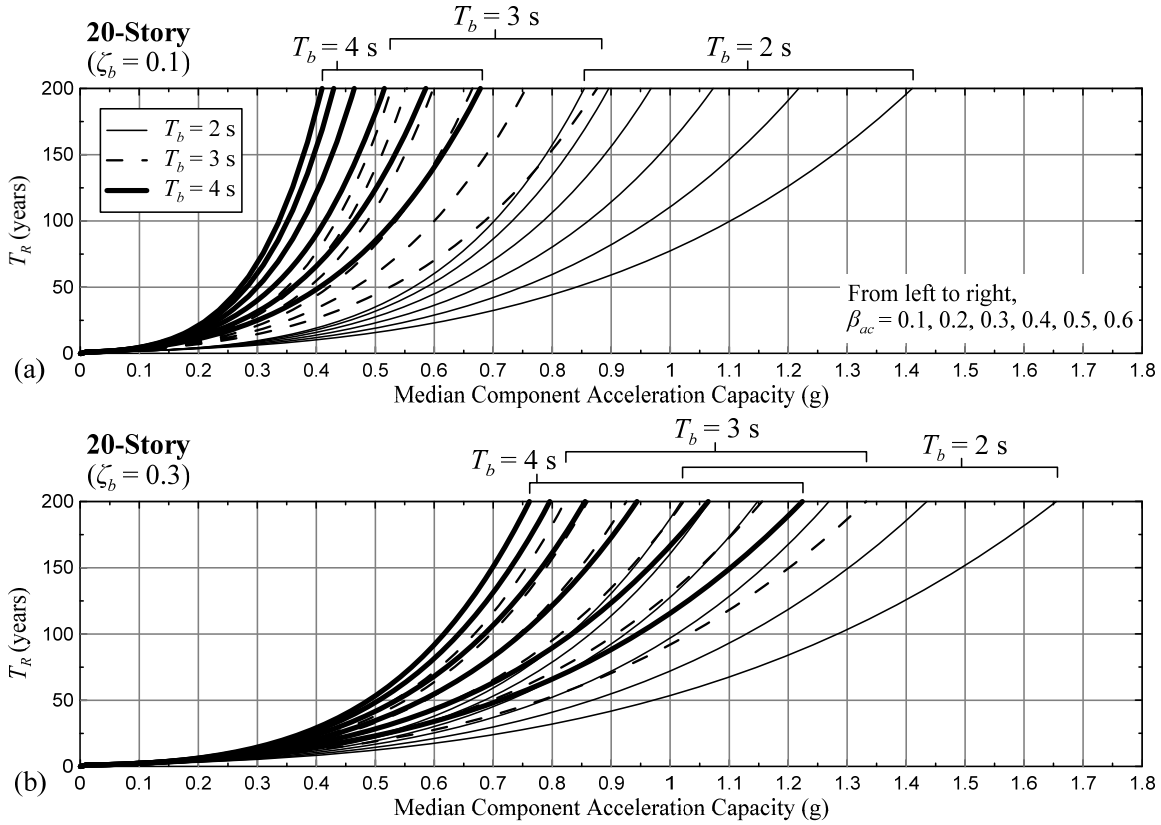

Figure 4.21 Performance curves for acceleration-sensitive components (20-story, T_c = 0.31 s)

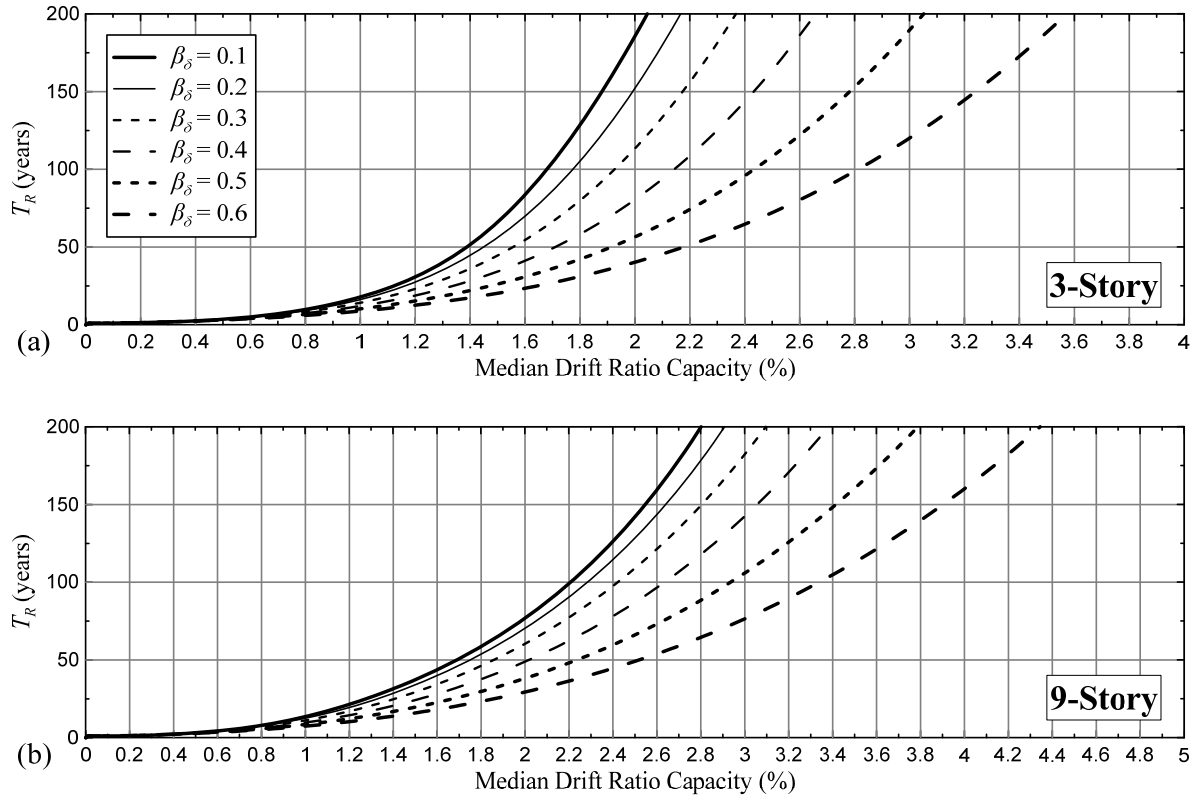

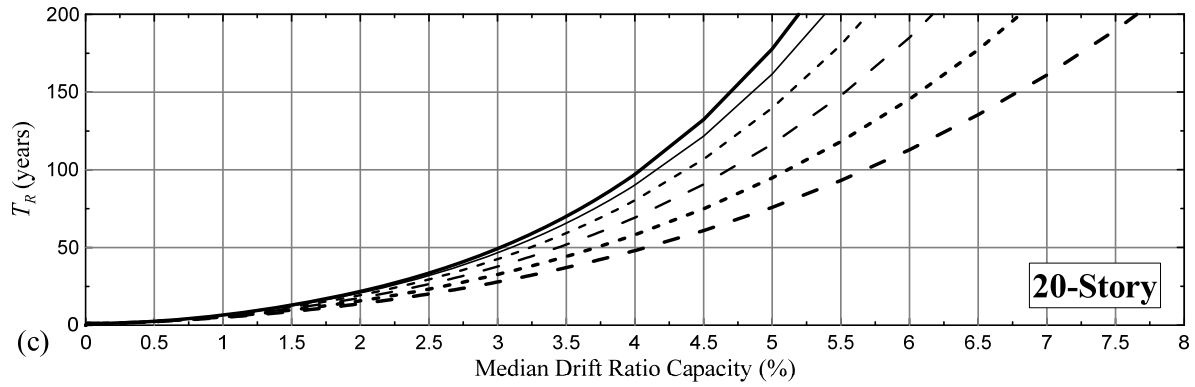

Figure 4.22 Performance curves for drift-sensitive components (fixed-base structures)

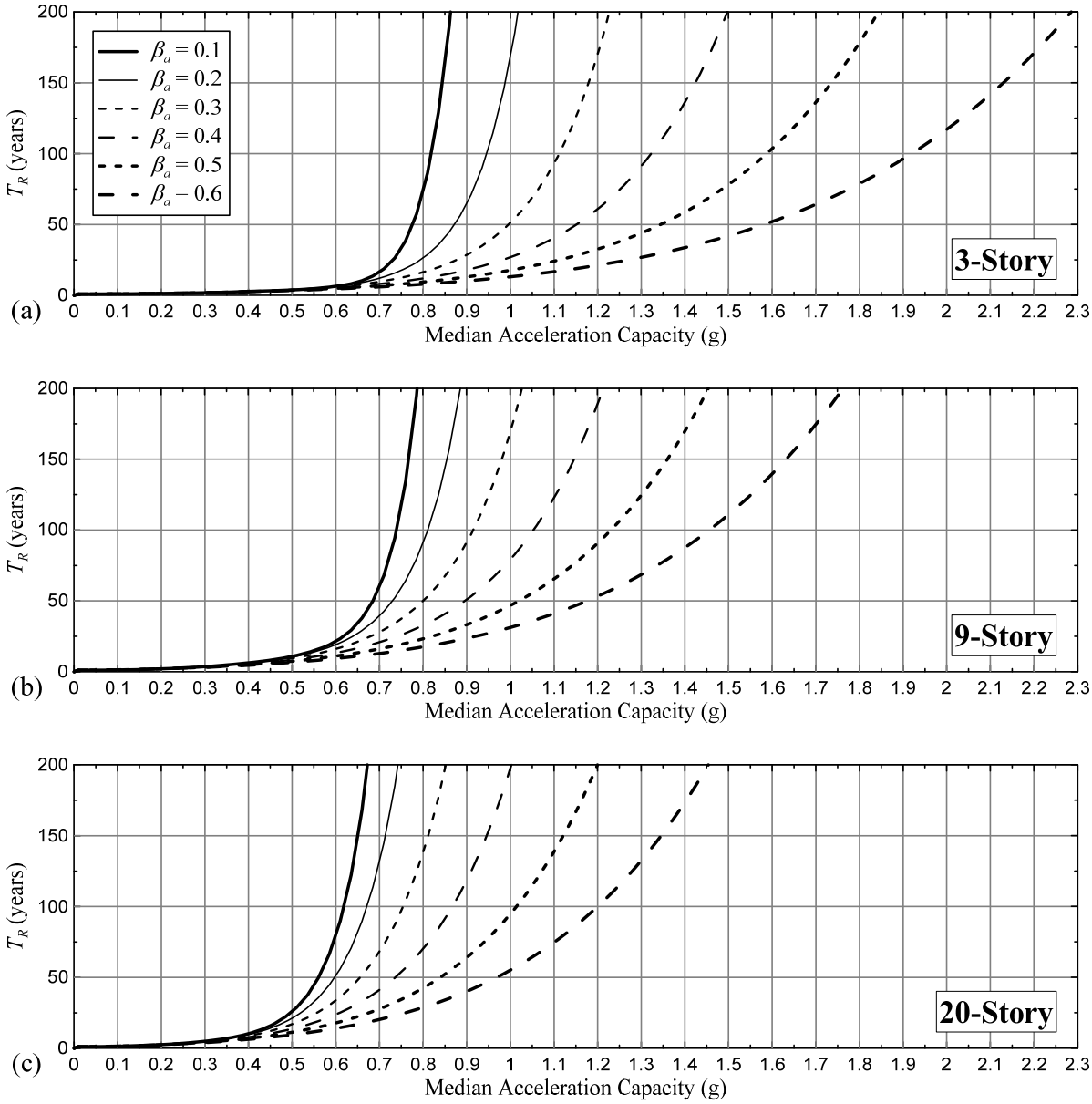

Figure 4.23 Performance curves for acceleration-sensitive components (fixed-base structures, T_c = 0 s)

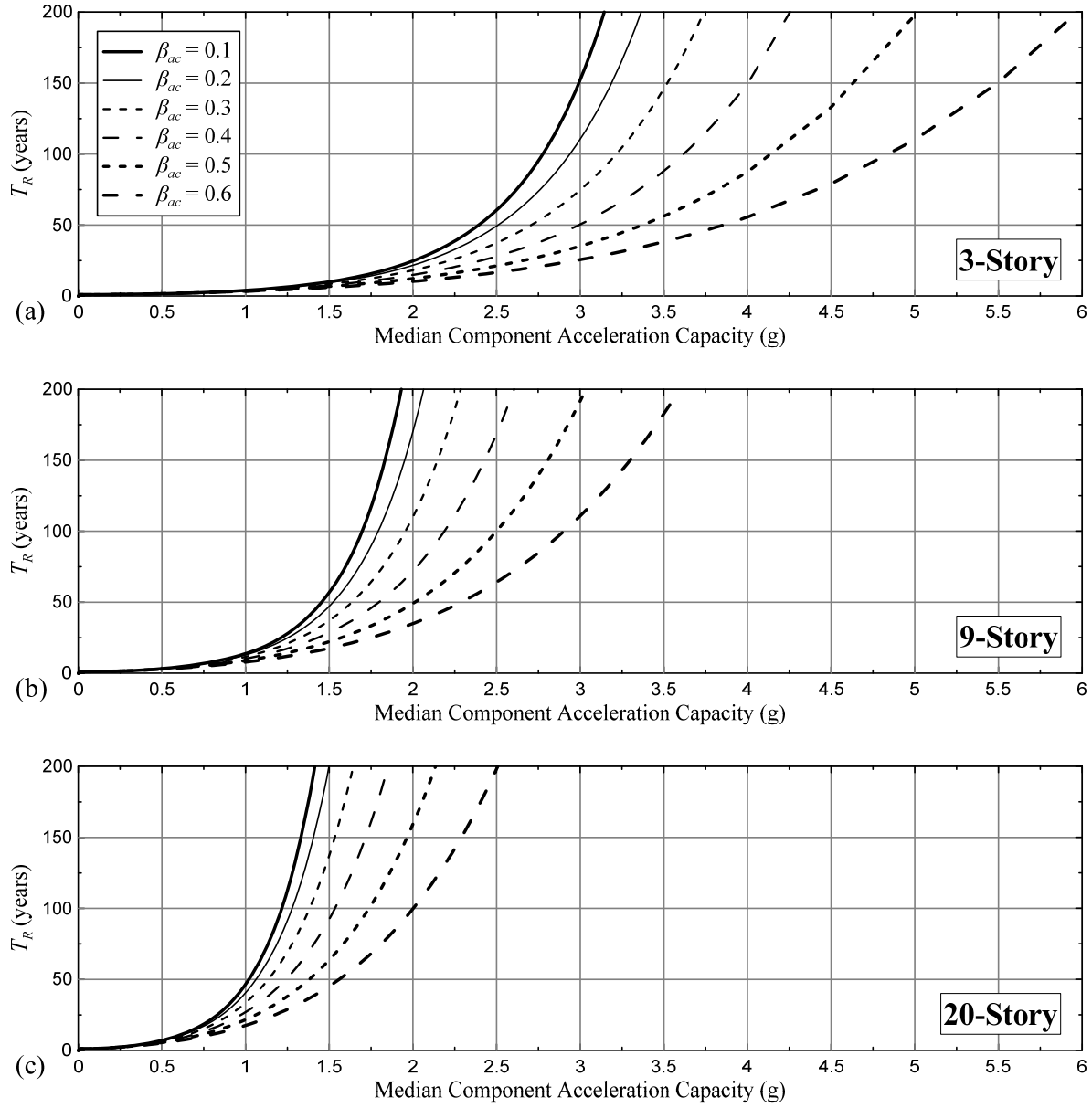

Figure 4.24 Performance curves for acceleration-sensitive components (fixed-base structures, T_c = 0.31 s)

Figures 4.13 – **Error! Reference source not found.** and 4.22 shows the performance curves for drift-sensitive components (using story drift ratio), Figures 4.16 – **Error! Reference source not found.** and 4.23 for acceleration-sensitive components at component's period T_c = 0 s (using peak floor acceleration), and Figures 4.19 – **Error! Reference source not found.** and 4.24 for acceleration-sensitive components at T_c (using acceleration at T_c = 0.31 s and ζ_c =

0.03). The performance curves in these figures are very useful for designing any drift- and acceleration-sensitive nonstructural components, not limited to only partition wall and suspended ceiling. And these curves can be constructed very quickly since the time consuming part from IDA is already complete. Note that this is the performance curve at the roof floor only. If the roof floor is not of importance, other floor could be selected instead. The plots are shown up to only 200 years, since usually the building will probably be renovated before reaching 200 years.

From the Figures plotted above, supposed we want to design a building such that it is continuously functional for 50 years (T_R = 50 years), then the required drift ratio capacity, floor acceleration capacity, and component acceleration capacity (for suspending ceiling in this study) with dispersion of 0.4 are as shown in Tables 4.1 and 4.2 for the base-isolated structures. And if desired T_R = 100 years, the required capacities are shown in Tables 4.3 and 4.4. The required capacities for the fixed-base structures are also shown in Table 4.5. The symbols δ, a, and a_c in these tables indicate drift-sensitive components and acceleration-sensitive components with T_c = 0 and 0.31 second, respectively.

Table 4.1 Required capacities for T_R = 50 years for base-isolated structures (ζ_b = 0.1)

	T_b = 2 s, ζ_b = 0.1			T_b = 3 s, ζ_b = 0.1			T_b = 4 s, ζ_b = 0.1		
Story	**δ (%) (β = 0.4)**	**a (g) (β = 0.4)**	**a_c (g) (β = 0.4)**	**δ (%) (β = 0.4)**	**a (g) (β = 0.4)**	**a_c (g) (β = 0.4)**	**δ (%) (β = 0.4)**	**a (g) (β = 0.4)**	**a_c (g) (β = 0.4)**
3	0.0478	0.2244	0.2593	0.0292	0.1370	0.1625	0.0225	0.1058	0.1241
9	0.1988	0.3115	0.5678	0.1206	0.1890	0.3696	0.0948	0.1487	0.3187
20	0.7577	0.5356	0.6759	0.4895	0.3455	0.4206	0.3745	0.2645	0.3251

Table 4.2 Required capacities for T_R = 50 years for base-isolated structures (ζ_b = 0.3)

	T_b = 2 s, ζ_b = 0.3			T_b = 3 s, ζ_b = 0.3			T_b = 4 s, ζ_b = 0.3		
Story	**δ (%) (β = 0.4)**	**a (g) (β = 0.4)**	**a_c (g) (β = 0.4)**	**δ (%) (β = 0.4)**	**a (g) (β = 0.4)**	**a_c (g) (β = 0.4)**	**δ (%) (β = 0.4)**	**a (g) (β = 0.4)**	**a_c (g) (β = 0.4)**
3	0.0423	0.1988	0.2713	0.0297	0.1394	0.2022	0.0251	0.1181	0.1731
9	0.2229	0.3497	0.8839	0.1527	0.2396	0.7381	0.1368	0.2146	0.7139
20	0.8094	0.5722	0.7870	0.6447	0.4560	0.6331	0.6032	0.4267	0.5790

Table 4.3 Required capacities for T_R = 100 years for base-isolated structures (ζ_b = 0.1)

	T_b = 2 s, ζ_b = 0.1			**T_b = 3 s, ζ_b = 0.1**			**T_b = 4 s, ζ_b = 0.1**		
Story	**δ (%) (β = 0.4)**	**a (g) (β = 0.4)**	**a_c (g) (β = 0.4)**	**δ (%) (β = 0.4)**	**a (g) (β = 0.4)**	**a_c (g) (β = 0.4)**	**δ (%) (β = 0.4)**	**a (g) (β = 0.4)**	**a_c (g) (β = 0.4)**
3	0.0590	0.2770	0.3207	0.0360	0.1689	0.2011	0.0278	0.1305	0.1537
9	0.2472	0.3874	0.7184	0.1497	0.2347	0.4698	0.1178	0.1849	0.4083
20	0.9598	0.6783	0.8610	0.6181	0.4368	0.5347	0.4747	0.3357	0.4138

Table 4.4 Required capacities for T_R = 100 years for base-isolated structures (ζ_b = 0.3)

	T_b = 2 s, ζ_b = 0.3			**T_b = 3 s, ζ_b = 0.3**			**T_b = 4 s, ζ_b = 0.3**		
Story	**δ (%) (β = 0.4)**	**a (g) (β = 0.4)**	**a_c (g) (β = 0.4)**	**δ (%) (β = 0.4)**	**a (g) (β = 0.4)**	**a_c (g) (β = 0.4)**	**δ (%) (β = 0.4)**	**a (g) (β = 0.4)**	**a_c (g) (β = 0.4)**
3	0.0526	0.2472	0.3398	0.0370	0.1739	0.2552	0.0313	0.1472	0.2180
9	0.2812	0.4411	1.1419	0.1930	0.3027	0.9702	0.1730	0.2715	0.9416
20	1.0334	0.7309	1.0107	0.8255	0.5841	0.8138	0.7785	0.5508	0.7476

Table 4.5 Required capacities for T_R = 50 and 100 years for fixed-base structures

	T_R = 50 years			**T_R = 100 years**		
Story	**δ (%) (β = 0.4)**	**a (g) (β = 0.4)**	**a_c (g) (β = 0.4)**	**δ (%) (β = 0.4)**	**a (g) (β = 0.4)**	**a_c (g) (β = 0.4)**
3	1.7097	1.1512	2.9918	2.1430	1.3225	3.6171
9	2.0168	0.8954	1.7962	2.6346	1.0528	2.1879
20	3.4383	0.7361	1.2400	4.6807	0.8670	1.5338

Since it is difficult to compare the required capacities from the tables, these values are plotted together as shown in Figures 4.25 – 4.27 and 4.28 – 4.30 for the return periods of 50 and 100 years, respectively.

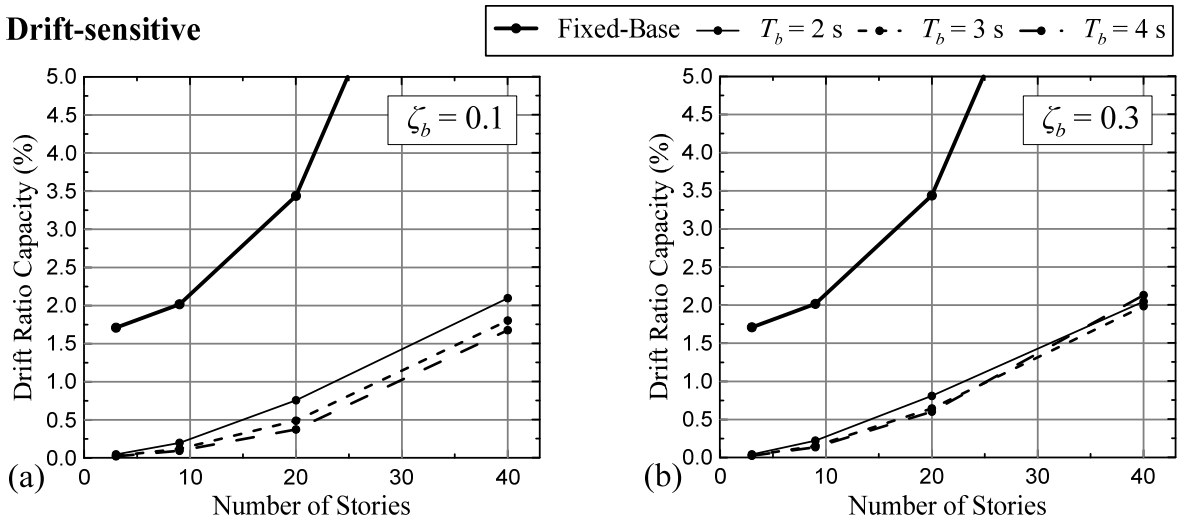

Figure 4.25 Drift ratio capacities for T_R = 50 years

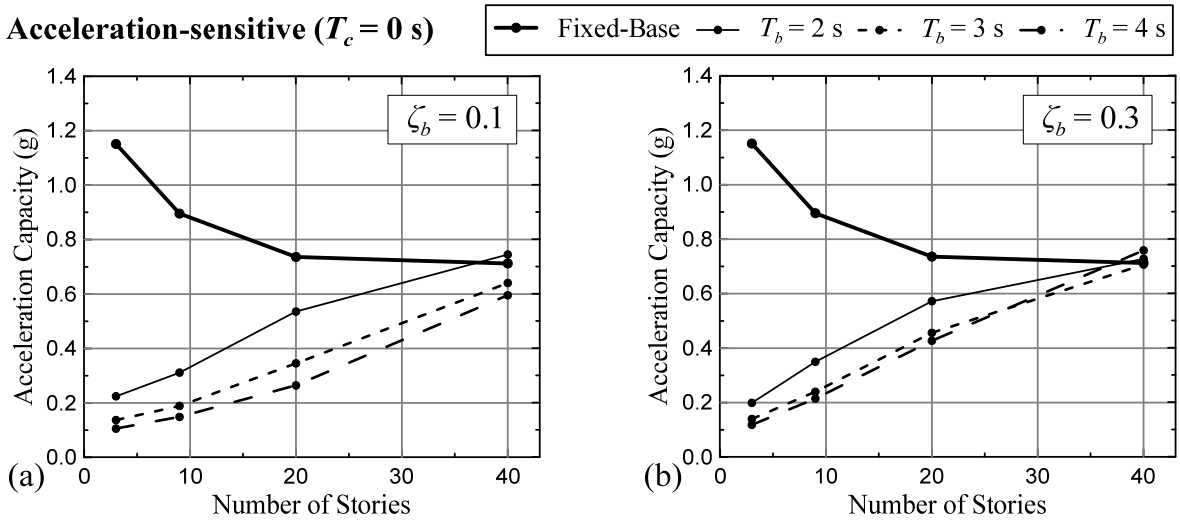

Figure 4.26 Acceleration capacities (T_c = 0 s) for T_R = 50 years

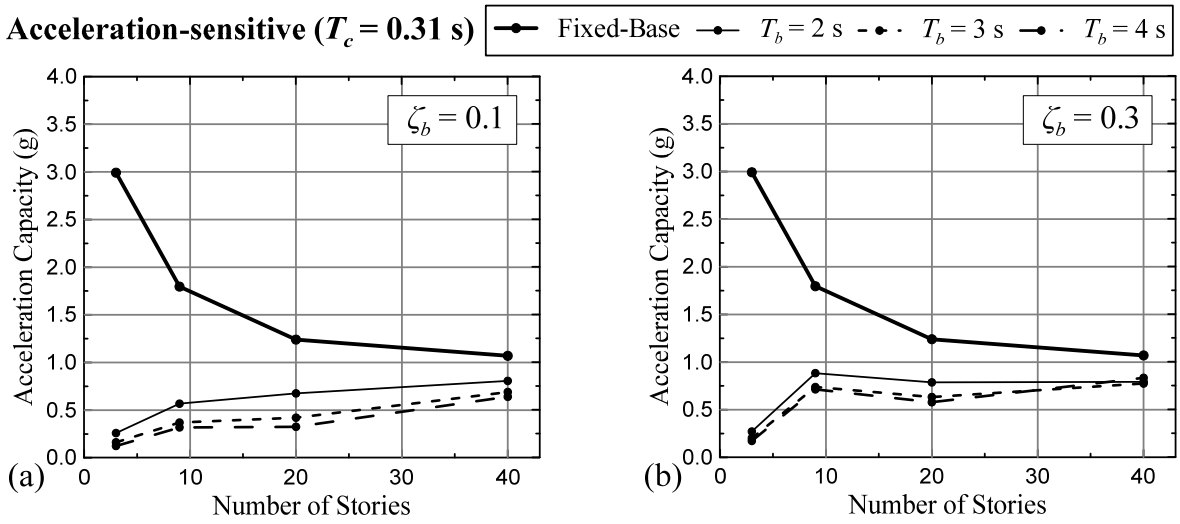

Figure 4.27 Acceleration capacities (T_c = 0.31 s) for T_R = 50 years

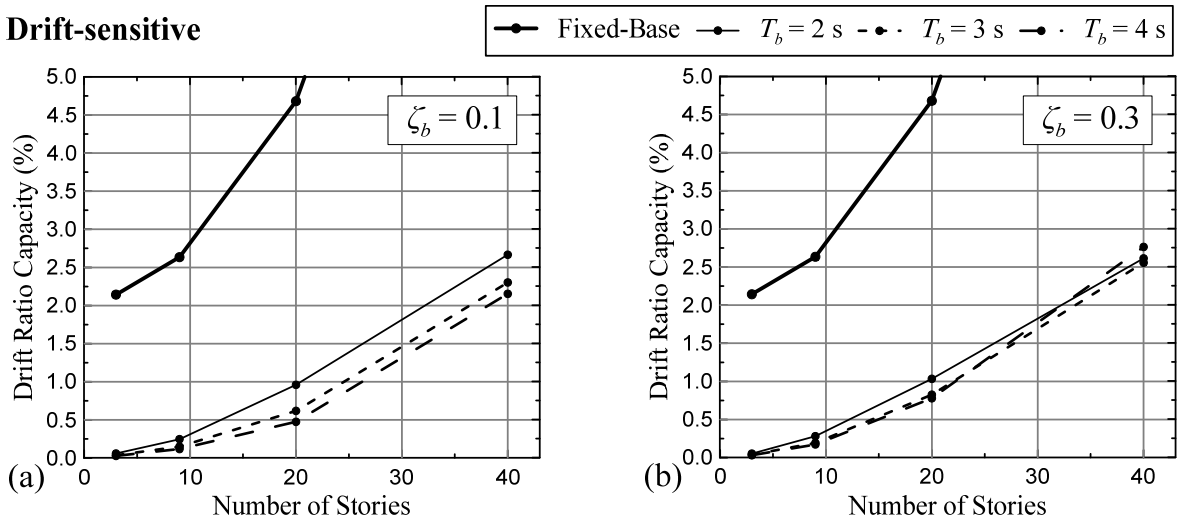

Figure 4.28 Drift ratio capacities for T_R = 100 years

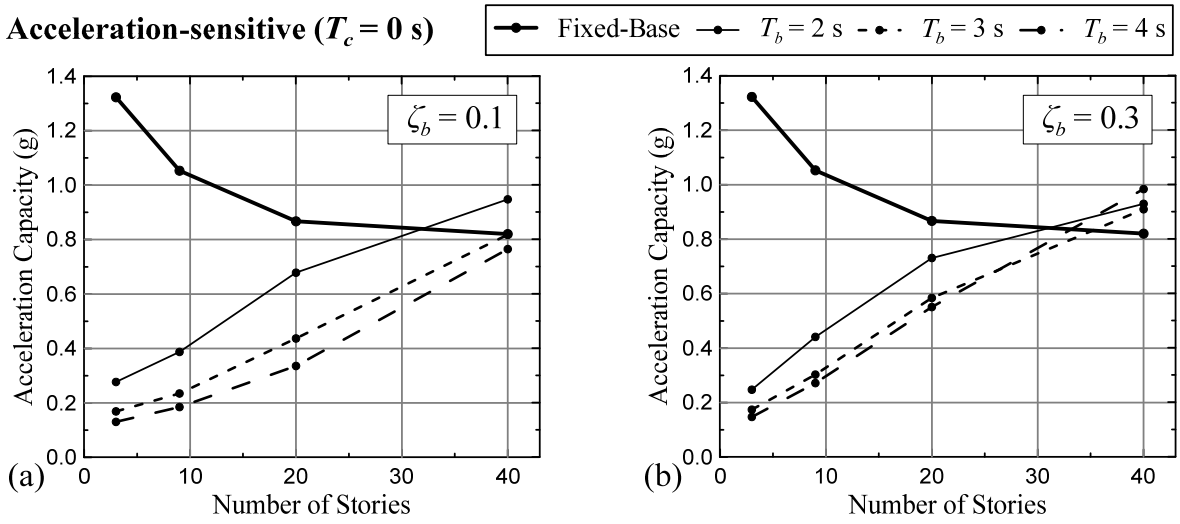

Figure 4.29 Acceleration capacities (T_c = 0 s) for T_R = 100 years

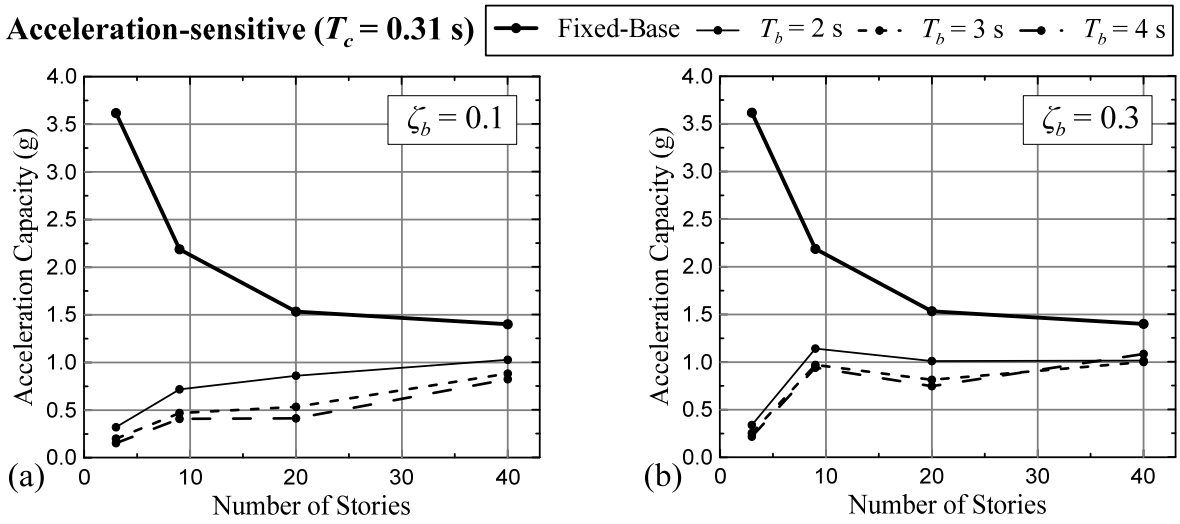

Figure 4.30 Acceleration capacities (T_c = 0.31 s) for T_R = 100 years

4.5 Conclusion

This chapter utilizes the PEER PBEE methodology and demonstrates a new application of the methodology to determine the required capacity x_m (drift ratio, floor acceleration, and component acceleration) and dispersion β that will satisfy the target performance level (T_R). x_m and β are plotted with respective to T_R, which is convenient for estimating desired median required capacity and dispersions in order to produce nonstructural components. Moreover, the plot will be useful for selecting and design particular nonstructural components during the initial design phase.

CHAPTER 5

SIMPLIFIED PERFORMANCE EVALUATION METHODOLOGY

5.1 Background and Objective

For vibration controlled buildings, the so-called performance curve can be constructed which is expressed by a function of few basic parameters that indicate the damping performance, and it can be used to estimate the maximum response, equipment connection, supporting material, and frame response. It is also meaningful to construct the seismic isolation performance curve with the same advantages as the vibration control performance curves. For vibration controlled buildings, a single mass model with 3 elements in series and 1 element in parallel is utilized. On the other hand, for base-isolated buildings, a series of two elements which represent the superstructure with various rigidity and low damping and isolation system with low rigidity and high damping. It is necessary to simulate the phase lag and decompose base and superstructure displacements which is shared by such simple model. Unlike typically used model of a SDOF with rigid superstructure, only the base responses can be obtained. Therefore, the objective for this chapter is to propose a simple model for base-isolated buildings which also gives dynamic characteristics as well as responses based on theory. From such simple model, the understanding of isolation system mechanism can be widely broadened. At last, the base isolation performance curve is proposed which can be used to illustrate various possibilities of isolation system to achieve a desired performance.

5.2 Base-Isolated Models

Figure 5.1(a) shows the 1st type of model which assumes rigid superstructure and is a one-mass system. When designing using this model, the isolation period T_b typically used is greater than 2.5 times the superstructure period T_s. However, this model cannot tell any information about superstructure response. In order to obtain the superstructure response, 2-mass system can be used as shown in Figure 5.1(b).

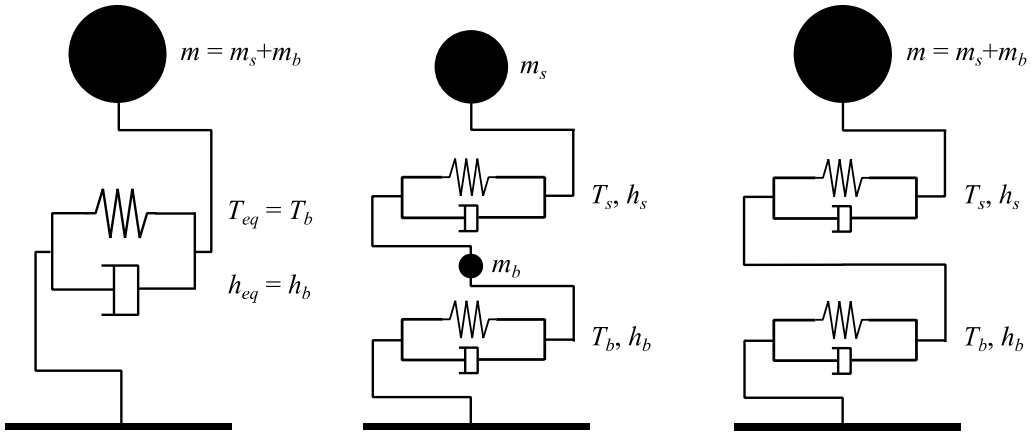

(a) 1-mass 1-layer model (b) 2-mass 2-layer model (c) 1-mass 2-layer model

Figure 5.1 Three types of base-isolated building model

In this study, 1-mass 2-layer system is proposed where the base mass m_b is shifted to be included with the superstructure mass m_s as shown in Figure 5.1(c). The taller the building, the smaller the mass ratio m_b/m_s is. The influence from the base becomes smaller resulting in higher accuracy.

In this proposed model, responses can be easily predicted from the response spectrum. Moreover, two complex springs representing superstructure and isolation are separated, hence, the balance between stiffness and damping parameters can be discussed. k_b and k_s are isolation and superstructure stiffnesses. c_b and c_s are isolation and superstructure damping coefficients. T_b and T_s are isolation and superstructure periods. h_b and h_s are isolation and superstructure

damping ratios. All springs are elastic. And natural periods and damping ratios can be obtained as follows.

$$T_b = 2\pi\sqrt{\frac{m}{k_b}} \quad , \quad T_s = 2\pi\sqrt{\frac{m}{k_s}} \tag{5.1}$$

$$h_b = \frac{c_b T_b}{4\pi m} \quad , \quad h_s = \frac{c_s T_s}{4\pi m} \tag{5.2}$$

5.2.1 Dynamic properties of the proposed model

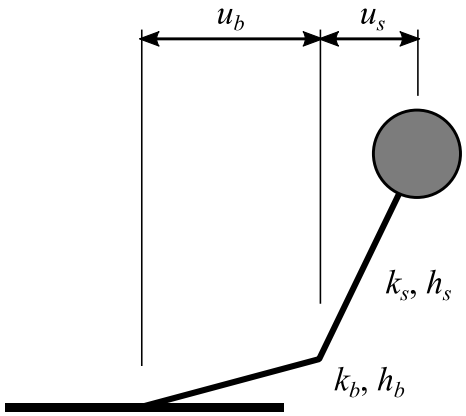

Figure 5.2 Proposed model

Considering steady-state response, the proposed model is shown in Figure 5.2. Since isolation system and superstructure have different damping coefficients c_b and c_s, base displacement u_b and superstructure u_s will not be in-phase. In order to consider this, complex isolation stiffness k_b^* and complex superstructure stiffness k_s^* are utilized which are composed of storage stiffnesses k_b', k_s' and lost stiffnesses k_b'', k_s'' and expressed as follows.

$$k_b^* = k_b' + ik_b'' = k_b'(1 + i\eta_b) \tag{5.3}$$

$$k_s^* = k_s' + ik_s'' = k_s'(1 + i\eta_s) \tag{5.4}$$

$$\eta_b = 2h_b\omega_{eq}/\omega_b \quad , \quad \eta_s = 2h_s\omega_{eq}/\omega_s \tag{5.5}$$

where η_b and η_s are loss factors. The equivalent complex stiffness can be obtained as follows.

$$k_{eq}^{*} = \frac{k_s^{*} k_b^{*}}{k_s^{*} + k_b^{*}} = \frac{k_s' k_b' (1 + i\eta_s)(1 + i\eta_b)}{(k_s' + k_b') + (k_s'\eta_s + k_b'\eta_b)i} = k_{eq}' (1 + i\eta_{eq}) \tag{5.6}$$

After manipulation, k_{eq} and η_{eq} of the system can be obtained as follows.

$$k_{eq}' = k_s' k_b' \frac{(k_s' + k_b')(1 - \eta_s\eta_b) + (\eta_s + \eta_b)(k_s'\eta_s + k_b'\eta_b)}{(k_s' + k_b')^2 + (k_s'\eta_s + k_b'\eta_b)^2} \tag{5.7}$$

$$\eta_{eq} = \frac{(k_s' + k_b')(\eta_s + \eta_b) - (1 - \eta_s\eta_b)(k_s'\eta_s + k_b'\eta_b)}{(k_s' + k_b')(1 - \eta_s\eta_b) + (\eta_s + \eta_b)(k_s'\eta_s + k_b'\eta_b)} \tag{5.8}$$

Substituting Equations (5.5) into Equations (5.7) and (5.8) and from $k_{eq} = m\omega_{eq}^2$, equivalent circular frequency ω_{eq} and equivalent damping ratio h_{eq} can be obtained as follows.

$$\omega_{eq} = \sqrt{\frac{-b + \sqrt{b^2 - 4ac}}{2a}} \tag{5.9}$$

where $a = 4(h_s\omega_s^2 + h_b\omega_b^2)$, $b = (\omega_s^2 + \omega_b^2)^2 - 4\omega_s^2\omega_b^2(h_s^2 + h_b^2)$, and $c = -\omega_s^2\omega_b^2(\omega_s^2 + \omega_b^2)$

$$h_{eq} = \frac{1}{2}\frac{(\omega_s^2 + \omega_b^2)(\eta_s + \eta_b) - (1 - \eta_s\eta_b)(\omega_s^2\eta_s + \omega_b^2\eta_b)}{(\omega_s^2 + \omega_b^2)(1 - \eta_s\eta_b) + (\eta_s + \eta_b)(\omega_s^2\eta_s + \omega_b^2\eta_b)} \tag{5.10}$$

From the 2DOF model (Figure 5.1(b)), dynamic properties are obtained from complex eigenvalue analysis. The results are compared with those obtained by Equations (5.9) and (5.10) from T_s = 0.5 – 3.0 seconds and h_b = 0.1 and 0.3 and shown in Figure 5.3. Solid lines are dynamic properties obtained from complex eigenvalue analyses and dashed lines are those obtained from the proposed model (Equations (5.9) and (5.10)). When T_b = 0, the base isolation floor is fixed, then T_{eq} and h_{eq} are equivalent to T_s and h_s of the superstructure. On the other hand, when T_b is very long, T_{eq} and h_{eq} tend to approach T_b and h_b. Comparison shows that when hb = 0.1, Teq and heq for the 1-mass systems are very close to those of the 2-mass

systems, and when $h_b = 0.3$, although h_{eq} appears to be slightly different, h_{eq} from the 1-mass systems are slightly different, within 10%, from those of the 2-mass systems.

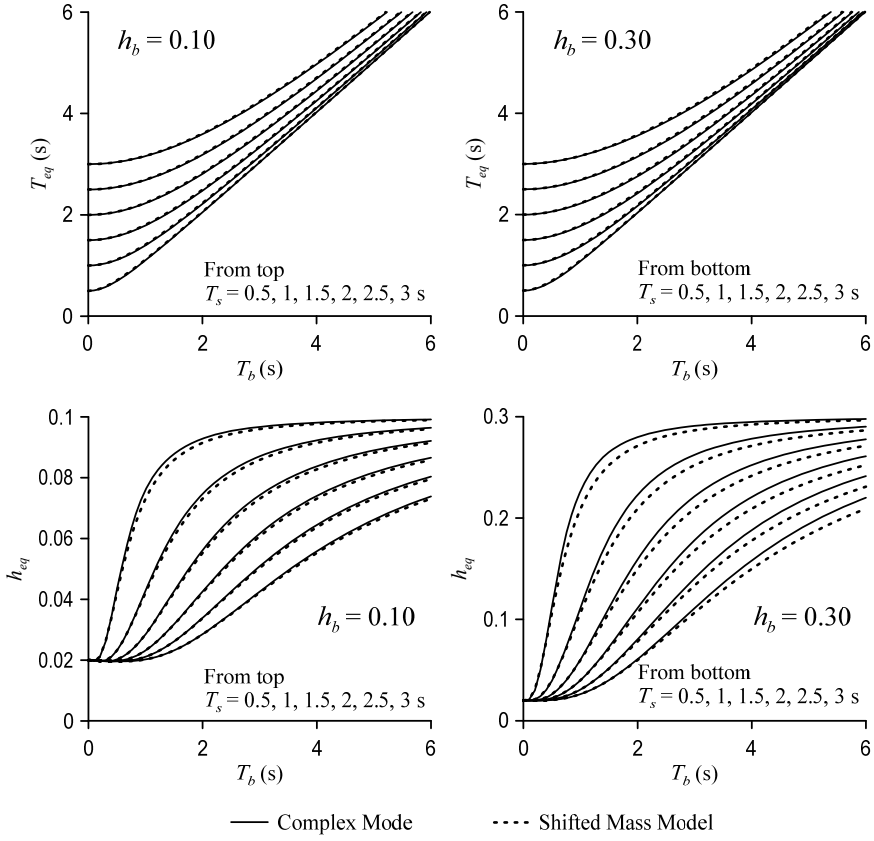

Figure 5.3 Comparison of 1st-mode period and damping ratio

5.2.2 Harmonic response of the proposed model

From Figure 5.2, harmonic response with equivalent circular frequency equal to ω_{eq} is considered. The maximum force and displacement for the system, base, and superstructure are obtained as follows.

$$F^* = k'_{eq}\left(1 + i\eta_{eq}\right)ue^{i\omega_{eq}t} \quad , \quad \left|F^*\right| = \sqrt{1 + 4h_{eq}^2}\,k'_{eq}u \tag{5.11}$$

$$F_b^* = k'_b\left(1 + i\eta_b\right)u_b e^{i\left(\omega_{eq}t + \delta_b\right)} \quad , \quad \left|F_b^*\right| = \sqrt{1 + \left(2h_b\frac{\omega_{eq}}{\omega_b}\right)^2}\,k'_b u_b \tag{5.12}$$

$$F_s^* = k_s'(1+i\eta_s)u_s e^{i(\omega_{eq}t+\delta_s)} \quad , \quad \left|F_s^*\right| = \sqrt{1+\left(2h_s\frac{\omega_{eq}}{\omega_s}\right)^2}\,k_s'u_s \tag{5.13}$$

where u, u_b, and u_s are system, base, and superstructure maximum displacements which occur at different timings. And because of 1-mass system, the maximum forces of the system, base, and superstructure are equal as shown below.

$$\left|F^*\right| = \left|F_b^*\right| = \left|F_s^*\right| \tag{5.14}$$

From Equations (5.11) – (5.14), u_b and u_s are obtained as follows.

$$u_b = u\left(\frac{\omega_{eq}}{\omega_b}\right)^2\sqrt{\frac{1+4h_{eq}^2}{1+\left(2h_b\omega_{eq}/\omega_b\right)^2}} \tag{5.15}$$

$$u_s = u\left(\frac{\omega_{eq}}{\omega_s}\right)^2\sqrt{\frac{1+4h_{eq}^2}{1+\left(2h_s\omega_{eq}/\omega_s\right)^2}} \tag{5.16}$$

Similar to Figure 5.3, Figure 5.4 shows the comparison of displacement ratio u_b/u and u_s/u obtained from the 1-mass system model and 2-mass 2-layer system using complex method. The comparison shows very good agreement with less than 10% difference.

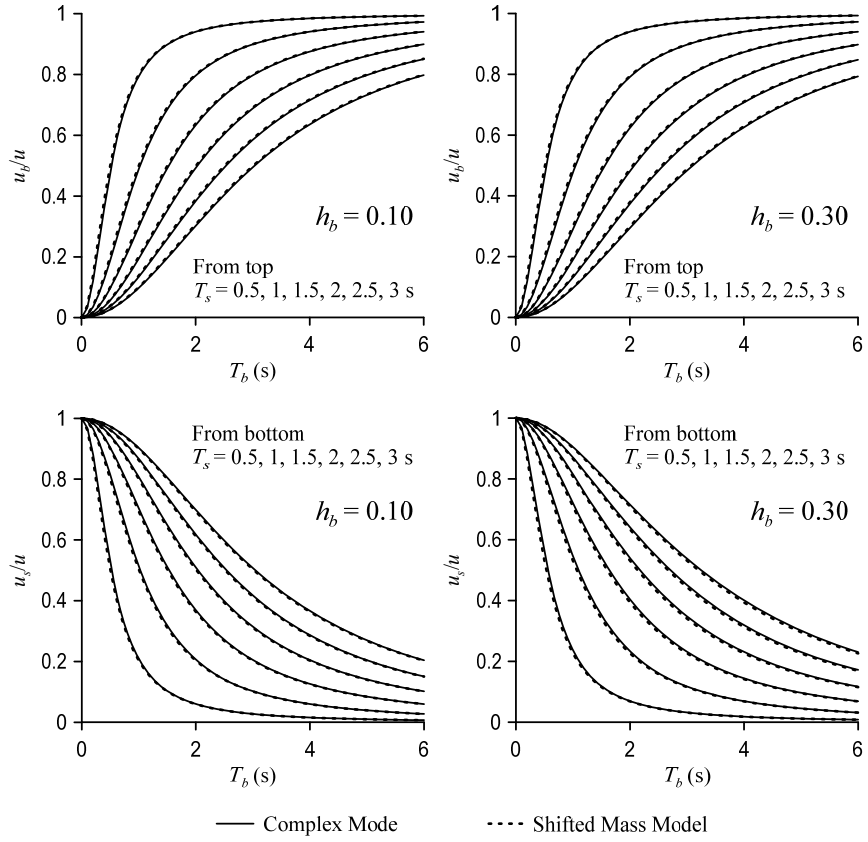

Figure 5.4 Comparison of u_b/u and u_s/u ratios

5.2.3 Earthquake response of the proposed model

Comparison of the response between the 2-mass 2-layer model (Figure 5.1 (b)) and the proposed 1-mass 2-layer model (Figure 5.1(c)) are conducted. The base-isolated buildings are assumed to 3- and 20-story building with T_s = 0.3 and 2.0 seconds, respectively, and same h_s = 0.02, T_b = 2 seconds, and h_b = 0.3. All floors have the same mass, that is $m_s/(m_b+m_s)$ = 3/4 and 20/21, respectively. Both models are subjected to the El Centro ground motion (EQ3 in Table 5.1). The displacements, velocities, and absolute accelerations for the base and superstructure are shown in Figure 5.5 and 5.6 for the 3- and 20-story buildings, respectively. Base isolation responses indicates that acceleration response from the proposed model is smaller than the 2-mass model due to lack of higher mode. On the other hand, for the superstructure responses,

the displacement, velocity, and acceleration are slightly different. However, in general, both of the models agree well with each other.

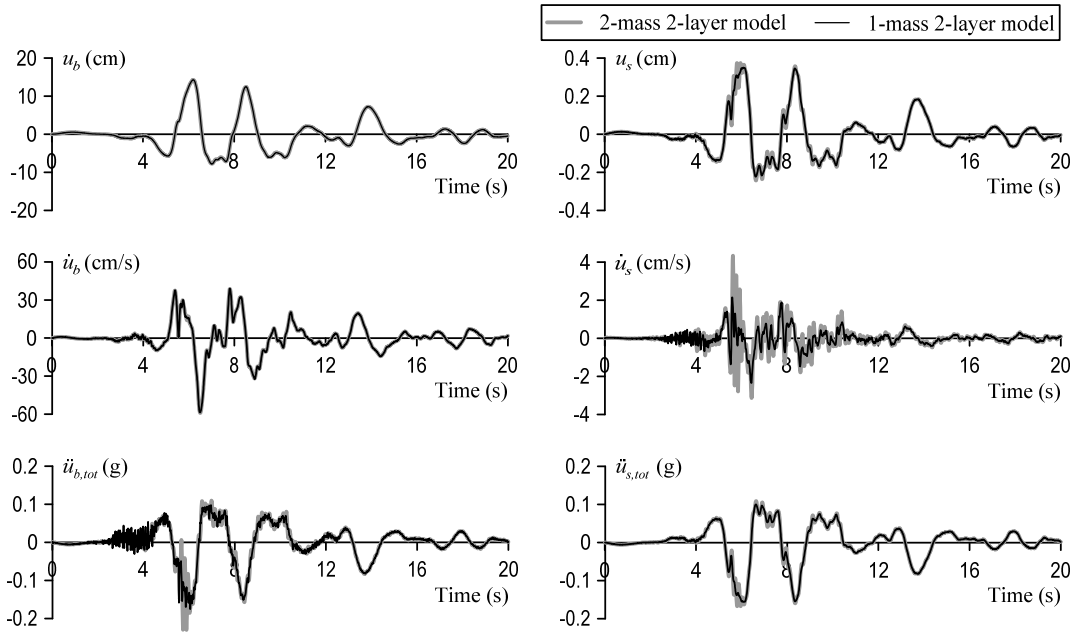

Figure 5.5 Time history responses of 2-mass 2-layer and 1-mass and 2-layer models

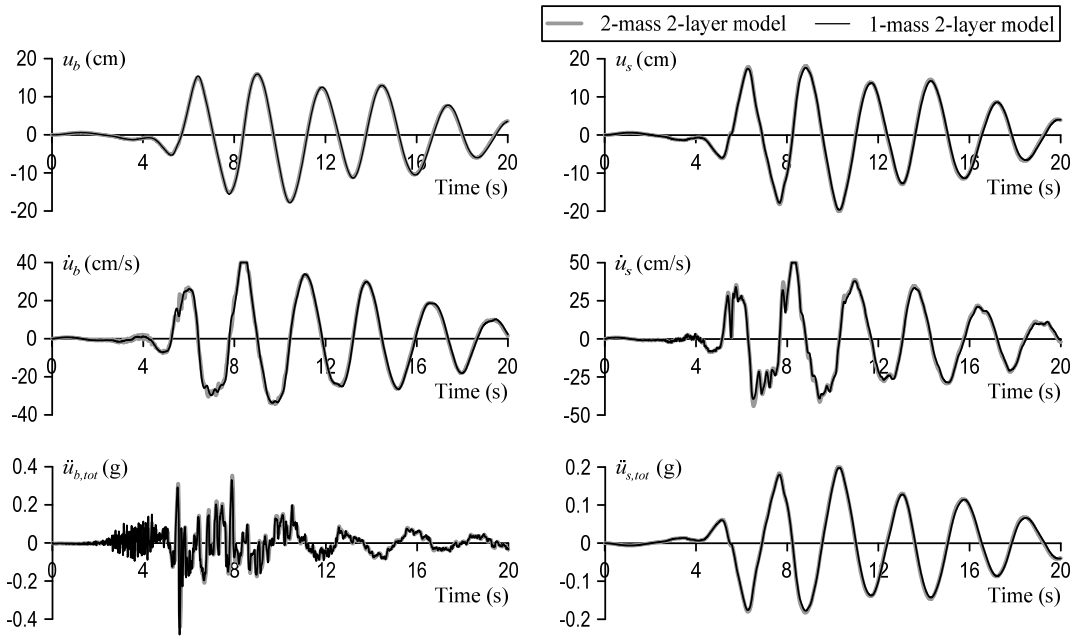

Figure 5.6 Time history responses of 2-mass 2-layer and 1-mass and 2-layer models

Figure 5.7 shows the transfer function of both models above. Figure 5.7(a,c) shows the transfer function between just above the isolation floor and the ground. Figure 5.7(b,d) shows the transfer function between the superstructure and just above the isolation floor. In Figure 5.7(a,c), the peaks for the 2nd mode have appear for the 2-mass system model, but not for the proposed model, however, for the 1st mode, they match almost completely. Also notice that effect of the 2nd mode is higher for the 3-story case which can also be observed from the response history in Figure 5.5. In Figure 5.7(b,d), at the short period region, some difference may appear, however, the curves are almost the same for both models. Hence, it is shown that the effects of shifting m_b to the superstructure part is very small.

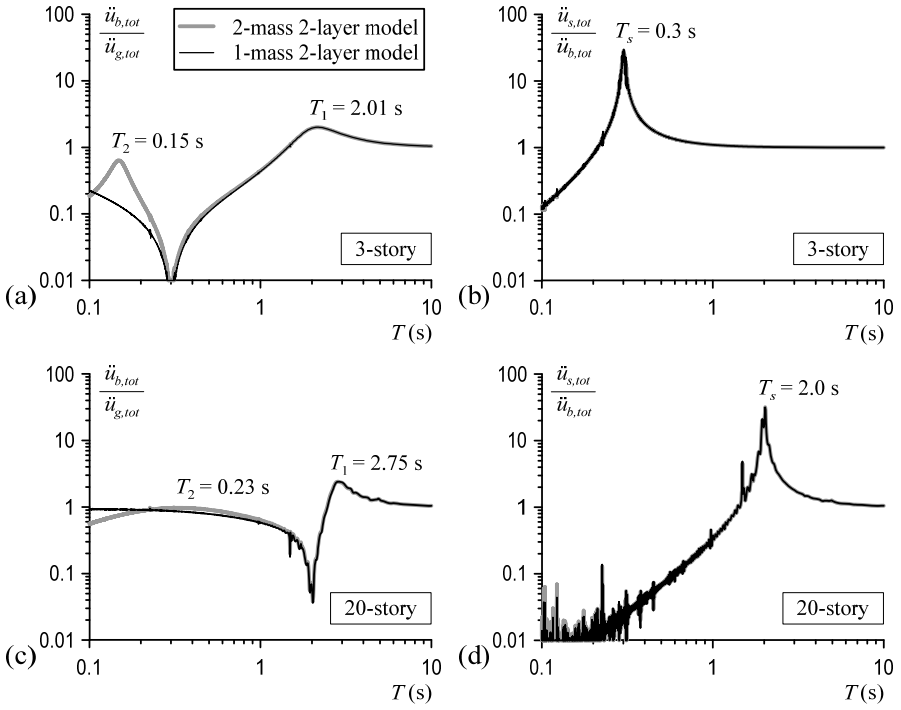

Figure 5.7 Transfer function of absolute acceleration response

5.2.4 Remarks regarding earthquake response

It is known that when building is subjected to actual ground motion, the response tends to be greater than that from the steady-state response assumption which becomes more obvious when isolation damping ratio is high. In this section, the effect of this is considered.

Table 5.1 List of ground motions

No	Earthquake	Year	Station	Magnitude	Component	PGA (g)
1	Tabas, Iran	1978	Tabas	7.35	TAB-LN	0.84
2					TAB-TR	0.85
3	Imperial Valley	1979	El Centro Array #5	6.53	H-E05140	0.52
4					H-E05230	0.38
5	Imperial Valley	1979	El Centro Array #6	6.53	H-E06140	0.41
6					H-E06230	0.44
7	Morgan Hill	1984	Gilroy Array #3	6.19	G03000	0.19
8					G03090	0.20
9	Loma Prieta	1989	Gilroy Array #3	6.93	G03000	0.56
10					G03090	0.37
11	Loma Prieta	1989	LGPC	6.93	LGP000	0.97
12					LGP090	0.59
13	Landers	1992	Barstow	7.28	BRS000	0.13
14					BRS090	0.14
15	Landers	1992	Fort Irwin	7.28	FTI000	0.11
16					FTI090	0.12
17	Landers	1992	Yermo Fire Station	7.28	YER270	0.24
18					YER360	0.15
19	Northridge	1994	Newhall - Fire Sta.	6.69	NWH090	0.58
20					NWH360	0.59
21	Northridge	1994	Rinaldi Receiving Sta.	6.69	RRS228	0.83
22					RRS318	0.49
23	Kobe, Japan	1995	KJMA	6.9	KJM000	0.82
24					KJM090	0.60
25	Kocaeli, Turkey	1999	Yarimca	7.51	YPT060	0.27
26					YPT330	0.35
27	Chi-Chi, Taiwan	1999	TCU065	7.62	TCU065-E	0.81
28					TCU065-N	0.60
29	Chi-Chi, Taiwan	1999	TCU068	7.62	TCU068-E	0.57
30					TCU068-N	0.46

Table 5.1 shows the ground motions from the PEER NGA database which will be used in this section. In general, for random ground motions, from elastic spectral displacement S_d, pseudo spectral velocity S_{pv} can be obtained by multiplying circular frequency ω, which is usually different from actual spectral velocity S_v. In past research, Kasai et al. proposed the β-factor ($=S_v/S_{pv}$), however, it was suitable for period range of 0.2 – 3.0 seconds. In this study, for base-isolated buildings which often possess long period, a new β-factor is proposed which is developed based on the ground motions in Table 5.1 from period T = 0.2 to 8.0 seconds and damping ratio h = 0.02, 0.05, 0.1, 0.15, 0.2, 0.3, 0.4 using least squares method. The approximation is shown in Equation (5.17).

$$\beta = 0.13T\left(0.1T + 2h + 0.3\right) + 0.93 \tag{5.17}$$

Figure 5.8 shows the hysteresis response of the viscous part (solid thin line), steady-state response (solid thick line), and β-adjusted steady-state response (dashed thick line) for a SDOF system with $T = 4$ seconds and $h = 0.3$ subjected to Gilroy Array (EQ7 in Table 5.1). It can be seen that with this β-factor, the steady-state response becomes much closer to that of the actual ground motion.

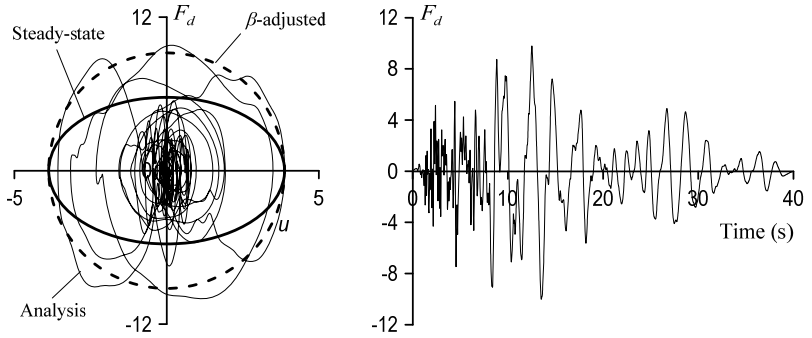

Figure 5.8 Comparison of time history, stead-state, and β-adjusted steady-state responses

Figure 5.9(a) shows the mean results of SDOF systems subjected to the 30 ground motions with various T and h (dotted) and those obtained from Equation (5.17) (solid line). The predicted β from the equation shows slightly different when $T = 2$ seconds. However, in general, the lines match very well with the actual data from the time history analyses.

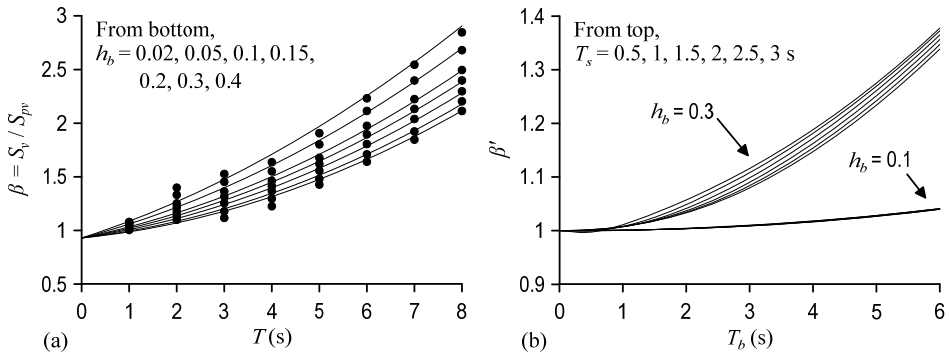

Figure 5.9 Amplification factors β and β'

The effect described above will be applied to the proposed model. Under ground motion excitation, the force at maximum displacement and the maximum force are generally different as a result of the viscous force. In order to apply the concept to the harmonic response assumed previously, β is multiplied to the viscous term in Equation (5.12). And in a similar way to Equation (5.14), the following equations can be obtained.

$$F^*_{b\_eq} = k'_b\left(1 + i\beta\eta_b\right)u_b e^{i\left(\omega_{eq}t+\delta_b\right)} \tag{5.18}$$

$$\left|F^*_{b\_eq}\right| = \sqrt{1+\left(2h_b\frac{\omega_{eq}}{\omega_b}\beta\right)^2}\,k'_b u_b = \left|F^*_{s\_eq}\right| = \left|F^*_{\_eq}\right| \tag{5.19}$$

where $\left|F^*_{\_eq}\right|$, $\left|F^*_{b\_eq}\right|$, and $\left|F^*_{s\_eq}\right|$ are the system, base, and superstructure forces, respectively. Dividing Equations (5.19) by (5.12(b)), we can obtained β' which indicates force increment as a result of β as follows.

$$\beta' = \sqrt{\frac{1+\left(2\beta h_b\omega_{eq}/\omega_b\right)^2}{1+\left(2h_b\omega_{eq}/\omega_b\right)^2}} \tag{5.20}$$

$$\left|F^*_{b\_eq}\right| = \left|F^*_{s\_eq}\right| = \left|F^*_{\_eq}\right| = \beta'\left|F^*_b\right| = \beta'\left|F^*_s\right| = \beta'\left|F^*\right| \tag{5.21}$$

Figure 5.9(b) shows the trend of β' as a function of isolation period T_b for the case of isolation damping ratio h_b = 0.1 and 0.3. And six cases of superstructure period T_s are considered from 0.5 to 3 seconds. It is seen that the change of β' is very small when h_b = 0.1, and becomes larger when h_b = 0.3. Nevertheless, β' is still much smaller than β shown in Figure 5.9(a). As an example of an actual case, if T_b = 4 seconds, β' is approximately 1.1 times, meaning that the effects on the overall responses are small. However, the amplification on the viscous force at T_b = 4 seconds is around 1.4 times which is large. Hence, when designing damper and its connection, this β should not be neglected.

5.2.5 Verification with responses from ground motions

Using the theory described in section 7.2.2 and considering the amplification effect in section 7.2.4, the accuracy of the proposed model subjected to ground motions are verified for 3-, 9-, and 20-story buildings (T_s = 0.3, 0.9, and 2.0 seconds, respectively) and h_s = 0.02. T_b of 2, 3, 4, and 5 seconds and h_b of 0.1 and 0.3 are considered for the isolation system. Ground motions shown in Table 5.1 are used. The analysis results are compared with those obtained from Equations (5.15) and (5.16). u_s from Equation (5.16) is then multiplied by β' in Equation (5.20). Both results are shown in Figure 5.10. u_s shows some scattering when h_b = 0.3, however for other cases, they all agree very well. The accuracy of u_s is slightly lower. For the 20-story building, the accuracy of u_s becomes higher than those of the 3- and 9-story buildings. u_s are observed to be much smaller than u_b. As seen in the figure, the accuracy of the proposed model is reasonably good.

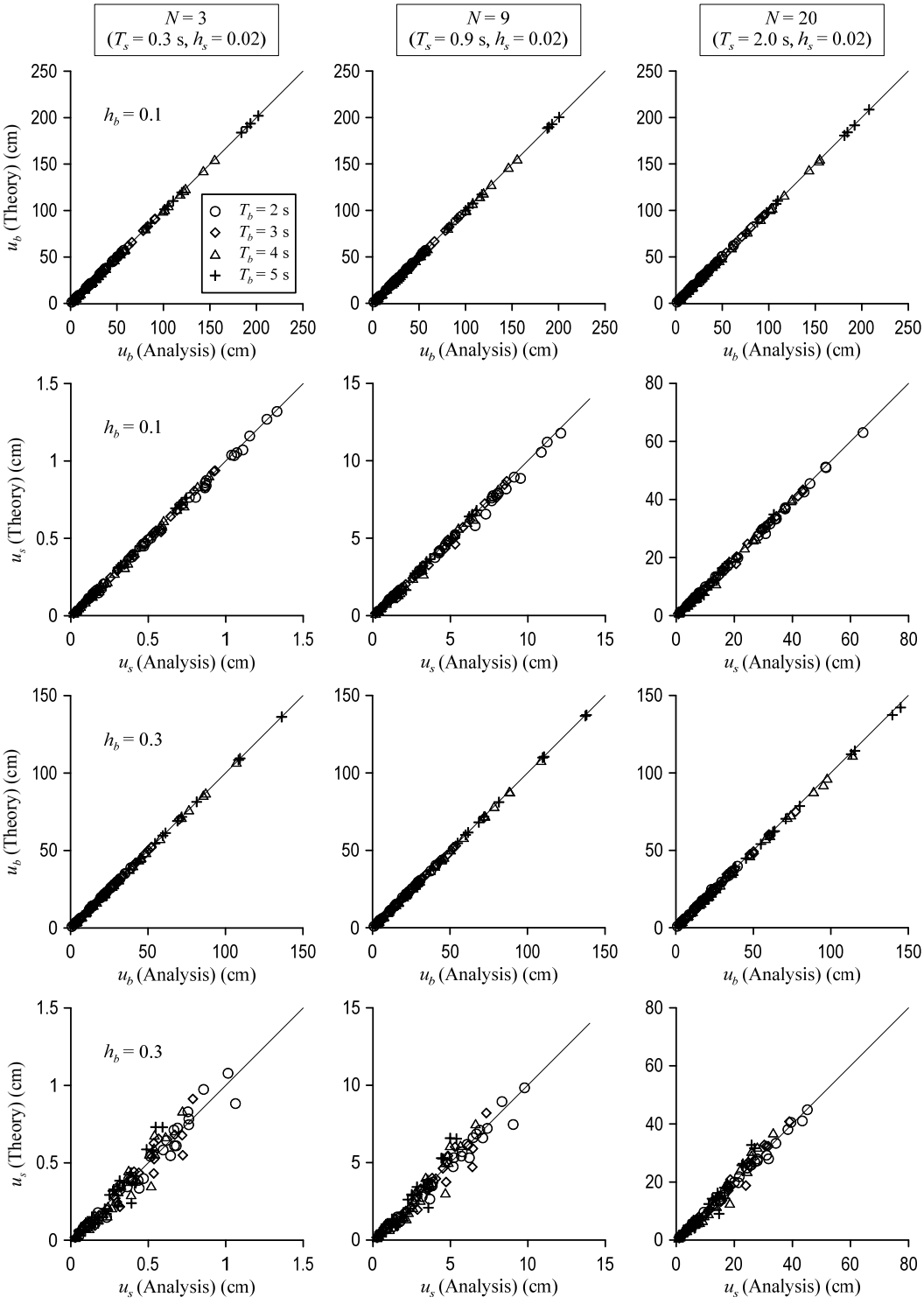

Figure 5.10 Comparison of u_s and u_b between the prediction equation and time history analyses (2-mass 2-layer model) for N = 3, 9, 20, and T_b = 2, 3, 4, 5 seconds and h_b = 0.1 and 0.3 under 30 ground motions

5.3 Base Isolation Performance Curve

5.3.1 Response prediction theory

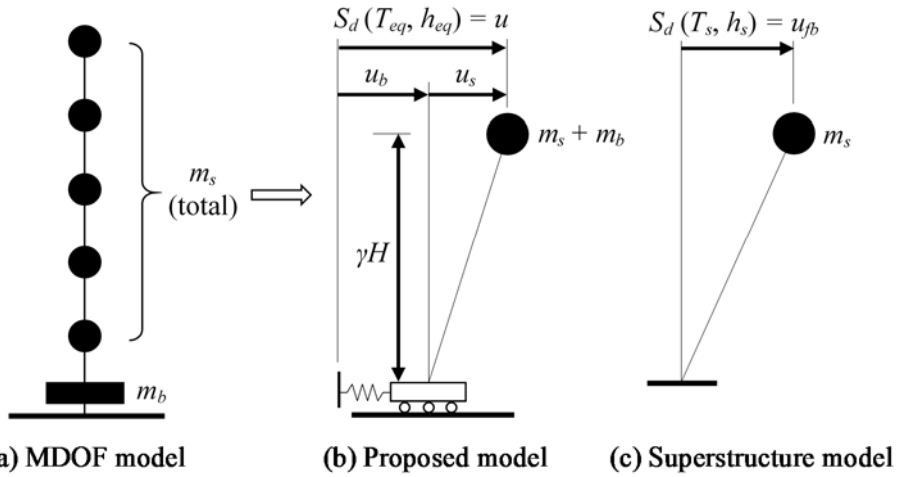

Figure 5.11 Base-isolated buildings models considered in this study

As shown in Figure 5.11(a,b), MDOF shear beam model is converted to SDOF shear beam model assuming the mass is located at the γH. And as described earlier, the base mass m_b is included in the superstructure. Also as shown in Figure 5.11(c), with the fixed isolation, u_{fb} is defined. With constant velocity assumption, the response ratio u/u_{fb} can be obtained as shown in the following equation.

$$\frac{u}{u_{fb}} = \frac{S_d(T_{eq}.h_{eq})}{S_d(T_s.h_s)} = \frac{D_h S_d(T_{eq}.h_s)}{S_d(T_s.h_s)} = D_h\left(\frac{T_{eq}}{T_s}\right) \tag{5.22}$$

$$D_h = \sqrt{\frac{1+\alpha h_s}{1+\alpha h_{eq}}} \tag{5.23}$$

where D_h is the effective damping coefficient. As a result of adding the isolation system to the fixed-base structure, h_{eq} becomes larger than h_s. α = 75 is used which is suitable for the BCJ-L2 ground motion. Substituting Equations (5.15) and (5.16) in Equation (5.22) gives the ratio u_b/u_{fb} and u_s/u_{fb} as follows. Note that β' is also used in the equation.

$$\frac{u_b}{u_{fb}} == D_h\left(\frac{T_b}{T_s}\right)\left(\frac{T_b}{T_{eq}}\right)\sqrt{\frac{1+4h_{eq}^2}{1+\left(2h_bT_b/T_{eq}\right)^2}} \tag{5.24}$$

$$\frac{u_s}{u_{fb}} == \beta' D_h\left(\frac{T_s}{T_{eq}}\right)\sqrt{\frac{1+4h_{eq}^2}{1+\left(2h_sT_s/T_{eq}\right)^2}} \tag{5.25}$$

With a variety of T_b/T_s and h_b, h_{eq} and T_{eq}/T_s can be obtained from Equations (5.9) and (5.10). The results are plotted in Figure 5.12(a). With h_s = 0.02, α = 75, β' = 1, the plots between u_b/u_{fb} and u_s/u_{fb} can be plotted from Equations (5.24) and (5.25) as shown in Figure 5.12(b). This performance curve contains a lot of useful information. For instance, we can understand the fundamental trend that when compared with T_s, if T_b is very long, and h_b is large, u_s becomes very small. If T_b is excessively long and h_b is small, u_b becomes very large, in which it should be careful. Together with h_{eq} and T_{eq} in Figure 5.12(a), we can understand the response trend more deeply.

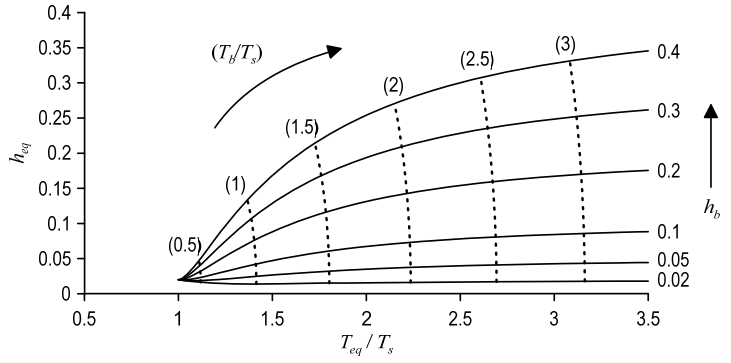

(a) Dynamic property

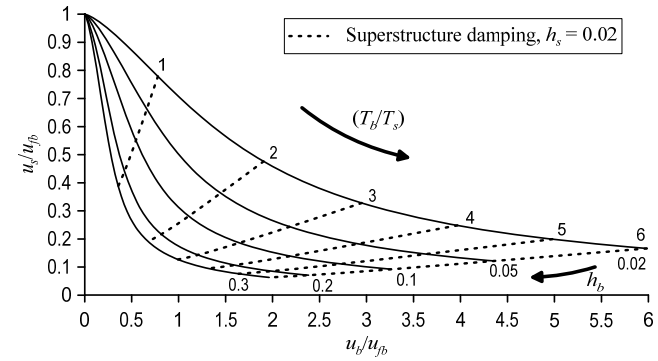

(b) Performance curve

Figure 5.12 Dynamic properties and performance curve when h_s = 0.02

On the other hand, not only we can understand the response trend, with the same figure, it can also be used for the design of the isolation system. For instance, if the clearance distance at the base is limited, we can then find appropriate u_b/u_{fb} that satisfies the condition. After that, several possibilities of T_b, T_s, and h_b can be selected from the performance curve immediately.

5.3.2 Building cases and input ground motions

In order to verify the accuracy of the proposed performance curve, several base-isolated buildings with a variety of number of stories, isolation periods, and isolation damping ratios are studied. A combination of isolation periods T_b of 2, 3, and 4 seconds and isolation damping ratios h_b of 0.1 and 0.3 are selected and obtained assuming rigid superstructure. All buildings have the same superstructure damping ratio h_s = 0.02. Two types of buildings will be investigated which are flexible and rigid buildings and are called Type A and Type B, respectively. The superstructure periods are determined from the following equations.

$$\text{Type A}: T_s = 1.4 \times 0.0724 H^{0.8} \tag{5.26a}$$

$$\text{Type B}: T_s = 0.03H \tag{5.26b}$$

where H is the superstructure height. The approximated periods shown above are from the ASCE 7-10 [4] and design guideline for steel structures in Japan. A value of 1.4 shown in the equation is a maximum period limited by [4] which reflects typically found building periods in the US. MDOF shear beam models are used for both building types. A_i-distribution is used to design the stiffness of each story of the buildings. 3-, 9-, and 20-story buildings representing short, medium, and tall buildings are considered. From Equations (5.26), the superstructure periods for Type A buildings are 0.665, 1.579, and 3.034 seconds and for Type B buildings are 0.315, 0.945, and 2.1 seconds. Four artificial ground motions having various different phase

characteristics are used. Their response spectra with h = 0.02 and scaled such that the median $S_{pv} \approx$ 140 cm/s are shown in Figure 5.13.

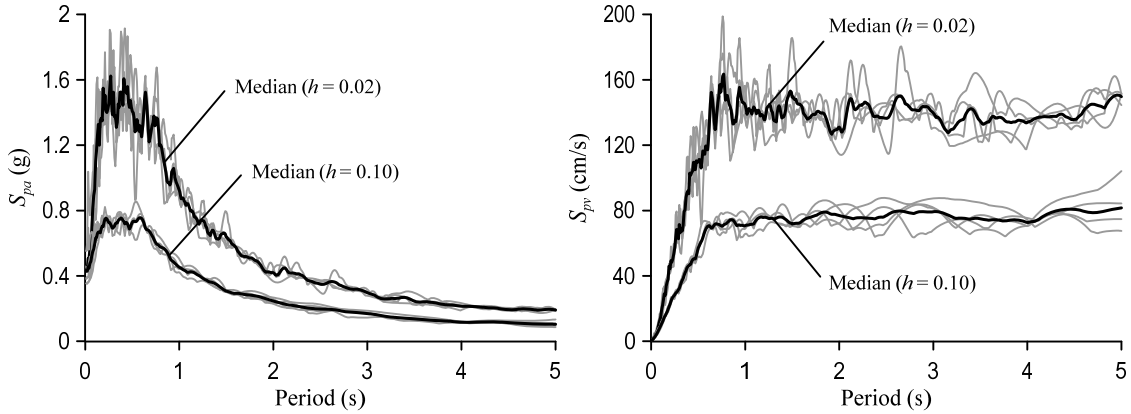

Figure 5.13 Response spectra of the artificial ground motions

And for the 4 ground motions used, α = 75 is used. Therefore, a total of 36 buildings (=3x2x2x3) and 144 time history analyses (=36x4) are performed. The accuracy of the proposed model and the performance curve are verified and shown in the following sections.

5.3.3 Accuracy of dynamic characteristics

The equivalent periods T_{eq} and equivalent damping ratios h_{eq} estimated from the proposed model are compared with those obtained from complex eigenvalue analyses. In this study, the values from the eigenvalue analyses are considered to be exact. The comparisons are shown in Table 5.2. For 3-story rigid buildings Type B, the isolation periods T_b and isolation damping ratios h_b are very close to the equivalent periods T_{eq} and equivalent damping ratios h_{eq}. On the other hand, for the 20-story flexible buildings Type A, h_{eq} are less than half of h_b. Hence, it is important to consider the flexibility in the superstructure.

Table 5.2 Comparison of dynamic properties between the proposed model and complex eigenvalue analysis

			Building Type A						Building Type B					
			T_{eq} (s)			h_{eq}			T_{eq} (s)			h_{eq}		
	T_b	h_b	Estimate	EVA	Ratio	Estimate	EVA	Ratio	Estimate	EVA	Ratio	Estimate	EVA	Ratio
3-Story Type A $T_s = 0.665$ Type B $T_s = 0.315$	2	0	2.105	2.072	1.016	0.086	0.090	0.955	2.024	2.016	1.004	0.096	0.098	0.987
		0	2.078	2.051	1.013	0.252	0.271	0.930	2.016	2.011	1.003	0.288	0.294	0.981
	3	0	3.070	3.047	1.008	0.093	0.095	0.977	3.016	3.010	1.002	0.098	0.099	0.994
		0	3.050	3.033	1.006	0.277	0.287	0.965	3.011	3.007	1.001	0.295	0.297	0.991
	4	0	4.053	4.035	1.004	0.096	0.097	0.986	4.012	4.008	1.001	0.099	0.099	0.997
		0	4.037	4.024	1.003	0.287	0.293	0.979	4.008	4.005	1.001	0.297	0.298	0.995
9-Story Type A $T_s = 1.579$ Type B $T_s = 0.945$	2	0	2.543	2.456	1.036	0.053	0.056	0.939	2.208	2.162	1.021	0.075	0.080	0.945
		0	2.490	2.393	1.040	0.142	0.159	0.894	2.167	2.122	1.021	0.216	0.239	0.906
	3	0	3.383	3.303	1.024	0.071	0.076	0.941	3.141	3.107	1.011	0.087	0.090	0.967
		0	3.315	3.234	1.025	0.202	0.226	0.897	3.105	3.076	1.009	0.257	0.272	0.945
	4	0	4.293	4.226	1.016	0.081	0.085	0.956	4.107	4.080	1.007	0.092	0.094	0.980
		0	4.226	4.165	1.015	0.237	0.256	0.924	4.076	4.055	1.005	0.274	0.284	0.966
20-Story Type A $T_s = 3.034$ Type B $T_s = 2.1$	2	0	3.632	3.531	1.029	0.028	0.028	1.003	2.896	2.799	1.034	0.040	0.042	0.967
		0	3.602	3.499	1.029	0.059	0.058	1.020	2.849	2.744	1.038	0.100	0.106	0.942
	3	0	4.260	4.119	1.034	0.042	0.043	0.964	3.654	3.549	1.029	0.058	0.062	0.941
		0	4.188	4.034	1.038	0.105	0.112	0.935	3.575	3.460	1.033	0.160	0.180	0.894
	4	0	5.010	4.859	1.031	0.055	0.058	0.944	4.508	4.412	1.022	0.071	0.075	0.946
		0	4.904	4.736	1.035	0.148	0.165	0.898	4.418	4.320	1.023	0.203	0.224	0.903

The comparisons are shown by the ratio between the estimated values and the exact values. It can be observed that the estimated T_{eq} tend to be slightly larger than the exact T_{eq}, however, less than 4% difference. On the other hand, the estimated h_{eq} tend to be smaller than the exact h_{eq}, however, within 10% difference. The accuracy of these properties are shown to be very good.

5.3.4 Verification with time history responses

The results of the time history analyses and those obtained from Equations (5.24) and (5.25) are plotted on the performance curve shown in Figure 5.14. Figure 5.14(a) and (b) shows the results of Type A and B buildings, respectively. u_b and u_s from time history analyses are obtained from the maximum base displacement and maximum superstructure displacement at the 2/3 height of the building. u_{fb} is obtained from the constant velocity assumption S_{pv} = 140

cm/s divided by the superstructure circular frequency ω_s. Also in order to plot the results of all buildings together in one figure, $\beta' = 1$ is used to plot all the data from the theory, and u_s from time history analyses are divided by actual β' (Equation (5.20)) instead. The data plots from the time history analyses are median responses from the 4 ground motions.

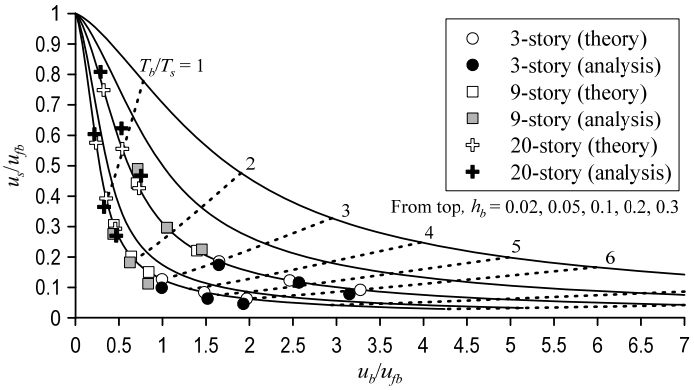

(a) Type A

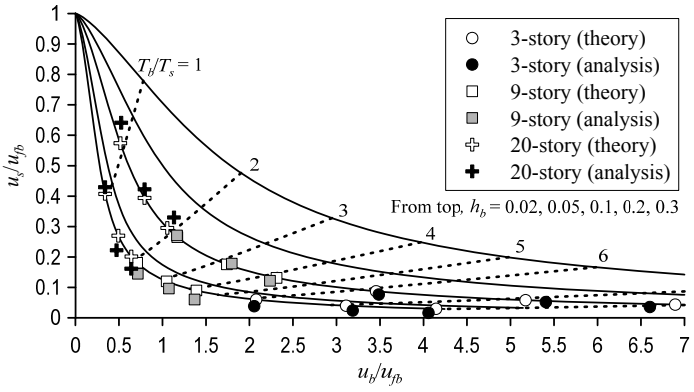

(b) Type B

Figure 5.14 Comparison between time history responses and the proposed model on performance curve when $h_s = 0.02$

As can be seen in the figure, the results from the proposed method match very well with those from the time history analyses. Moreover, the cases that could contribute to the scatterings shown in the figure are that the effective height is considered at 2/3 height for all the buildings, the effect of the 1st mode modal mass is not considered. These can be further improved in the future.

Figure 5.15 shows the hysteresis of the viscous force and displacement at the base story for the 3-, 9-, and 20-story buildings with h_b = 0.1 and 0.3 subjected to the BCJ-L2 ground motion together with the steady-state responses and β-adjusted steady-state responses. As can be observed, the responses from the time history analyses are larger than those of the stead-state responses only, however, slightly smaller than those of the β-adjusted steady-state responses. This confirms that β obtained previously can also be used for the MDOF system.

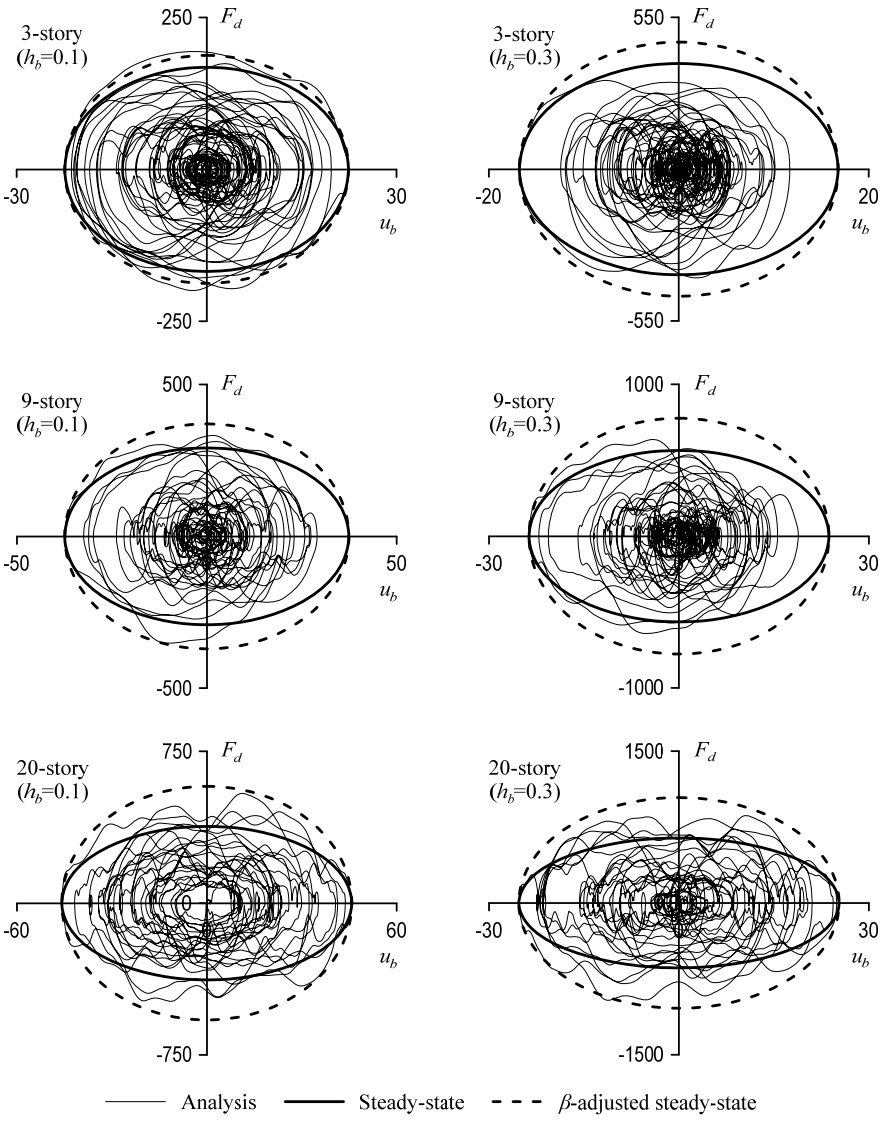

Figure 5.15 Hysteretic viscous force at the base story (h_s = 0.02)

Figure 5.16 shows the modal responses for the 20-story base-isolated building Type A with T_b = 2 seconds and h_b = 0.1 subjected to the BCJ-L2 ground motion obtained from the complex mode modal analysis. The 1st mode response, 1st and 2nd mode response, and 1st to 5th mode response, and 1st to 21st mode response are shown in the figure. In Figure 5.16(a), only the displacements considering the 1st mode only is different, the others are almost the same with those considering all modes. However, the maximum displacements for each story are almost the same even when considering just the 1st mode. This indicates that for displacement response, only the 1st mode is sufficient for the response prediction. In Figure 5.16(c), base shear response time history of the 1st mode only appears slightly different. Also, the maximum story shears are almost the same, slightly lower. However, if considering up to 2nd mode, the maximum story shears are almost the same as those considering all modes. On the other hand, in Figure 5.16(b), responses up to 5th modes are needed in order to agree with those from all modes. The accelerations of the 1st mode only are significantly different from those from all modes. In this study, only the 1st mode is considered, therefore, it should be careful when considering the acceleration response. This study focuses on the performance curve which considers the displacement. And high accuracy can be obtained.

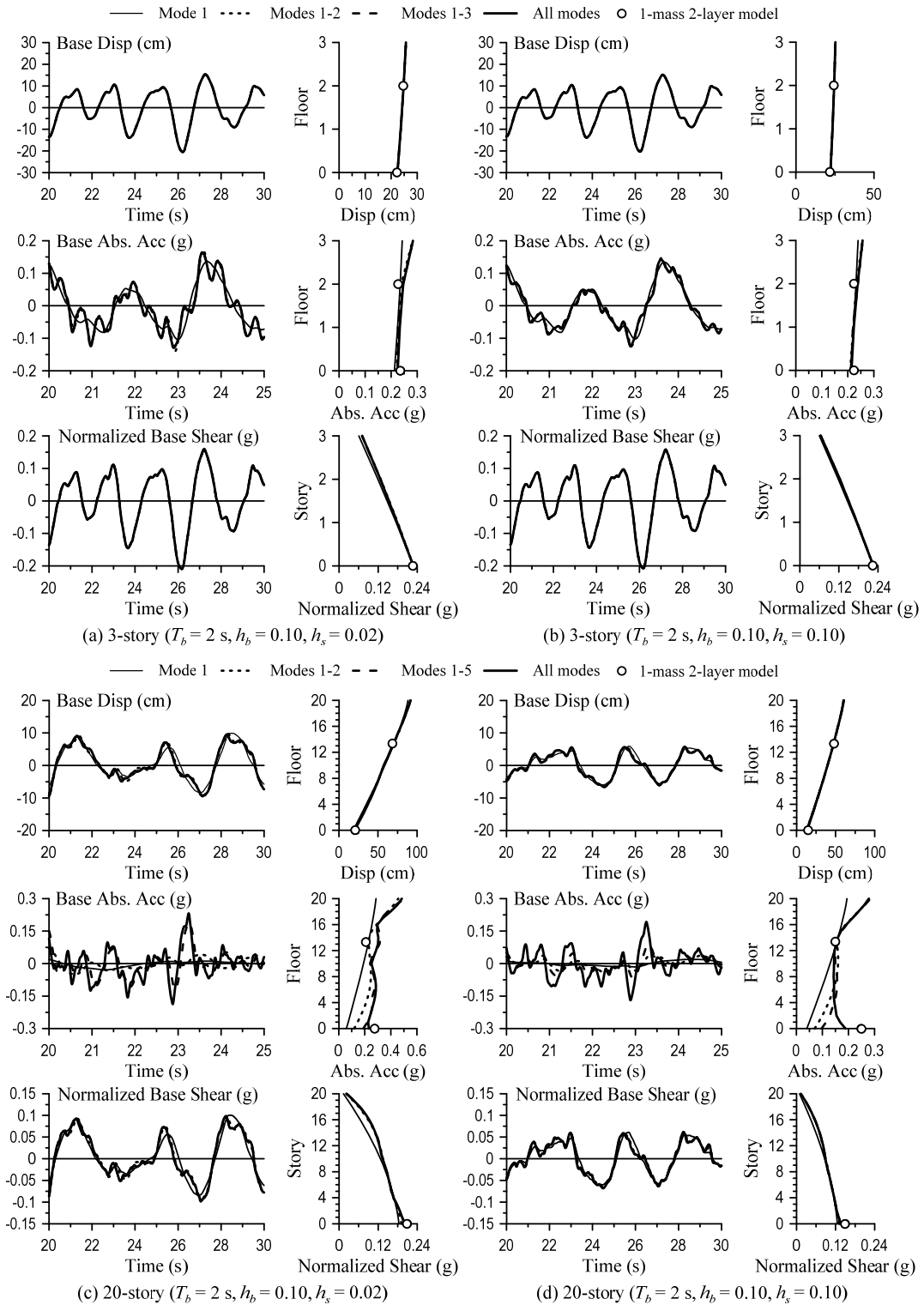

Figure 5.16 Modal response contribution from complex eigenvalue analyses: (a) displacement, (b) absolute acceleration, and (c) shear coefficient

5.4 Extension to Other Cases

5.4.1 Highly damped superstructure

Up to the previous section, superstructure damping h_s = 0.02 was considered. In this section, h_s = 0.10 will be considered to represent highly damped superstructure. When h_s = 0.10, the dynamic characteristics as well as the performance curve will be changed as shown in Figure 5.17. Figure 5.17(a,b) shows the dynamic properties and the performance curve when h_s = 0.02 and 0.10. Note that in Figure 5.17(b), the performance curve is created using u_{fb} obtained considering damping ratio of 0.02.

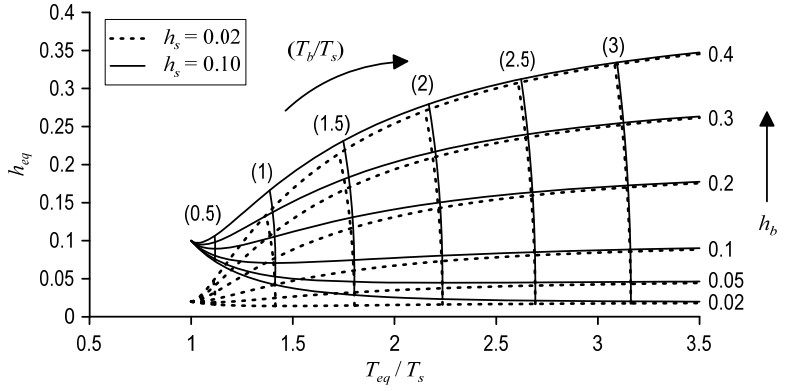

(a) Dynamic property

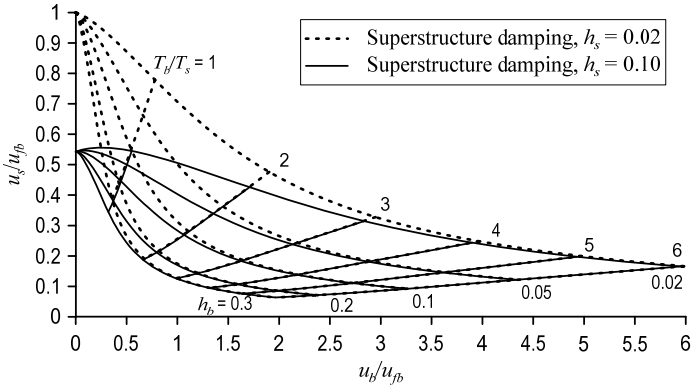

(b) Performance curve

Figure 5.17 Dynamic properties and performance curve when h_s = 0.02 and 0.10

Looking at the performance curve in Figure 5.17(b), when T_b/T_s is greater than 2.0, the effect of increasing damping from 0.02 to 0.10 is very small. For most short or low-rise buildings, T_b/T_s is usually greater than 2.0, therefore for those buildings, it is not necessary to increase the damping in the superstructure. The trend can also be understood when looking at Figure 5.17(a) that when T_b/T_s is greater 2.0, the dynamic characteristics of the buildings change very slightly. On the other hand, when T_b/T_s is less than 2.0, the effect of adding supplemental damping to the superstructure becomes more significant. This can also be understood from Figure 5.17(a) that when T_b/T_s is less than 2.0, h_{eq} becomes larger. Especially in Japan, because the clearance distance at the base is usually limited, T_b/T_s will be possibly around 1.0 in most cases. Hence, in order to increase the performance of the base-isolated building, either increasing the isolation damping ratio h_b or the superstructure damping h_s would be sufficient to reduce the responses on superstructure significantly. Figure 5.18 shows the comparison of the time history responses and the proposed method. The accuracy of the proposed method is very high.

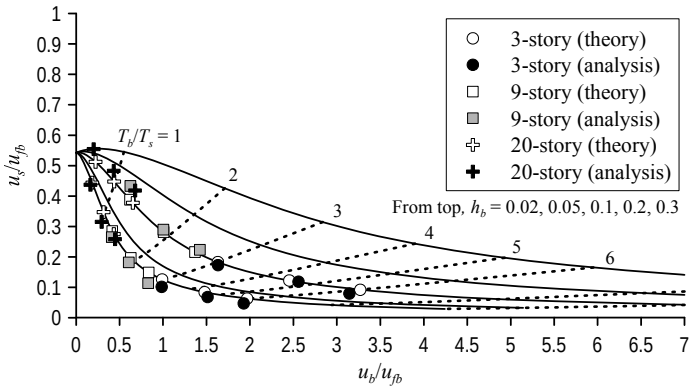

(a) Type A

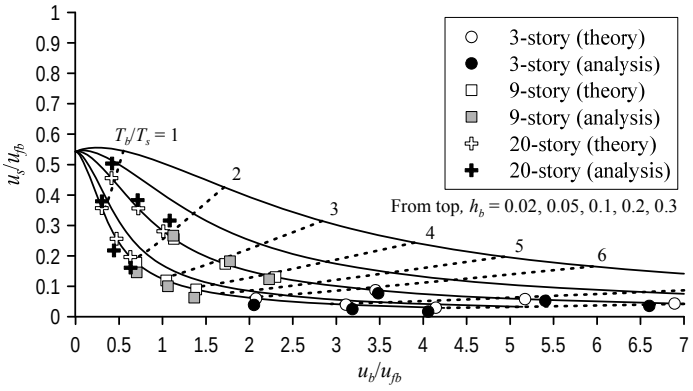

(b) Type B

Figure 5.18 Comparison between time history responses and the proposed model on performance curve when $h_s = 0.10$

5.4.2 Base-isolated building with bilinear hysteretic behavior

Up until the previous section, the isolation system was idealized as a linearly viscous system. In this section, typically used isolation system having a bilinear behavior will be investigated. Especially in Japan, steel and lead dampers are typically used to increase damping. Therefore, in this study, the applicability of the proposed method to bilinear hysteretic isolation is investigated. From the buildings used for the verification in section 7.3.4, the isolation system will be changed to having a bilinear hysteretic behavior by using the conversion rule as follows. The results will be compared.

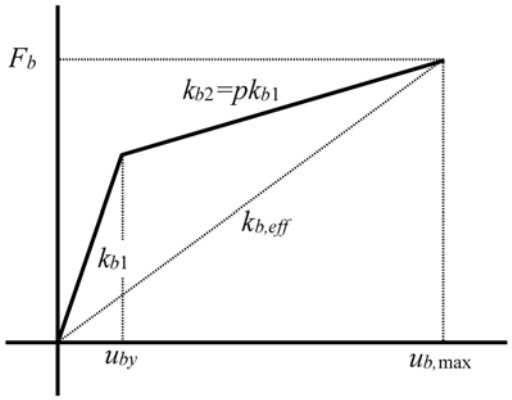

Figure 5.19 Bilinear hysteretic behavior backbone

The backbone of the bilinear behavior is as shown in Figure 5.19. k_{b1} is initial stiffness, u_{by} is yield displacement, $u_{b,\max}$ is maximum displacement, p is post-yield stiffness ratio, and $k_{b,eff}$ is effective stiffness at maximum displacement. μ is ductility which is $u_{b,\max}/u_{by}$. $h_{b,eff}$ is defined from the ratio of one cycle energy dissipation of bilinear to strain energy and is set to be equal to h_b in the previous sections. Also, after manipulation, p is obtained.

$$p = \frac{2 - \left(\pi h_{b,eff}\mu\right)/\left(\mu - 1\right)}{2 + \left(\pi h_{b,eff}\mu\right)} \tag{5.27}$$

$$h_{b,eff} = h_b = \frac{2\left(1-p\right)\left(\mu - 1\right)}{\pi\mu\left(1 - p + p\mu\right)} \tag{5.28}$$

$T_{b,eff}$ is the effective stiffness which is obtained from the effective stiffness $k_{b,eff}$ and is set to be equal to T_b. The relationship between k_{b1} and $k_{b,eff}$ from bilinear system can be obtained as shown below.

$$k_{b1} = \frac{k_{b,eff}\,\mu}{1 - p + p\mu} \quad , \quad k_{b,eff} = \frac{4\pi^2}{T_{b,eff}^2}\left(m_b + m_s\right) \quad , \quad T_{b,eff} = T_b \tag{5.29}$$

The maximum displacement $u_{b,\max}$ is obtained assuming S_{pv} = 140 cm/s. From $\omega_{b,eff} = T_{b,eff}/2\pi$, the yield displacement u_{by} can be obtained as follows.

$$u_{by} = \frac{u_{b,\max}}{\mu} = \frac{1}{\mu}\frac{S_{pv}\left(T_{b,eff}, h_s\right)}{\omega_{b,eff}}\sqrt{\frac{1+75h_s}{1+75h_{b,eff}}} \tag{5.30}$$

Once μ is selected, the properties for the bilinear system that has $T_{b,eff} = T_b$ and $h_{b,eff} = h_b$ can be obtained from Equations (5.27) – (5.30). Figure 5.20 shows the comparison between linearly viscous system and bilinear hysteretic system with μ = 15. As can be seen from the figure, at the maximum displacement, $k_{b,eff} = k_b$ and energy dissipations are equal at one cycle.

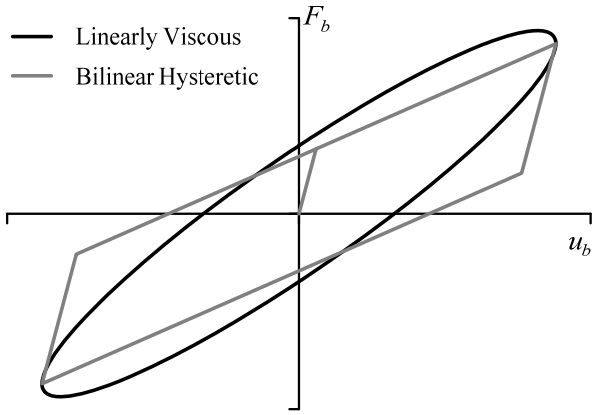

Figure 5.20 Conversion from linearly viscous to bilinear hysteretic system

With μ = 15, the isolation systems of the models used in section 7.3.4 are then converted using the method described above, then time history analyses are conducted. The results of the base-isolated buildings are plotted in Figure 5.21. Note that since it is bilinear system, β' described earlier for the viscous systems is not applied. Comparison of the responses from the proposed model and time history analyses shows that they agree well with each other. However, the accuracy is lower when compared with those from the previous sections (linearly viscous isolation). The reason is that the actual damping ratio of the bilinear system depends on the displacement and will be equal to h_b when the displacement reaches $u_{b,\max}$ defined earlier. Because for bilinear hysteretic system, the displacements vary from small to large, hence, it may not be appropriate to define effective damping ratio from one cycle at the maximum displacement.

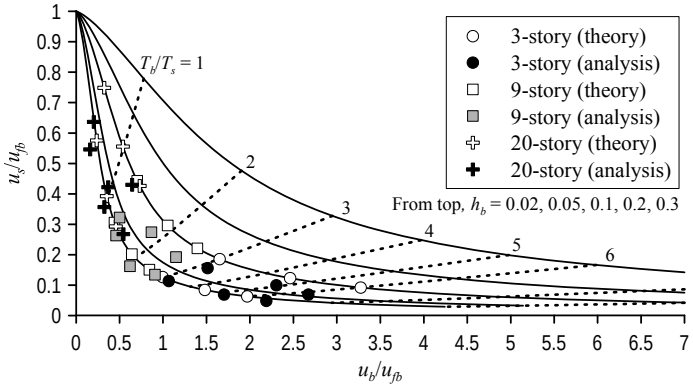

(a) Type A

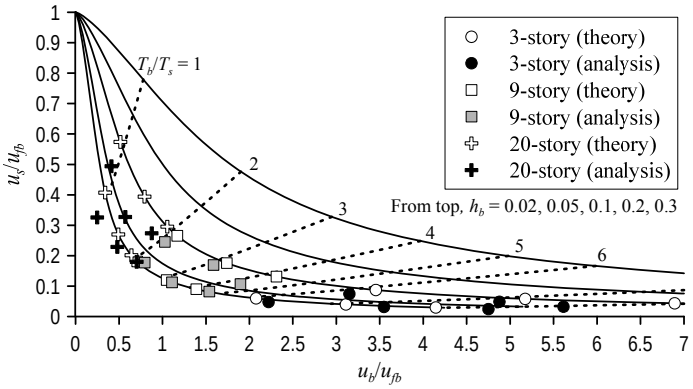

(b) Type B

Figure 5.21 Comparison between time history responses and the proposed model on performance curve when h_s = 0.02

The so-called average damping ratio may be used instead. The equation for the average damping ratio is shown in the following Equation (5.31). Figure 5.22 shows the relationship between ductility and average damping ratio with a variety of post-yield stiffness. In order to compare with the previous cases using the damping at maximum displacement of one-cycle, the same ductility μ = 15 is specified, and post-yield stiffness p can be obtained accordingly from Figure 5.22. The solid and broken lines are obtained from Equations (5.28) and (5.31), respectively. As shown in Figure 5.22, the differences between damping ratios estimated from the two equations are quite different. The responses from time history analyses together with the prediction values are shown in Figure 5.23. As can be seen in Figure 5.23, overall the time history responses become closer to the prediction values as compared with those in Figure 5.21.

$$h_{b,avg} = \frac{2}{\mu\pi p} \cdot \ln\left(\frac{1-p+p\mu}{\mu^p}\right) \tag{5.31}$$

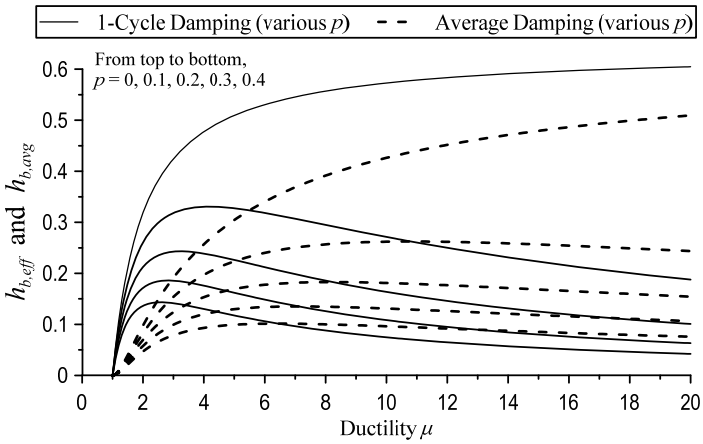

Figure 5.22 Relationship between ductility μ and effective damping ratio with various post-yield stiffness p

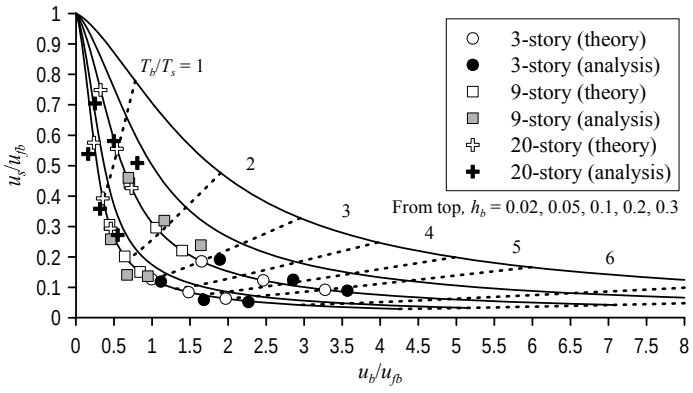

(a) Type A

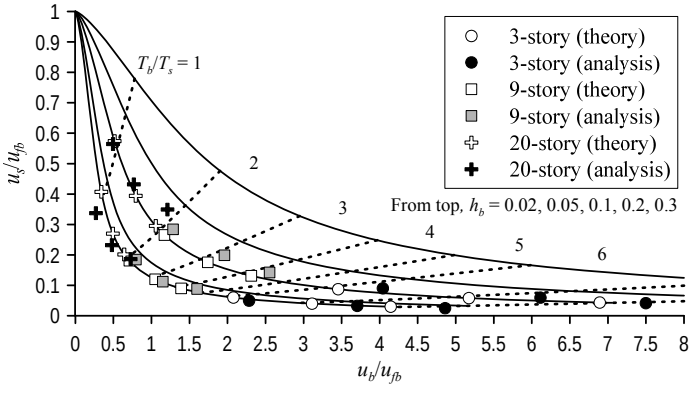

(b) Type B

Figure 5.23 Comparison between time history responses and the proposed model on performance curve when h_s = 0.02 (average damping ratio)

CHAPTER 6

APPLICATION TO AN EXISTING BASE-ISOLATED BUILDING

6.1 Objective

In the previous chapters, only multi-degree of freedom MDOF shear beam (stick) models have been used for investigation. To clarify the validity of the previous models as well as to investigate a real existing base-isolated structure, a 3-dimensional sophisticated nonlinear frame model is created. The target building is the well-known J2 base-isolated building located in Suzukakedai campus of Tokyo Institute of Technology. Lastly, the performance evaluation methodologies described in Chapters 4 and 5 are applied to the building for further investigation.

6.2 Outline of J2 Base-Isolated Building and Monitoring System

Figure 6.1 shows the illustration of the 20-story seismic isolated building, located in Suzukakedai campus of Tokyo Institute of Technology. The building is called as “J2 building”. The seismic isolation floor (MFL) in the building is in between the first floor (1F) and the second floor (2F). Hence, from 2F upwards, it is considered as the superstructure of this building. The columns in the superstructure are Concrete-Filled Tube (CFT) columns. The beams in the superstructure are steel beams. The first floor (1F) components are reinforced-concrete beams and columns. The columns in the first story are very large, twice the size of the columns, so that the ground accelerations and the accelerations just below the isolation level (MFL) are almost identical.

In the isolation floor, several types of dampers are installed. Figure 6.2 shows the location of the dampers. Rubber bearings with conical spring washer (Figure 6.3(a)) are installed at the corner of the building. Steel dampers (Figure 6.3(b)) and oil dampers (Figure 6.3(e)) are installed at the sides of the short direction. Rubber bearings with steel dampers (Figure 6.3(c,d)) are installed at the sides along the long direction of the building.

In the superstructure, in order to render the structure to be very stiff, so that the isolation could be most efficient, mega-braces are installed on the both sides of the building in the short direction. Due to large and slender nature of the building, large up-lift forces may develop during a major earthquake. To prevent this, rubber bearings with conical spring are installed at the corners to accommodate tensile forces that may develop.

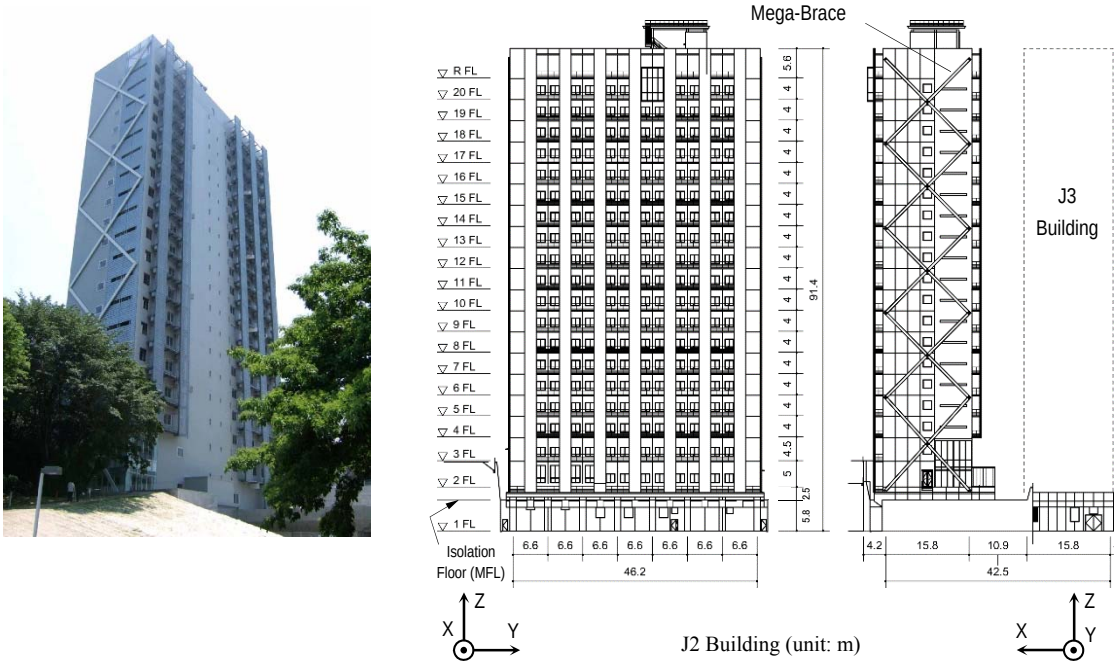

Figure 6.1 Picture and illustration of the J2 base-isolated building

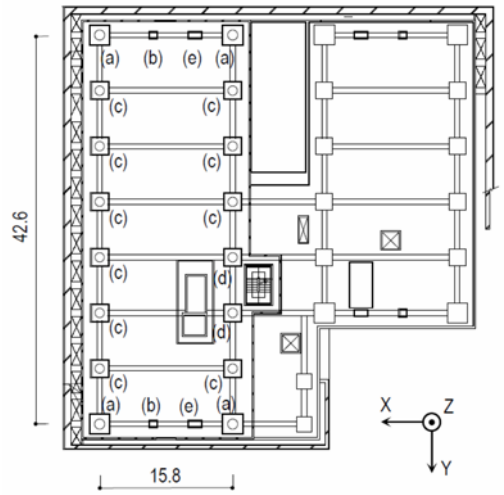

Figure 6.2 Isolation floor plan of the J2 base-isolated building

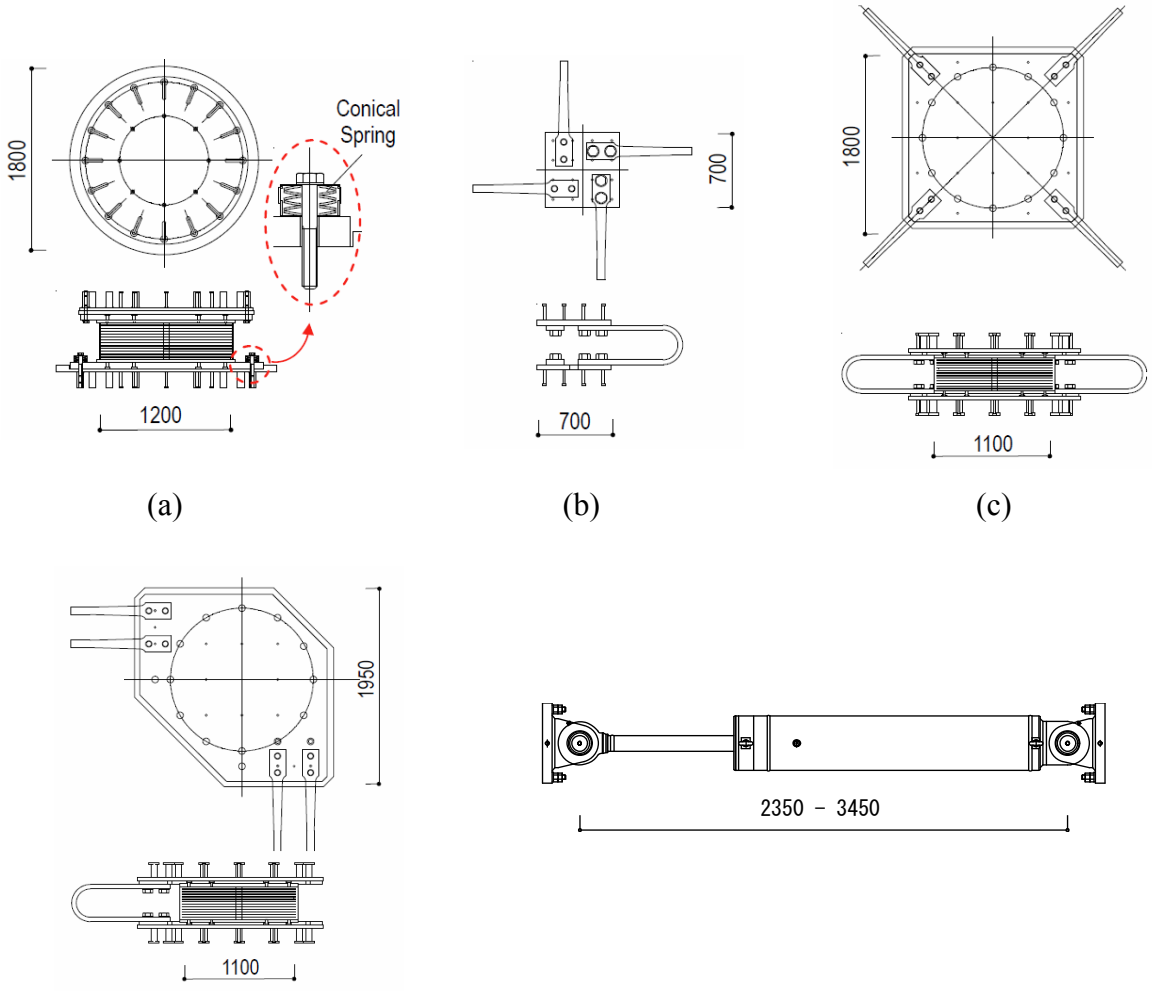

Figure 6.3 Rubber bearings and dampers used in the J2 base-isolated building (unit: mm)

Figure 6.4 shows the locations of the accelerometers installed in the building. They are placed on the 1st floor, isolation floor, 2nd, 7th, 14th, and 20th floors. From the recorded acceleration histories, the displacement time histories can be computed by conducting double integration of the acceleration time histories. The displacement transducers are installed to measure the displacement of the isolation devices. A trace recorder is also installed to measure large as well as small inter-story displacement in the isolation story. The trace recorder is fixed to the steel beam at the bottom of the superstructure while the stainless steel board, on which the behavior of the isolated story is drawn, is fixed to concrete slab at the top of the substructure. Oil damper force and deformation are also measured. Table 6.1 indicates the list of the sensors installed in the building.

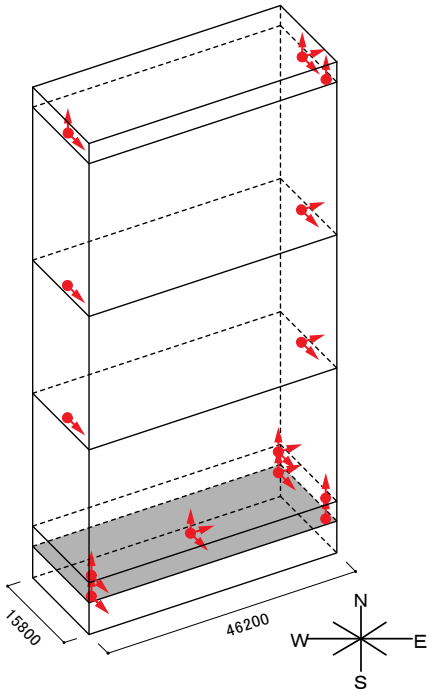

Figure 6.4 Locations of the accelerometers

Table 6.1 List of the sensors

Floor	Item	Capacity	Sensitivity
2^{nd}, 7^{th}, 14^{th}, 20^{th}	Acceleration	2G	1 μG
	Column, Brace Strain	(Strain Gauge)	1 μstrain
Isolation Floor	Acceleration	2G	1 μG
	Small Story Drift	±100 mm	0.05 mm
	Large Story Drift	±500 mm	0.5 mm
	Drift Trace	-	-
	Damper Force	(Strain Gauge)	1 μstrain
	Damper Deformation	1000 mm	0.5mm
	Isolator Up-Lift	50 mm (Video)	0.03mm
1^{st} Floor (Ground)	Acceleration	2G	1 μG

6.3 Response Verification of J2 Base-Isolated Building (Superstructure)

The model of this building is created using the nonlinear structural analysis program called PC-ANSR by Bruce F. Maison. The analysis is divided into 2 parts, first is the superstructure only (this section), and second is the extended the model in this section to include the base isolation system.

6.3.1 Superstructure modelling overview

Figure 6.5 shows the coordinate system used in PC-ANSR. Note that the axis orientations used in the recorded data are different from the ones used in PC-ANSR for the analysis.

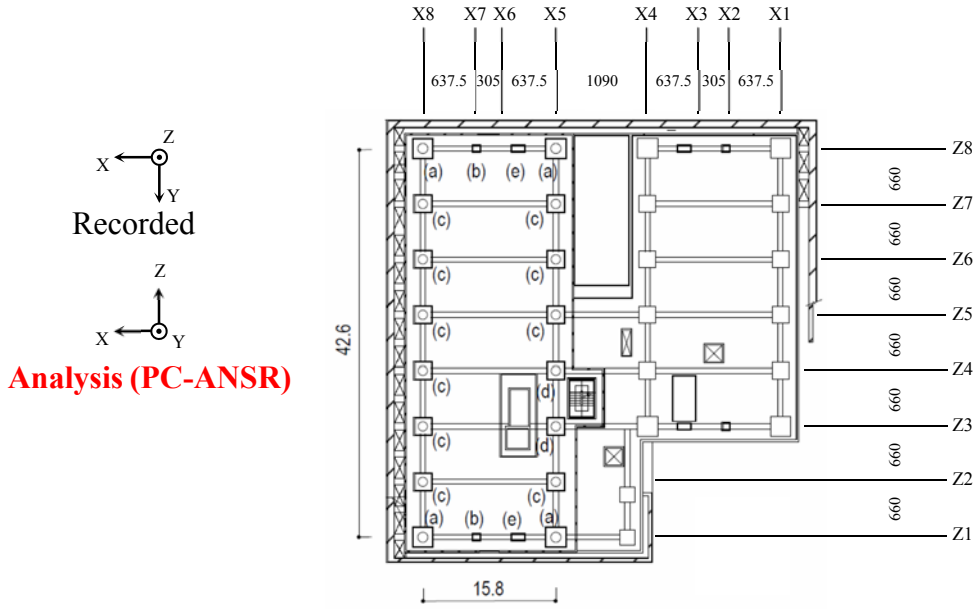

Figure 6.5 Coordinate system used in PC-ANSR (unit: cm)

Since the superstructure behaves mainly elastic due to large energy dissipation in the isolation floor, the beam and column of the superstructure are simply modeled as one piece of element connecting from one element to the connecting element. The units used in the model are kilonewton (kN) and centimeter (cm).

Figures 6.6 - 6.8 illustrate the model used in the analysis. Diagonal elements shown in Figure 6.6(a) are used for mega-braces. Diagonal elements in Figures 6.6(b,e) and 6.7(a,b) are walls. Diagonal elements in Figure 6.6(d) are inner braces. Diagonal elements shown in Figure 6.8(a) are used to represent the rigidity of slab components. The modeling for each component is described below. Figure 6.9 shows the 3D sophisticated model constructed in PC-ANSR.

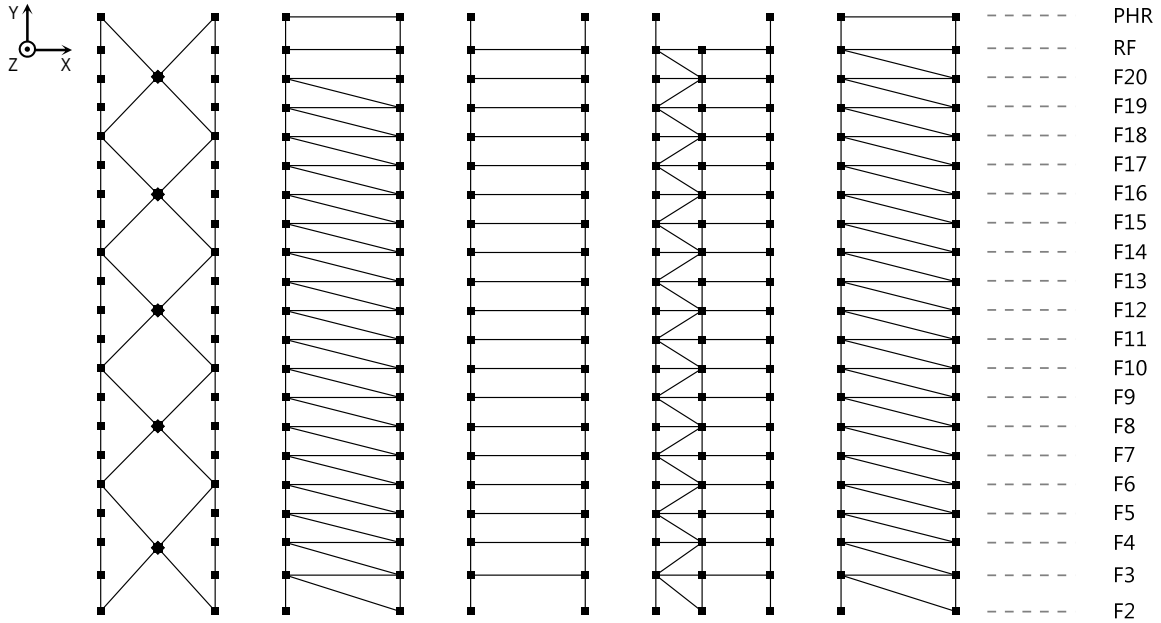

(a) Z1' & Z8' (b) Z1 (c) Z2, Z3, Z4, Z6, Z7 (d) Z5 (e) Z8

Figure 6.6 Model drawing along X-axis for each frame

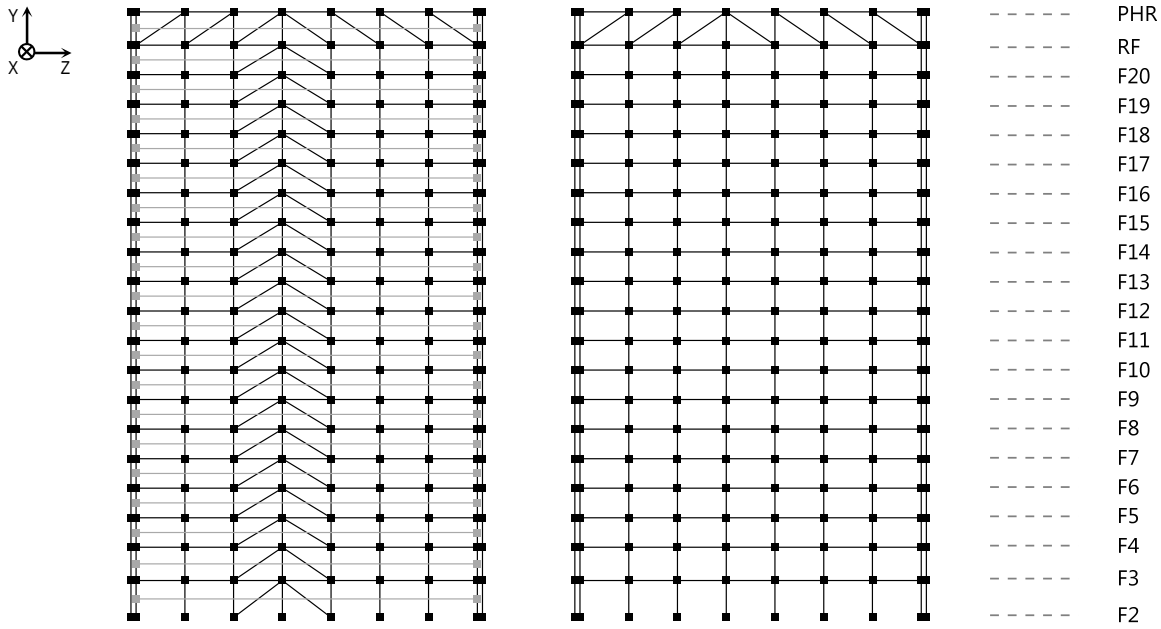

(a) Frame X5 (b) Frame X8

Figure 6.7 Model drawing along Z-axis for each frame

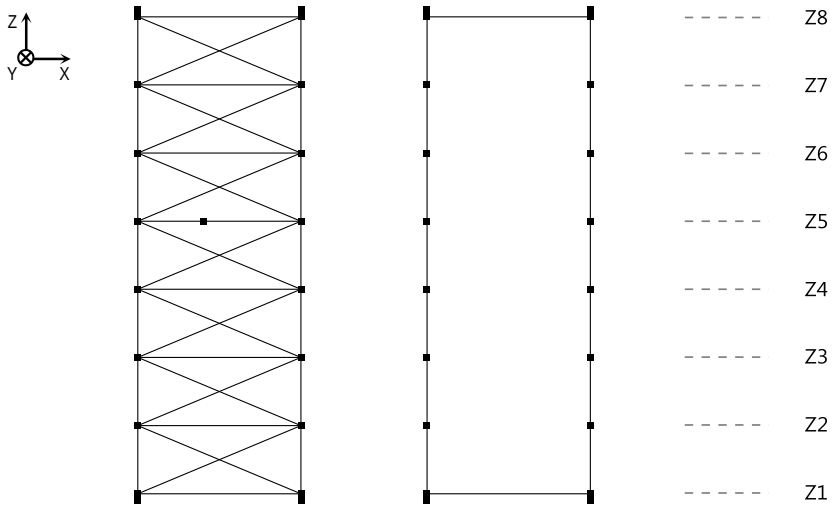

(a) 3th – RF floors (b) PHR floor

Figure 6.8 Model drawing (floor plan)

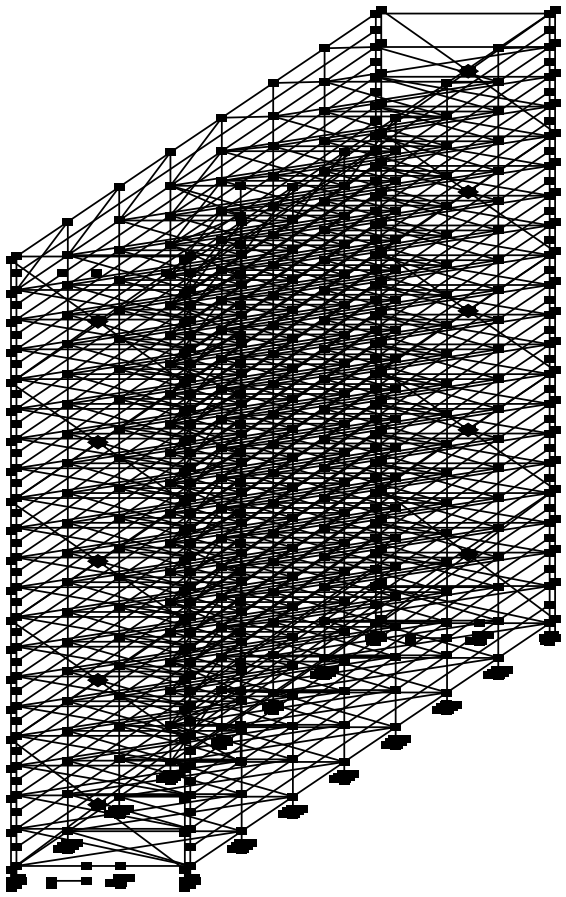

Figure 6.9 3D model illustration of J2 base-isolated building in PC-ANSR

6.3.2 Modelling of the structural components

Beam components

Nonlinear beam-column elements (G4) in PC-ANSR are used to model the behavior of the beams. All beams in the superstructure are steel H-beams. Hence, the necessary section properties of the beams, which are section moduli Z_x and Z_y, moments of inertia I_x and I_y, and cross sectional area A, can be obtained from the material property handbook (orange book). For steel material property, young's modulus E of 20500 kN/cm^2, shear modulus G of 7900 kN/cm^2, and yield stress σ_y of 32.5 kN/cm^2 are used. From these properties, the yield axial force P_n and yield moments M_{nx} and M_{ny} for both directions, can be obtained from the following equations. Appendix A shows the list of beam properties used in PC-ANSR.

$$P_n = \sigma_y A \tag{6.1}$$

$$M_{nx} = \sigma_y Z_x \quad \text{and} \quad M_{ny} = \sigma_y Z_y \tag{6.2}$$

Column components

Three dimensional beam-column elements (G10) in PC-ANSR are used. Since all columns are CFT which are composite columns, the stiffness and strength cannot be simply obtained or calculated from the material property handbook. In this case, fiber analysis of the section is conducted to obtain the stiffness and strength. The sectional analysis is conducted by using the SAP program. By inserting the concrete and steel material properties and the shape of the section into the SAP program, the sectional moduli, moments of inertia, as well as initial stiffness and yield strength can be obtained. For nonlinearity, it is assumed that the post yield stiffness is 1% of the initial stiffness in all columns. Appendix B shows the list of beam properties used in PC-ANSR.

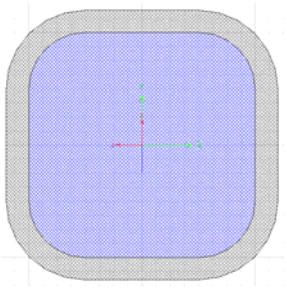

(a) Cross section

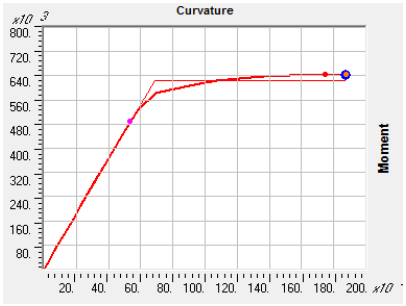

(b) Moment-curvature relationship

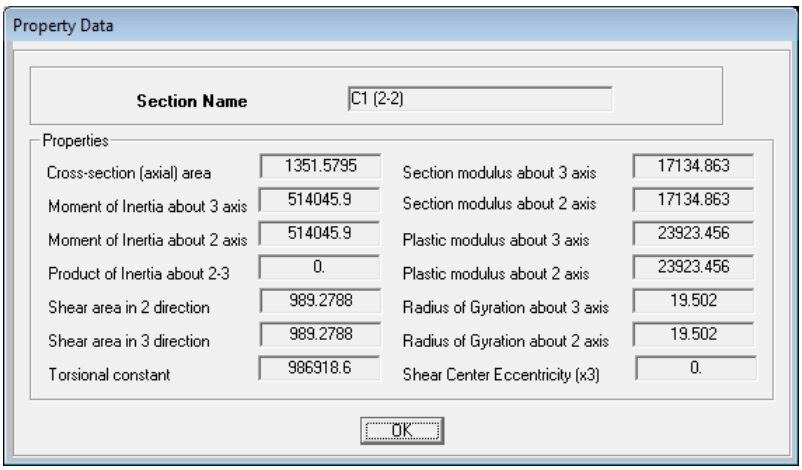

(c) Column sectional property

Figure 6.10 Property of a column obtained from sectional analysis in SAP program

Slab components

To reflect the rigidity of the slab, very stiff struts, using nonlinear truss elements (G2), are inserted across the area of the slab as shown in Figure 6.11. The stiffness assigned is equal to 10^{15} kN/cm.

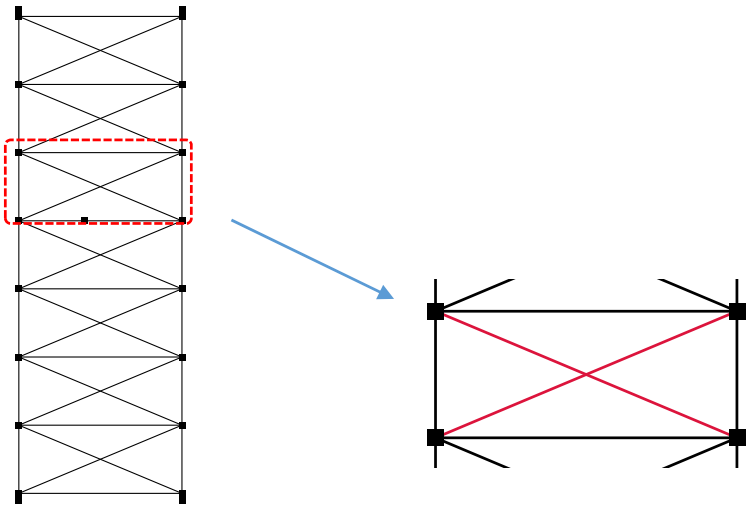

Figure 6.11 Slab element

Wall components

A diagonal strut, using nonlinear truss elements (G2), is inserted to represent the wall component. The horizontal stiffness of the wall K_w is determined by calibration. First, the stiffness of a column is calculated to be used as a reference. Since *EI* property of a column is known, therefore the stiffness of a column is as follows,

$$K_{\text{col}} = \frac{12EI}{h^3} \tag{6.3}$$

where h is the height the column. Then a formula used for calibration is as follows,

$$K_{\text{w}} = \alpha_i K_{\text{col}} \tag{6.4}$$

where α_i is a factor for i^{th} story used for calibration. In this analysis, the column of the 2nd story located at X5Z3 is arbitrarily chosen as a reference. Then α for each story for the walls along the X-plane and Z-plane are shown in Tables 6.2 and 6.3, respectively.

Table 6.2 α Factors for the Wall Components in X-plane

Story	2	3	4	5	6	7	8	9	10	11
α_i	1.3	1.3	1.3	1.3	1.3	2.6	2.6	2.6	2.6	2.6
Story	12	13	14	15	16	17	18	19	20	
α_i	2.6	2.6	2.6	2.6	2.6	2.6	2.6	2.6	2.6	

Table 6.3 α Factors for the Wall Components in Z-plane

Story	2	3	4	5	6	7	8	9	10	11
α_i	3.2	3.2	3.2	3.2	3.2	6.4	6.4	6.4	6.4	6.4
Story	12	13	14	15	16	17	18	19	20	
α_i	6.4	6.4	6.4	6.4	6.4	6.4	6.4	6.4	6.4	

From the horizontal stiffness K_w, it is converted by using Equation (6.6) to be used as a diagonal element shown in Figure 6.12.

$$L = \sqrt{L_1^2 + L_2^2} \ , \ \cos\theta = \frac{L_1}{L} \tag{6.5}$$

$$\hat{K}_{\mathrm{w}} = \frac{K_{\mathrm{w}}}{\cos^2\theta} \tag{6.6}$$

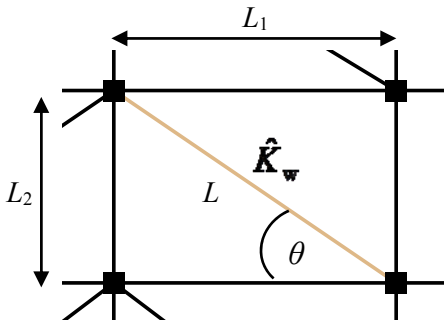

Figure 6.12 Wall element

Mega-brace components

In this building, the material used as a mega-brace is a steel box tube. Therefore, the section moduli, stiffness, and strength can be obtained similarly to the beams. G2 element is used to represent a mega-brace and placed as shown in Figure 6.13. Note that the braces are constraint at the mid-point as can also be seen in the figure.

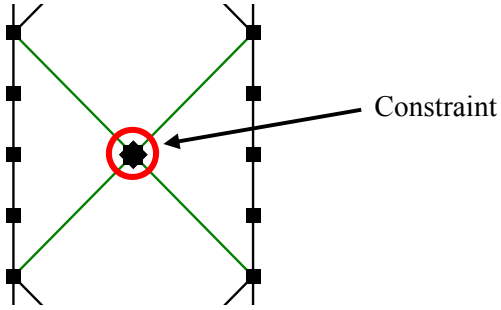

Figure 6.13 Mega-brace element

Connection between the structure and the mega-brace

Nonlinear beam-column element (G4) is used to connect between the structure and the mega-brace (Figure 6.14). The property of the connection is obtained from calibration. First the Y-direction (vertical) between the two nodes are constraint to move together. Then only the stiffness in the X-direction (horizontal) is calibrated such that it produces best results

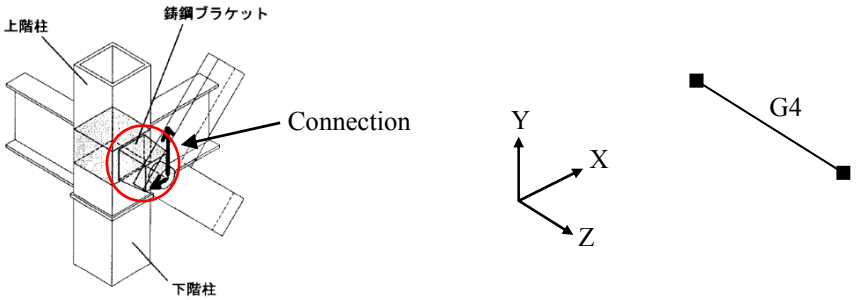

Figure 6.14 Connection between the frame and mega-brace

Weight assignment

According to the measured data of the weights, the total weight for each column is shown Table 6.4.

Table 6.4 Total weights at the base story's columns (unit: kN)

	X5	**X8**
Z1	9565	11559
Z2	10945	12504
Z3	11565	10903
Z4	11388	10743
Z5	12641	12438
Z6	11617	12347
Z7	10915	11799
Z8	9401	11134

The total load for each floor is shown in Table 6.5. The nodal load for each floor is then calculated as follows. First, from the values in Table 6.5(column 2), the ratio of each floor weight to the total weight, α_i, is calculated as shown in Table 6.5(column 3). Then the load assigned to each column node is obtained from Equation (6.7).

Table 6.5 Weight of each floor (unit: kN)

Floor	**Weight**	**Weight / Total Weight, α_i**
PHR	3618.9	3618.9/163750.4 = 0.022100099
RF	10462.1	0.063891
20F	7012.9	0.042827
19F	6982.1	0.042639
18F	7105.1	0.04339
17F	6973.2	0.042584
16F	7139.2	0.043598
15F	7113	0.043438
14F	7232.9	0.04417
13F	7122.4	0.043495
12F	7280.1	0.044459
11F	7194.6	0.043936

10F	7336.4	0.044802
9F	7212	0.044043
8F	7323.4	0.044723
7F	7593.1	0.04637
6F	7804.4	0.04766
5F	7652.3	0.046731
4F	7326.5	0.044742
3F	7637.6	0.046642
2F	18628.2	0.11376
	Σ : 163750.4	**Σ :** 1.00

$$\hat{W}_{ijk} = \alpha_i W_{jk} \tag{6.7}$$

where α_i is the ratio of i^{th} floor weight to total weight (from Table 6.5, column 3), W_{jk} is the weight at Z_j and X_k (from Table 6.6). Figure 6.15 shows the loads used in this model.

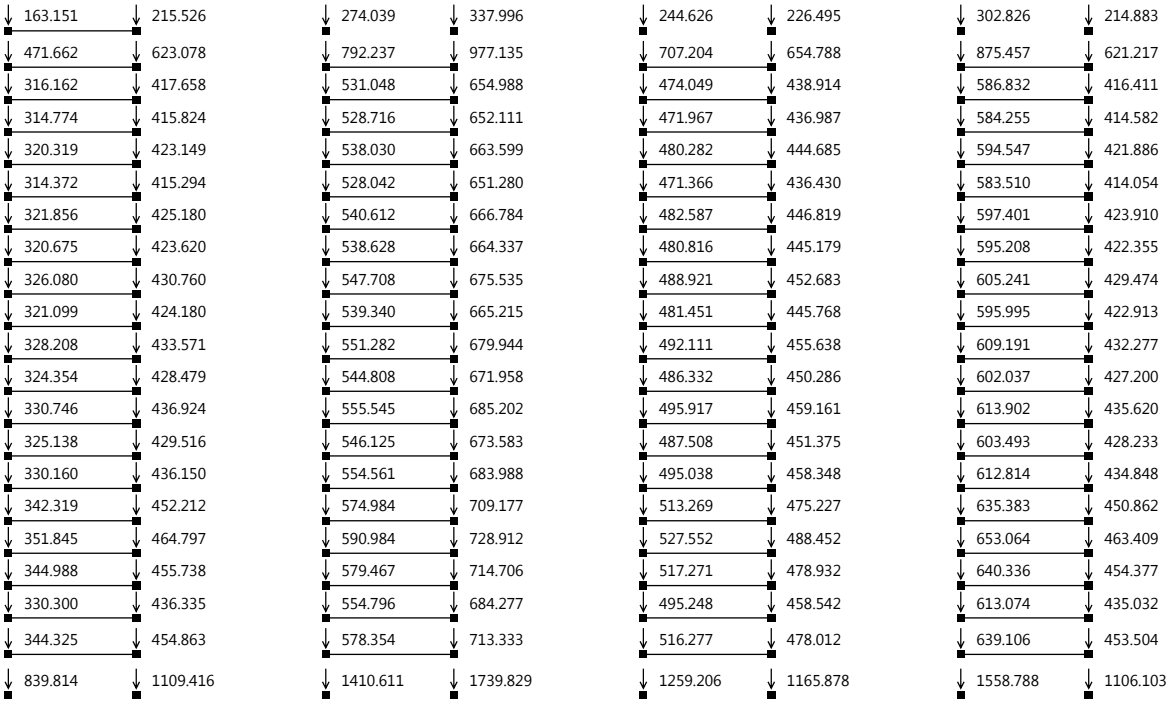

(a) Frame Z1 (b) Frame Z2 (c) Frame Z3 (d) Frame Z4

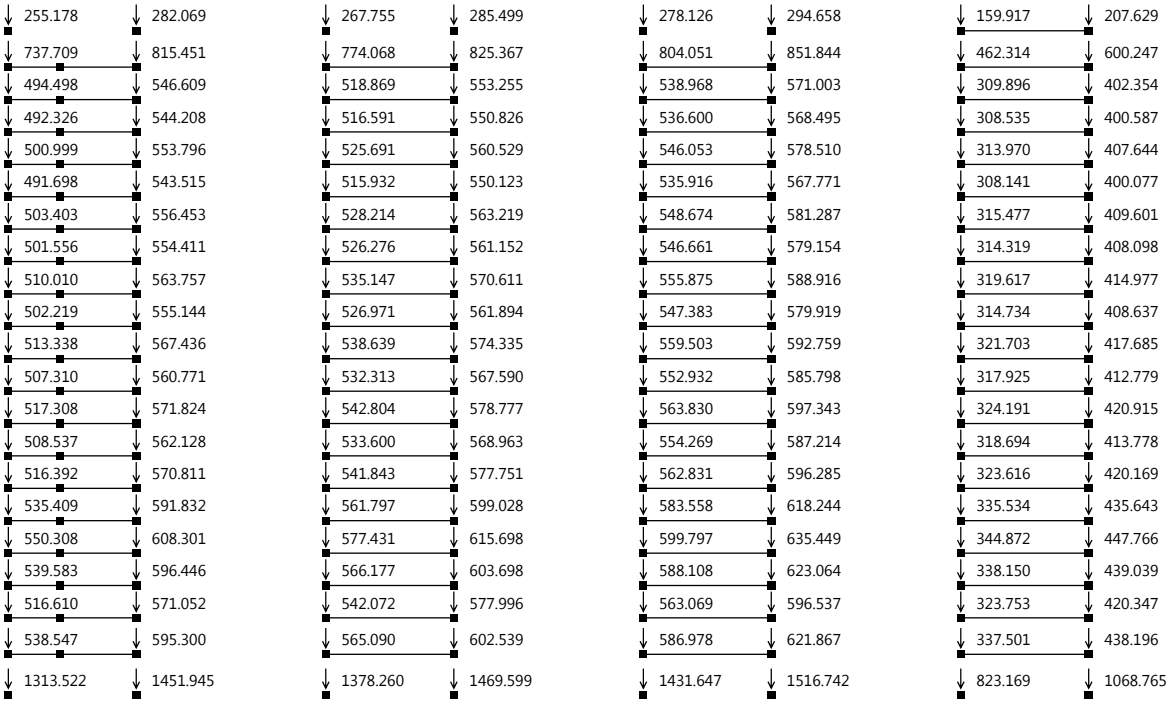

(e) Frame Z5 (f) Frame Z6 (g) Frame Z7 (h) Frame Z8

Figure 6.15 Assigned loads at each node in each frame

6.3.3 Dynamic properties of the superstructure model

Knowing all the necessary properties for each component in the superstructure, the model for the superstructure is created in PC-ANSR. Then Eigenvalue analysis is conducted on the superstructure model. The superstructure periods are shown in the following Table 6.7 for the first 3 modes in both X- and Z-directions. The second and fourth columns in table are the vibration periods from our model and in the third and fifth columns are the vibration periods obtained from System Identification conducted previously by Matsuda and Kasai as described in their paper.

Table 6.7 Superstructure periods

	X-Direction		Z-Direction	
Mode	***T* (our model)**	***T* (System ID)**	***T* (our model)**	***T* (System ID)**
1	1.968	2.009	2.172	2.147
2	0.677	0.612	0.738	0.682
3	0.382	0.348	0.408	0.385

According the system identification by (Kazuhiro MATSUDA and Kazuhiko KASAI), the damping ratios of the superstructure in long direction (1st mode) and short directions (2nd mode) are 0.046 and 0.021 respectively. In this case, if the damping ratio of 0.046 were to be assigned to the first mode of the superstructure, the second mode damping of 0.021 could never be achieved. This problem is solved by assigning the second mode damping of 0.021 instead. Assuming the stiffness proportional ($\underset{\sim}{C} = \beta \underset{\sim}{K}$) damping, then β can be obtained from the following equation.

$$\beta = \frac{T_2 \zeta_2}{\pi} \tag{6.8}$$

By doing this, the first mode damping of 0.21 in short direction would be achieved. However, there would not be enough damping in the long direction. The required damping ratio in the long direction is 0.046. To increase the damping, several dashpots are inserted along the superstructure height in the long direction as shown in Figure 6.16 below.

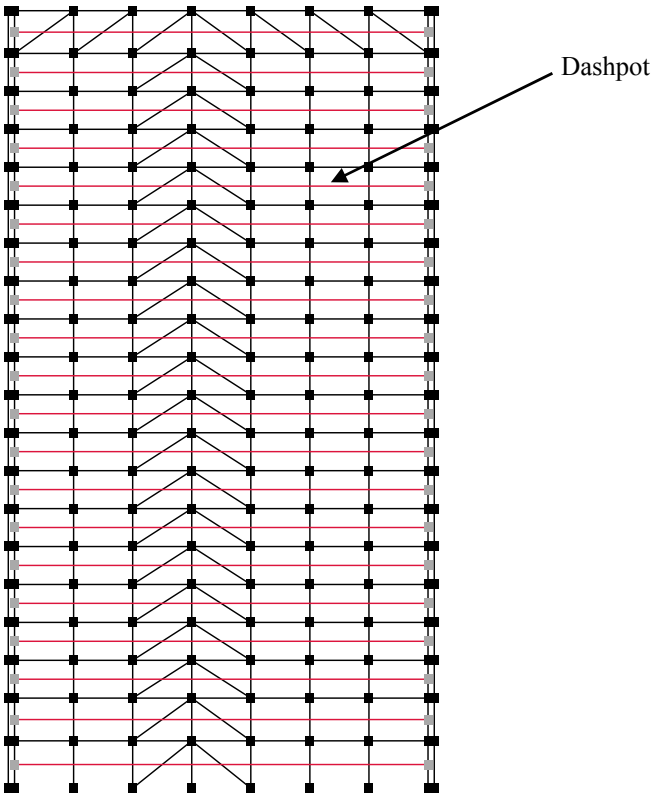

Figure 6.16 Dashpot elements along the superstructure height (red line)

The additional dashpot coefficients for each story are estimated as shown in Equation (6.9).

$$\begin{aligned} C_i &= C_{desired,i} - C_{available,i} \\ &= \beta_{desired} K_i - \beta_{available} K_i \\ &= \frac{\zeta_1 T_1}{\pi} K_i - \frac{\zeta_2 T_2}{\pi} K_i \end{aligned} \tag{6.9}$$

where K_i is the summation of the stiffnesses in the long direction of the i^{th} story.

6.3.4 Superstructure response verification

In order to compare the responses from the model with the actual responses from the ground motion, the acceleration histories recorded during the March 11 Earthquake are used. In J2 buildings, accelerometers have been installed at the isolation floor (MFL), 2nd, 7th, 14th,

and 20th floors. In this section, only the modelling of the superstructure part of the J2 isolated building is complete. Hence, to compare with the responses from the records, the acceleration histories recorded at the 2nd floor (just above the isolation level) is used as an input to this superstructure model.

The input directions of the accelerations are in horizontal directions, X- and Z-directions. The full length of the acceleration histories is 10 minutes. However, in this analysis, only the first 5 minutes are used, since it already covers the strong acceleration portion. The accelerations used are shown in Figure 6.17.

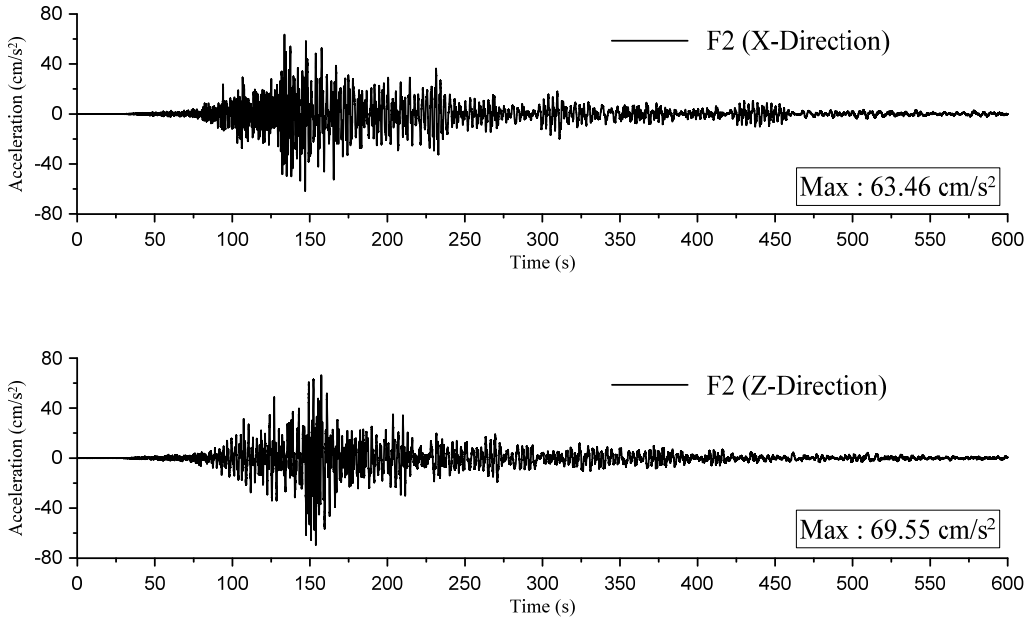

Figure 6.17 Acceleration records at the 2nd floor (just above the isolation level)

The response for each floor is obtained by taking the average of the responses at the corner of the building as shown in Figure 6.18.

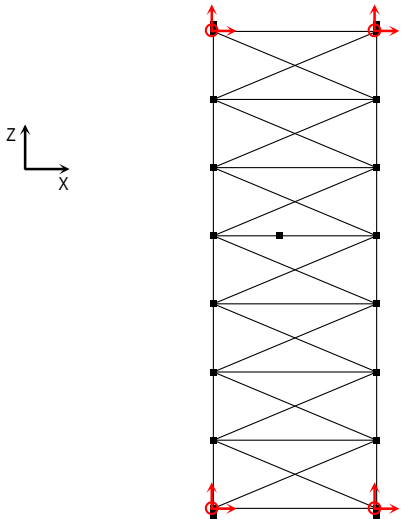

Figure 6.18 Responses taken as average from the corner nodes

Figure 6.19 and 6.20 shows the displacement response histories from the analysis of the 7th, 14th, and 20th floors in X- and Z-directions, respectively. The displacements from the analysis are compared with the recorded displacement responses, which are obtained by conducting double integration of the acceleration records with hi-pass filtering in frequency domain. The cut-off frequency is 0.05Hz. Figure 6.21 and 6.22 shows the absolute acceleration response histories from the analysis of the 7th, 14th, and 20th floors in X- and Z-directions, respectively. They are compared directly with the recorded data of the floor accelerations.

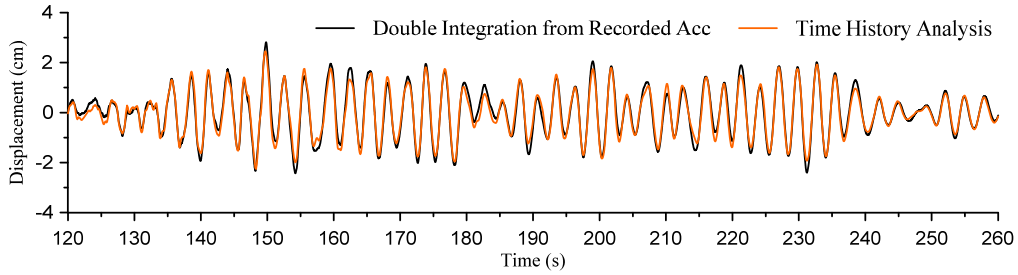

(a) 7th floor

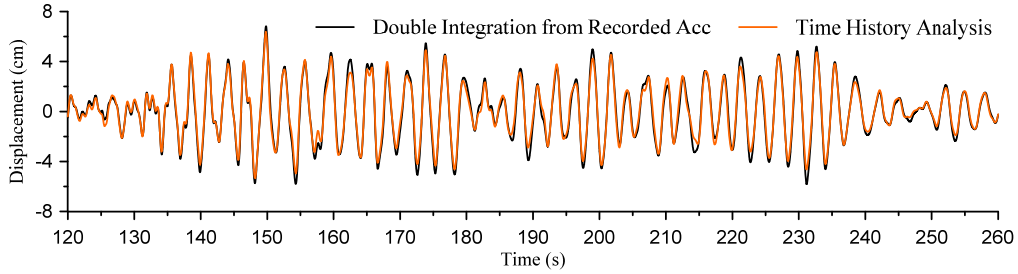

(b) 14th floor

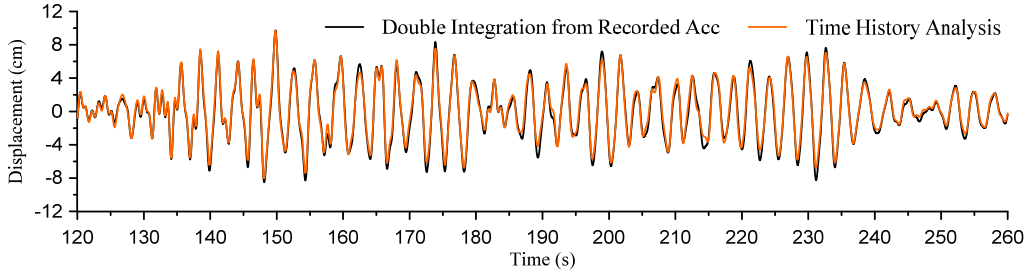

(c) 20th floor

Figure 6.19 Floor displacement relative to the 2nd floor (X-direction)

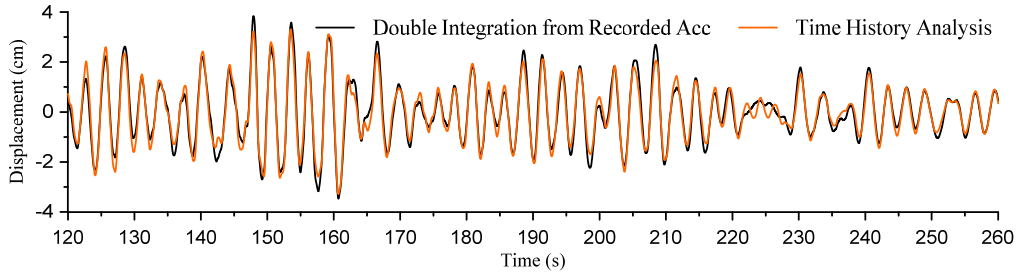

(a) 7th floor

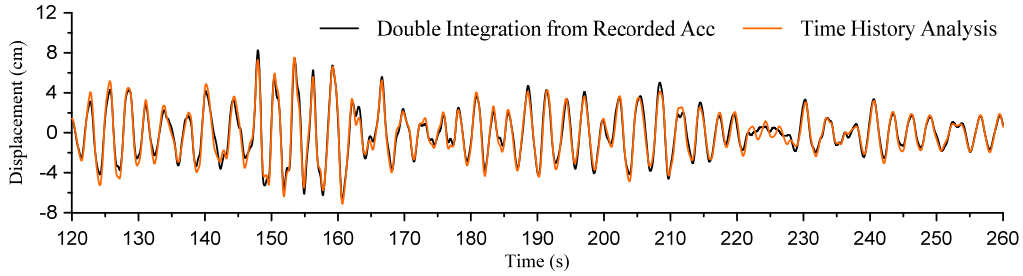

(b) 14th floor

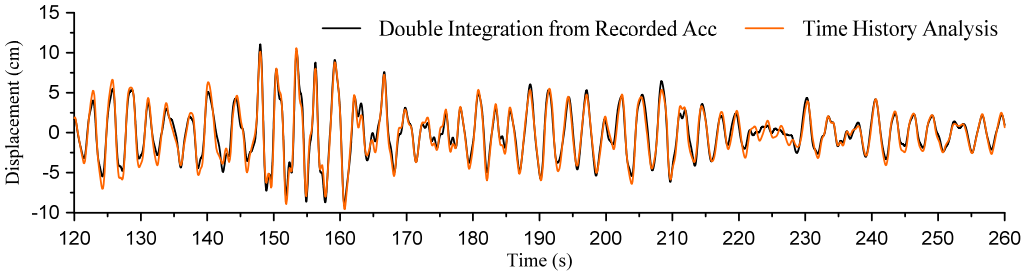

(c) 20th floor

Figure 6.20 Floor displacement relative to the 2nd floor (Z-direction)

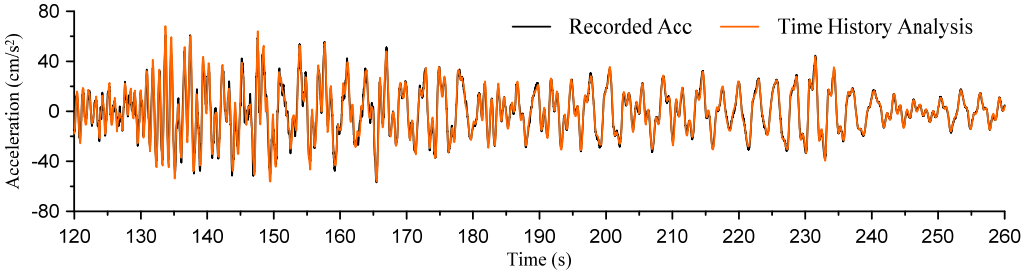

(a) 7th floor

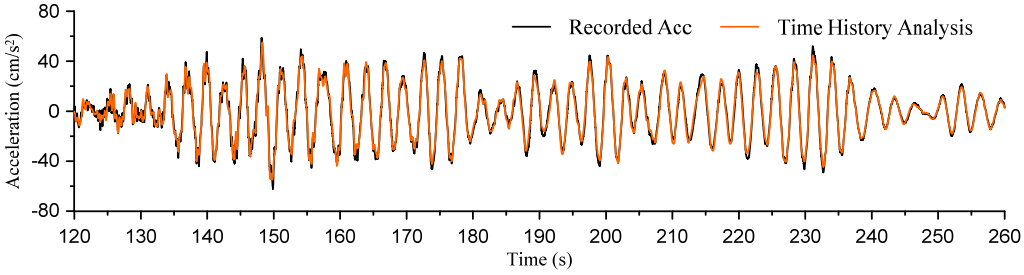

(b) 14th floor

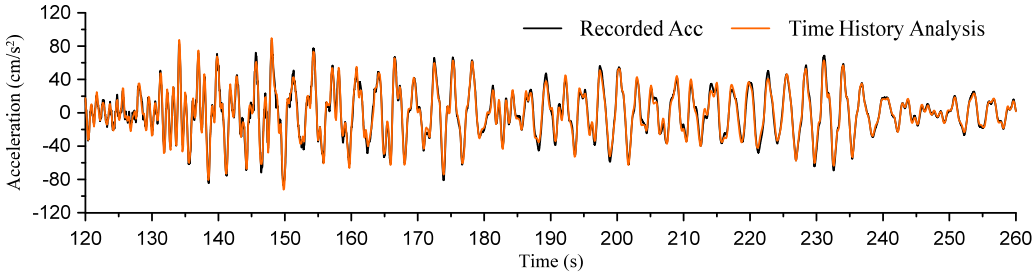

(c) 20th floor

Figure 6.21 Absolute floor acceleration (X-direction)

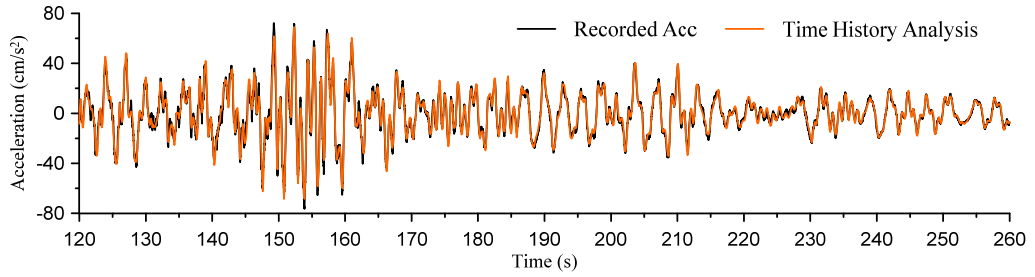

(a) 7th floor

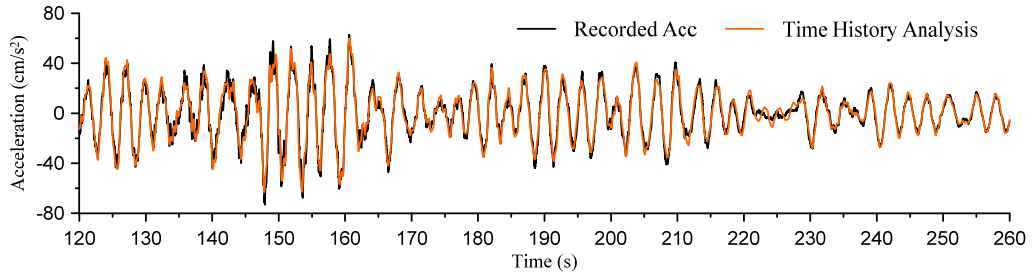

(b) 14th floor

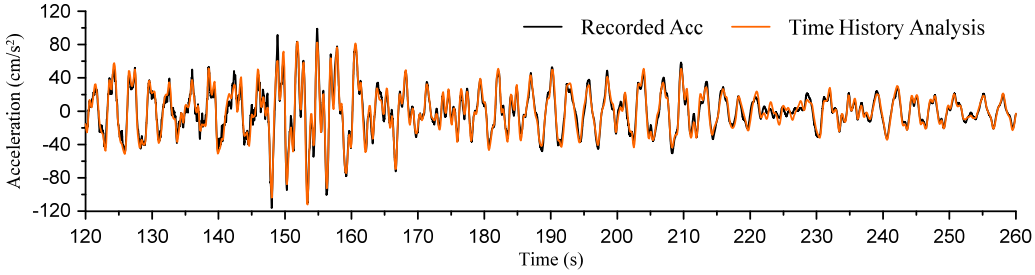

(c) 20th floor

Figure 6.22 Absolute floor acceleration (Z-direction)

The analysis results show very good agreements with those obtained from the double integrations for both displacement and acceleration in all floors as shown in the figures. This indicates that the analytical model for the superstructure is reasonably accurate and can be used for further investigation.

To examine the accelerations at other periods, floor response spectrum (FRS) analysis is conducted and compared. The accelerations in Figures 6.21 and 6.22 are used and the damping ratio is 2%. Figures 6.23 and 6.24 show the results of the FRS in X- and Z-directions, respectively. The shows show very good agreement between those FRS obtained from the recorded data and the analysis. This confirms the accuracy of the model.

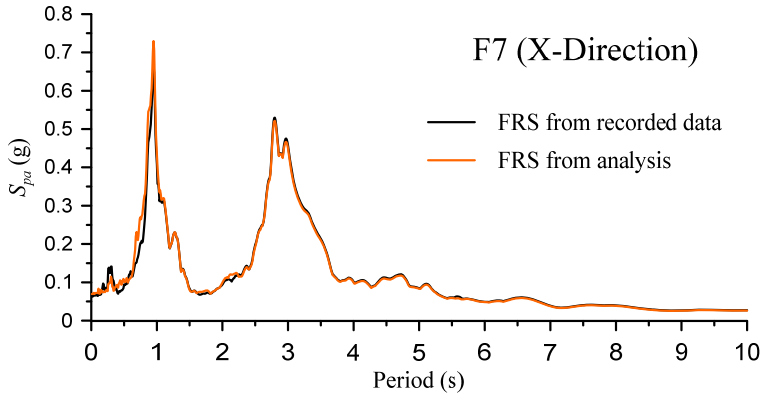

(a) 7th floor

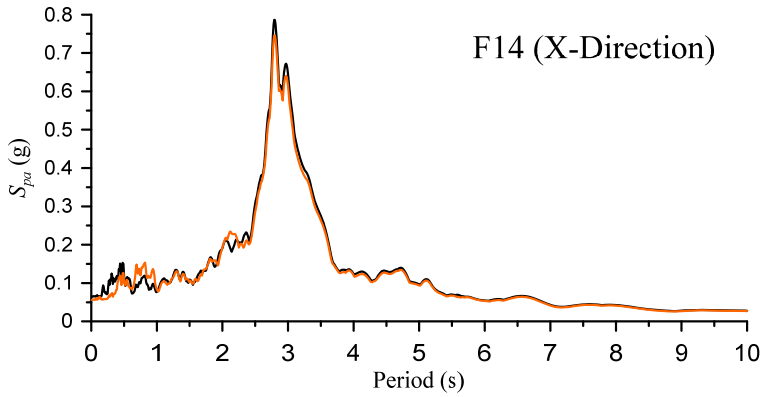

(b) 14th floor

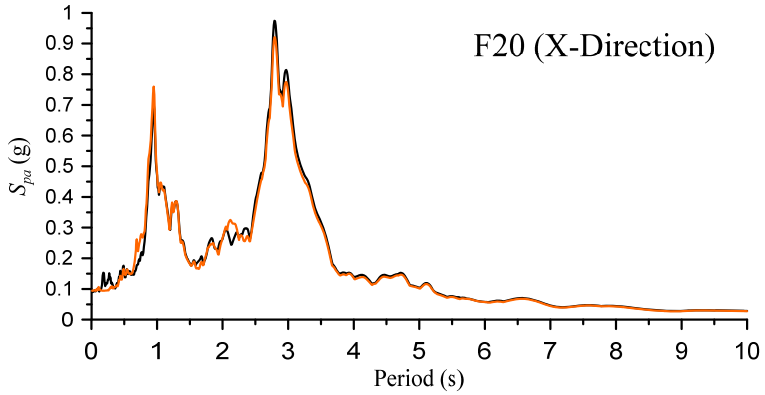

(c) 20th floor

Figure 6.23 Comparison of floor response spectra (X-direction)

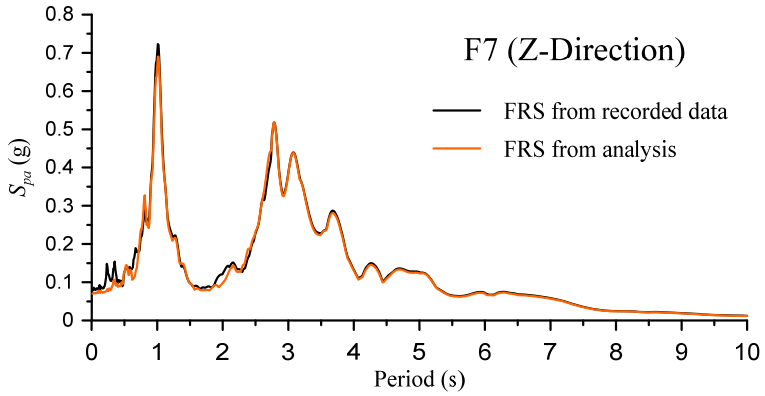

(a) 7th floor

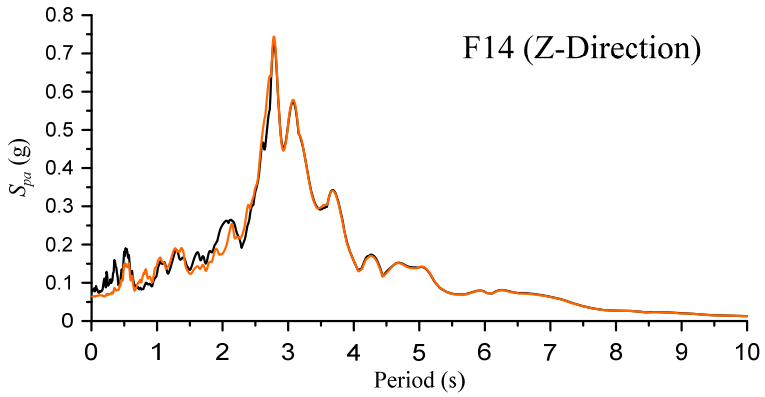

(b) 14th floor

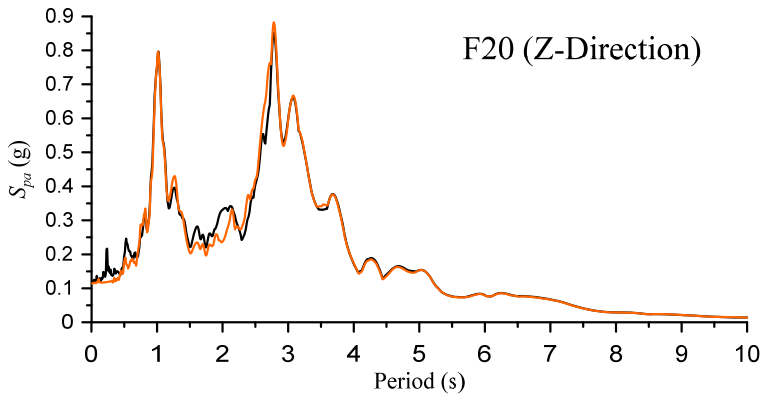

(c) 20th floor

Figure 6.24 Comparison of floor response spectra (Z-direction)

Figures 6.25 and 6.26 show the displacement and acceleration envelope responses in all floors, respectively together with the recorded data at 7th, 14th, and 20th floors. The distribution of the displacement and acceleration along the superstructure height shows similar trends. Accelerations are also concentrated at the uppers stories.

Knowing the displacement response histories for all floors, then we can obtain the story drift ratio histories for each story, then obtain the maximum story drift ratio for each story. The results are plotted in Figure 6.27. It can be seen than most of the stories have a story drift ratio of around 0.15% in both directions, and have lower story drift ratio at the upper stories.

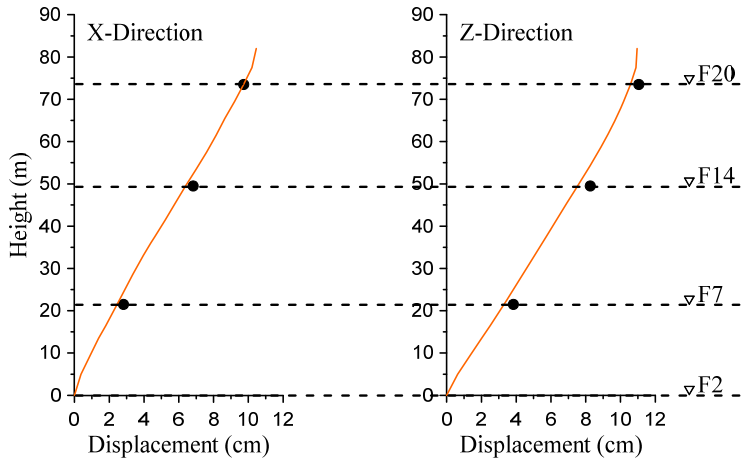

Figure 6.25 Comparison of displacement envelope responses

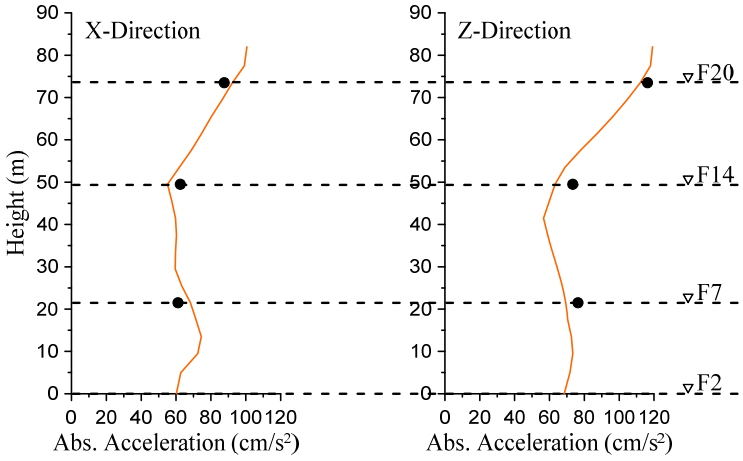

Figure 6.26 Comparison of floor acceleration envelope responses

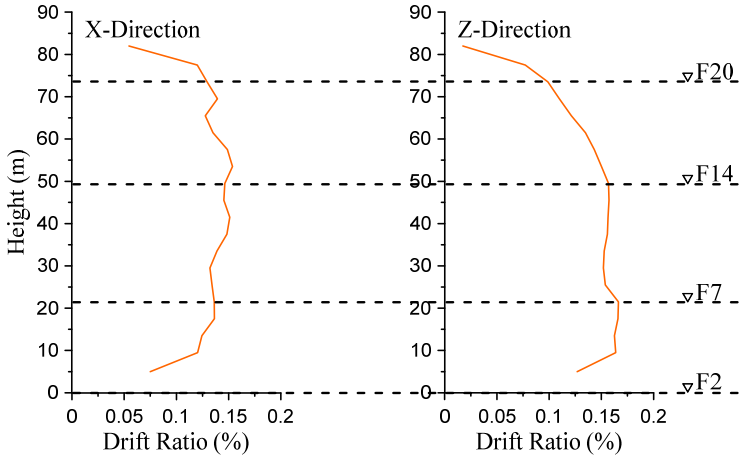

Figure 6.27 Story drift ratio envelope responses

6.4 Response Verification of J2 Base-Isolated Building (Whole Building)

6.4.1 Modelling of dampers

Rubber bearing

Rubber bearing are placed at all columns around the perimeter of the building as shown in Figure 6.28. Figure 6.29(a) is the rubber bearing placed at the 4 corners of the building as shown as the purple circles in Figure 6.28. And Figure 6.29(b) is the rubber bearing placed along the long direction of the buildings at both sides as shown as the red circles in Figure 6.28.

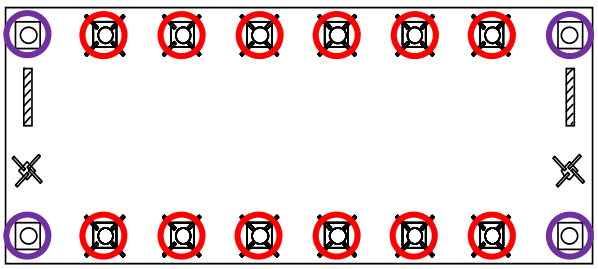

Figure 6.28 Locations of the rubber bearings

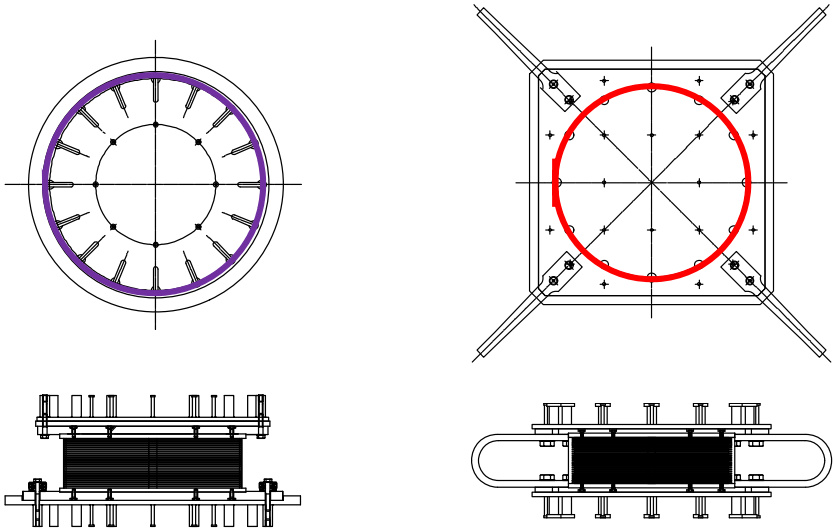

(a) (b)

Figure 6.29 Rubber bearings

Table 6.8 shows the rubber bearing properties used in the building. Linear behavior is assumed in the rubber bearing, hence, G2 Element in PC-ANSR is used to represent the rubber bearings using the stiffness shown in the table. The elements are placed in X- and Z-horizontal directions at each column.

Table 6.8 Rubber bearing properties

	Rubber Bearing	
Property	**(a)**	**(b)**
Diameter (mm)	1200	1100
Horizontal Stiffness (kN/cm)	21.3	19.4
Vertical Stiffness (kN/cm)	50600	45900

U-shaped steel damper

The type of steel dampers used in the building is U-shaped steel damper. They are placed along the long direction of the J2 building and one on each side of the short direction as shown in Figure 6.30. The shapes of the dampers are slightly different as shown in Figure 6.31, but the steel materials used are the same, hence having the same properties. Table 6.9 shows the damper property used in the building.

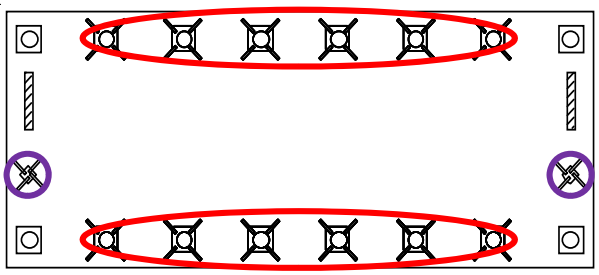

Figure 6.30 Locations of the U-shaped steel dampers

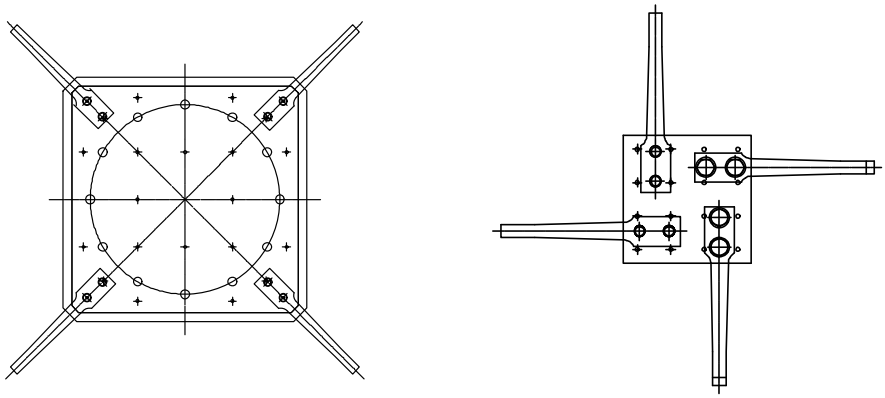

(a) (b)

Figure 6.31 Steel dampers

Table 6.9 U-shape steel damper properties

Property	U-Shaped Steel Damper
Model	NSUD55
Steel Material	SN490B
Horizontal Displacement Limit (cm)	85.0
Horizontal 1st Stiffness (kN/cm)	96.0
Horizontal 2nd Stiffness (kN/cm)	1.60
Yield Shear Force (kN)	304

Having known all these properties as well as the locations of the dampers, nonlinear truss elements (G2) in PC-ANSR are used to represent these steel dampers, and they are placed according the location shown in Figure 6.30. However, the directions of the elements are different from those used in the rubber bearing. As also shown in Figure 6.30, each piece of the steel dampers is in diagonal direction, 45 degree from X- and Z-directions. Hence, in the model, these elements are also placed in 45 degree following exactly the plan.

However, the displacement is applied in the direction shown in Figure 6.32, ignoring any torsion or twisting, the resisting force developed due to this displacement will come from

the longitudinal steel part (0-degree, red color) and the transverse steel part (90-degree, purple color). The values shown in the Table 6.9 represent the behavior of the steel damper as a whole system, not individual piece where each stiffness and strength are different. Therefore, using the properties in Table 6.9 would not be able to produce accurate results.

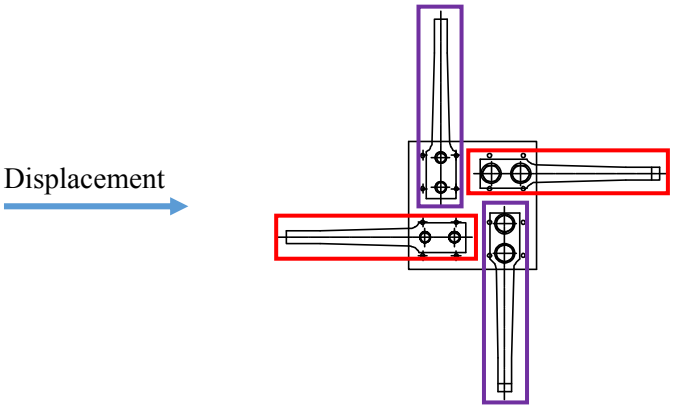

Figure 6.32 Contribution from 0-degree and 90-degree stiffnesses

There has been some test regarding the development of U-shaped steel damper for seismic isolation system described in **Nippon Steel Technical Report (2005)**. They perform several tests on different directions of loading on the steel dampers and plot the hysteresis behaviors for each direction of the test. The U-shaped steel damper model used in their test is UD40 which is smaller than the ones used in the J2 building. However, the behavior and different of the stiffnesses as well as the yield strengths for each direction can be observed which can be applied to be used in this model.

Figure 6.33 shows the results of the force-displacement hystereses under different 0-degree, 45-degree, and 90-degree loading directions, and Figure 6.34 shows the effects of loading angle on yield shear force and elastic limit taken from their report. From Figure 6.34, it is possible to determine the ratios between the 1st stiffness as well as the yield shear force of the 0-degree and 90-dgree.

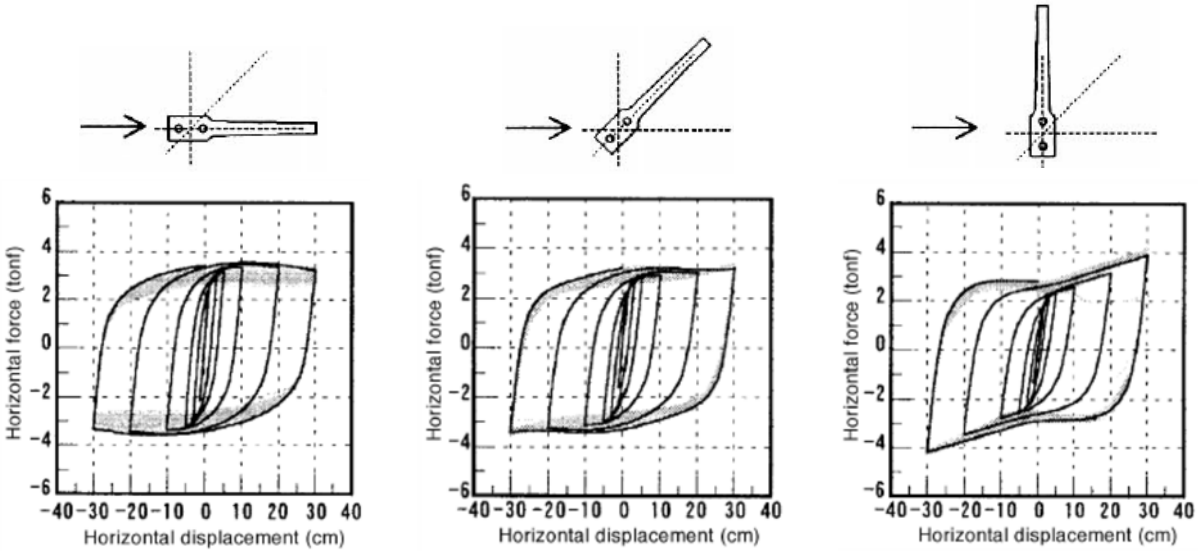

Figure 6.33 Force-displacement hystereses under different loading angles (Nippon Steel, 2005)

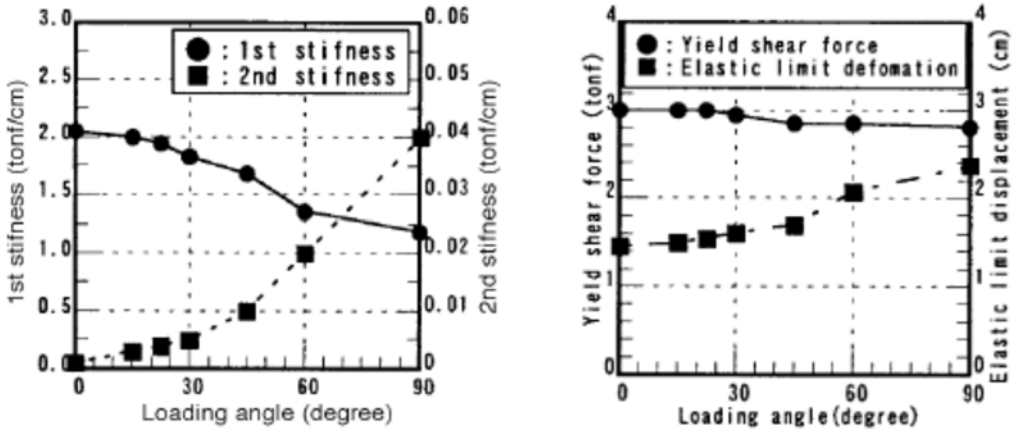

Figure 6.34 Effects of loading angle on yield shear force and elastic limit (Nippon Steel, 2005)

After knowing the ratios of these properties, they are applied to be used for our model. And the model for the U-shaped steel damper is represented by two bilinear springs connected

in parallel, one for the 0-degree part and the other for the 90-degree part as shown in Figure 6.35.

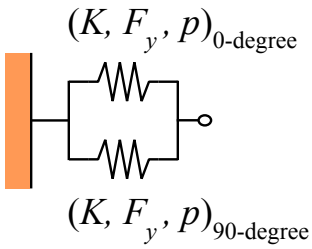

Figure 6.35 Modelling of the U-shaped steel damper

The results of one cycle loop of the 0-degree and 90-degree steel damper used in the model are shown in Figure 6.36(a) and 6.36(b), respectively, and the combined hysteresis is shown in Figure 6.36(c).

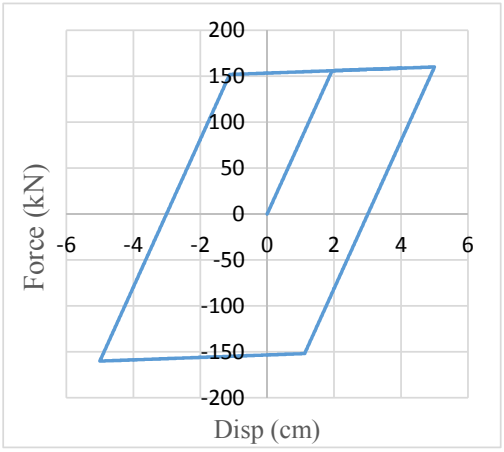

(a) 0-degree

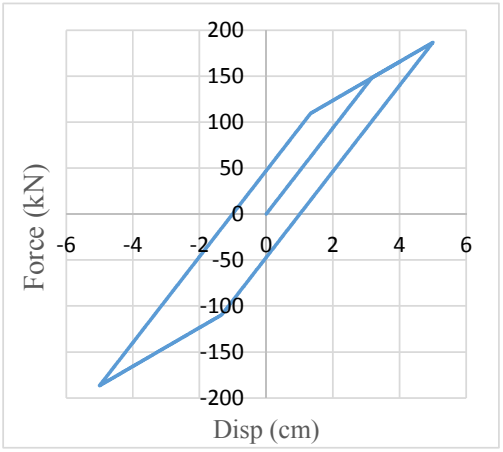

(b) 90-degree

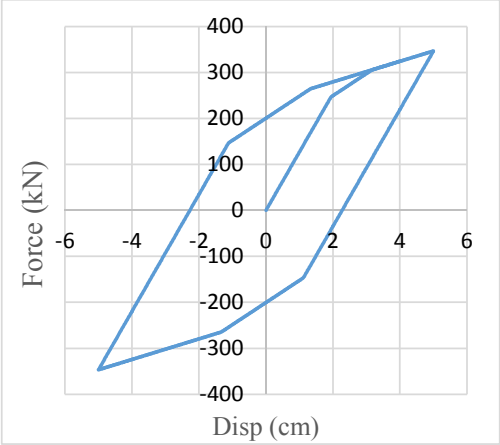

(c) Combined

Figure 6.36 One cycle hysteresis of the U-shaped steel damper used in the model

Oil damper

There are two oil dampers placed in short direct direction as shown in Figure 6.37. Table 6.10 shows the oil damper properties.

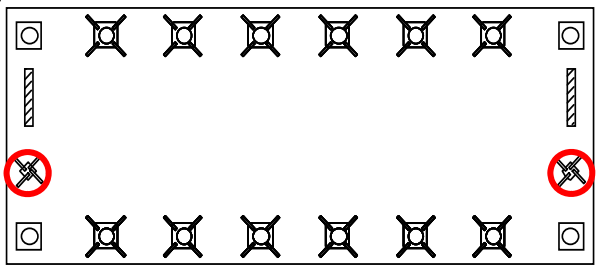

Figure 6.37 Locations of the oil dampers

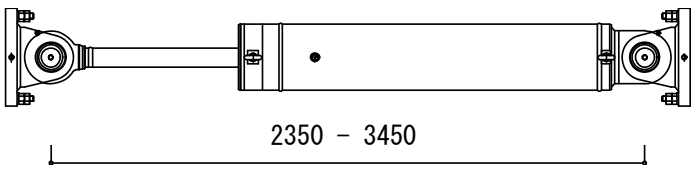

Figure 6.38 Oil dampers

Table 6.10 Oil damper properties

Property	Oil Damper
Model	BDS1201100-B-1
Horizontal Displacement Limit (mm)	550
Horizontal Velocity Limit (kine)	150
Maximum Damping Force (kN)	1000
Relief Damping Force (kN)	800
1st Viscous Coefficient (kN/kine)	25
2nd Viscous Coefficient (kN/kine)	1.695

Figure 6.39 shows the force-velocity relationship plot during the March 11 Earthquake. It can be seen that the design value of C_1 = 25 kN/kine is smaller than the observed slope. The observed C_1 value is around 35 kN/kine. In order to be able to simulate the behavior of oil damper more accurately, this observed C_1 value of 35 kN/kine is used for modeling of the oil damper.

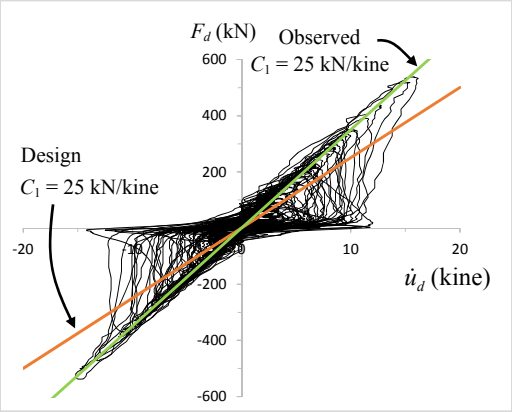

Figure 6.39 Force-velocity relationship during March 11 East Japan Earthquake

Figure 6.40 shows the force displacement of the oil damper during the March 11 East Japan Earthquake. It can be seen that the behavior is strange. There seems to be some kinds of slipping occurring in the oil damper.

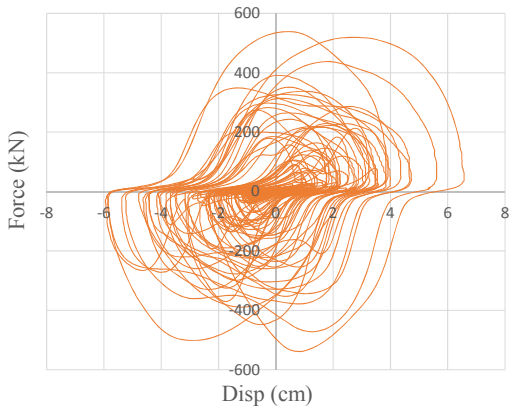

Figure 6.40 Force-displacement relationship during March 11 East Japan Earthquake

Typical way of modeling oil damper is shown in Figure 6.41(a). It is composed of the dashpot part which bilinear force-velocity with 1st and 2nd viscous coefficients, C_1 and C_2 connected with stiffness of the damper and brace. However, this would not be able to accurately reproduce such behavior. In order to account for this behavior, the oil damper is model as shown in Figure 6.41(b), by changing the brace part into several parallel gap elements to account for the slip.

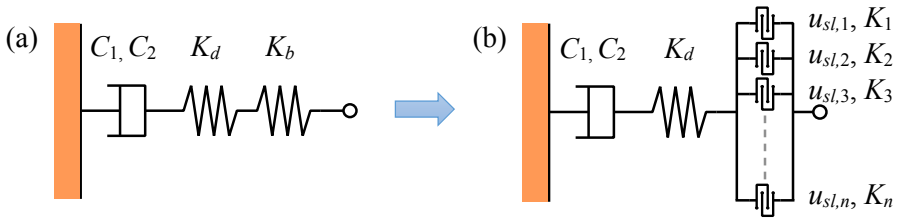

Figure 6.41 Modelling of the oil dampers

Figure 6.42 shows one cycle loop of the oil models in Figure 6.41. In Figure 6.42(a), it can be seen that the bracing part (left) is linear and the stiffness is the series of the damper and

bracing stiffnesses. The result of the oil damper behavior is as shown in the right hand side. However, in Figure 6.42(b), by using several gap elements having different gap lengths and stiffnesses, it is possible to similar nonlinearity as shown. The result of the oil damper is as shown in the right hand side.

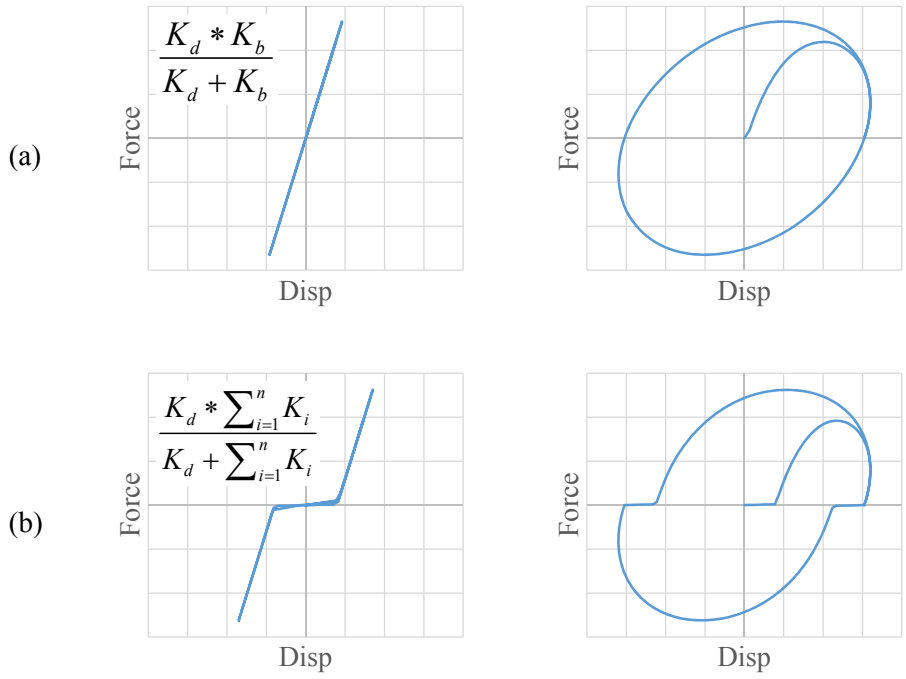

Figure 6.42 One cycle of force-displacement relationship

In order to simulate the behavior of the oil damper observed, calibration of the gap lengths and stiffnesses used in the bracing part of the oil damper element is needed. The result is that there are a total of 18 gap elements, 11 on the left and 7 on the right hand sides. The behavior of this oil damper model is shown in Figure 6.43. It can be seen that the shape is getting closer to the observed shape in Figure

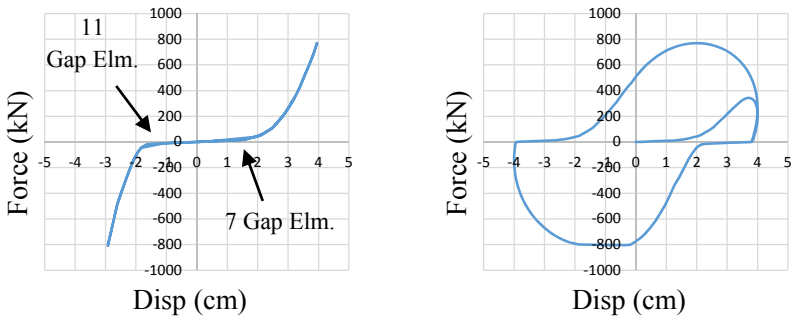

Figure 6.43 One cycle of force-displacement relationship of the oil damper used

As mentioned previously, since we already have the force-displacement relationship of the actual behavior of the oil damper, it is possible to verify whether the oil damper model is accurate or not by inputting the displacement histories to the oil damper element to produce the force histories and then comparing the response with the recorded data. Figure 6.44 shows the comparison between the recorded data and the oil element used in this model. The force-displacement histories from this oil element match very well with the recorded data.

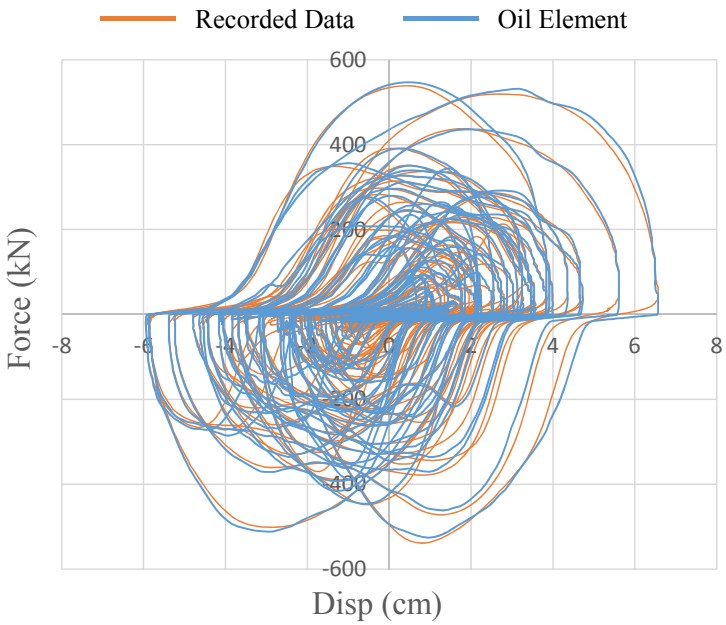

Figure 6.44 Comparison of response of the oil damper model with the recorded data

6.4.2 Dynamic properties of J2 base-isolated structure model

Eigenvalue analysis is conducted on the full model. The periods are shown in the following Table 6.11 for the first 3 modes in both X- and Z-directions. The second and fourth columns in table are the vibration periods from our model and in the third and fifth columns are the vibration periods obtained from System Identification conducted previously by Matsuda and Kasai as described in their paper.

Table 6.11 J2 Base-isolated periods

	X-Direction		**Z-Direction**	
Mode	***T* (our model)**	***T* (System ID)**	***T* (our model)**	***T* (System ID)**
1	2.555	2.916	2.769	2.972
2	0.993	0.979	0.994	0.942
3	0.342	0.447	0.358	0.526

6.4.3 Building response verification

In order to compare the responses from the model with the actual responses from the ground motion, the acceleration histories recorded during the March 11 East Japan Earthquake are used. The acceleration histories recorded at the isolation floor (just below the isolation level) is used as an input to the building model.

The input directions of the accelerations are in horizontal directions, X- and Z-directions. The full length of the acceleration histories is 10 minutes. However, in this analysis, only the first 5 minutes are used, since it already covers the strong acceleration portion. The accelerations used are shown in Figure 6.45.

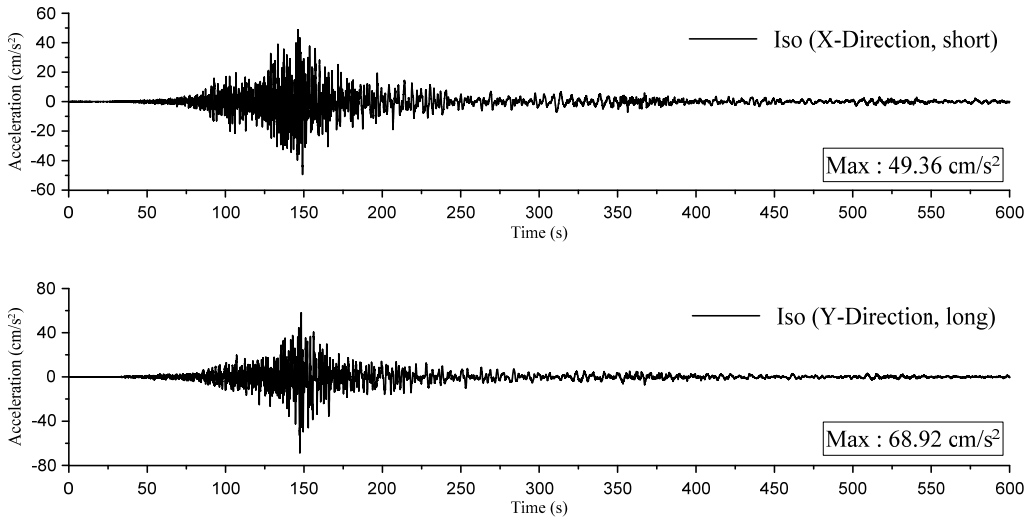

Figure 6.45 Acceleration records at the isolation floor (just below the isolation level)

The response for each floor is obtained by taking the average of the responses at the corner of the building as shown in Figure 6.46.

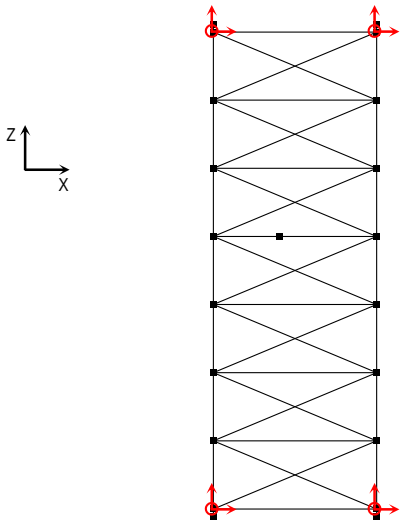

Figure 6.46 Responses taken as average from the corner nodes

Figure 6.47 and 6.48 shows the displacement response histories from the analysis of the 2nd, 7th, 14th, and 20th floors in X- and Z-directions, respectively. The displacements from the analysis are compared with the recorded displacement responses, which are obtained by conducting double integration of the acceleration records with hi-pass filtering in frequency

domain. The cut-off frequency is 0.05Hz. Figure 6.49 and 6.50 shows the absolute acceleration response histories from the analysis of the 2^{nd}, 7^{th}, 14^{th}, and 20^{th} floors in X- and Z-directions, respectively. They are compared directly with the recorded data of the floor accelerations.

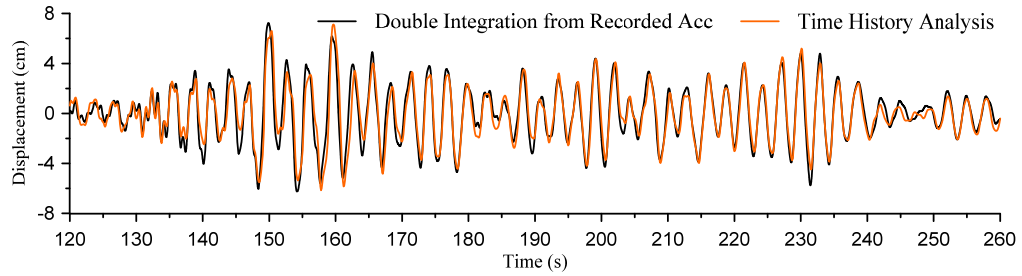

(a) 2nd floor

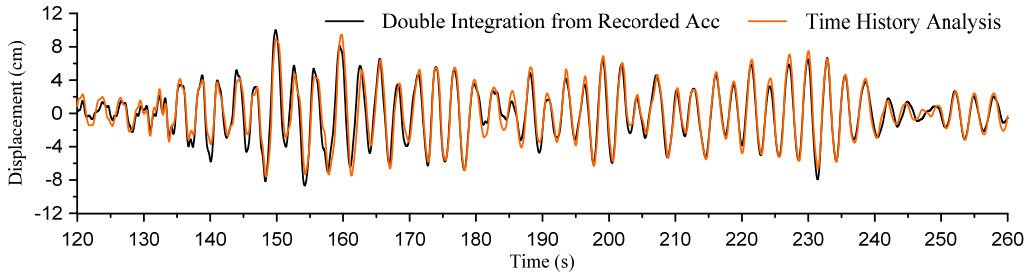

(b) 7th floor

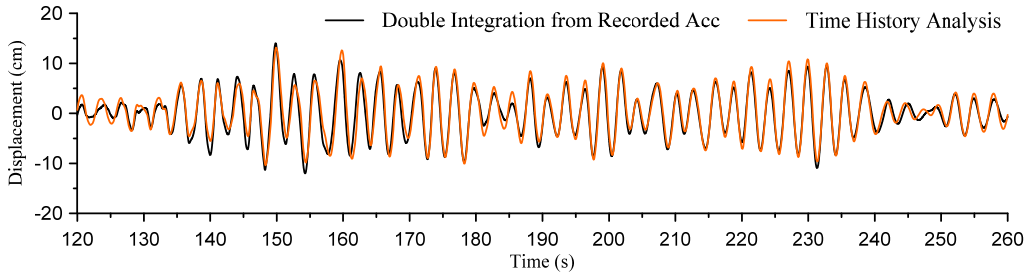

(c) 14th floor

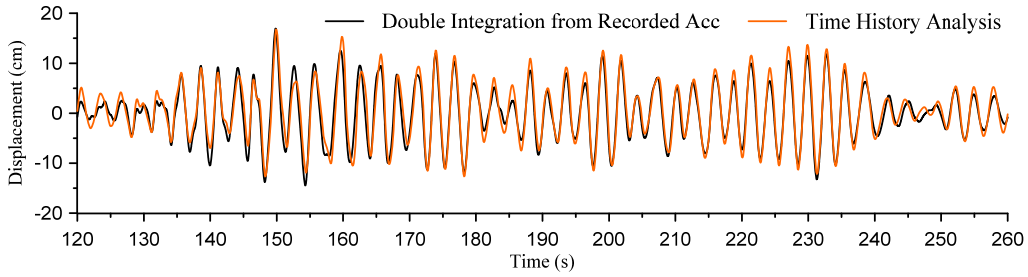

(d) 20th floor

Figure 6.47 Floor displacement relative to the isolation floor (X-direction)

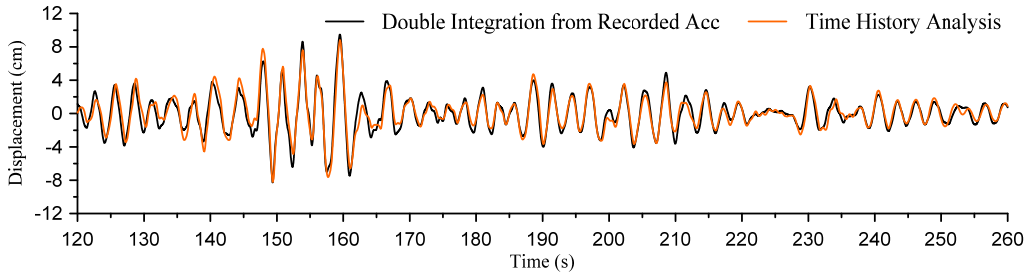

(a) 2nd floor

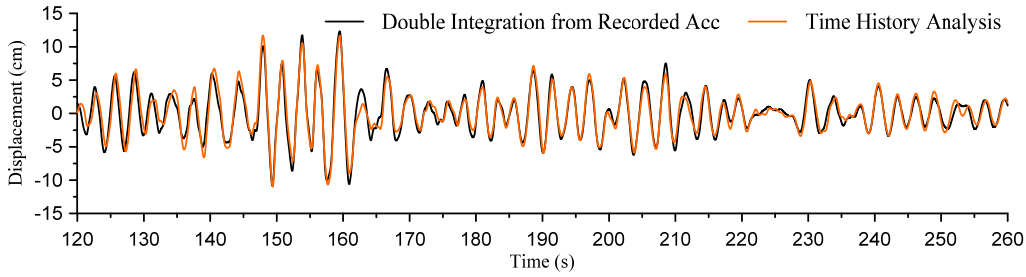

(b) 7th floor

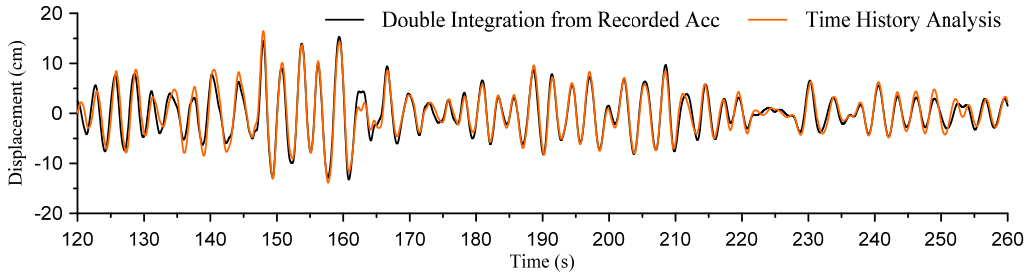

(c) 14th floor

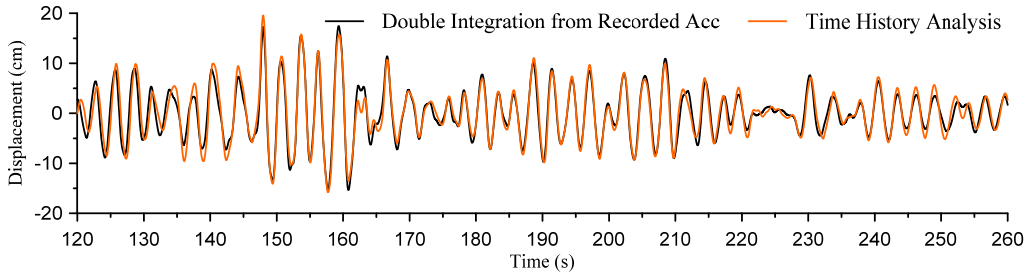

(d) 20th floor

Figure 6.48 Floor displacement relative to the isolation floor (Z-direction)

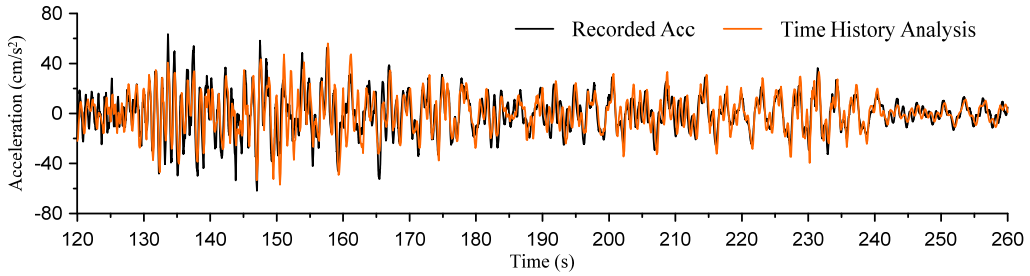

(a) 2nd floor

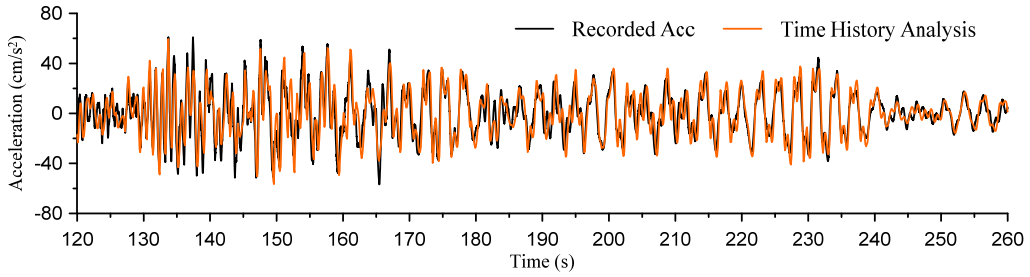

(b) 7th floor

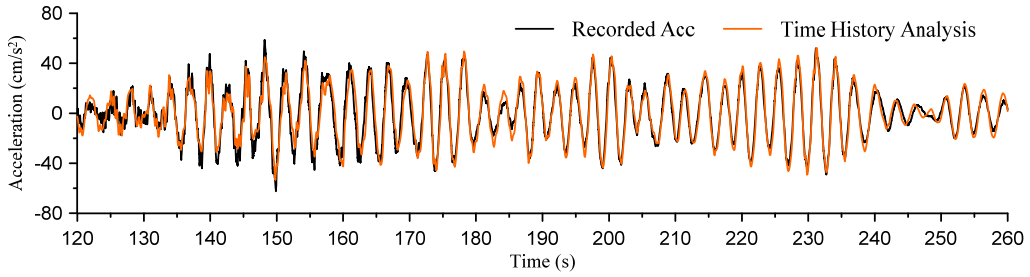

(c) 14th floor

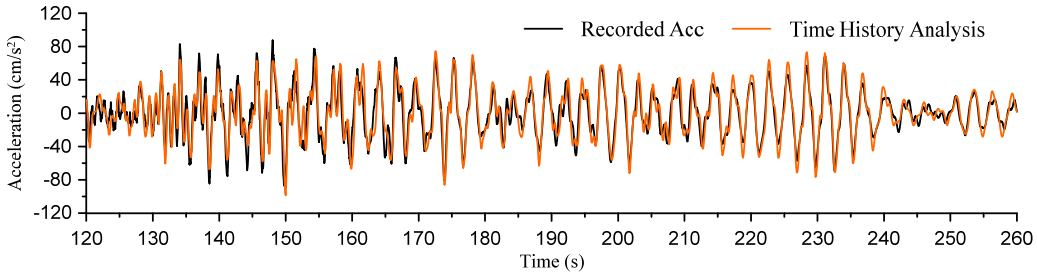

(d) 20th floor

Figure 6.49 Absolute floor acceleration (X-direction)

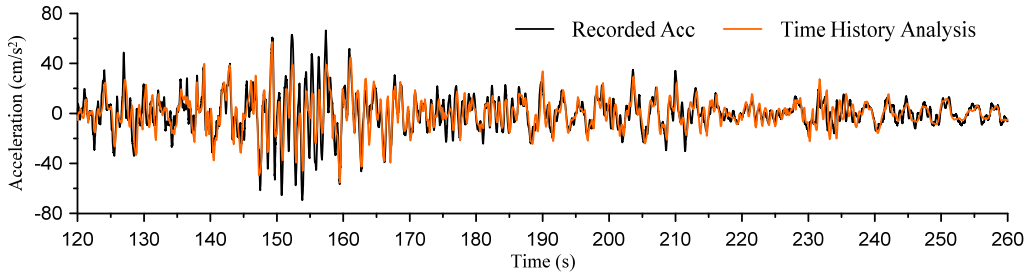

(a) 2nd floor

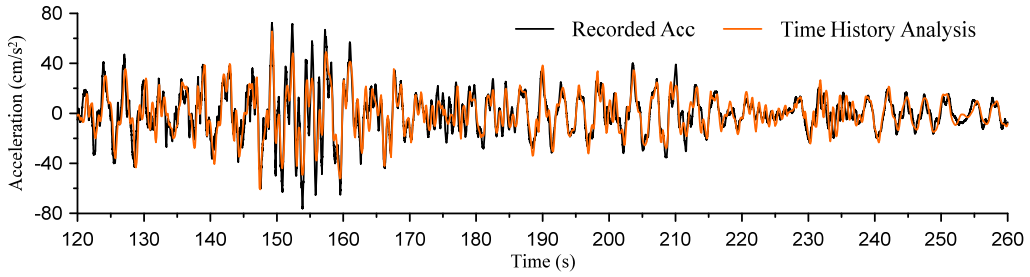

(b) 7th floor

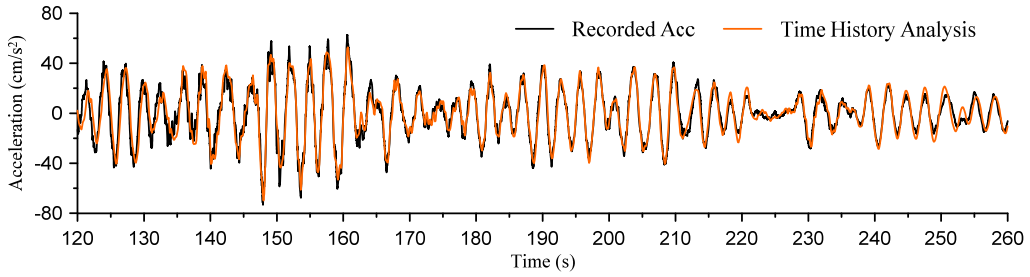

(c) 14th floor

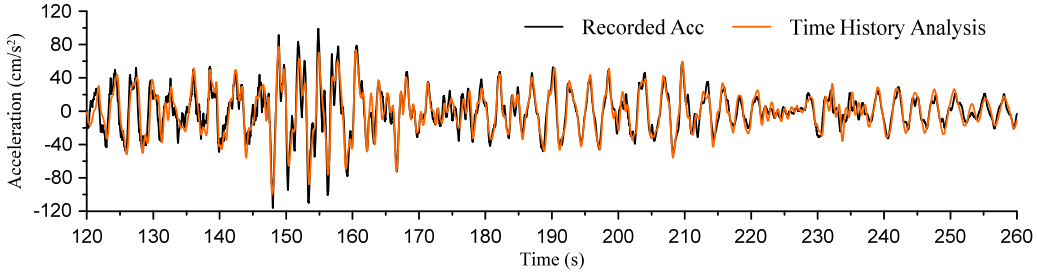

(d) 20th floor

Figure 6.50 Absolute floor acceleration (Z-direction)

The analysis results show good agreements with those obtained from the double integrations for both displacement and acceleration in all floors as shown in the figures even though there is highly nonlinearity happening in the isolation system. This indicates that the analytical model for this J2 base-isolated building is reasonably accurate and can be used for investigation.

To examine the accelerations at other periods, floor response spectrum (FRS) analysis is conducted and compared. The accelerations in Figures 6.49 and 6.50 are used and the damping ratio is 2%. Figures 6.51 and 6.52 show the results of the FRS at the 2nd, 7th, 14th, and 20th floors in X- and Z-directions, respectively. The shows show good agreement between those FRS obtained from the recorded data and the analysis. However in Z-direction, the accelerations at around 1 second which is corresponding to the second mode of the building obtained from the model appear to be less than those from the recorded data. Nevertheless, the overall responses seem to match very well.

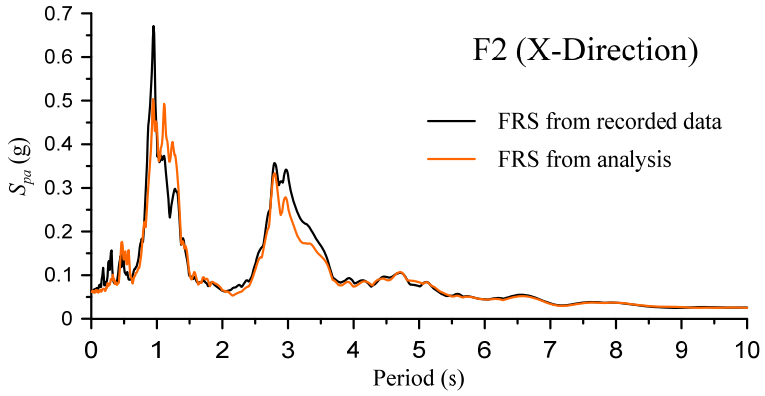

(a) 2nd floor

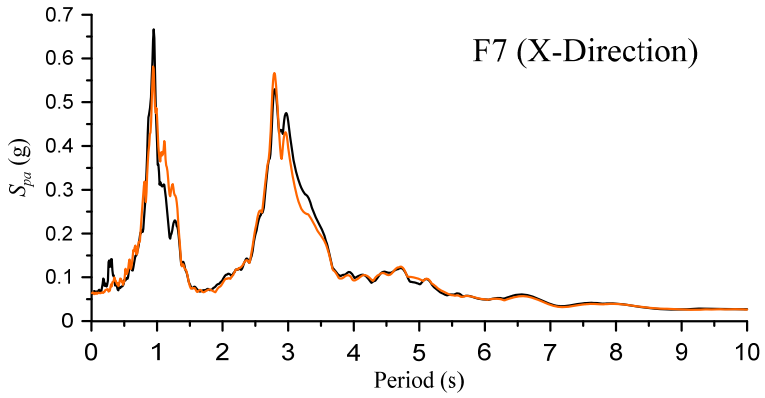

(b) 7th floor

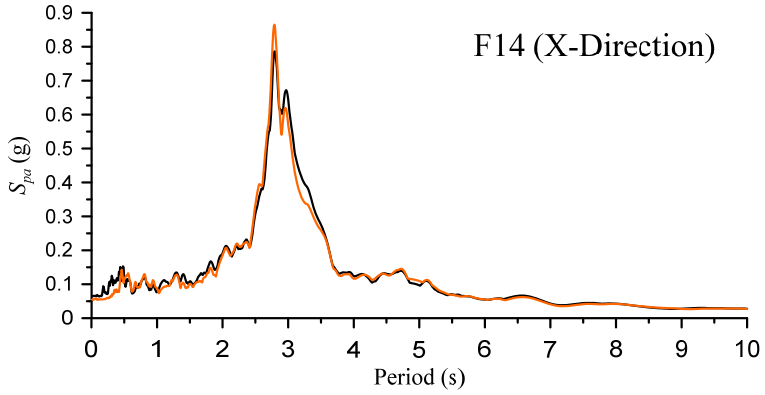

(c) 14th floor

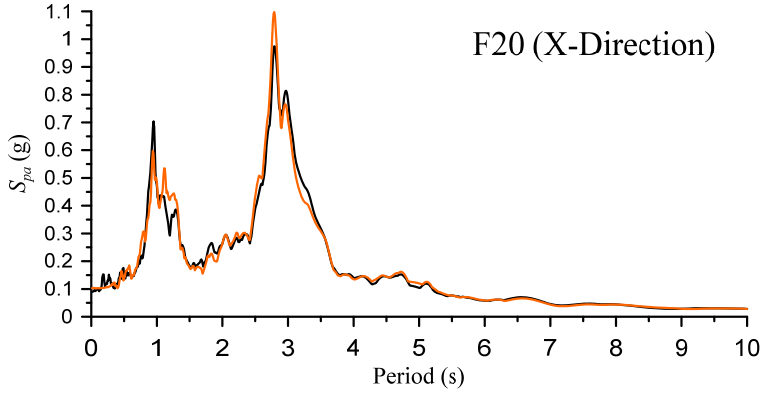

(d) 20th floor

Figure 6.51 Comparison of floor response spectra (X-direction)

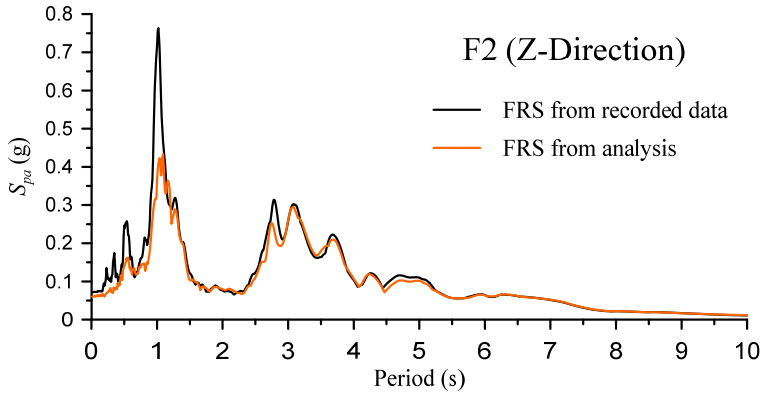

(a) 2nd floor

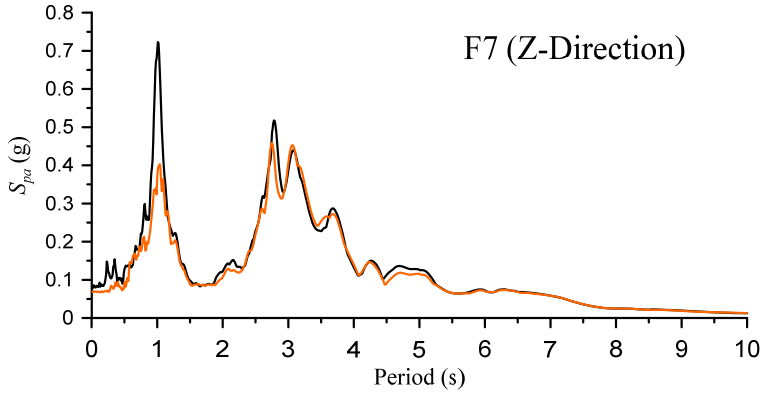

(b) 7th floor

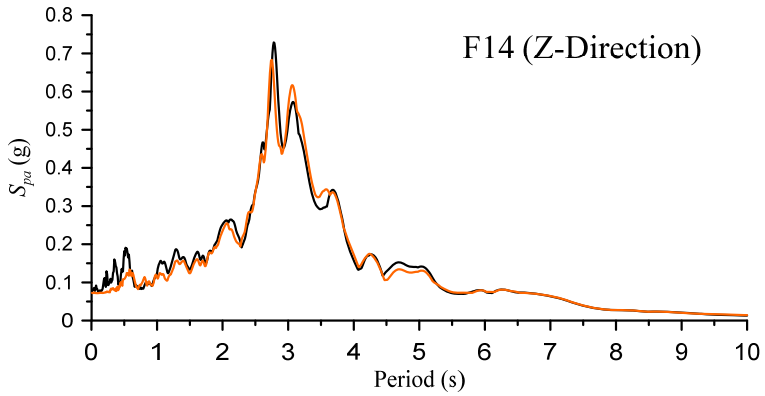

(c) 14th floor

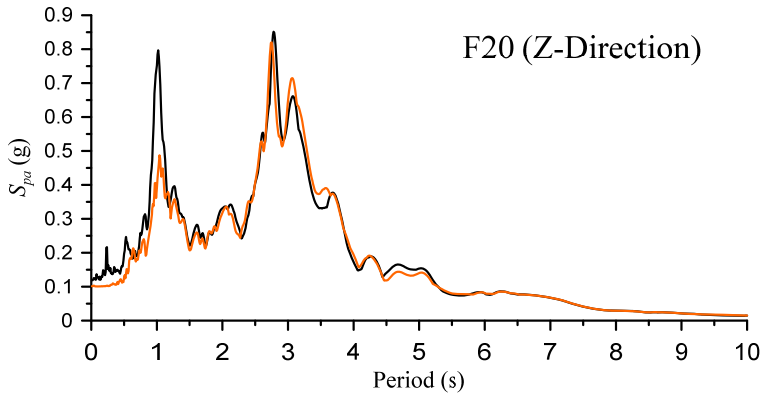

(d) 20th floor

Figure 6.52 Comparison of floor response spectra (Z-direction)

Figures 6.53 and 6.54 show the displacement and acceleration envelope responses in all floors, respectively together with the recorded data at 7th, 14th, and 20th floors. The distribution of the displacement and acceleration along the superstructure height shows similar trends. Accelerations are also concentrated at the uppers stories.

Knowing the displacement response histories for all floors, then we can obtain the story drift ratio histories for each story, then obtain the maximum story drift ratio for each story. The results are plotted in Figure 6.55. It can be seen than most of the stories have a story drift ratio of around 0.15% in X-direction and a liter higher than 0.15% in Z-direction. The trend is similar that drift ratios appear to be larger at lower stories and become smaller at upper stories.

Comparing the story drift ratios obtained for full building model with those from the superstructure model only in the previous section, in X-direction, they are slightly higher those from the superstructure model consistently in all stories, and in Z-direction, from the 3rd to around 17th stories, they are higher, and from 17th to the top story, they are almost equal. Because of highly nonlinear behavior happening in the isolation system due to several steel and oil dampers, the model becomes very complicated, hence it becomes difficult to obtain exactly same or almost identical results. However, with these similar responses, it is considered accurate enough and it will be used for further investigation.

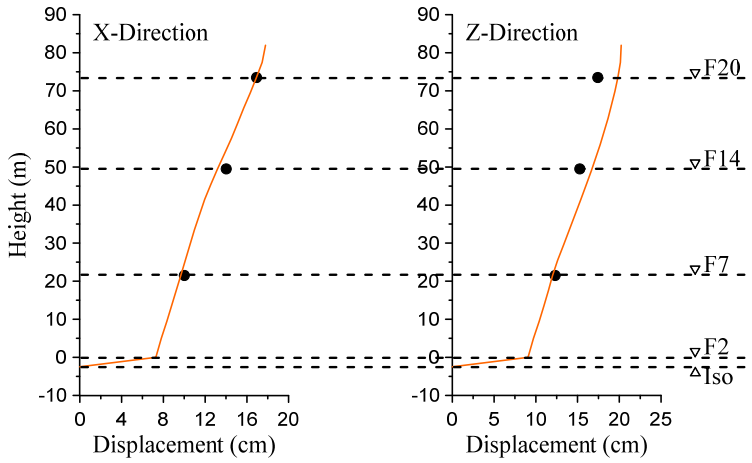

Figure 6.53 Comparison of displacement envelope responses

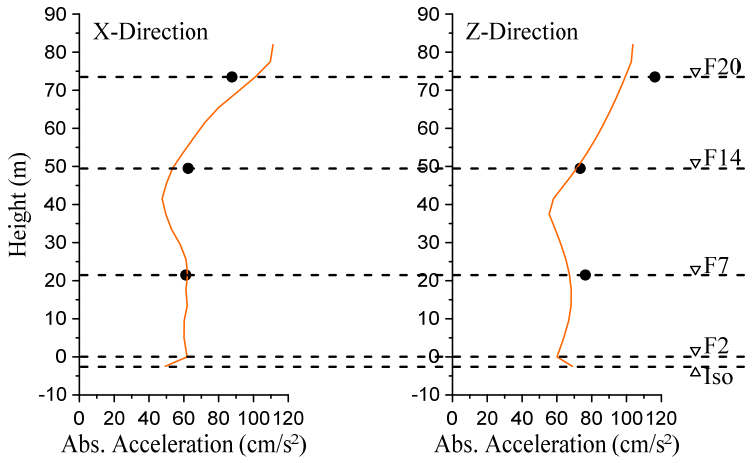

Figure 6.54 Comparison of floor acceleration envelope responses

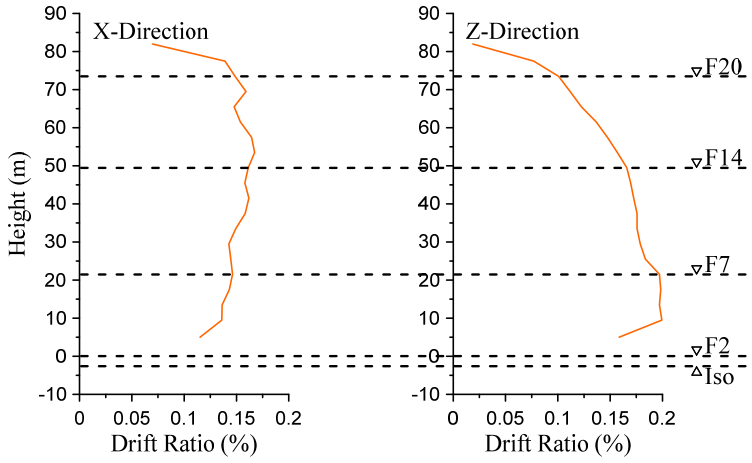

Figure 6.55 Comparison of story drift ratio envelope responses

6.5 Response of J2 Base-Isolated Structure

In the previous sections, the modelling of the J2 base-isolated building has been described, and its verification has been identified. In this section, several weak and strong ground motions will be used as ground acceleration inputs to the building in order to investigate the responses of the building.

Six ground motions will be used for investigation. Three ground motions are from Japan and three are from outside of Japan. Table 6.12 lists the ground motions used in this section. The building will be subjected to these ground motions in both X- and Z- directions for both NW and EW ground motions, for instance, for Miyagi 1978 Earthquake, two analyses will be performed, one is NS and EW motions are input to X- and Z- directions, and another one is NS and EW are input to Z- and X-directions. Figures 6.56 and 6.57 show the ground motion histories. Figures 6.58 and 6.59 show the response spectra of the ground motions.

Table 6.12 List of ground motions

	Earthquake		PGA (cm/s^2)
In Japan	**Miyagi 1978**	Tohoku University NS	257.98
		Tohoku University EW	203.10
	Hyougo 1995	Takatori NS	605.55
		Takatori EW	656.98
	Hyougo 1995	JMA Kobe NS	820.56
		JMA Kobe EW	619.20
Out of Japan	**Kern Country 1952**	Taft NS	152.70
		Taft EW	175.90
	Imperial Valley 1940	El Centro NS	341.70
		El Centro EW	210.10
	Northridge	New Hall NS	578.19
		New Hall EW	571.62

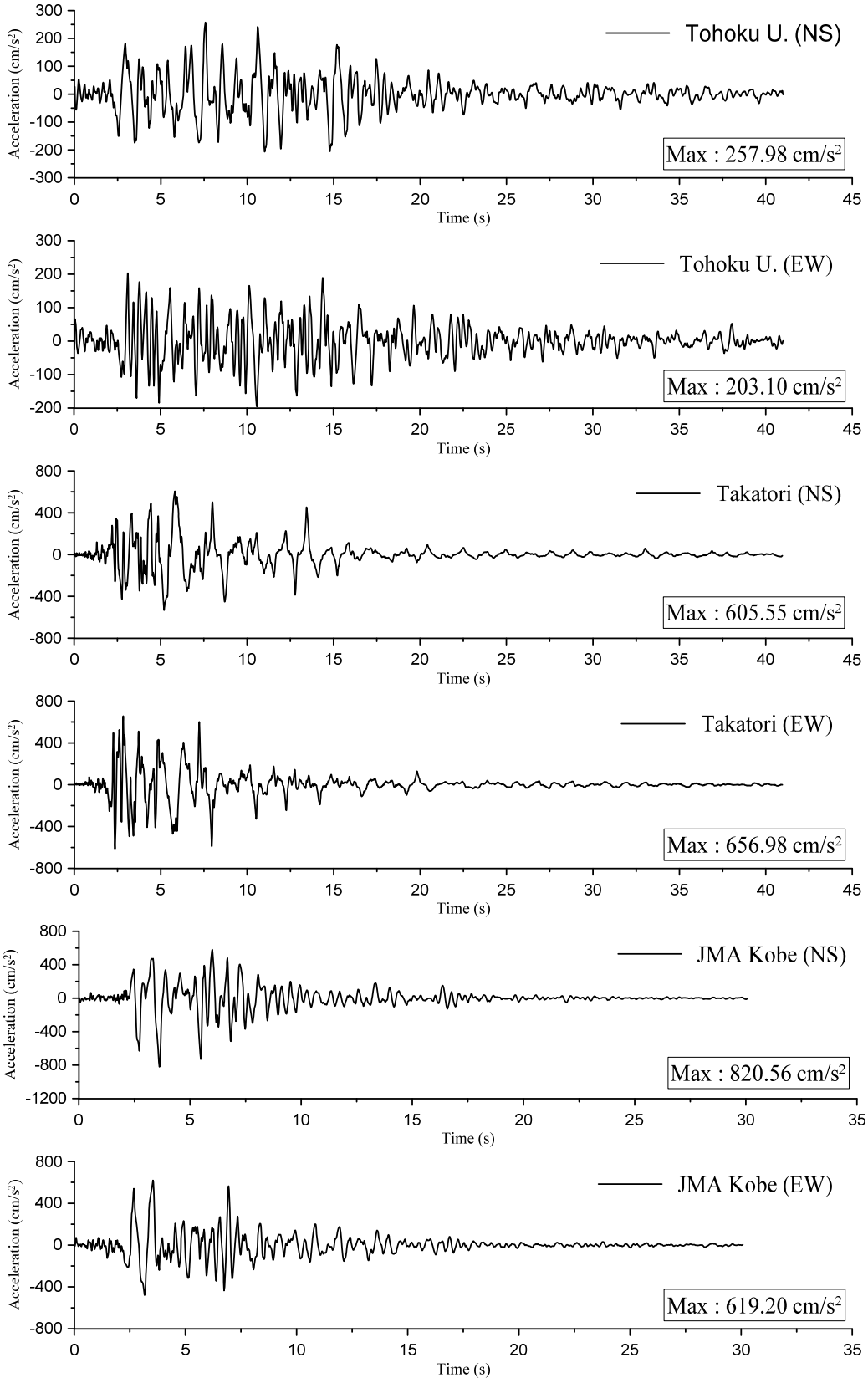

Figure 6.56 Ground motion histories (in Japan)

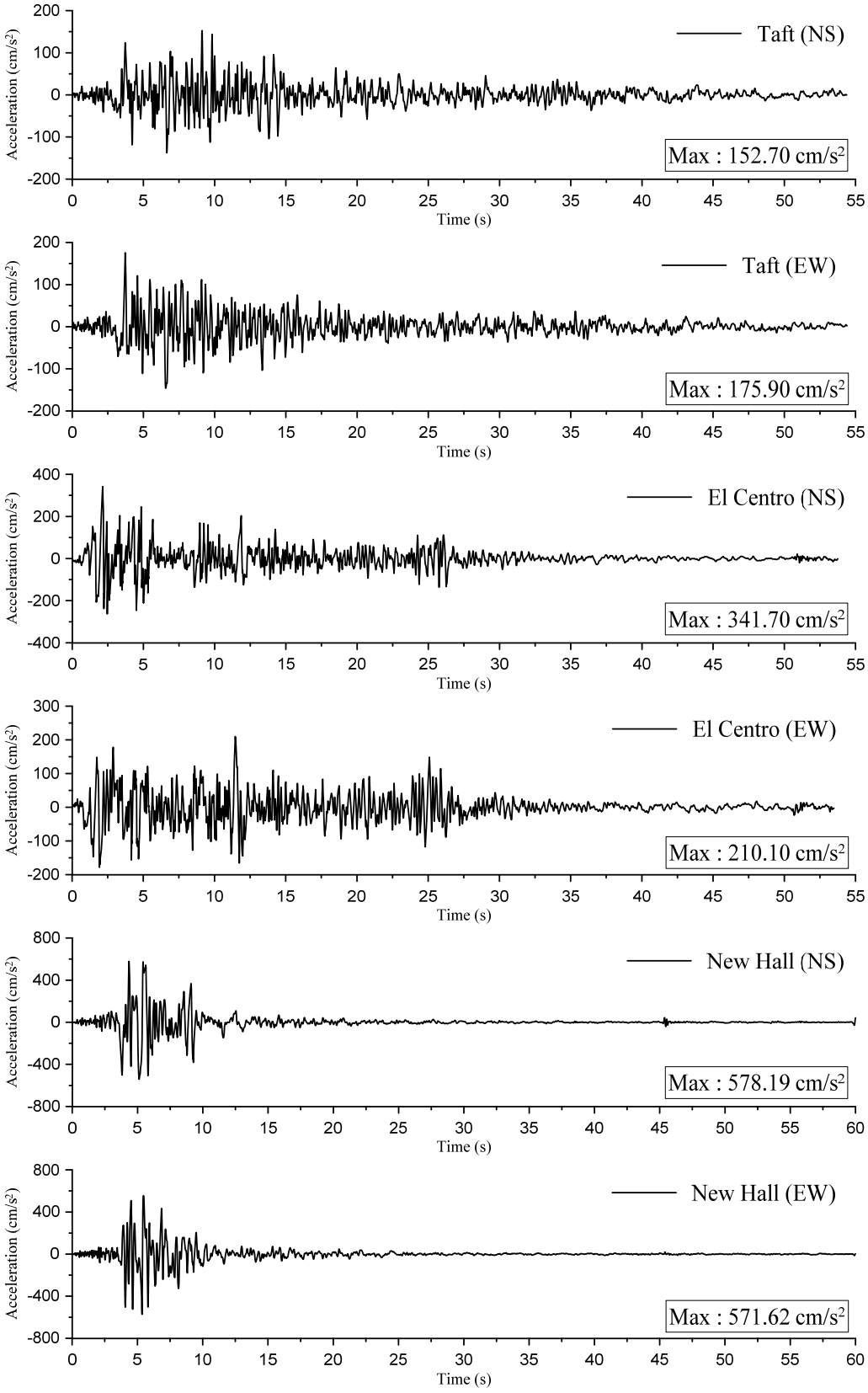

Figure 6.57 Ground motion histories (out of Japan)

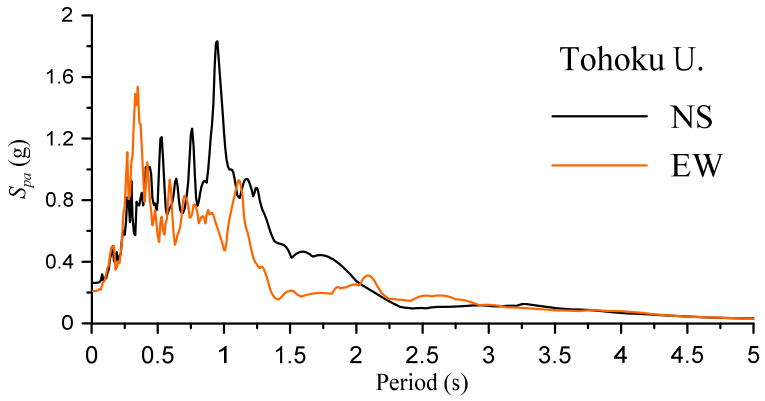

(a) Tohoku University

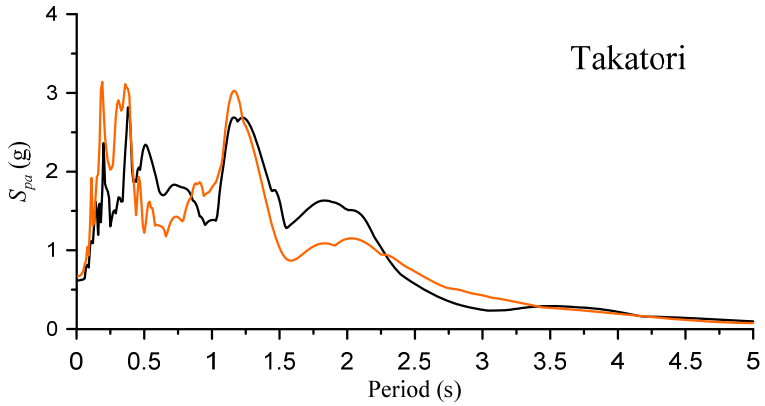

(b) Takatori

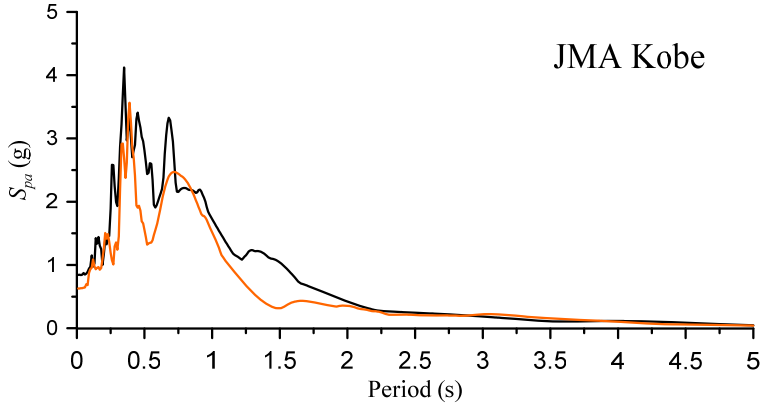

(c) JMA Kobe

Figure 6.58 Response spectra of ground motions (in Japan)

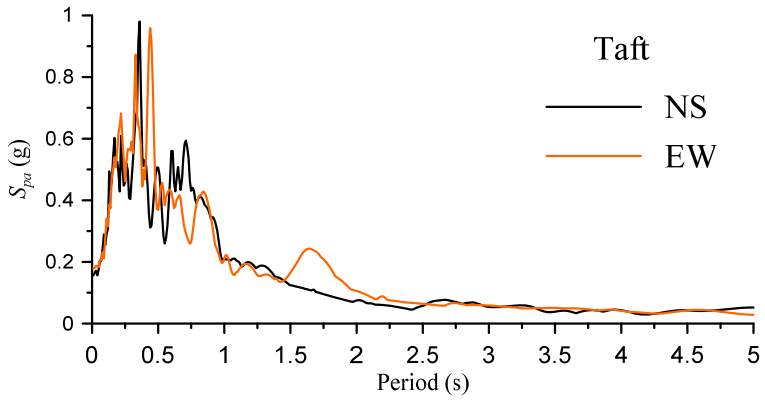

(a) Taft

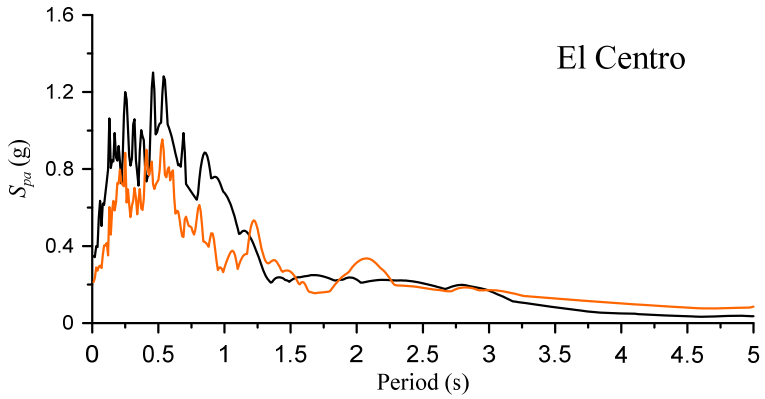

(b) El Centro

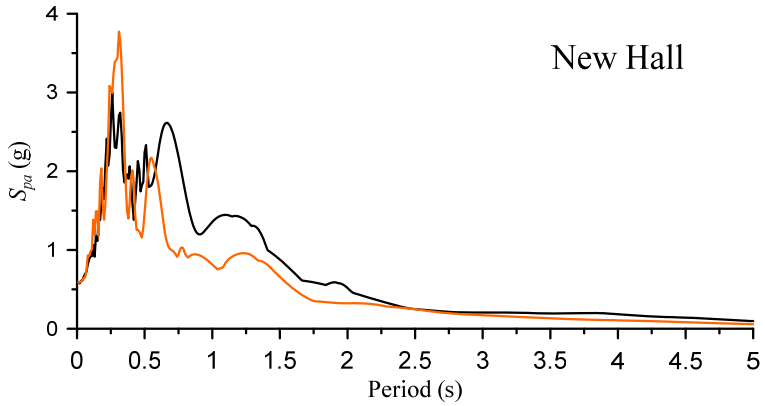

(c) New Hall

Figure 6.59 Response spectra of ground motions (out of Japan)

Figures 6.60 – 6.71 show the envelope responses for each ground motion. Note that at the caption of these figures, NS(X) indicates that ground motion specified by NS is used as input in X-direction of the building. For others, EW(Z), NS(Z), and EW(X), they can be interpreted the same way. Also note that the response histories are shown in Appendix C.

Looking that displacement response, we can see that the displacement gets higher along the structure height rather uniformly, like a triangular shape, in all cases. However, the inter-story drift ratios do not seem to exhibit uniform distribution along the structure height. This is normal since the maximum displacement for each story does not occur at the same time, due to higher mode contribution.

Acceleration responses appear to be higher in the lower and upper floors, and smaller in the middle floors, as can be seen in all cases of ground motions. Several cases show that the accelerations at around the 14th floor seem be almost always lower than the other floors. Comparing between peak ground accelerations (PGA) and the absolute floor accelerations in the structures, the results show that the floor accelerations are reduced significantly from the PGA in all cases. Even though there seems to be some concentration in the upper floors, still they are lower than the PGA for the corresponding ground motion.

For story drift ratio, at the upper stories, story drift ratios seem to be much smaller than the other stories. Looking at the 14th story, it is interesting to see that the story drift ratios seem to be concentrated at this story. Around half of the cases, story drift ratios appear to be highest at the 14th story, and for the other half, they appear to be more concentrated at the lower stories, around 4th to 7th stories. For strong ground motions, such as Takatori and Kobe, the maximum story drift ratios produced are around 0.9% and 0.45%, respectively.

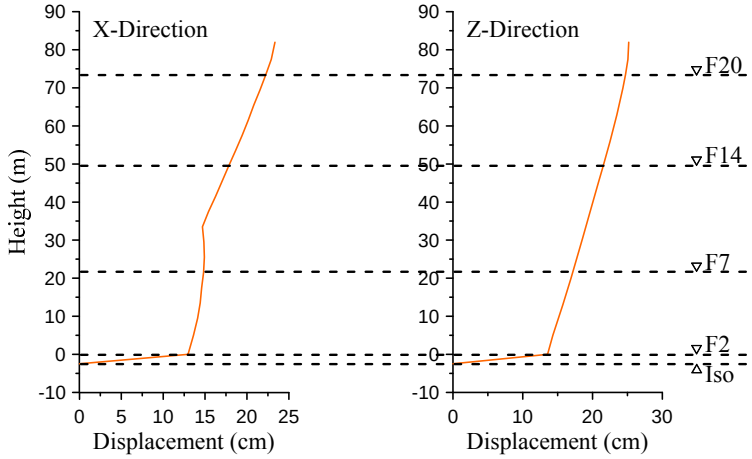

(a) Displacement

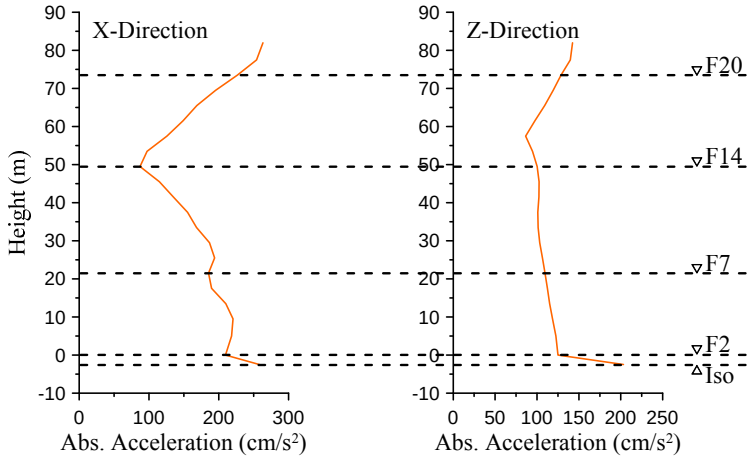

(b) Acceleration

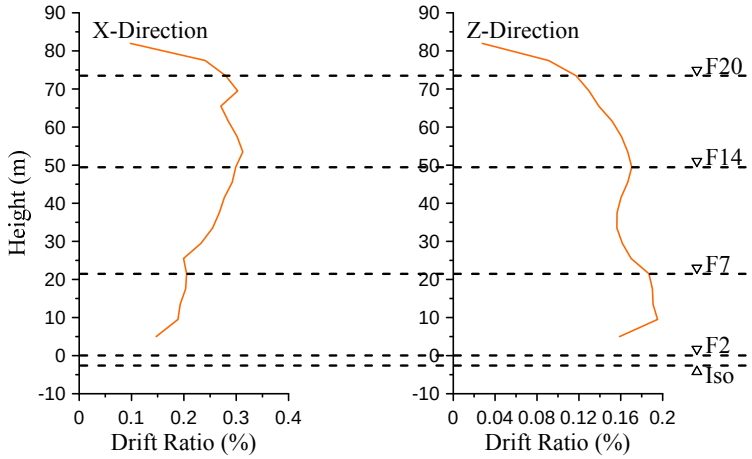

(c) Story drift ratio

Figure 6.60 Envelope responses (Tohoku U – NS(X), EW(Z)))

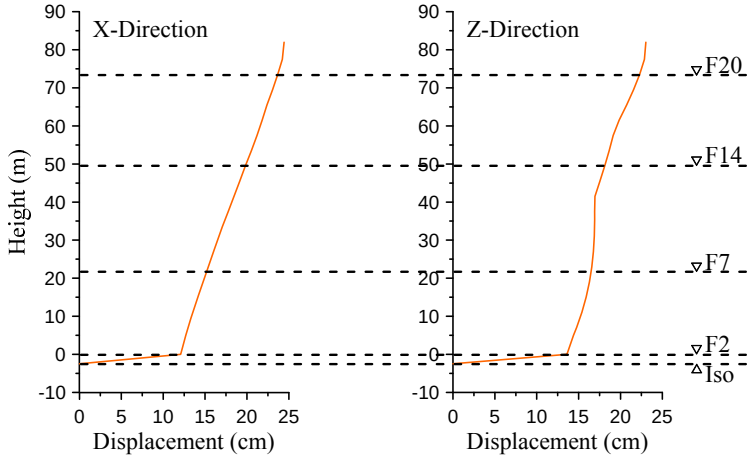

(a) Displacement

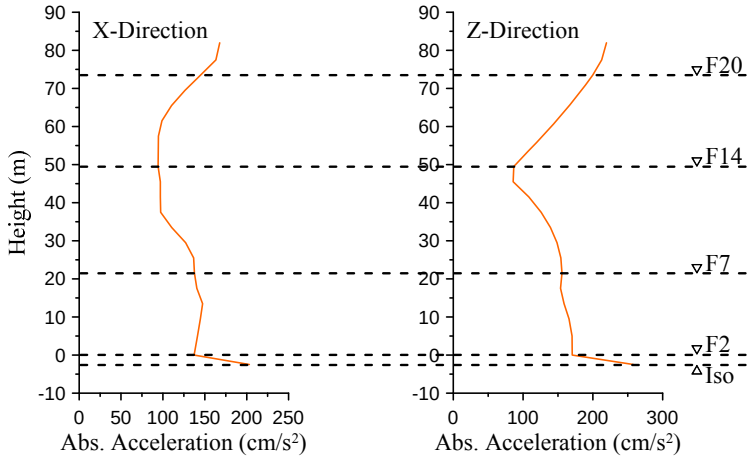

(b) Acceleration

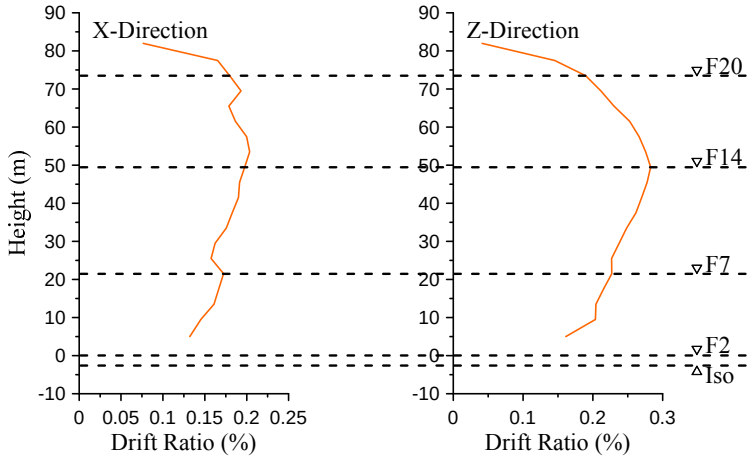

(c) Story drift ratio

Figure 6.61 Envelope responses (Tohoku U – NS(Z), EW(X)))

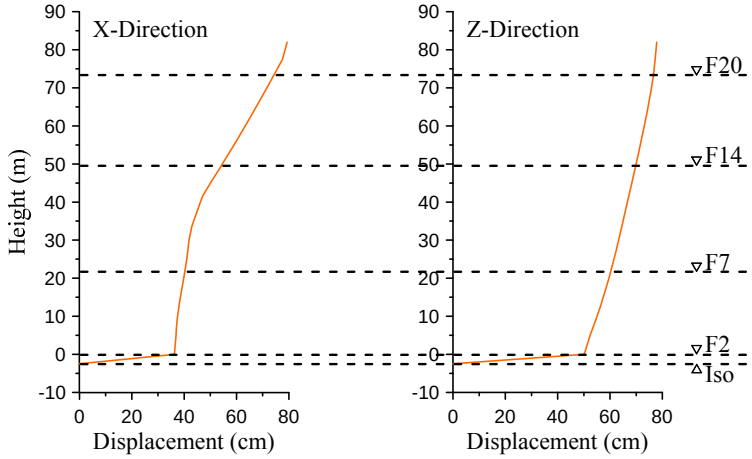

(a) Displacement

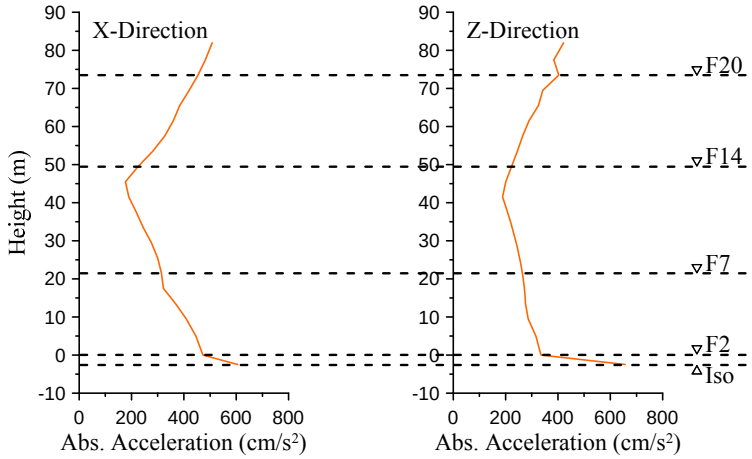

(b) Acceleration

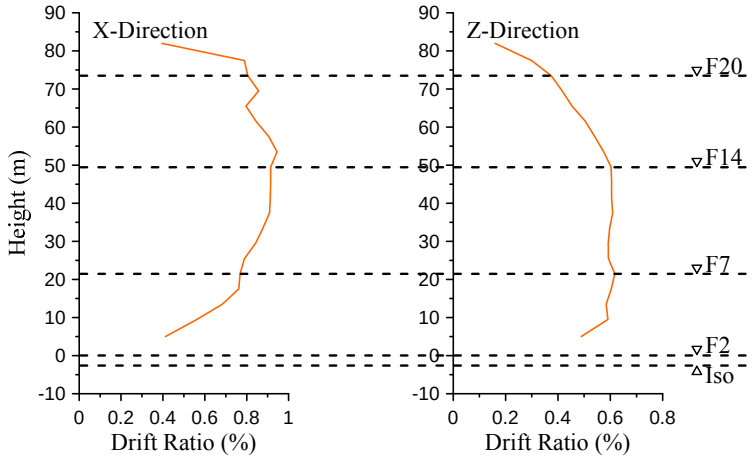

(c) Story drift ratio

Figure 6.62 Envelope responses (Takatori – NS(X), EW(Z)))

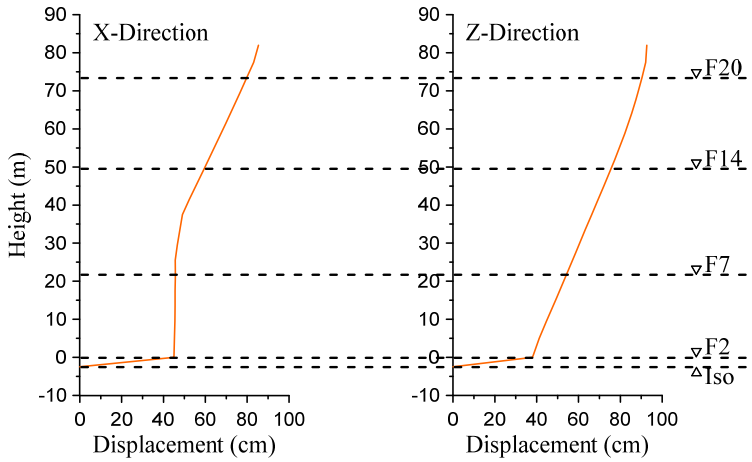

(a) Displacement

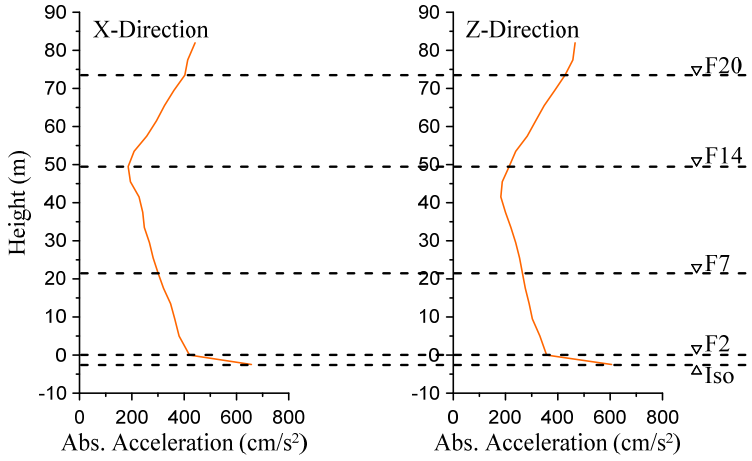

(b) Acceleration

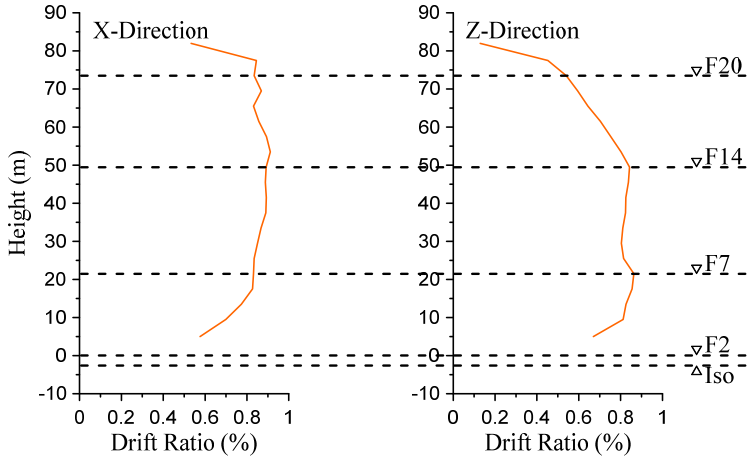

(c) Story drift ratio

Figure 6.63 Envelope responses (Takatori – NS(Z), EW(X)))

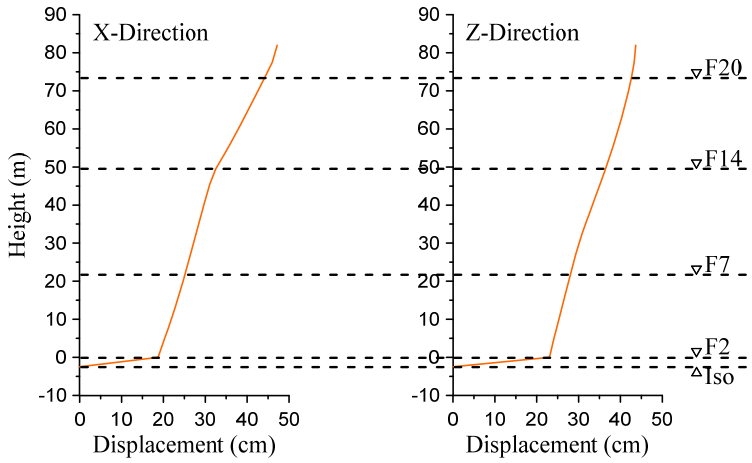

(a) Displacement

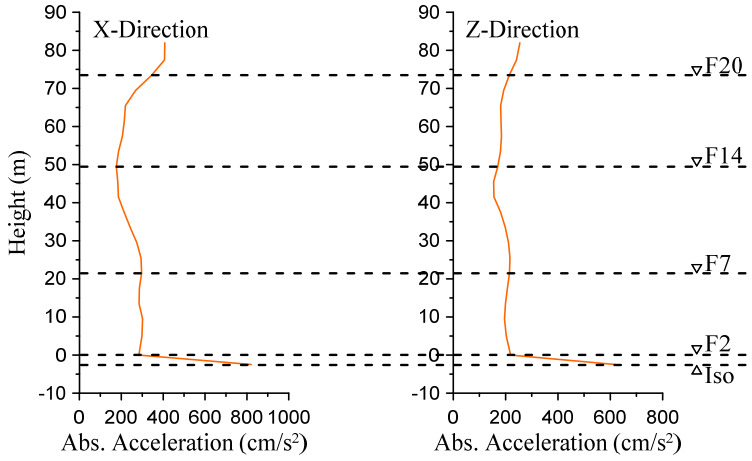

(b) Acceleration

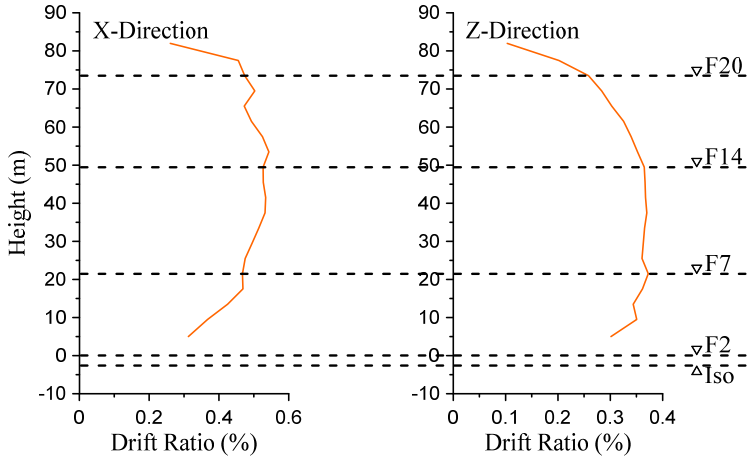

(c) Story drift ratio

Figure 6.64 Envelope responses (JMA Kobe – NS(X), EW(Z)))

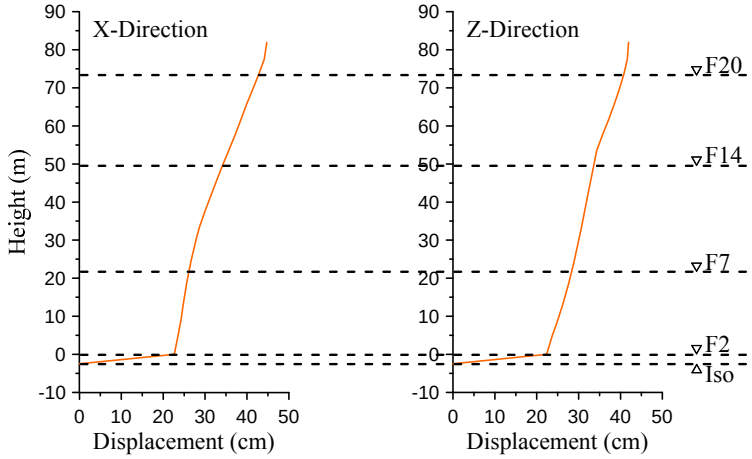

(a) Displacement

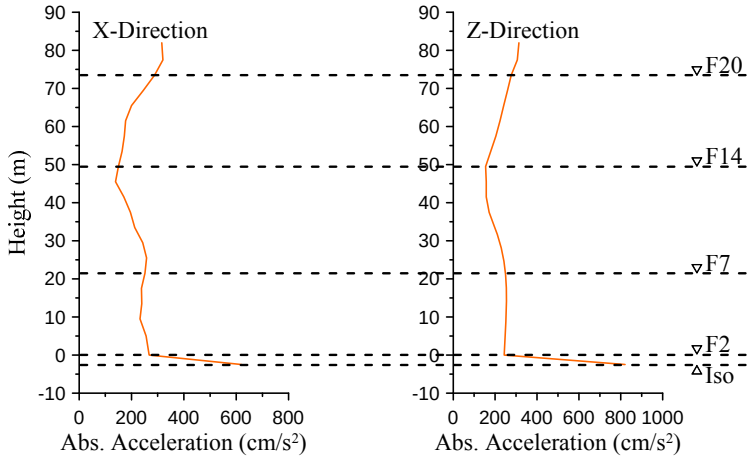

(b) Acceleration

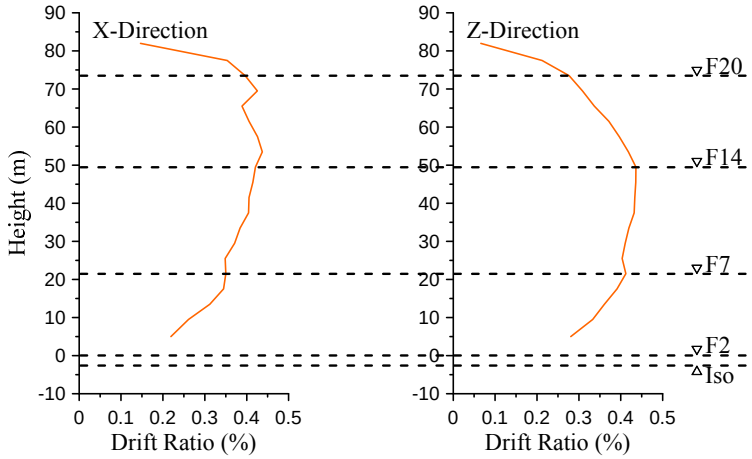

(c) Story drift ratio

Figure 6.65 Envelope responses (JMA Kobe – NS(Z), EW(X)))

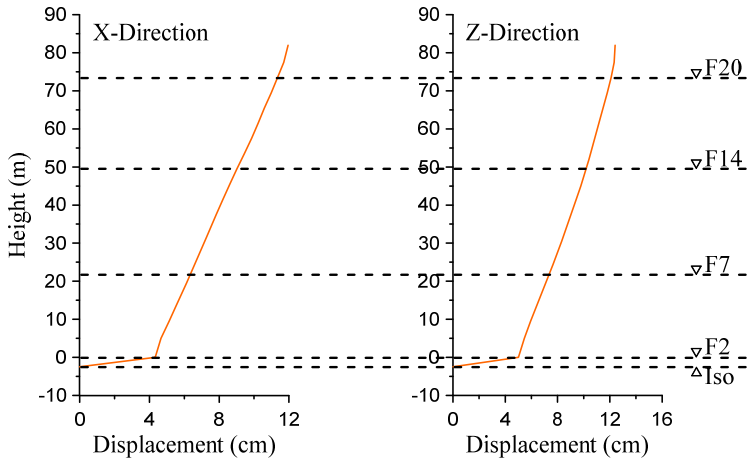

(a) Displacement

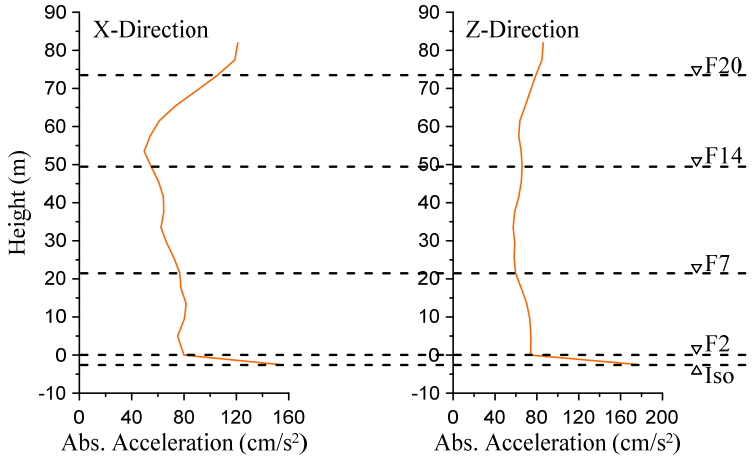

(b) Acceleration

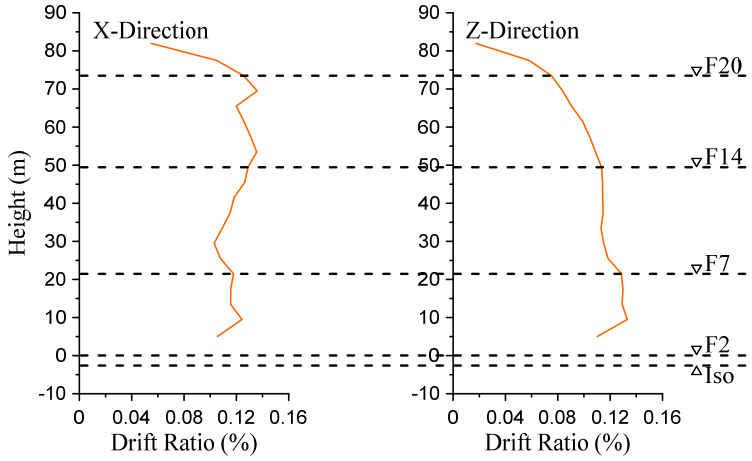

(c) Story drift ratio

Figure 6.66 Eenvelope responses (Taft – NS(X), EW(Z)))

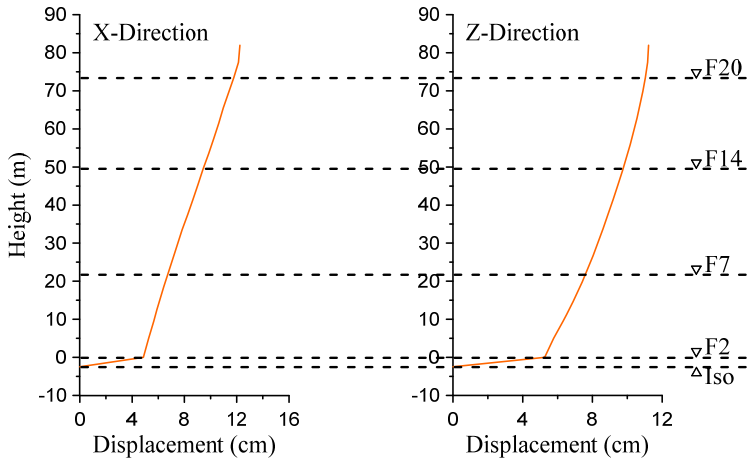

(a) Displacement

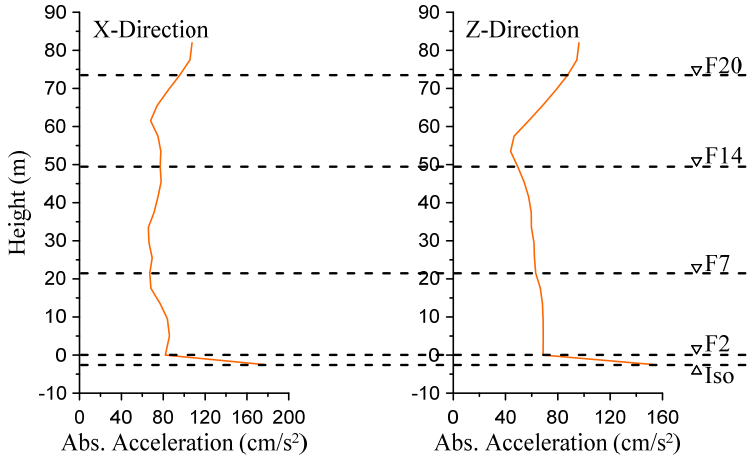

(b) Acceleration

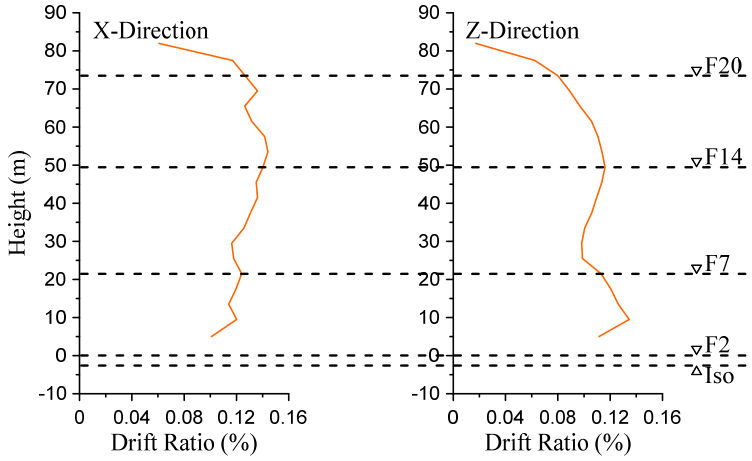

(c) Story drift ratio

Figure 6.67 Eenvelope responses (Taft – NS(Z), EW(X)))

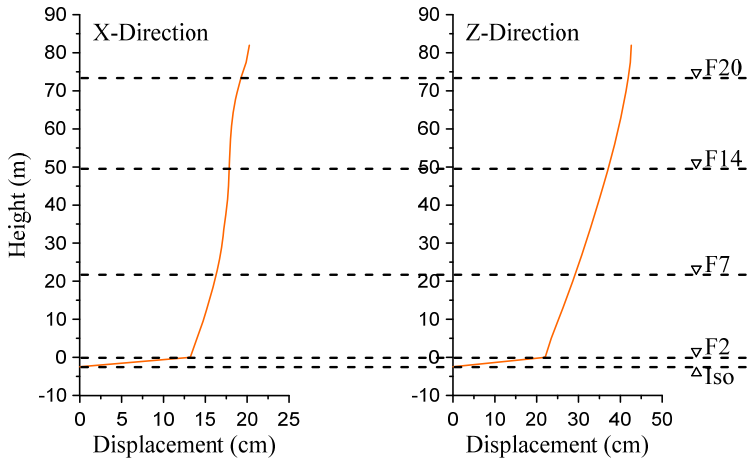

(a) Displacement

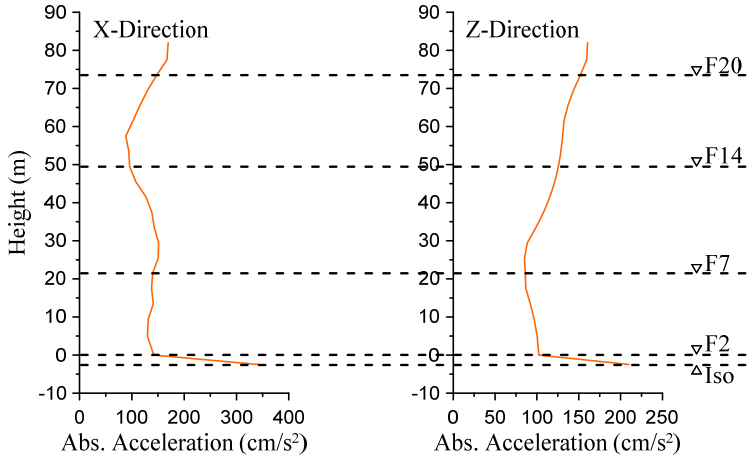

(b) Acceleration

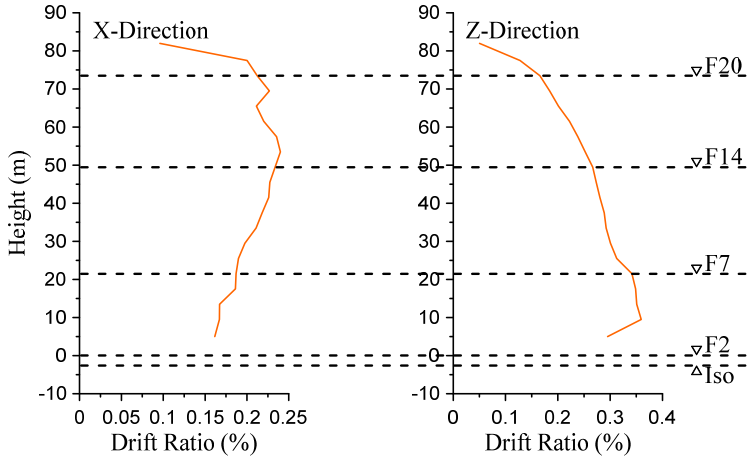

(c) Story drift ratio

Figure 6.68 Envelope responses (El Centro – NS(X), EW(Z)))

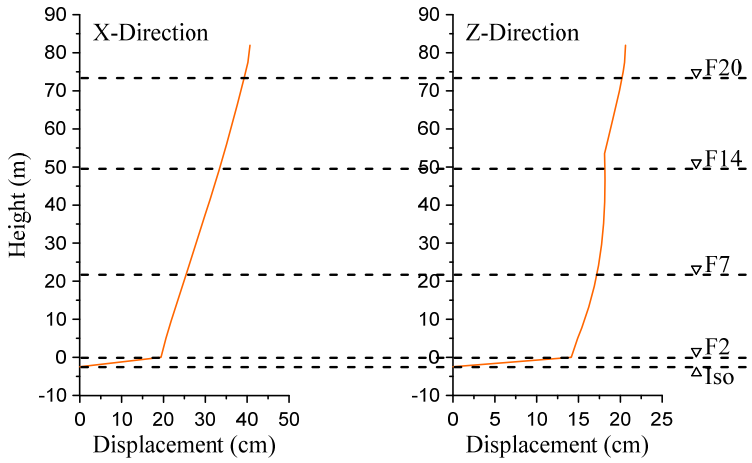

(a) Displacement

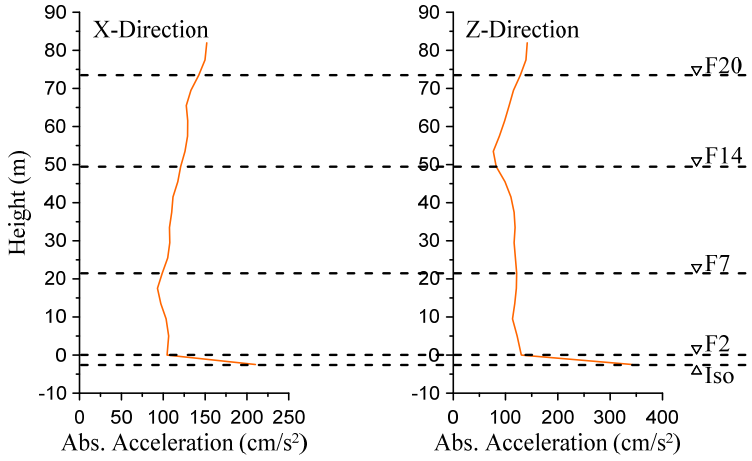

(b) Acceleration

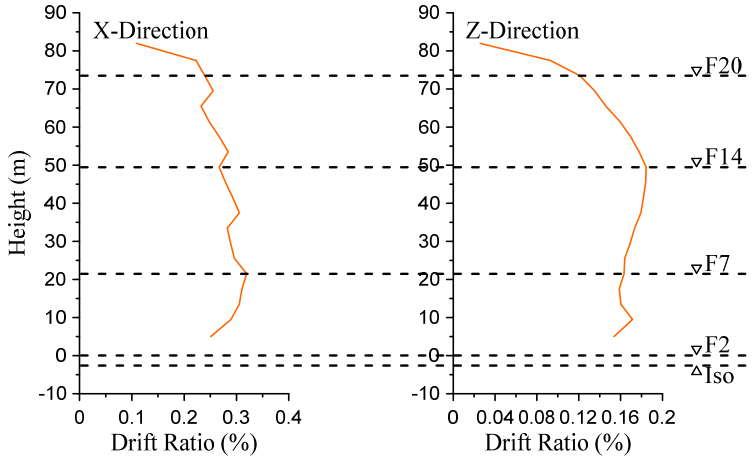

(c) Story drift ratio

Figure 6.69 Envelope responses (El Centro – NS(Z), EW(X)))

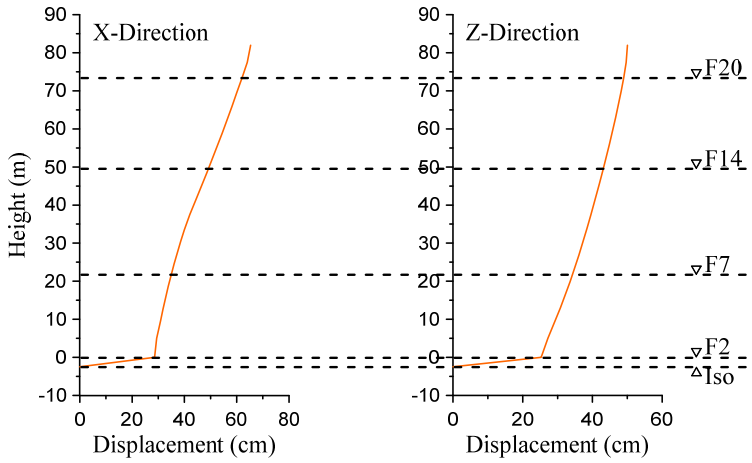

(a) Displacement

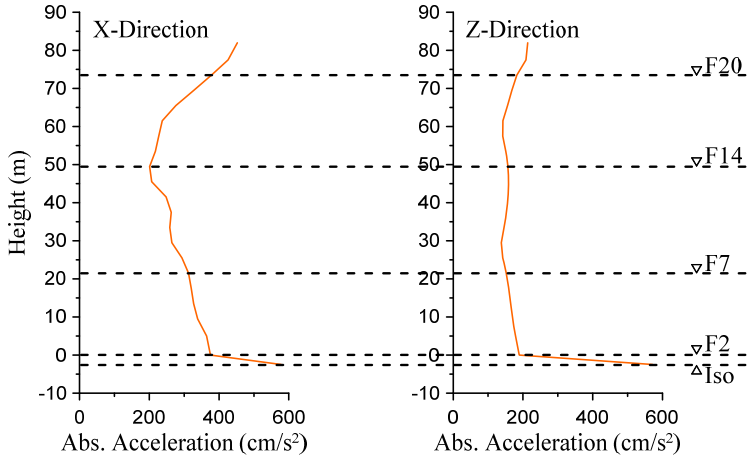

(b) Acceleration

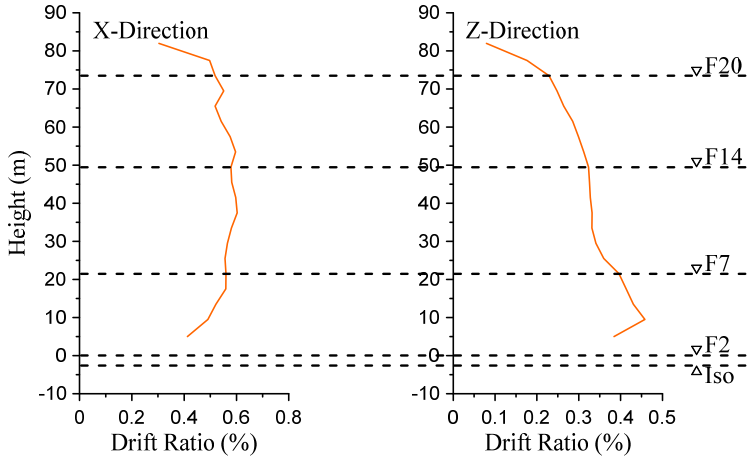

(c) Story drift ratio

Figure 6.70 Envelope responses (New Hall – NS(X), EW(Z)))

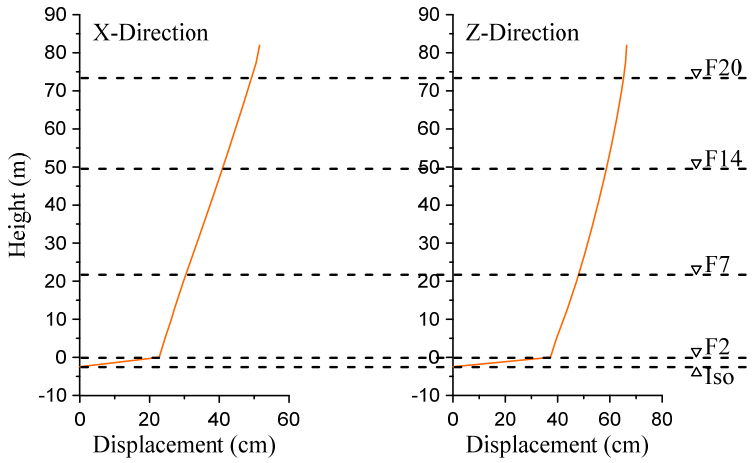

(a) Displacement

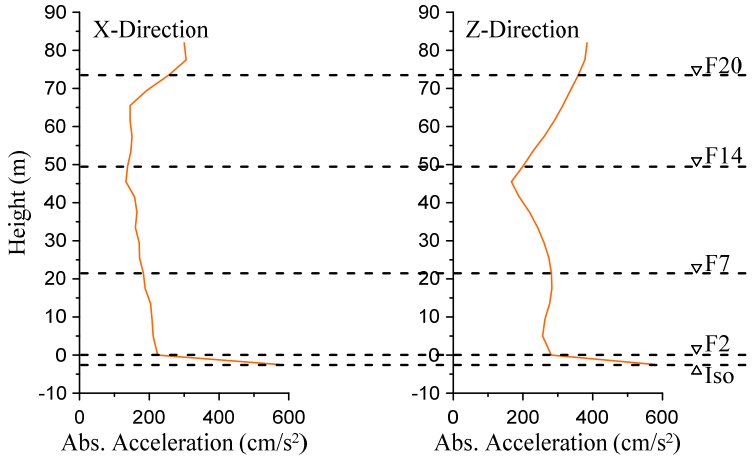

(b) Acceleration

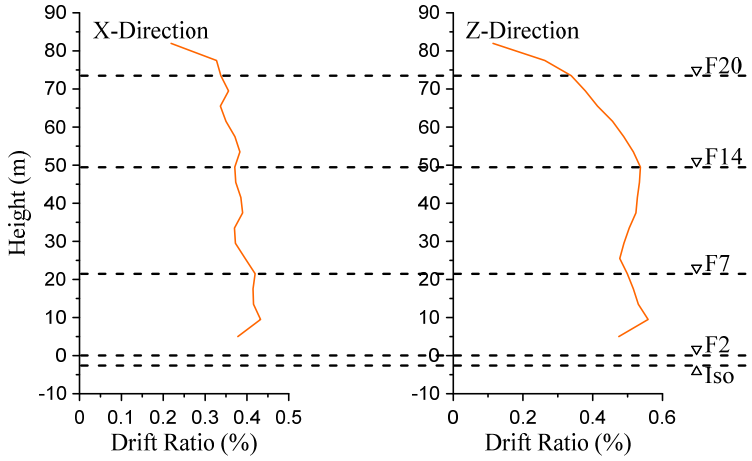

(c) Story drift ratio

Figure 6.71 Envelope responses (New Hall – NS(Z), EW(X)))

6.6 Conversion from Sophisticated Model to Shear Model

In the previous sections, we use the 3D sophisticated model to investigate the responses under several ground motions. It is time-consuming and not convenient. In Chapters 2 to 5, we have been using simply shear models to represent the whole structures, either fixed-base or base-isolated structures. Therefore, in order to justify the appropriateness of the shear beam model, in this section, the 3D sophisticated frame model of the J2 building will be converted to a shear beam model. The responses obtained from the simple model will be compared with those from the full frame model. The accuracy and appropriateness of using the simple model can then be justified.

6.6.1 Modelling of the superstructure part and its response verification

We already have the 3D full frame sophisticated superstructure model and base-isolated isolated model. From the model of the superstructure part only, we can get the natural periods and their corresponding mode shapes from the model by conducting Eigenvalue analysis. In this study, only the Z-direction will be performed since the fundamental mode is in this direction. Figure 6.72 shows the first 3 mode shapes obtained from the model in Z-direction.

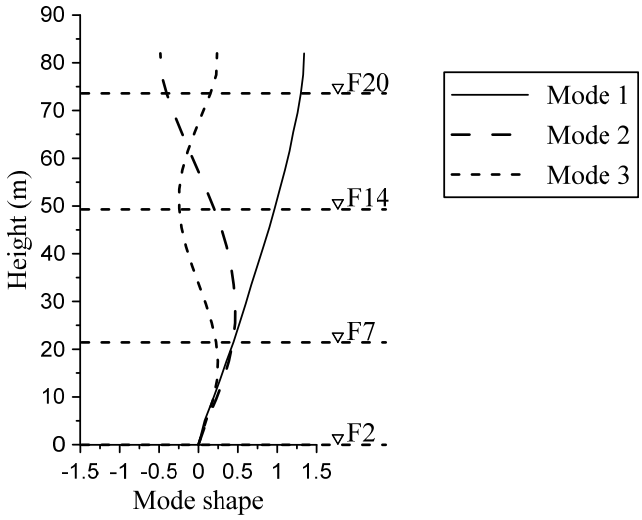

Figure 6.72 Superstructure mode shapes

We also already know the weights for each floor which can then be converted to masses for each floor as shown in Table 6.13.

Table 6.13 Masses for each floor

Floor	Weight (kN)	Mass (kN.s^2/cm)
PHR	3618.9	3.6890
RF	10462.1	10.6647
20F	7012.9	7.1487
19F	6982.1	7.1173
18F	7105.1	7.2427
17F	6973.2	7.1083
16F	7139.2	7.2775
15F	7113	7.2508
14F	7232.9	7.3730
13F	7122.4	7.2603
12F	7280.1	7.4211
11F	7194.6	7.3339
10F	7336.4	7.4785
9F	7212	7.3517
8F	7323.4	7.4652
7F	7593.1	7.7402
6F	7804.4	7.9556
5F	7652.3	7.8005
4F	7326.5	7.4684
3F	7637.6	7.7855

Knowing the masses, the first mode shape, and the first mode superstructure period are known, it is then possible to obtain the stiffness for each story by solving simultaneous Equation 6.10

$$\left(\underset{\sim}{K}_s - \frac{4\pi^2}{T_{s,1}^2} \underset{\sim}{M}_s \right) \underset{\sim}{\phi}_{s,1} = 0 \tag{6.10}$$

where $\underset{\sim}{K}_s$ is the stiffness matrix which is of tri-diagonal form, $\underset{\sim}{M}_s$ is the mass matrix in diagonal form. This Equation 6.10 is actually an Eigenvalue problem equation. But since we already know the Eigen properties of period and mode shape, then we make use of this equation of find the stiffness for each story instead. This equation becomes simply a simultaneous equations. Table 6.14 shows the stiffness for each story.

Table 6.14 Stiffness for each story

Story	Stiffness (kN/cm)
PHR	3488.40
RF	5393.59
20F	5724.17
19F	5855.11
18F	8124.97
17F	7659.92
16F	7987.80
15F	8947.60
14F	9861.88
13F	9055.06
12F	9719.07
11F	10313.92
10F	11762.73
9F	11335.88
8F	11758.77
7F	10514.80
6F	11551.17
5F	10981.28
4F	9258.70
3F	12884.89

Then we need to find the damping matrix $\underset{\sim}{C}_s$. We assume that the damping matrix is proportional to the stiffness matrix. And the first mode damping is also already known which is $\zeta_{s,1} = 0.046$. Therefore, the damping matrix $\underset{\sim}{C}_s$ can be obtained from Equation 6.11.

$$\underset{\sim}{C}_s = \beta \underset{\sim}{K}_s = \frac{T_{s,1}\zeta_{s,1}}{\pi} \underset{\sim}{K}_s \tag{6.11}$$

After knowing all the necessary stiffness and damping matrices, now it is possible to construct the shear beam model or stick model as shown in Figure 6.73.

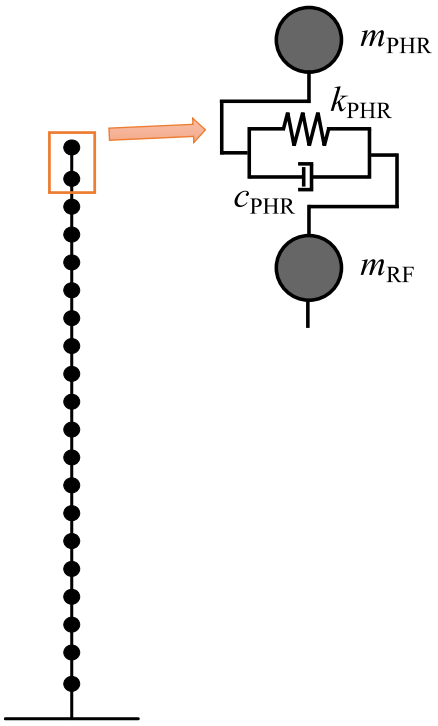

Figure 6.73 Superstructure stick model

The input accelerations used will be the acceleration histories recorded at the 2nd floor (just above the isolation level) in Z-direction. The results are shown in Figure 6.74 and 6.75 for the displacement and acceleration response histories, respectively. Figure 6.76 shows the envelope responses. The responses from this simple model show very good agreement with the recorded data.

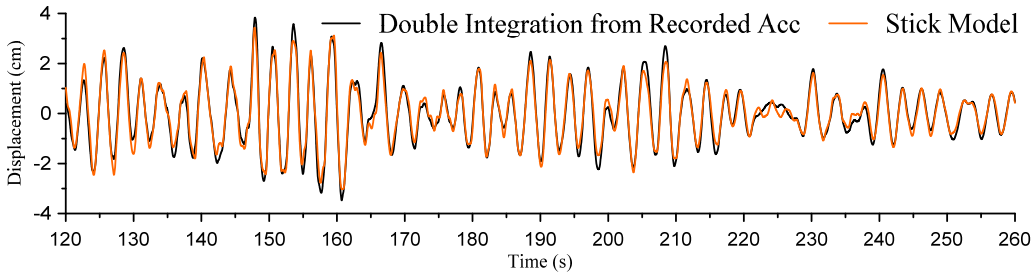

(a) 7th floor

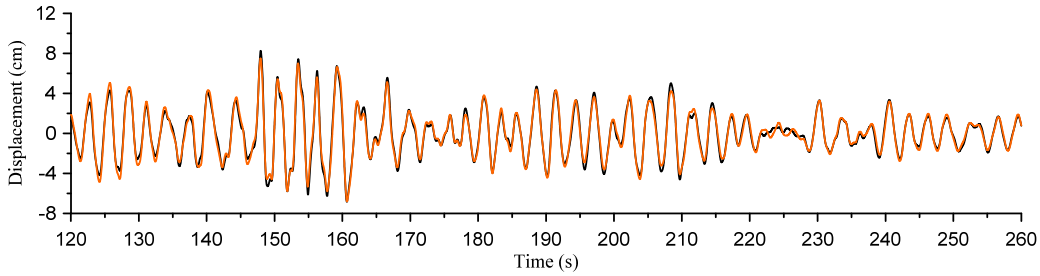

(b) 14th floor

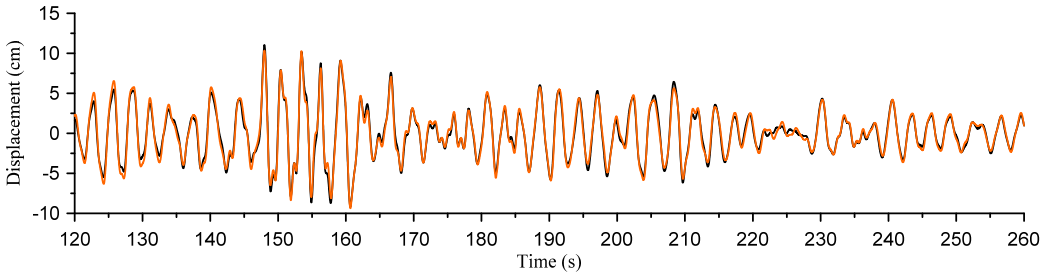

(c) 20th floor

Figure 6.74 Floor displacement relative to the 2nd floor

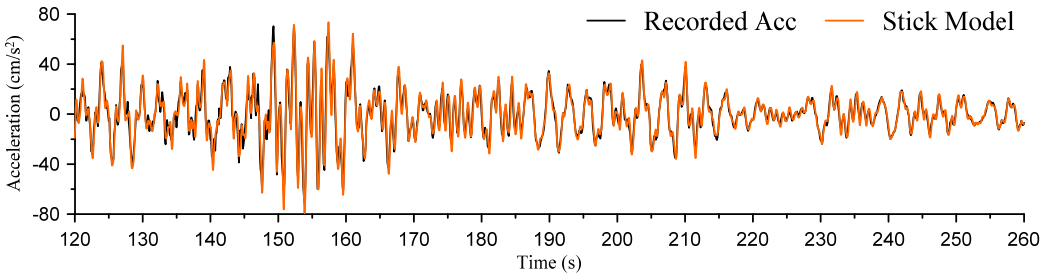

(a) 7th floor

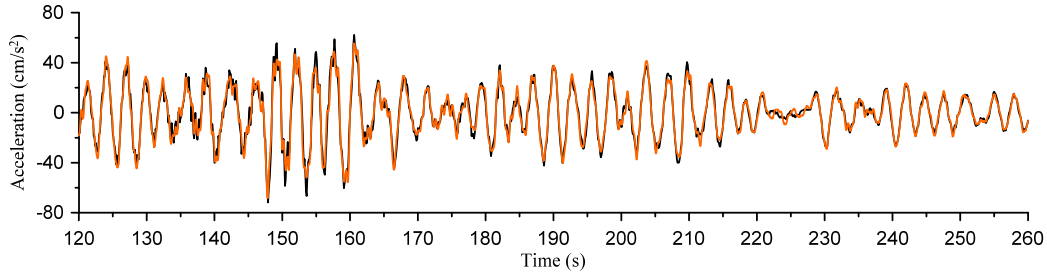

(b) 14th floor

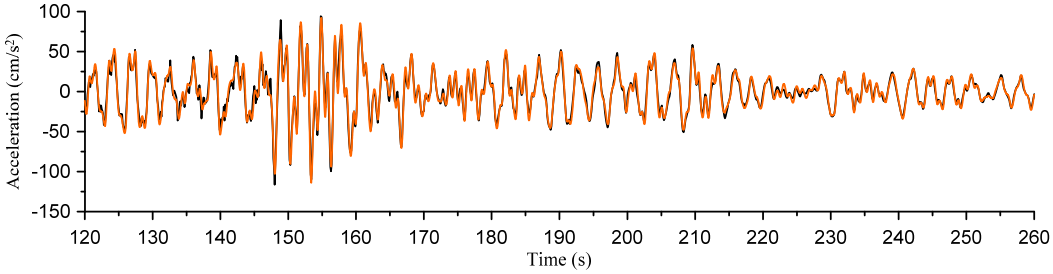

(c) 20th floor

Figure 6.75 Absolute floor acceleration

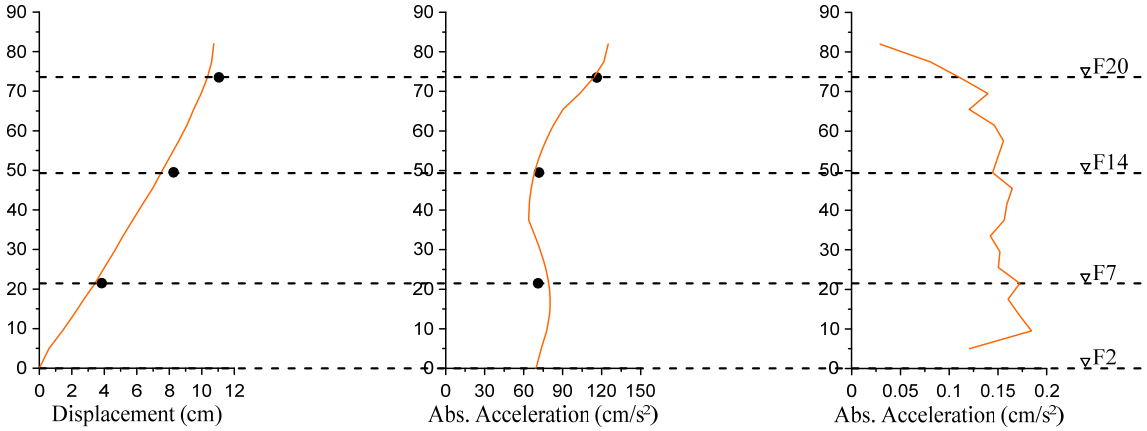

Figure 6.76 Envelope responses

6.6.2 Modelling of isolation system and building's response verification

ViscoElastic isolation

This section will show how to obtain the stiffness and damping coefficient for the isolation system. From the previous section, we already have the stiffnesses and damping coefficients for each story above the isolation level. The only remain part is the stiffness and damping coefficient for the isolation system. We also already know the first mode period in Z-direction from the System Identification which is equal to T_1 = 2.972 seconds. Then we can find the isolation stiffness such that it gives the first mode period $T_{1,c}$ equal to T_1. This can be done by solving Eigenvalue problem to find $T_{1,c}$ in Equation 6.12. By trying a few times, it will be possible to obtain the target isolation stiffness. The result of the isolation stiffness is 1350 kN/cm which gives the fundamental period of 2.978 seconds. It is possible to fine-tune until we get it equal to 2.792, but it is not necessary, since it will not change the responses so much.

$$\left(\underset{\sim}{K} - \frac{4\pi^2}{T_{1,c}^2} \underset{\sim}{M} \right) \underset{\sim}{\phi}_{1,c} = 0 \tag{6.12}$$

Now we need to find the damping coefficient for the isolation system. Similarly we already know the first mode damping ratio ζ_1 = 0.105. It is possible to estimate the first mode damping ratio by using modal strain energy as shown in Equation 6.13.

$$\zeta_{1,c} = \frac{\pi \underset{\sim}{\phi}_{1,c}^T \underset{\sim}{C} \underset{\sim}{\phi}_{1,c}}{T_{1,c} \underset{\sim}{\phi}_{1,c}^T \underset{\sim}{K} \underset{\sim}{\phi}_{1,c}} \tag{6.13}$$

Previously, we already know the damping coefficients for each story in the superstructures (C_3 to C_{PHR}), then by substituting a trial C_2 value in Matrix $\underset{\sim}{C}$ Equation 6.14, then solve for $\zeta_{1,c}$ using Equation 6.13 until $\zeta_{1,c} = \zeta_1$. From this method, we then can obtain the damping coefficient for the isolation system. The resulting C_2 value is 221.4 which gives the first mode period of 0.105.

$$\underset{\sim}{C} = \begin{bmatrix} C_2 + C_3 & -C_3 & 0 & 0 & 0 \\ -C_3 & C_3 + C_4 & -C_4 & 0 & 0 \\ 0 & -C_4 & \ddots & \ddots & 0 \\ 0 & 0 & \ddots & \ddots & -C_{\mathrm{PHR}} \\ 0 & 0 & 0 & -C_{\mathrm{PHR}} & C_{\mathrm{PHR}} \end{bmatrix} \tag{6.14}$$

The input accelerations used will be the acceleration histories recorded at the isolation floor (just below the isolation level) in Z-direction. The results are shown in Figure 6.77 and 6.78 for the displacement and acceleration response histories, respectively. Figure 6.79 shows the envelope responses. Overall, the responses from this simple model show very good agreement with the recorded data, with slightly smaller displacement and acceleration responses than the recorded data. Figure 6.80 shows the base shear-displacement hysteresis in the isolation story. Since this model is idealized by linear viscous damper, therefore, it cannot match the recorded data very well when large displacement occurs.

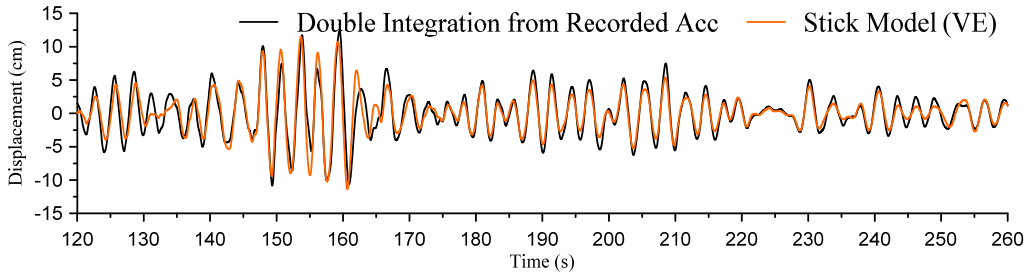

(a) 7th floor

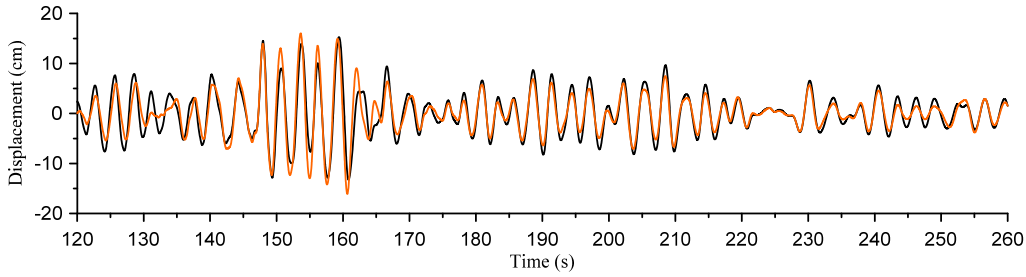

(b) 14th floor

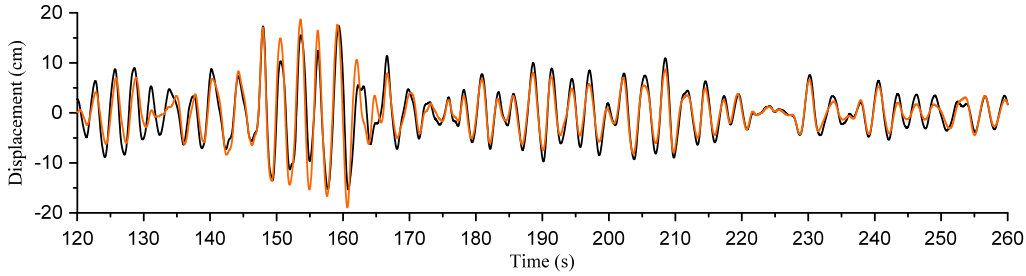

(c) 20th floor

Figure 6.77 Floor displacement relative to the 2nd floor

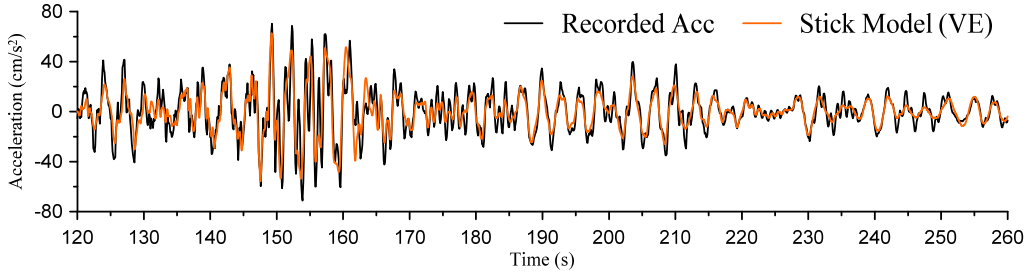

(a) 7th floor

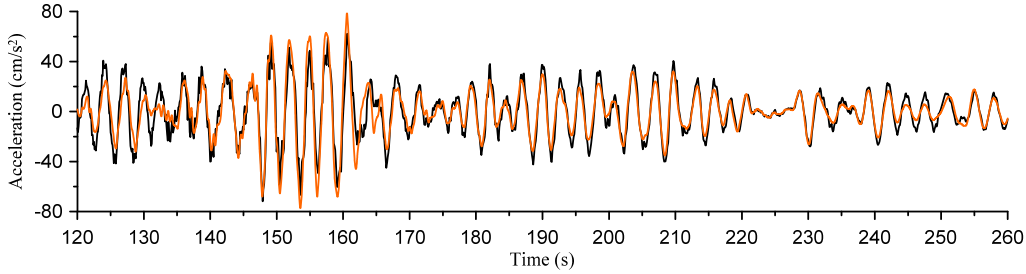

(b) 14th floor

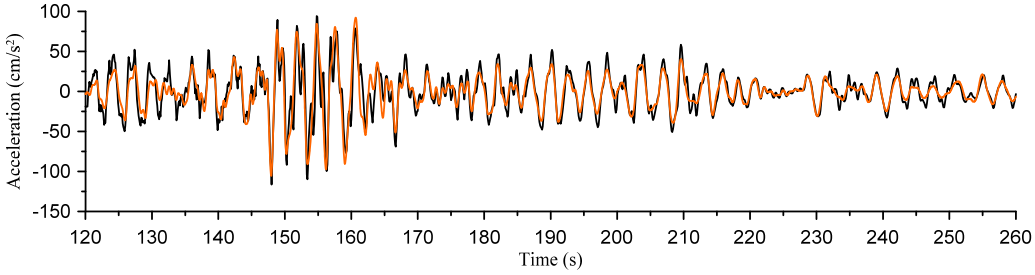

(c) 20th floor

Figure 6.78 Absolute floor acceleration

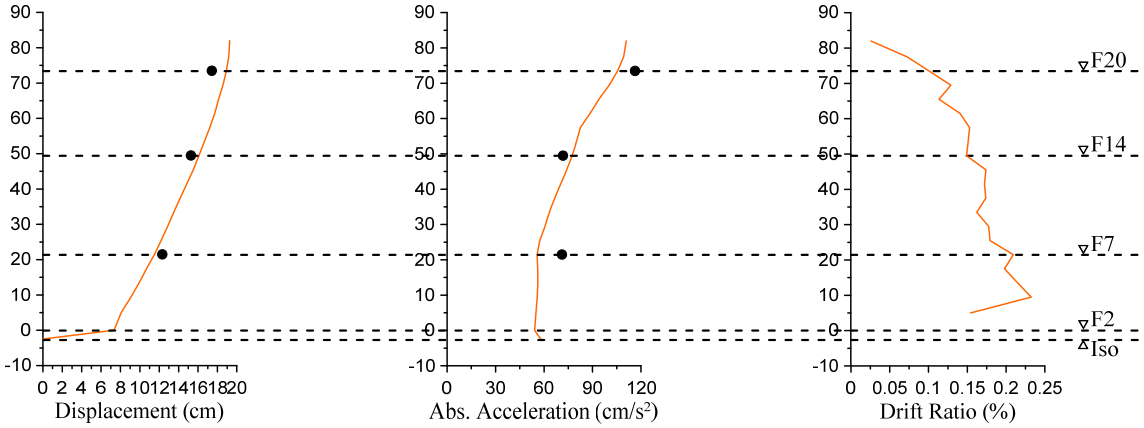

Figure 6.79 Envelope responses

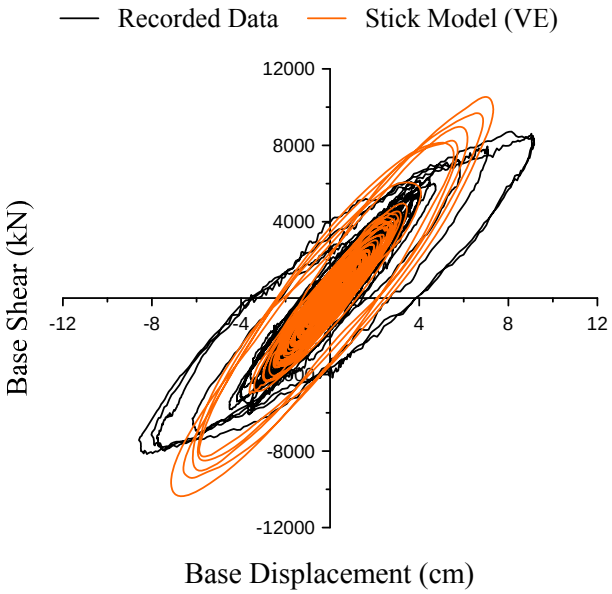

Figure 6.80 Base shear-displacement hysteresis in the isolation story

Nonlinear isolation

This section fine-tunes the previous section by using nonlinear behavior of the isolation system instead of the viscoelastic behavior. The model is as shown in Figure 6.81.

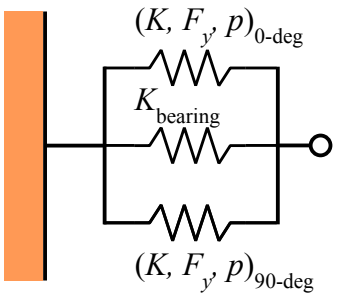

Figure 6.81 Modelling of the isolation system

Since we already all the properties of the bearing and steel dampers, it is possible to construct the isolation model as shown. And the result of one cycle is shown in Figure 6.82(a). It is then further fine-tuned to have a smooth transition from the first stiffness to the second stiffness by using Menegotto-Pinto model. The result of one cycle is shown in Figure 6.82(b).

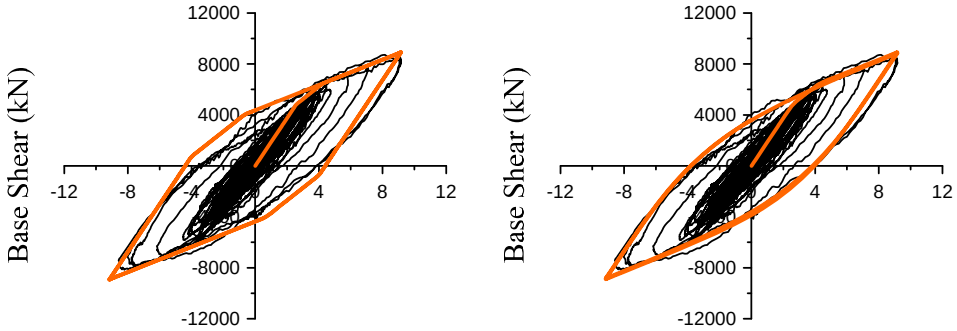

(a) Bilinear (b) Menegotto-Pinto

Figure 6.82 Modelling of the isolation system

The same input accelerations used in previously will be used. The results are shown in Figure 6.83 and 6.84 for the displacement and acceleration response histories, respectively. Overall, the responses from this simple model show good agreement with the recorded data. Figure 6.85 shows the envelope responses. Figure 6.86 shows the base shear-displacement hysteresis in the isolation story. The hysteresis shows very good agreement with the recorded data. This nonlinear model will be used for further investigation.

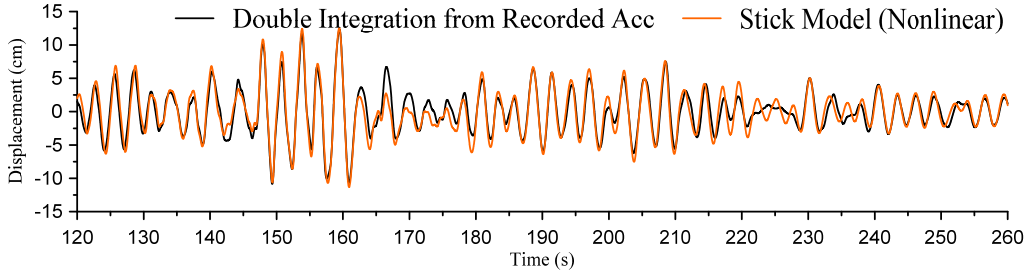

(a) 7th floor

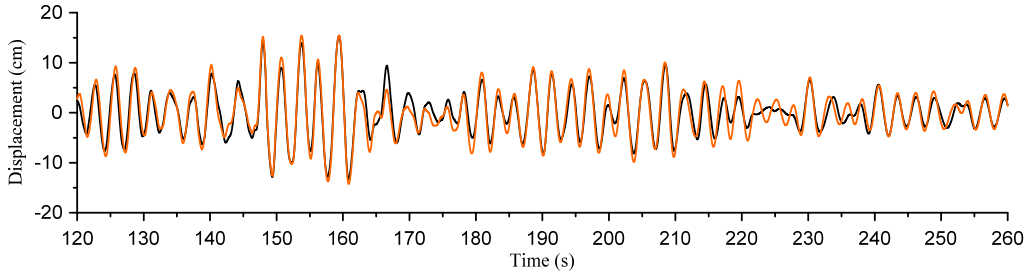

(b) 14th floor

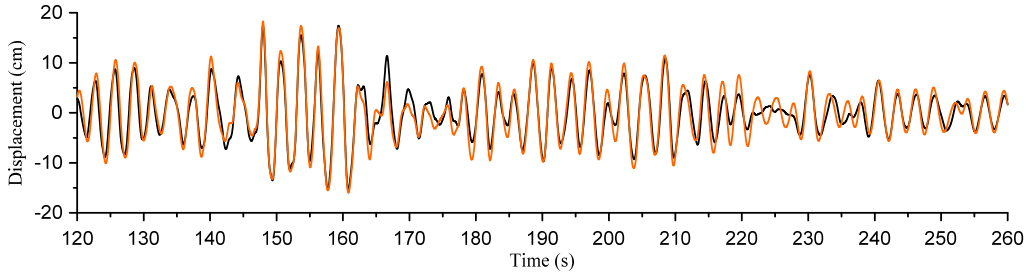

(c) 20th floor

Figure 6.83 Floor displacement relative to the 2nd floor

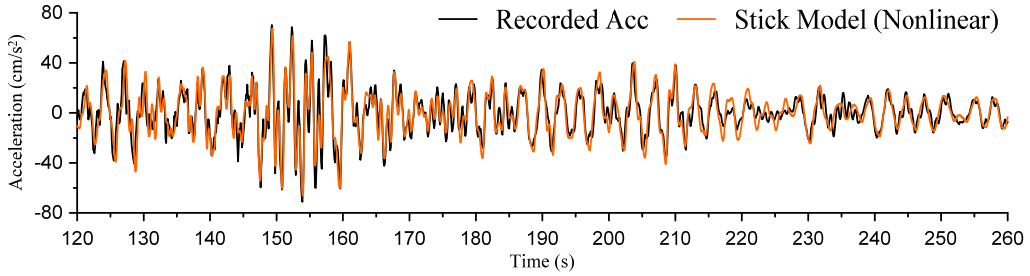

(a) 7th floor

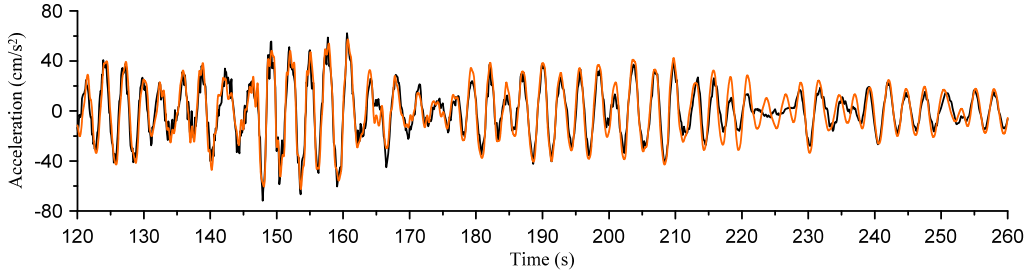

(b) 14th floor

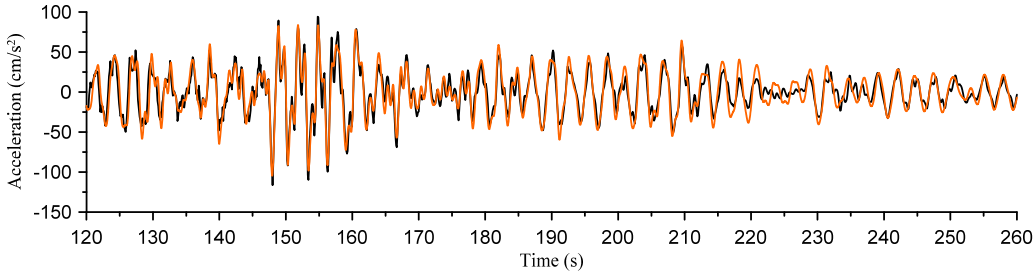

(c) 20th floor

Figure 6.84 Absolute floor acceleration

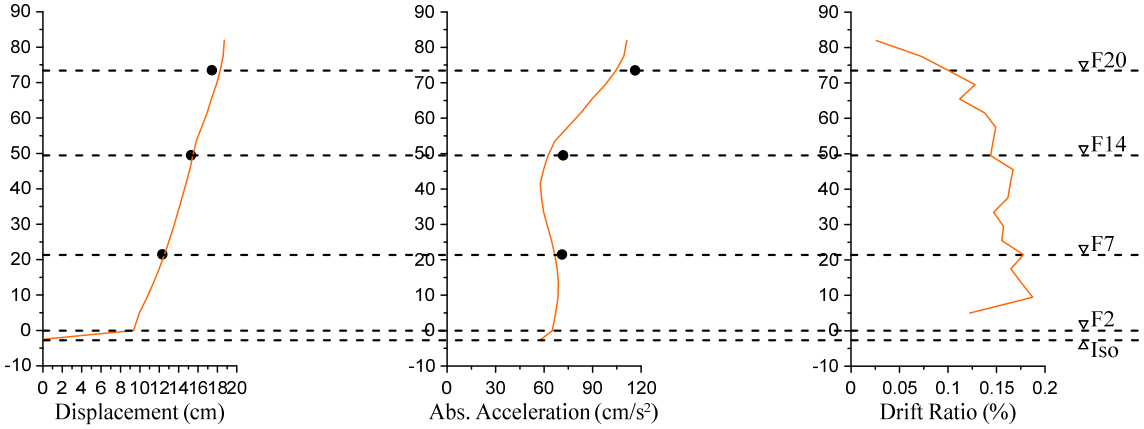

Figure 6.85 Envelope responses

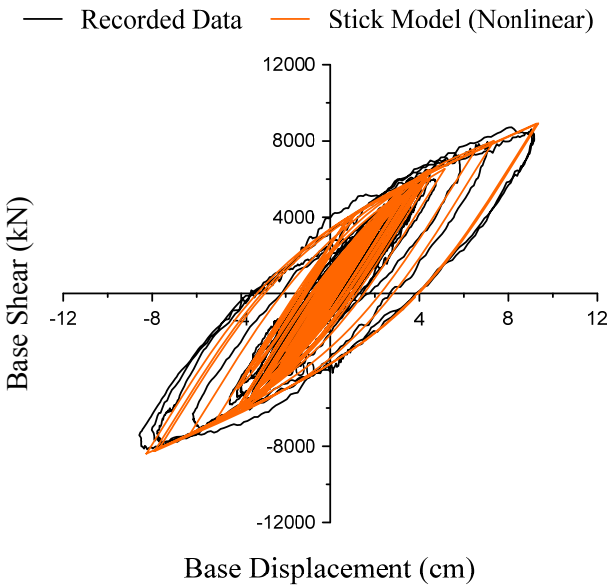

Figure 6.86 Base shear-displacement hysteresis in the isolation story

6.6.3 Response of the Shear Model of J2 Base-Isolated Structure

The same six ground motions defined earlier will be used for investigation. Since the shear model is a single direction model, the total ground motions used for analyses will be 12. The displacement and acceleration responses obtained from the shear model will be compared with those obtained the full 3D frame model. The response history comparisons are shown in Figures 6.87 – 6.92. The results show very good agreement between the 3D frame model and the shear model in all cases.

The envelope responses are then compared as shown in Figures 6.93 – 6.96. It can be observed that the maximum displacement can be captured very well in almost all cases. The maximum drift ratios also show good agreement with the frame model. And maximum floor accelerations are shown to be excellent. They are very close to the frame model in all cases of ground motions. Figure 6.97 shows the median of the envelope response from all twelve ground motions. As shown in the figure, the responses from the shear model match very well with the 3D frame model.

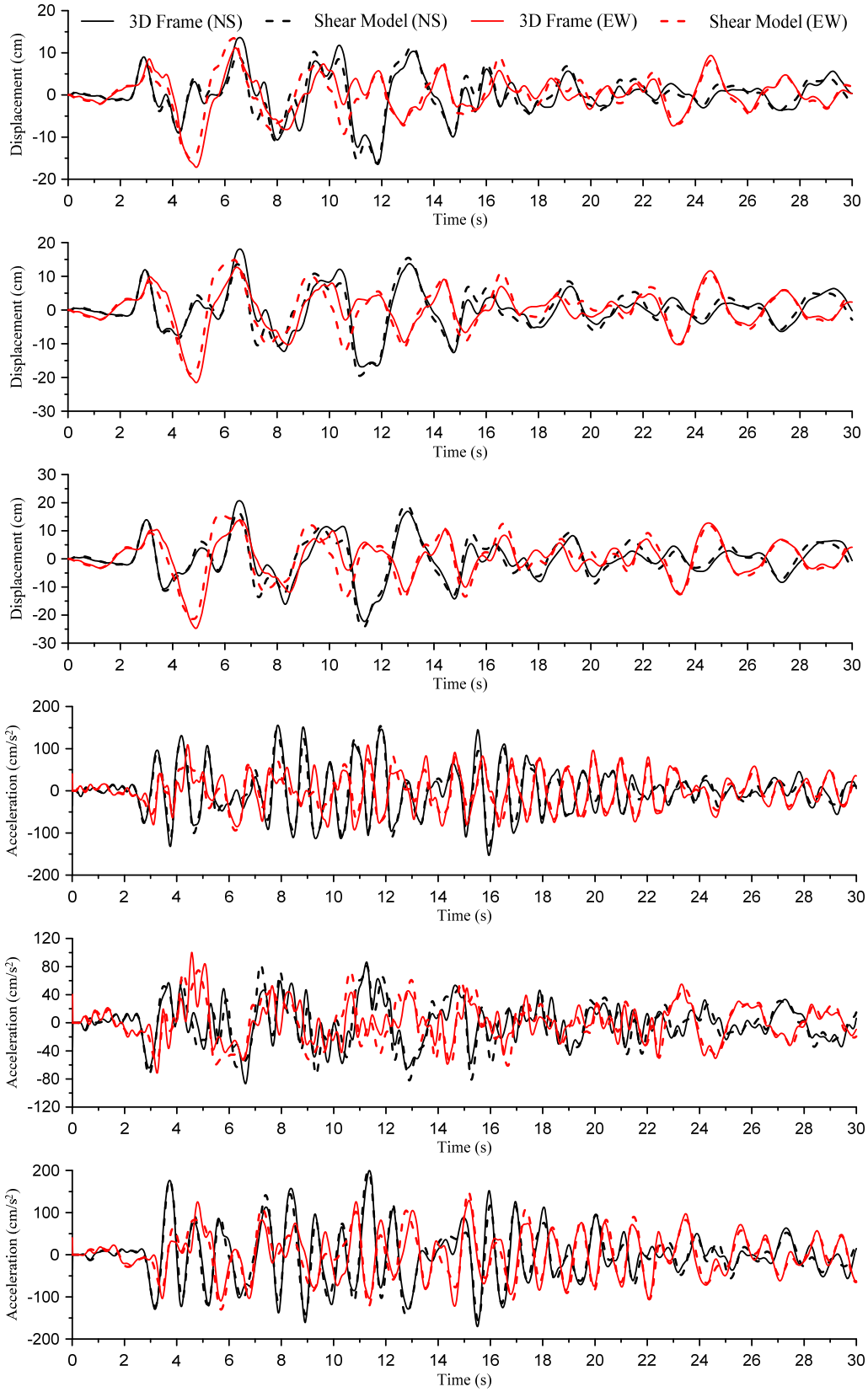

Figure 6.87 Comparison between 3D frame and shear models, first three and last three are displacements and accelerations in the 7th, 14th, and 20th floors, respectively (Tohoku U)

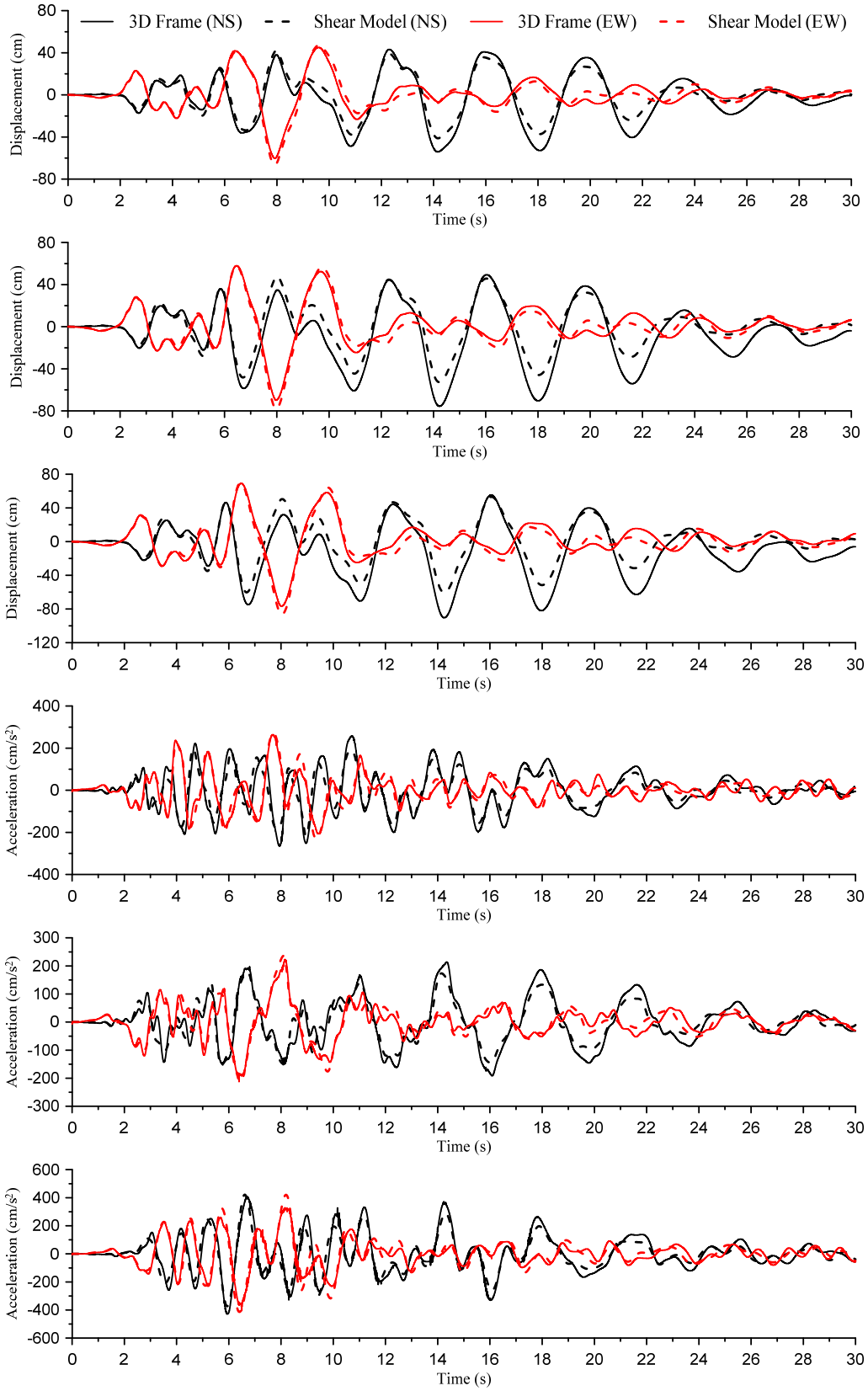

Figure 6.88 Comparison between 3D frame and shear models, first three and last three are displacements and accelerations in the 7th, 14th, and 20th floors, respectively (Takatori)

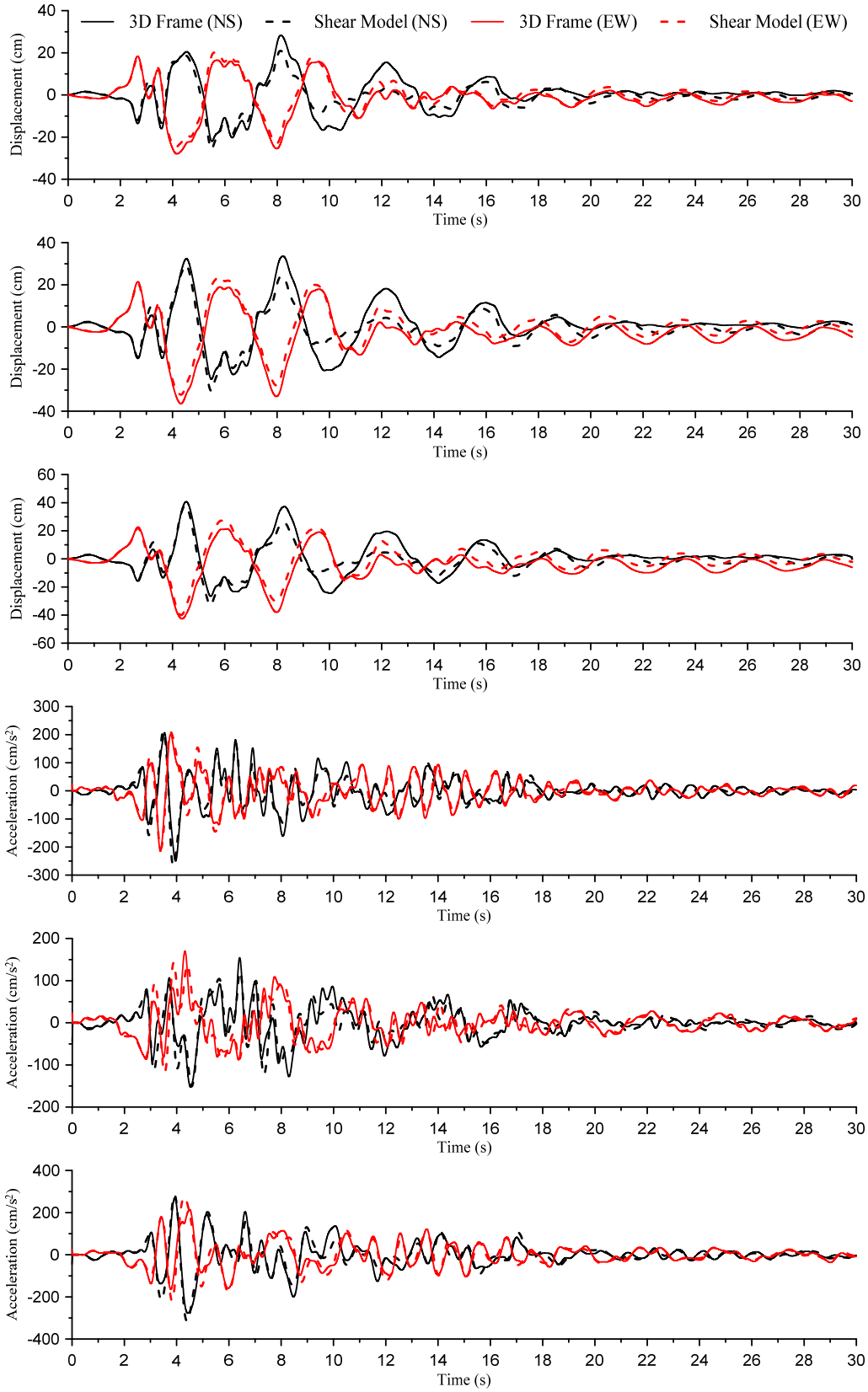

Figure 6.89 Comparison between 3D frame and shear models, first three and last three are displacements and accelerations in the 7th, 14th, and 20th floors, respectively (JMA Kobe)

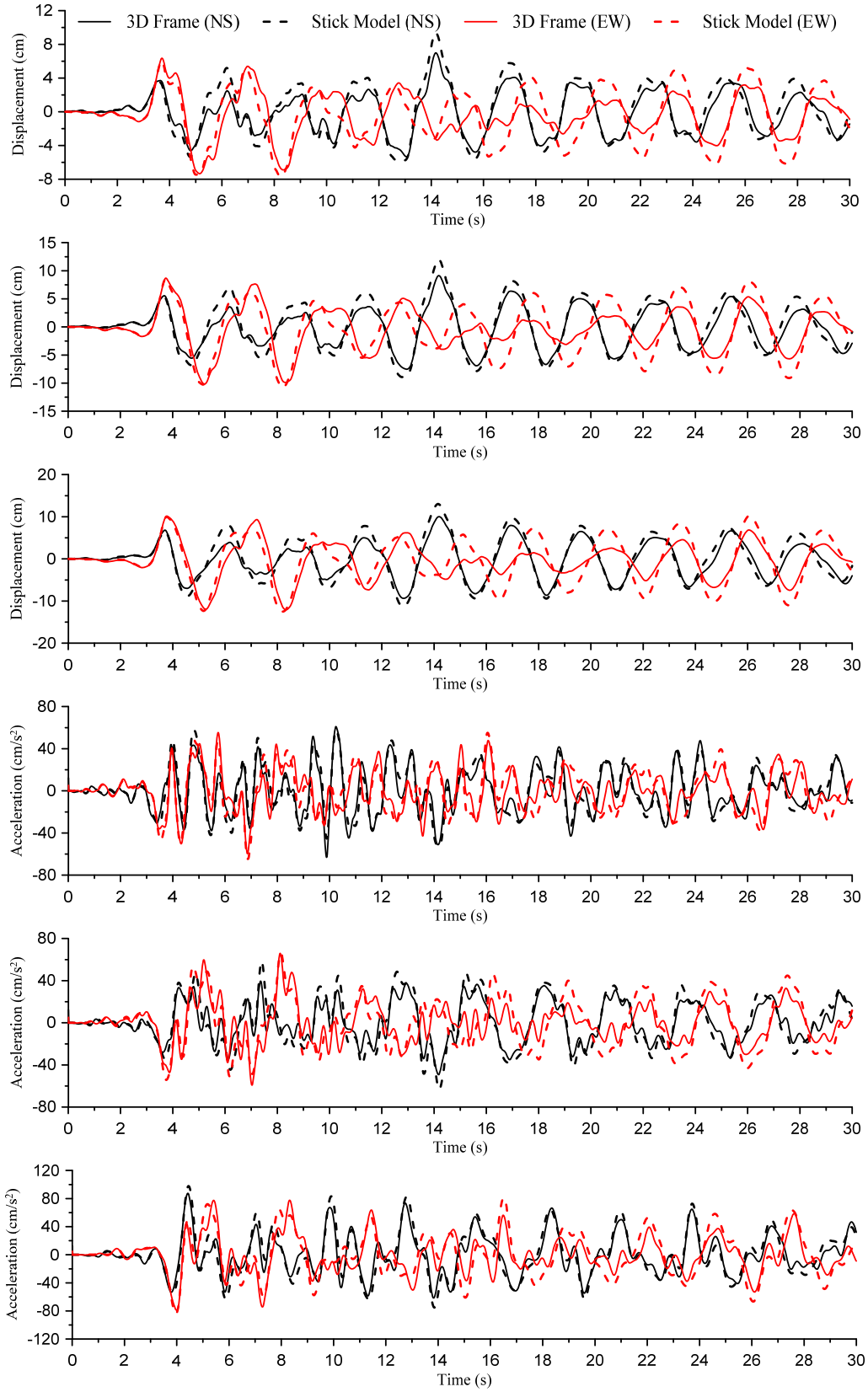

Figure 6.90 Comparison between 3D frame and shear models, first three and last three are displacements and accelerations in the 7th, 14th, and 20th floors, respectively (Taft)

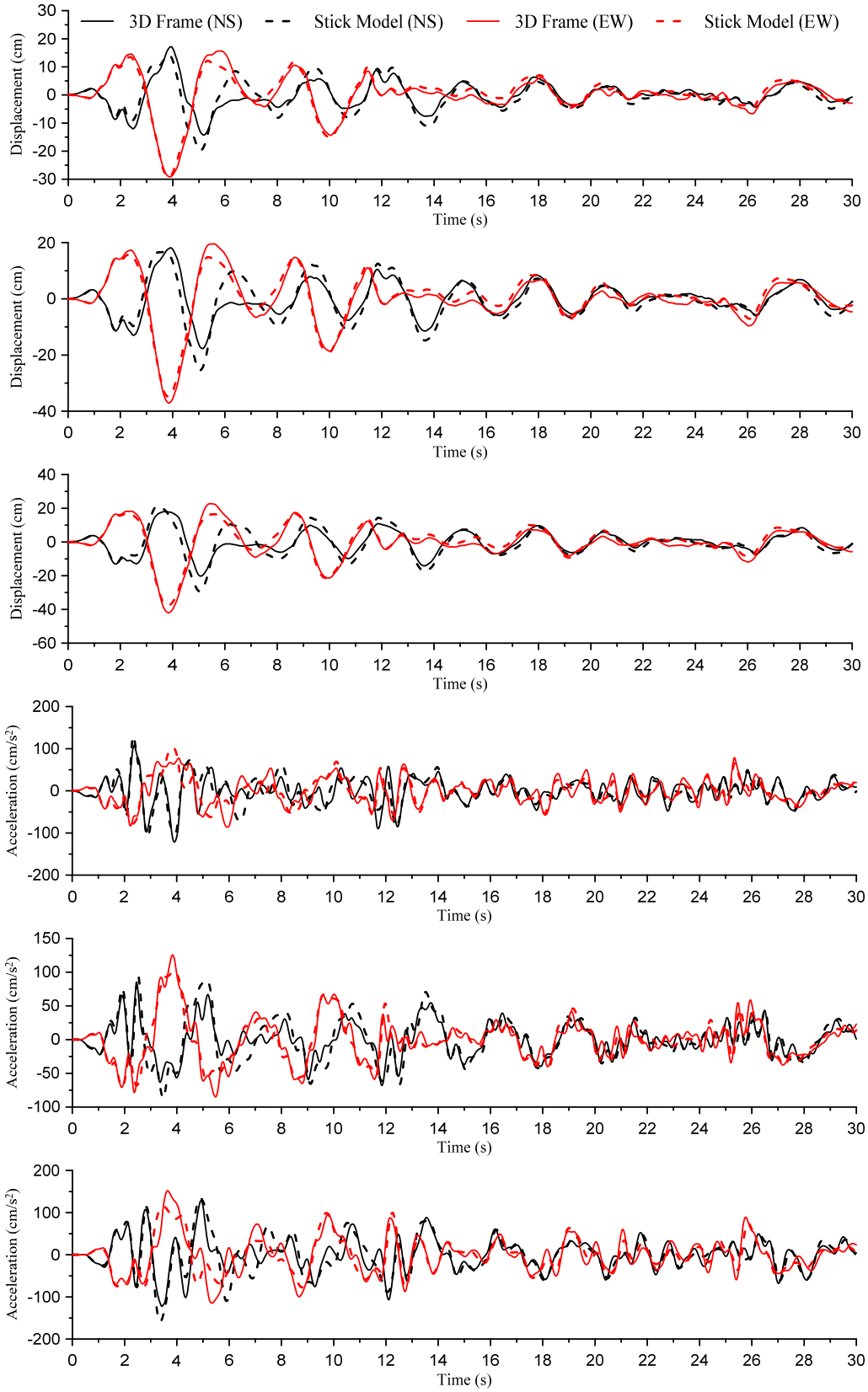

Figure 6.91 Comparison between 3D frame and shear models, first three and last three are displacements and accelerations in the 7th, 14th, and 20th floors, respectively (El Centro)

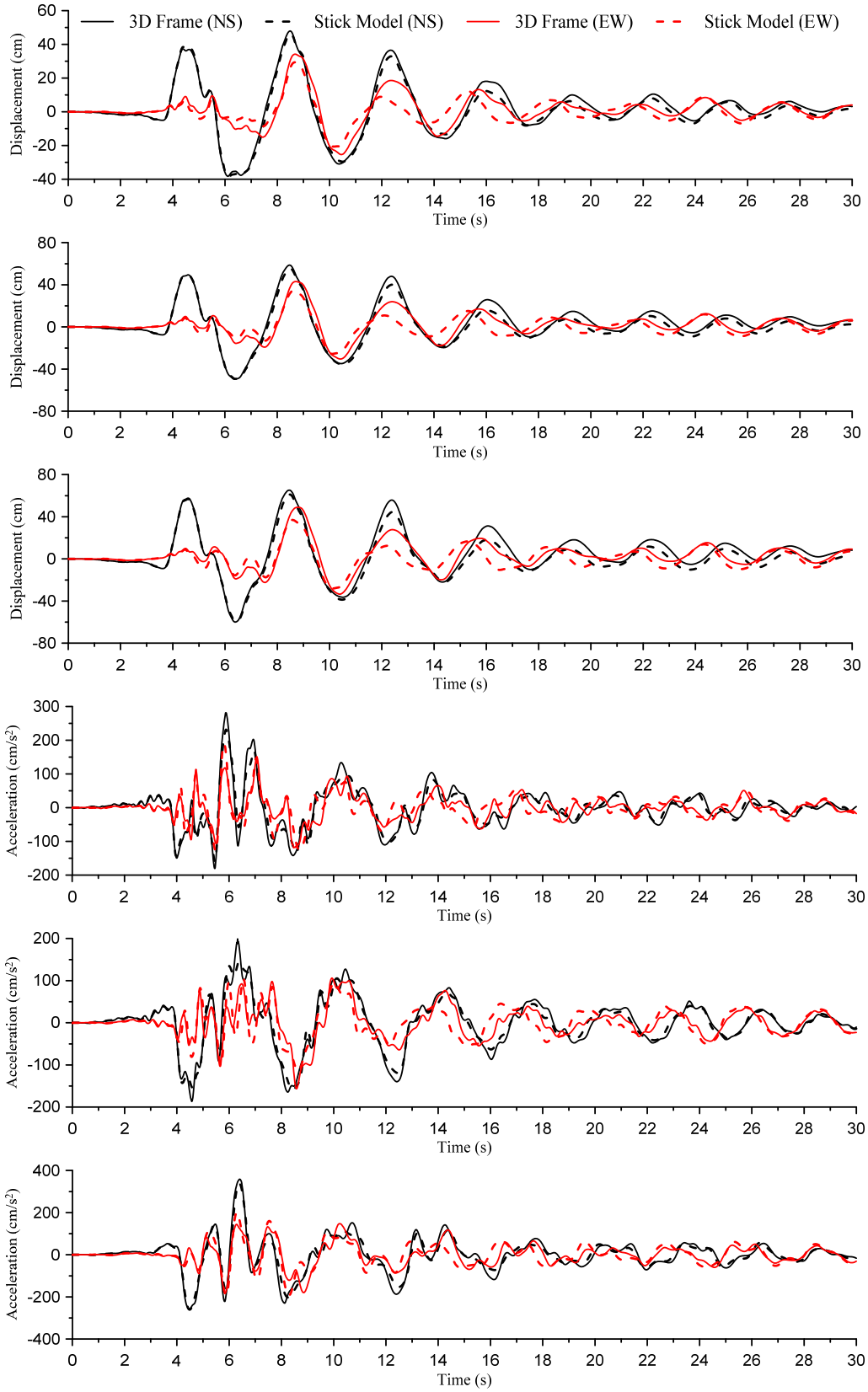

Figure 6.92 Comparison between 3D frame and shear models, first three and last three are displacements and accelerations in the 7th, 14th, and 20th floors, respectively (New Hall)

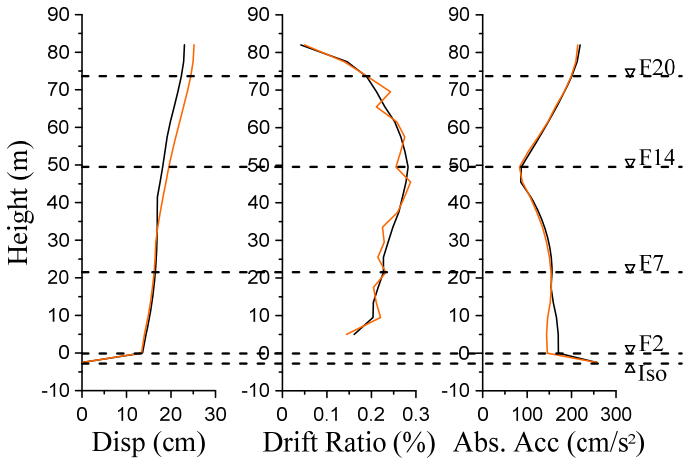

(a) Tohoku U (NS)

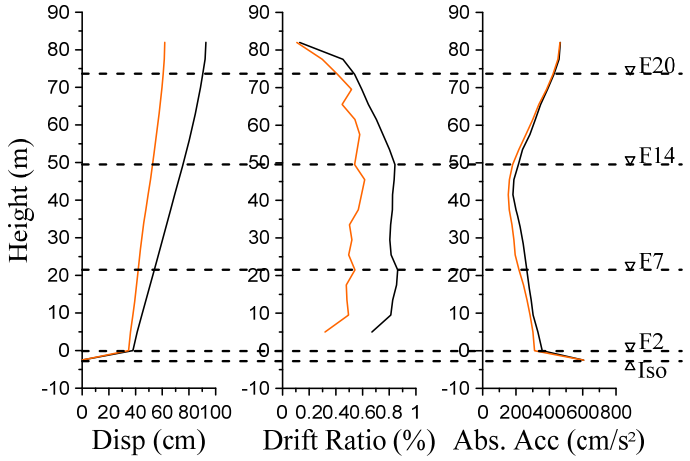

(b) Takatori (NS)

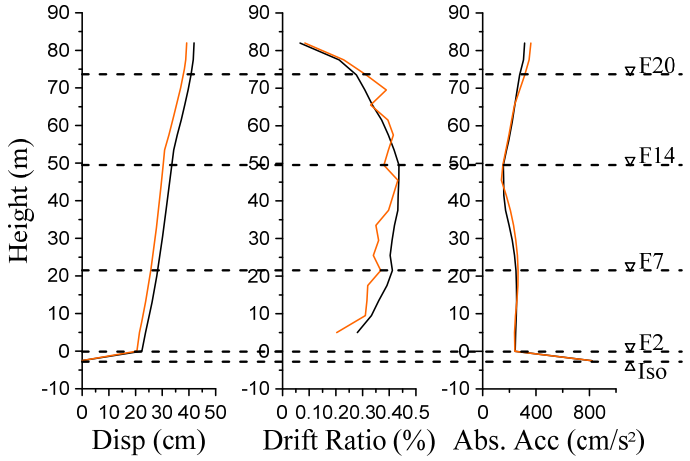

(c) JMA Kobe (NS)

Figure 6.93 Envelope response comparison between

3D frame model (black line) and shear model (orange line)

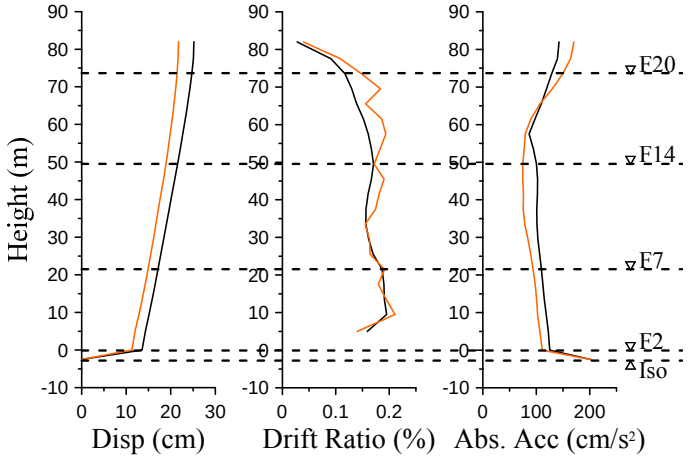

(a) Tohoku U (EW)

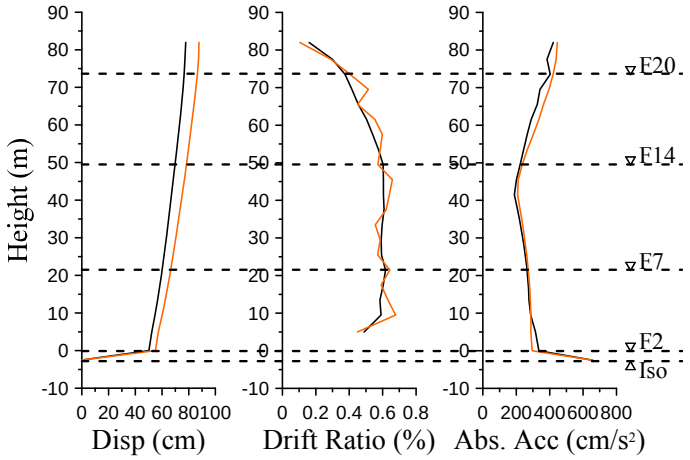

(b) Takatori (EW)

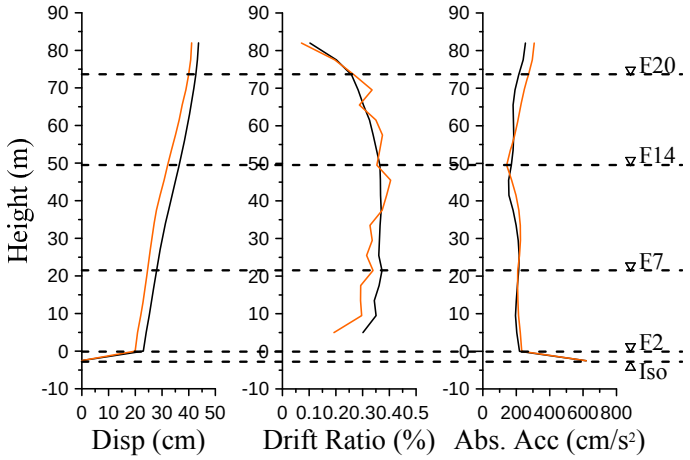

(c) JMA Kobe (EW)

Figure 6.94 Envelope response comparison between

3D frame model (black line) and shear model (orange line)

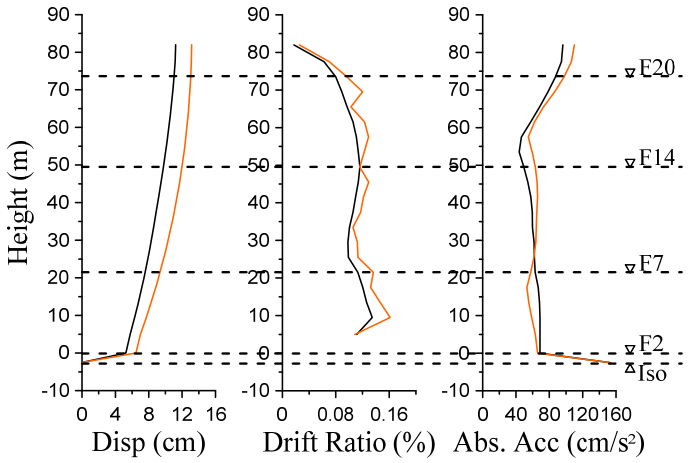

(a) Taft (NS)

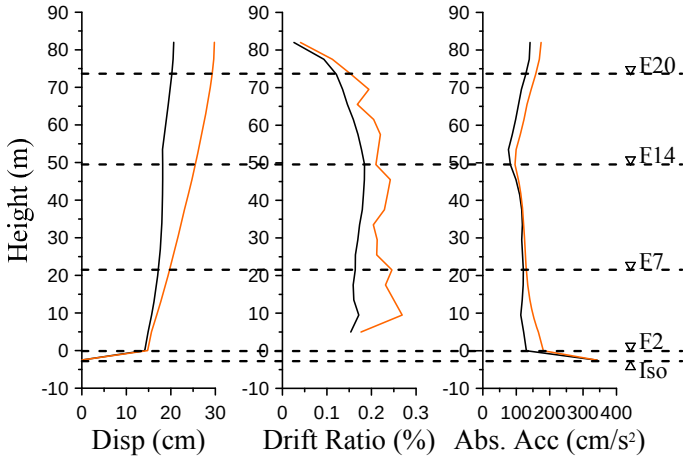

(b) El Centro (NS)

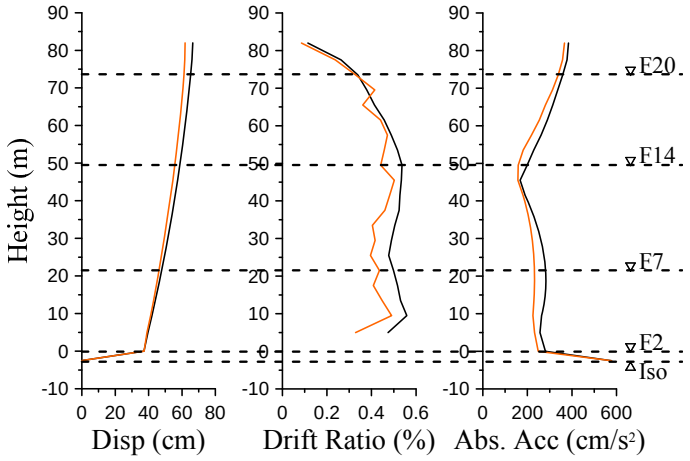

(c) New Hall (NS)

Figure 6.95 Envelope response comparison between

3D frame model (black line) and shear model (orange line)

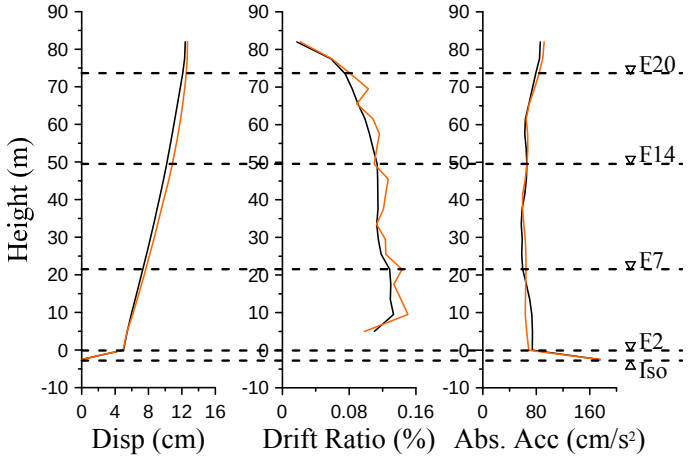

(a) Taft (EW)

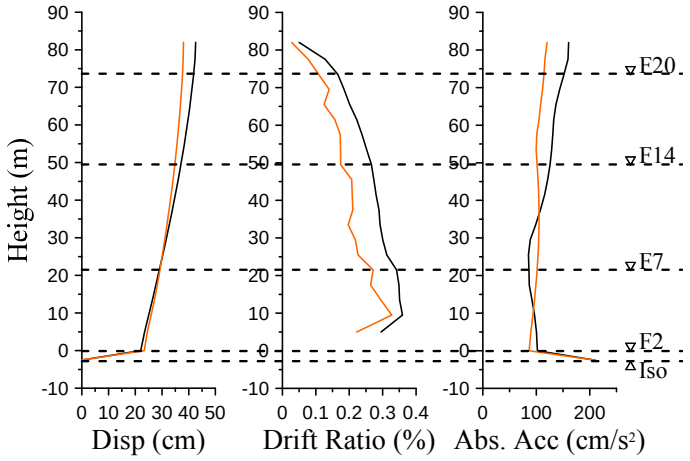

(b) El Centro (EW)

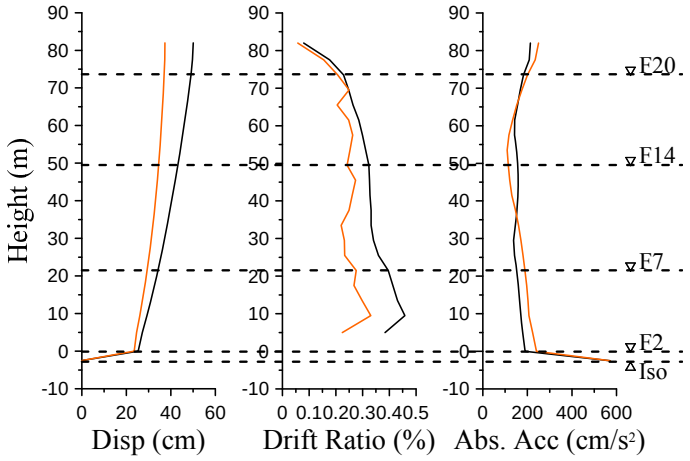

(c) New Hall (EW)

Figure 6.96 Envelope response comparison between

3D frame model (black line) and shear model (orange line)

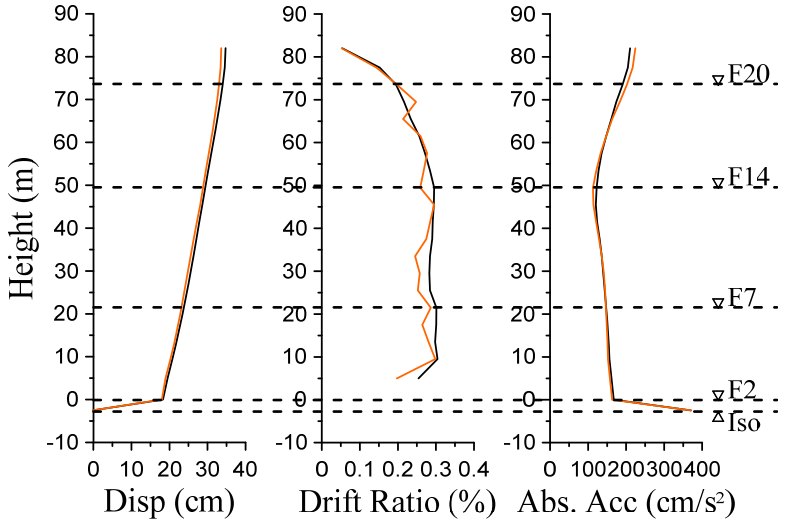

Figure 6.97 Median envelope response comparison between 3D frame model (black line) and shear model (orange line)

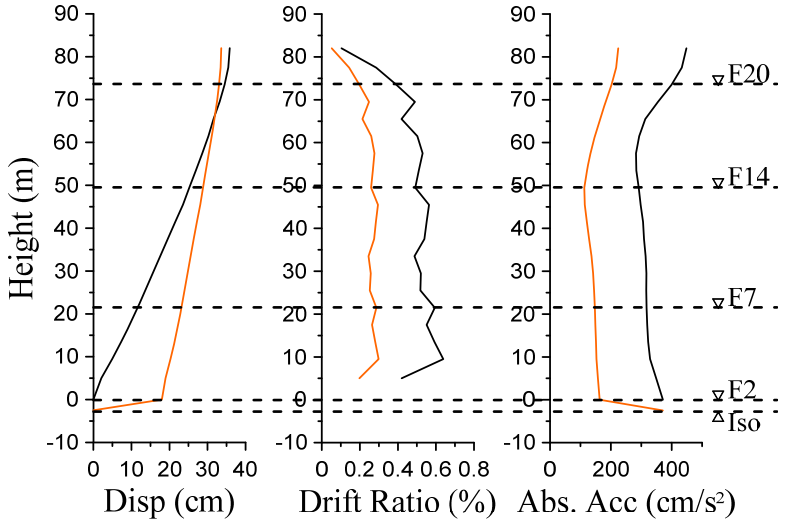

Figure 6.98 Median envelope response comparison between superstructure (black line) and base-isolated structure (orange line)

Figure 6.98 shows the comparison between the median responses of the superstructure part only (using the model from Section 6.6.1) and the whole base-isolated structure under the same 12 ground motions. This shows clearly the effects of the isolation system of the J2 base-isolated building. From Figures 6.87 – 6.97, these results shows very good agreement between

shear model and frame model, which proves the validity of the stick models as well as the results which have been described in the previous chapters.

6.7 Use of Probabilistic and Time-Based Approach

6.7.1 Application of the framework

Previously in Chapter 4, the PEER PBEE framework which is based on probabilistic approach was described. The framework can be divided into three different types of performance assessment: intensity-based assessment, scenario-based assessment, and time-based assessment. This research utilized the time-based assessment which is most rigorous. In order to apply the framework to the J2 building, some assumptions are made as follows.

According to the derivation described earlier in Section 4.1.1, hazard curve, structural analysis, and damage analysis are necessary. For the hazard curve, it is obtained based on the location of the building. In this study, it is assumed that the hazard curves for the J2 building which is located in Suzukakedai campus, Tokyo Institute of Technology are the same as the hazard curves for the Los Angeles area used in Chapter 4. In other words, it is assumed that the J2 building was located in the Los Angeles area. Therefore, the hazard curves used previously in Chapter 4 will be used in this section.

Next part is the incremental dynamic analysis (IDA). The ground motions used for time history analyses are the same as those used previously which are the SAC ground motions (LA21 – LA40). In the IDA, the ground motions need to be scaled from very small intensity to large intensity to cover a wide range of possibilities of ground motion occurrence. Since the ground motions are scaled, that means if the response spectra of the SAC ground motions have similar shape with the Japan design response spectra, then they can be used for the time history analyses. Figure 6.99 shows the comparison between the US and JPN response spectra. For Japan, BCJ-L2 ground motion is used for comparison. As can be seen in the figure, the spectral accelerations of BCJ-L2 match very well with those of the US design spectra. Only at short periods, spectral accelerations from BCJ-L2 are higher than those of the US ground motions. However, this region is not important since base-isolated structures usually have very long

fundamental periods. Therefore, these SAC ground motions is utilized for the purpose of performance evaluation. Also, since IDA is time consuming, it is not convenient to use the full frame model for analysis. In this study, the shear model for the J2 base-isolated building developed in the previous section will be used for investigation.

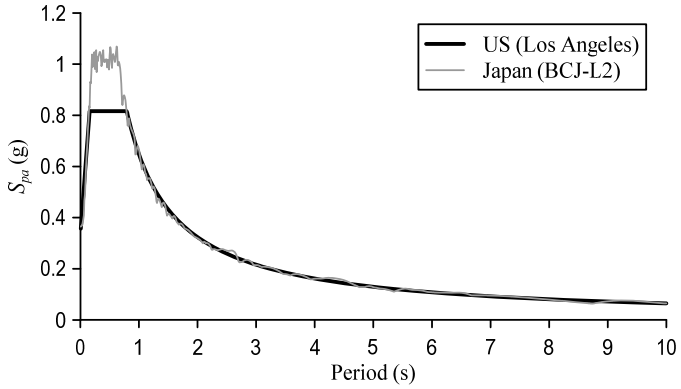

Figure 6.99 Response spectra (h = 0.05) comparison between US (Los Angeles area) and Japan (BCJ-L2)

The last part is the damage analysis from the nonstructural components. The fragility functions for the partition wall and the suspended ceiling used in Chapter 4 are also used in this section for performance evaluation. However, the fragility function of the partition wall which was developed based on the wall configuration used in the US may not be appropriate for representing the partition wall used in Japan. Therefore, sensitivity of the performance to the fragility functions will also be conducted for comparison. Figures 6.100 and 6.101 show the fragility functions of the partition wall and suspended ceiling, respectively, used in this section.

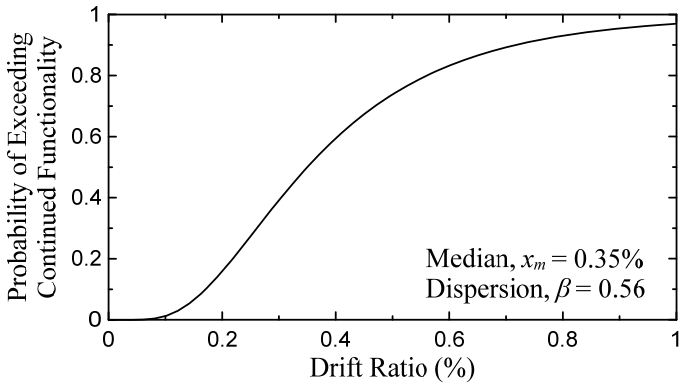

Figure 6.100 Fragility function of the considered partition wall

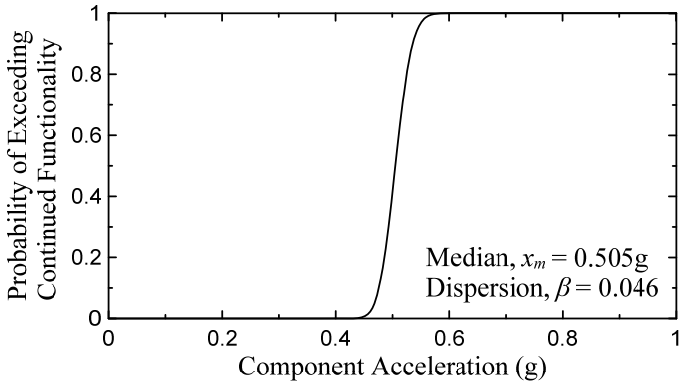

Figure 6.101 Fragility function of the considered suspended ceiling

6.7.2 Performance evaluation results

Using the PEER methodology with time-based approach described in the previous section, the results of the performance or return periods are shown in Figure 6.102. As shown in Figure 6.102(a), the return periods considering the partition wall's continued functionality are approximately 30 years. This indicates that in approximately 30 years, some partition walls in the building may be damaged such that they need to be replaced or fixed which will cause disruption of the building's continued functionality. However, it may be noted that the fragility function of the partition wall used in the evaluation is adopted from the partition wall in the US which may not correctly represent the behavior of the typical partition wall in Japan. In the next section, the sensitivity of the return period to the fragility function will be discussed.

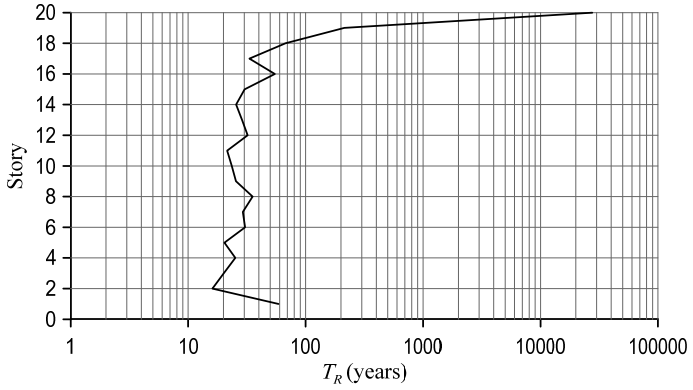

(a) T_R considering partition wall

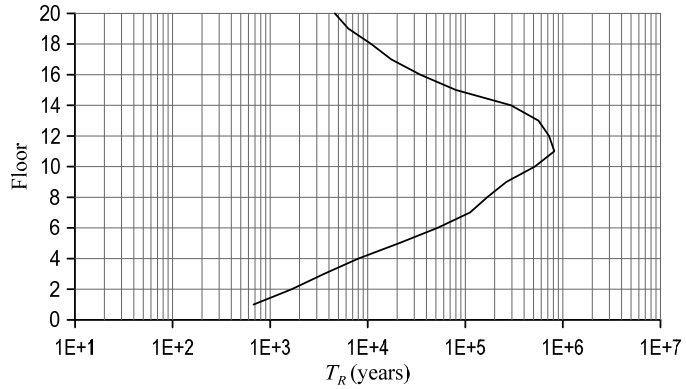

(b) T_R considering suspended ceiling

Figure 6.102 Return periods T_R considering (a) partition wall and (b) suspended ceiling

In Figure 6.102(b), the return periods T_R considering the suspended ceiling's continued functionality appear to be around 700 years at the first floor which is lowest. This fragility function of the suspended ceiling used here is the Japanese ceiling. Therefore, this indicates that for J2 building, it will be approximately 700 years until the suspended ceiling would fall due to very strong earthquake.

In the US, to avoid pounding of the base floor to adjacent buildings or moat wall, the clearance distance to accommodate the base displacement is designed against MCE level of ground motions which corresponds to a 2475-year event. And there is no such limitation on the maximum clearance distance to save usage of the space. However, in Japan, unlike the US practice, the maximum base displacement is usually limited to 50 cm. to avoid pounding.

Therefore, in order to apply the knowledge of this PEER methodology, the fragility function for the clearance distance can be constructed as shown in Figure 6.103(solid line). The figure can be interpreted that if the base displacement is less than 50 cm., then the probability of exceeding this limit is 0 meaning that it never exceeded. But if the base displacement is greater than or equal to 50 cm., then the probability of exceeding this limit is 1.0 meaning that it's already and surely exceeded. If we consider the base displacement limit to 50 cm. only, then the return period considering only that 50 cm. will be obtained. In order to observe that trend and use the results for design purpose, several fragility functions can be varied as shown in Figure 6.103(dashed lines), and then the performance evaluations are conducted based on these base displacements. The results of the return periods considering base displacement limit are shown in Figure 6.104. As shown in the Figure 6.104, if we consider the limit at 50 cm. meaning that for this J2 building if we allow the base displacement to move up to 50 cm., the building will not pound for at least 1000 years. Also from Figure 6.104, it can be also used for design purpose, for instance, if we want to make sure that the building will not pound for 100 years, that means only provision of approximately 25 cm. of clearance distance is sufficient.

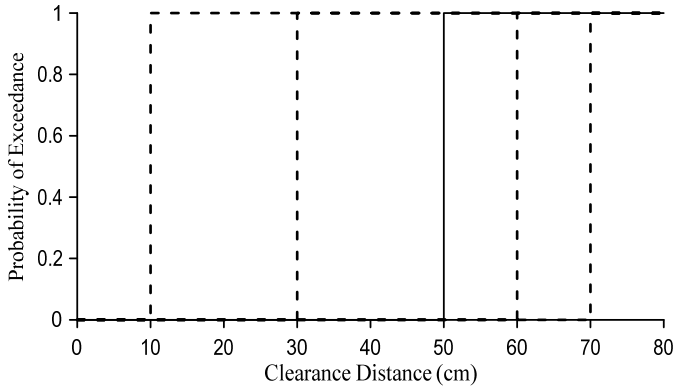

Figure 6.103 Several fragility functions for the base displacement

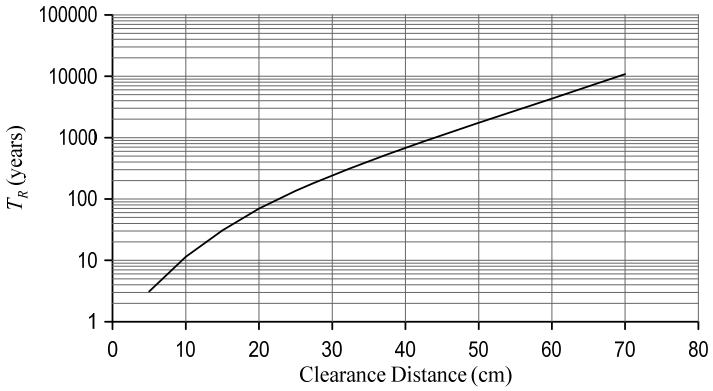

Figure 6.104 Return period T_R considering the base displacement

6.7.3 Sensitivity of performance to fragility functions

As discussed previously that the fragility function of the partition wall may not correctly represent the partition wall in Japan, fragility functions with various medians x_m and dispersions β are constructed and used for performance evaluation in this section. Originally, the median x_m and dispersion β for the partition wall are 0.35% and 0.56, respectively. The median x_m is varied as follows: x_m = 0.2%, 0.3%, 0.35%, 0.4%, and 0.5%. And the dispersion β is varied as follows: β = 0.1, 0.2, 0.3, 0.4, 0.56, and 0.7. The results of the return periods are shown in Figure 6.105. In Figure 6.105(a), it can be seen that compared with the original x_m of 0.35%, if the median x_m is reduced to 0.2% (≈0.57 times 0.35%), the return period T_R will be approximately 6 years (≈0.2 times 30 years). On the other hand, if the median x_m is increased to 0.5% (≈1.43 times 0.35%), the return period T_R will be approximately 80 years (≈2.67 times 30 years).

Figure 6.105(b) shows the results of return periods by varying dispersion. Compared with the original β of 0.56, if the dispersion β is increased to 0.7 (1.25 times 0.56), the return period T_R will be approximately 14 years (≈0.47 times 30 years). On the other hand, if the dispersion β is reduced to 0.1 (≈0.18 times 0.56), the return period T_R will be approximately 200 years (≈6.67 times 30 years).

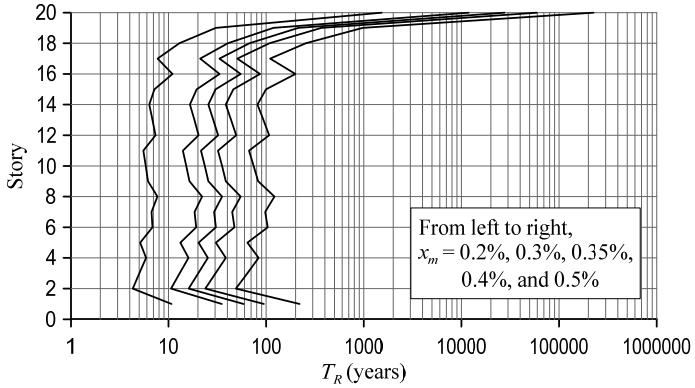

(a) Sensitivity of return period T_R to median x_m for partition wall

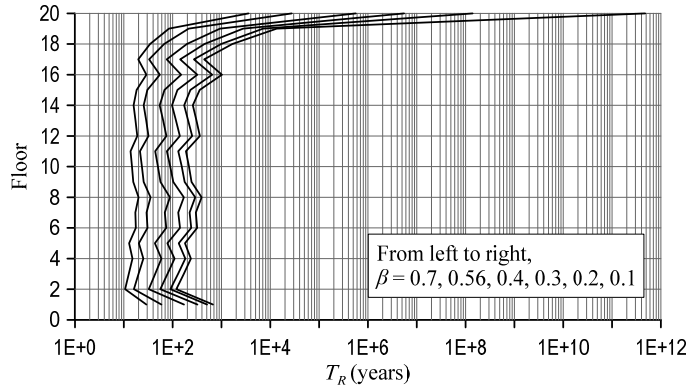

(b) Sensitivity of return period T_R to dispersion β for partition wall

Figure 6.105 Sensitivity of return T_R considering partition wall's continued functionality

Sensitivity of performance considering the suspended ceiling's continued functionality to fragility functions is also investigated. Originally, the median x_m and dispersion β for the suspended ceiling are 0.505g and 0.046, respectively. The median x_m is varied as follows: x_m = 0.3g, 0.4g, 0.505g, 0.6g, and 0.7g. And the dispersion β is varied as follows: β = 0.046, 0.1, 0.2, 0.3, 0.4, and 0.5. The results of the return periods are shown in Figure 6.106. In Figure 6.106(a), it can be seen that compared with the original x_m of 0.505g, if the median x_m is reduced to 0.3 (≈0.6 times 0.505g), the return period T_R will be approximately 70 years (≈0.1 times 700 years). On the other hand, if the median x_m is increased to 0.7g (≈1.39 times 0.505g), the return period T_R will be approximately 5000 years (≈7.14 times 700 years).

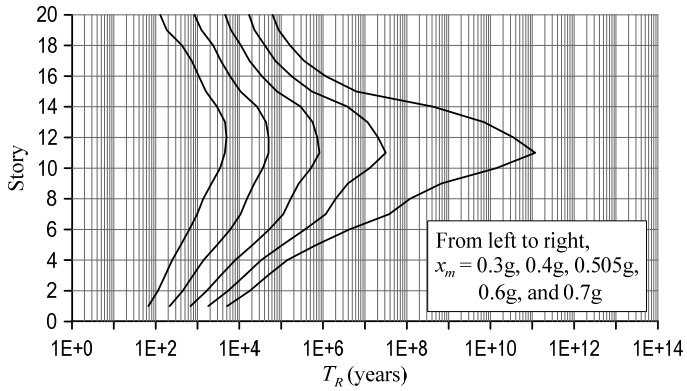

(a) Sensitivity of return period T_R to median x_m for suspended ceiling

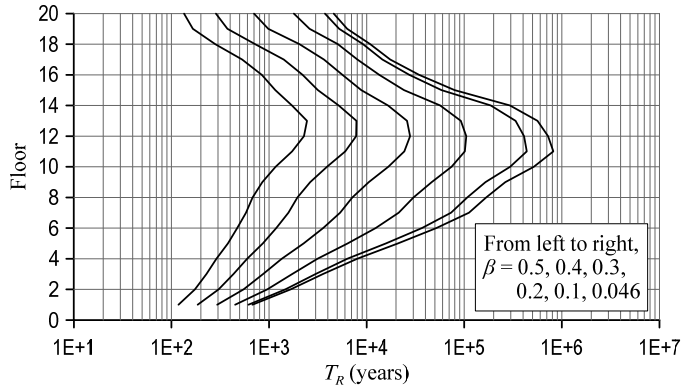

(b) Sensitivity of return period T_R to dispersion β for suspended ceiling

Figure 6.106 Sensitivity of return T_R considering suspended ceiling's continued functionality

Figure 6.106(b) shows the results of return periods by varying dispersion. Compared with the original β of 0.046, if the dispersion β is increased to 0.5 (≈12.17 times 0.046), the return period T_R will be approximately 110 years (≈0.16 times 700 years).

6.8 Use of Deterministic and Simplified Approach

From the recorded data of the J2 base-isolated building under March 11 Tohoku Earthquake, the analysis of the 3D sophisticated model of the building has been verified in Section 6.4.3. And from the sophisticated model, it was converted to a simple shear model in Section 6.6. And the response of the J2 building from the shear model has also been verified

and shown to be very accurate. Therefore, in this section, the responses from the shear model will be used for investigation.

6.8.1 Property determination

In order to use the performance curve developed earlier in Chapter 5 which is simplified and deterministic, basic properties of the buildings, which are isolation period, isolation damping ratio, superstructure period, and superstructure damping ratio, must be known. For this J2 building, as shown in Table 6.7, the superstructure period T_s is 2.172 seconds. Also according the system identification by (Kazuhiro MATSUDA and Kazuhiko KASAI, 2014), the superstructure damping ratio h_s is 0.046. However, for the isolation system, since the isolation behavior is nonlinear, isolation period T_{eff} and isolation damping ratio h_{eff} change according to the base displacement. Since the isolation period and isolation damping ratio used the methodology described in Chapter 5 was defined with the rigid superstructure, T_{eff} and h_{eff} will be obtained with rigid superstructure as described in the following.

Figure 6.107(left) shows the base isolation hysteresis response of the J2 base-isolated building under March 11 Tohoku Earthquake together with a bilinear behavior representation with post-yield stiffness p = 0.3 and yield displacement is 3.17 cm. according to the design value. From this figure, it is possible to determine the effective isolation period T_{eff} and effective damping ratio h_{eff} assuming rigid superstructure if the total mass is known. From Table 6.13, we know the mass for each floor in the superstructure, and the base mass is also known and equal to 18.989 kN.s^2/cm. Hence, the total mass M_{total} can be obtained by summation of the mass in all floors and is equal to 166.922 kN.s^2/cm. And K_{eff} can be obtained simply from Figure 6.107(right). Therefore, the effective isolation period T_{eff} can obtained from $T_{eff} = 2\pi\sqrt{M_{total} / K_{eff}}$ and is equal to 2.62 seconds.

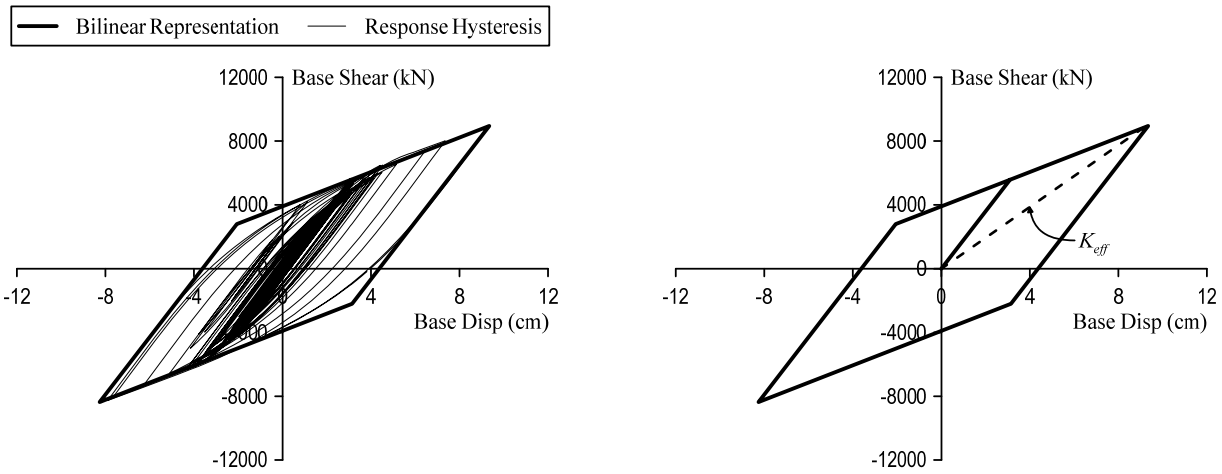

Figure 6.107 Hysteresis response of the J2 base story under March 11 Tohoku Earthquake

As explained in Chapter 5, Section 5.4.2, average damping will be used and the equation is shown again here as follows.

$$h_{eff} = \frac{2}{\mu\pi p} \cdot \ln\left(\frac{1-p+p\mu}{\mu^{p}}\right) \tag{6.15}$$

The effective damping ratio estimated from the average damping equation is $h_{eff} = 0.10$. The effective isolation period T_{eff} and effective damping ratio h_{eff} estimated from this section will be used to predict the response in the next section.

6.8.2 Response prediction

For time history analysis, the response envelope of the building is shown in Figure 6.108. From Figure 6.108, u_b is equal to 9.35 cm and and u_s is obtained at the 2/3 height of the building which is equal to 6.64 cm. Note that u_s is relative to the base floor. And u_{fb} can be obtained from $S_{pv}(T_s, h_s = 0.02) \times T_s / 2\pi$. Figure 6.109 shows the pseudo spectral velocity for the March 11 Tohoku Earthquake. It is assumed that S_{pv} is approximately 50 cm/s from the figure. Therefore, u_{fb} is equal to $50 \times 2.172 / 2\pi = 17.28$ cm. Knowing u_b, u_s, and u_{fb}, then u_b/u_{fb} and u_s/u_{fb} can be obtained. The result is plotted in Figure 6.110 (black dot).

From the previous section, all required properties, $T_{eff}/T_s = 2.62/2.172 = 1.21$ and $h_{eff} = 0.10$ are known, it is possible to predict u_b/u_{fb} and u_s/u_{fb} as described in Chapter 5. The prediction is plotted in Figure 6.110 (white dot). It can be seen that the result from the proposed equations is very close to that of the time history analysis result.

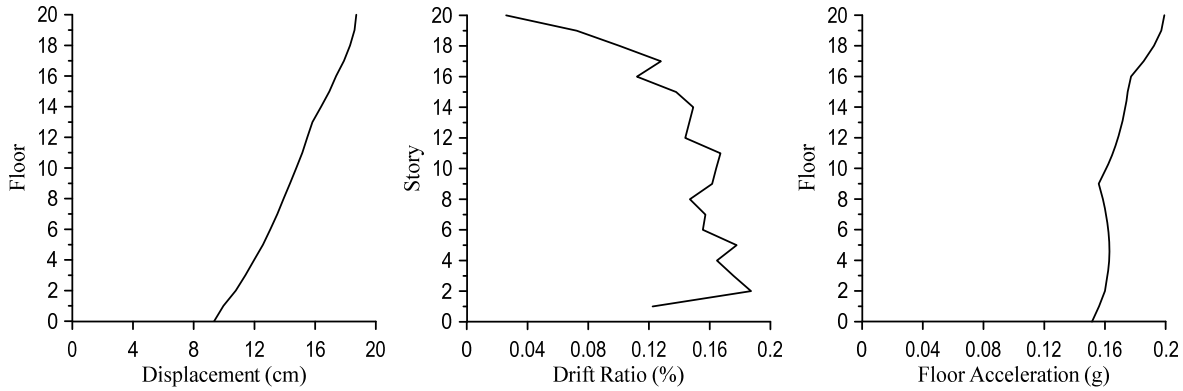

Figure 6.108 Response envelopes under March 11 Tohoku Earthquake

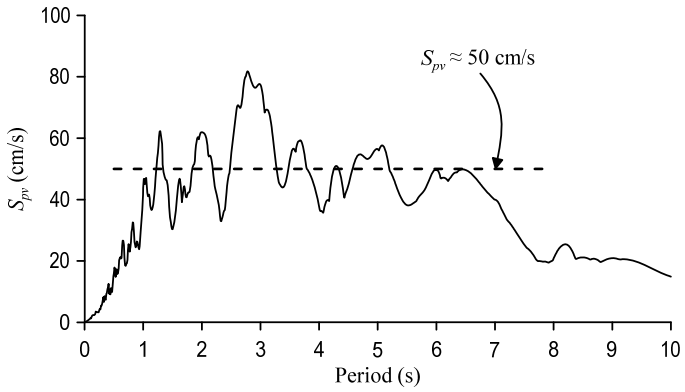

Figure 6.109 Pseudo spectral velocity for March 11 Tohoku Earthquake

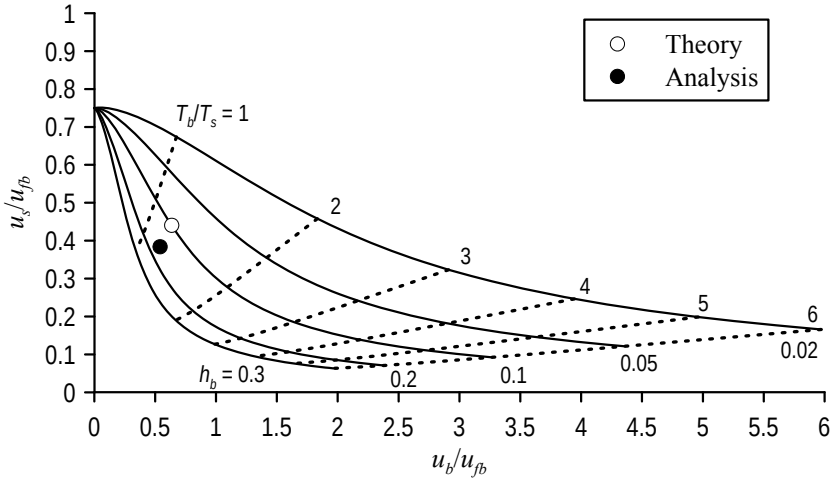

Figure 6.110 Response prediction of J2 building under March 11 Tohoku Earthquake

In order to verify with more cases, in addition to the March 11 Tohoku Earthquake, artificial ground motions described previously in Chapter 5 are used for investigation. And the ground motions are scaled to three different level of intensities. Originally, the mean spectral velocity for the ground motions are 140 cm/s. In this section, the grounds motions are scaled by 0.5 and 2.0 times additionally in order to represent smaller and larger ground motions which will induce smaller and larger ductility leading to various effective isolation period and effective isolation damping ratio. Figure 6.111 shows the response spectra of the artificial ground motions used in this section.

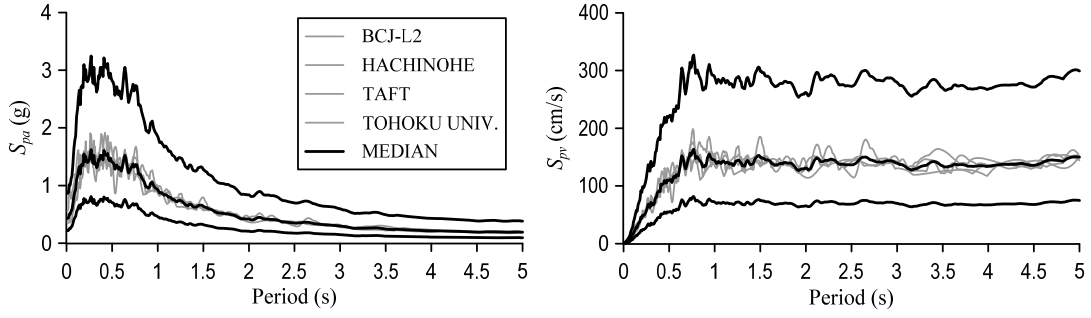

Figure 6.111 Response spectra of the artificial ground motions (h = 0.02)

Figure 6.112 shows the median displacement, story drift ratio, and acceleration response envelopes for the J2 building under the ground motions. It can be seen that for ground motions with S_{pv} = 70 and 140 cm/s, the base displacements are around 13 and 30 cm, respectively, which are still under 50 cm limit. However, if the ground motions are twice larger, S_{pv} = 280 cm/s, the base displacement goes to around 89 cm, which is much larger than 50 cm limit. From the figure, it can also be guessed that if the ground motions were to be 1.5 times stronger, S_{pv} = 210 cm/s, which is equivalent to the MCE level in the US since BCJ-L2 is equivalent to DBE level in the US, the base displacement would go to approximately 60 cm which is also exceeding 50 cm. The story drift ratios at around mid-height of the building go up to around 0.2%, 0.3% and 0.7% for the 0.5x, 1.0x, and 2.0x ground motions, respectively. The peak floor accelerations at around mid-height of the building go up to around 0.1g, 0.15g, and 0.3g, respectively.

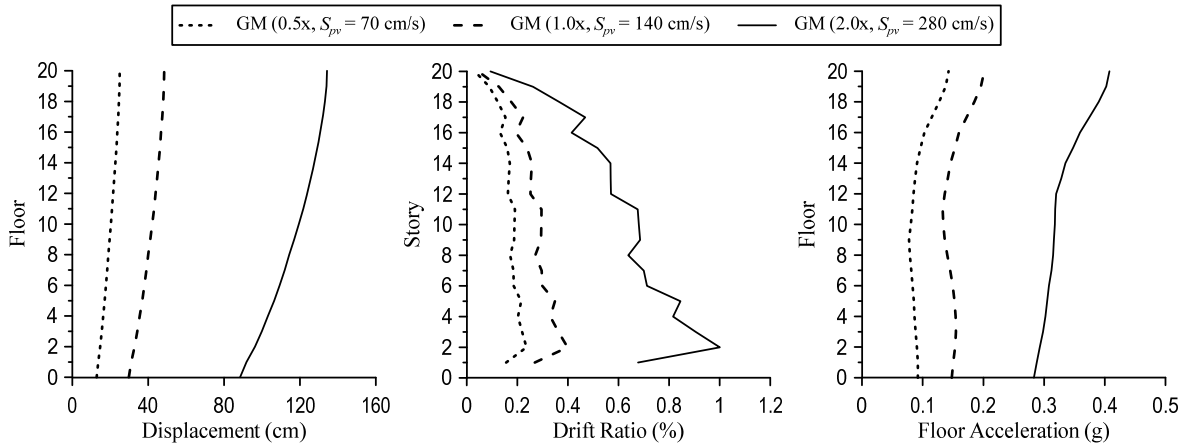

Figure 6.112 Response envelopes under the ground motions

From the displacement envelopes shown in Figure 6.112, base displacement u_b are known which are 12.89, 29.77, and 88.47 cm. And u_s are also known and obtained at the 2/3 height of the building which are 9.45, 15.20, and 37.80 cm. Note that the superstructure displacements u_s are relative to the base floor, not the ground. Next, u_{fb} are needed in order to calculate u_b/u_{fb} and u_s/u_{fb}. From the assumption of constant velocity, S_{pv} for each ground motion intensity are known. Therefore, u_{fb} can be obtained from $S_{pv}(T_s, h_s = 0.02) \times T_s / 2\pi$ which are

24.20, 48.40, and 96.80 cm, for S_{pv} = 70, 140, and 280 cm/s, respectively. u_b/u_{fb} and u_s/u_{fb} from time history analyses are now obtained and plotted in Figure 6.114 (black dots).

For the prediction of the responses, properties of the J2 buildings are necessary. T_s and h_s are already known previously. However, effective isolation period and effective isolation damping ratio changes according to ground motion. So, they need to be obtained for each case. Figure 6.113 shows the hysteresis of the base story under 3 intensities of the BCJ-L2 ground motion. T_{eff} and h_{eff} can then be obtained similarly as described in the previous section and the T_{eff} are 2.80, 3.21, and 3.46 seconds, respectively, and h_{eff} are 0.12, 0.14, and 0.10, respectively. Now all properties are known, the prediction can be made as described in Chapter 5. The results of the prediction are also plotted together in Figure 6.114(white dots). It can be seen that the predicted values from the theory are very close to those results from the time history analyses.

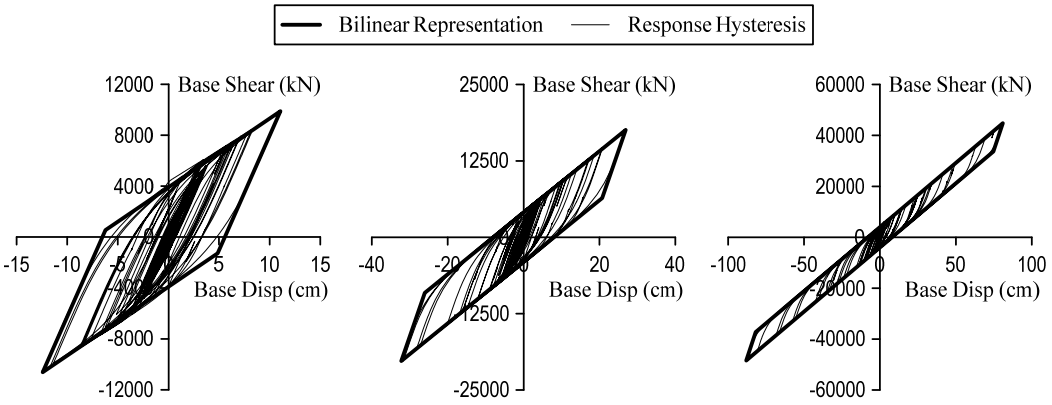

Figure 6.113 Hysteresis responses of the J2 base story under BCJ-L2

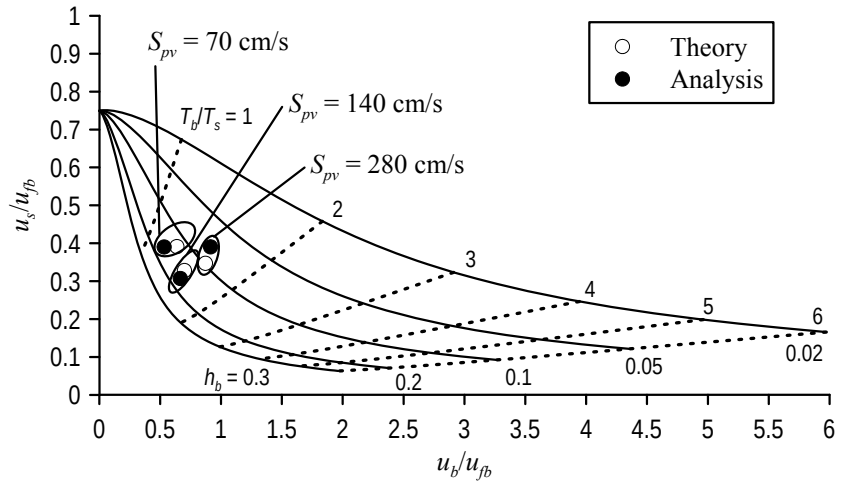

Figure 6.114 Response prediction of J2 building under artificial ground motions (average)

6.8.3 Application for design of base isolation properties

In the previous section, the prediction of the J2 base-isolated building responses under Tohoku March 11 Earthquake as well as artificial ground motions are verified with the time history analyses. The results are shown to be very accurate. This section will show another application that could be considered and will be very useful not only just for the J2 base-isolated building, but also for other base-isolated buildings.

Supposed it is desirable that this J2 base-isolated building does not pound when subjected to ground motions having S_{pv} = 140 cm/s and the maximum allowable or provided clearance distance is 50 cm, then we can obtain u_b/u_{fb} as follows.

First, u_{fb} can be obtained from $S_{pv}(T_s, h_s = 0.02) \times T_s / 2\pi = 140 \times 2.172 / 2\pi = 48.4$ cm. And u_b = 50 cm, hence u_b/u_{fb} = 1.03. Then we can draw a vertical line at u_b/u_{fb} = 1.03, and the area on the left hand side indicates the permissible area that defines that properties of the base-isolated building that will satisfy the condition above. Figure 6.116(a) shows the results of the design for the above condition. From the shaded area in the Figure 6.116(a), there could be several possibilities of T_b/T_s and h_b that could be designed such that the J2 base-isolated building will not pound. If the isolation damping ratio h_b is approximately around 0.1, then T_b/T_s would be approximately 1.9. However, if $h_b \approx 0.3$, then $T_b/T_s \approx 3$ which could be larger, or more flexible isolation is allowed. And because of nonlinearity in the isolation, T_b and h_b are not constant. Therefore, T_{eff} and h_{eff} were defined earlier.

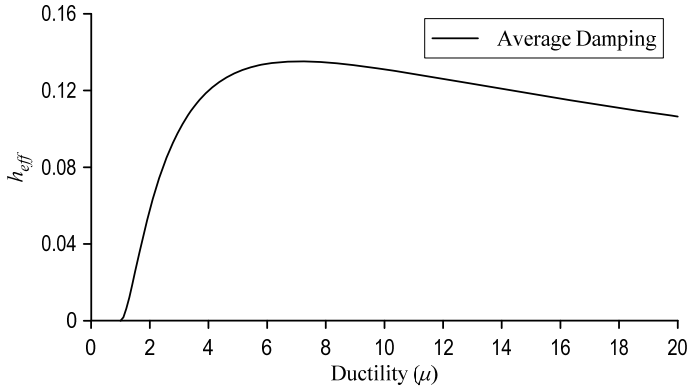

Figure 6.115 Average damping plot for J2 base-isolated building (p = 0.3)

For the J2 base-isolated building, Figure 6.115 shows the plot of Equation (6.15) with $p = 0.3$. The maximum effective damping ratio it could attain is around 0.14. Therefore, when designing the isolation system, if the ductility μ and post-yield stiffness p can be defined, the maximum effective damping ratio h_{eff} could be estimated from the damping equations shown earlier and can be further used to constrain the permissible region that can be used for design as shown in Figure 6.116(b).

If the ground motions interested were to be weaker such as S_{pv} = 70 cm/s, then u_b/u_{fb} could be obtained similarly as above and the result of the performance and permissible region is shown in Figure 6.117. Comparing between Figure 6.117 and 6.116(b) shows that when design for weaker ground motion or smaller earthquake, T_b/T_s could be larger meaning that the isolation could be designed to be more flexible.

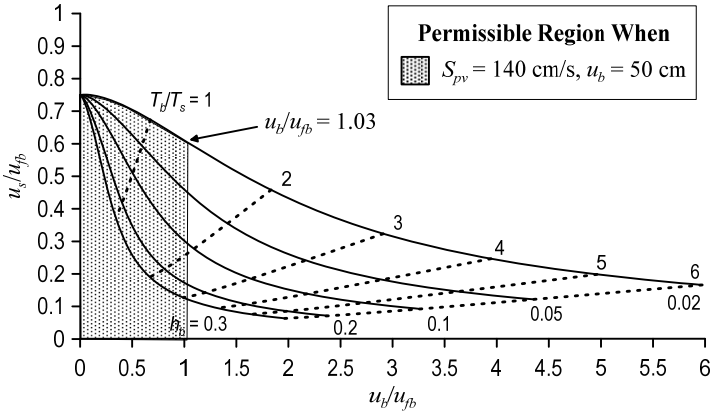

(a) Limit u_b = 50 cm

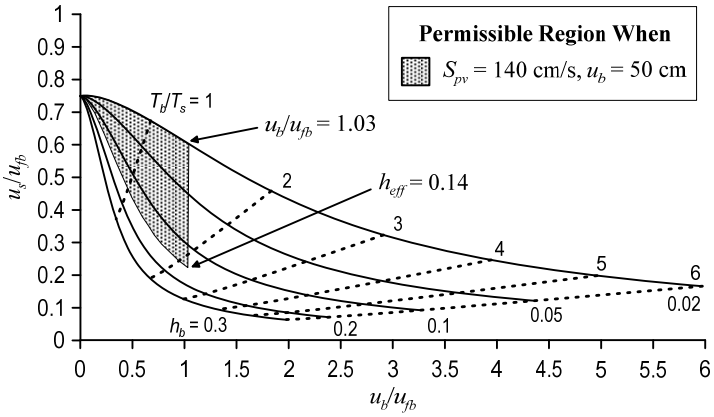

(b) Limit u_b = 50 cm and h_{eff} = 0.14

Figure 6.116 Permissible region for design of base isolation properties (S_{pv} = 140 cm/s)

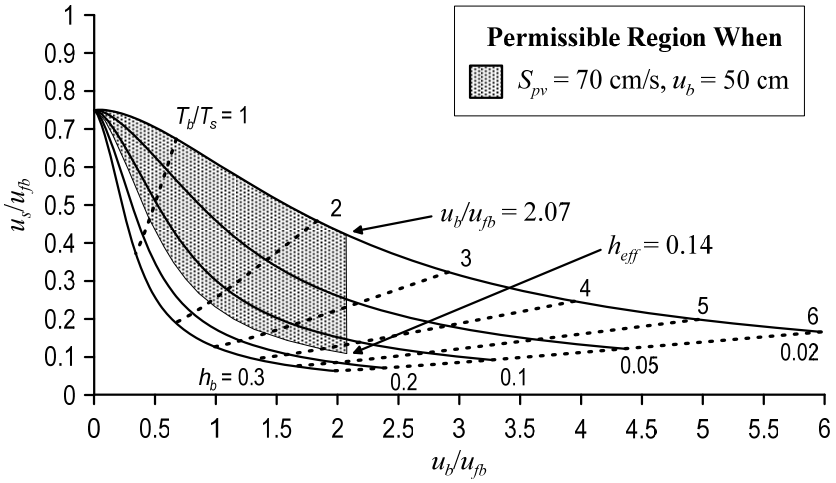

(b) Limit u_b = 50 cm and h_{eff} = 0.14

Figure 6.117 Permissible region for design of base isolation properties (S_{pv} = 70 cm/s)

As mentioned in the first paragraph of this section, this concept is applicable to not only the J2 base-isolated building in this example, but it can be used for design of new base-isolated buildings.

CHAPTER 7

CONCLUSIONS

7.1 Summary and Conclusions for Each Chapter

Chapter 2 Seismic Responses of Base-Isolated Structures

The effects of isolation period T_b, isolation damping ratio ζ_b, and number of stories N or structure height are investigated parametrically. Simple shear beam (stick) model is utilized to represent the base-isolated structures. The base-isolated structures are designed following the ASCE 7-10 standard code, which appear to be stronger than the fixed-base structures. Firstly, the isolation system is idealized as a ViscoElastic system. The vibration periods and damping ratios of the base-isolated structures that were estimated from the real-mode and complex-mode eigenvalue analyses are very close. Comparing the isolation period T_b with isolation damping ratio ζ_b, which are assigned based on the rigid superstructure assumption stipulated by the US code, the first mode period T_1 is greater than the isolation period T_b, and the first mode damping ratio ζ_1 is smaller than the isolation damping ratio ζ_b, and this can be significant for taller buildings. Base-isolated structures with longer isolation periods always show smaller drift ratios and less acceleration. In contrast, structures with higher isolation damping ratios do not necessarily show reduced responses owing to the greater mode participation, which increases the drift ratio and acceleration responses. Then, the effects of isolation hysteresis is studied through the use of ElastoPlastic isolation system with various post-yield stiffness p. The isolation system is designed such that it has the effective isolation period T_{eff} equal to the isolation period T_b and the effective isolation damping ratio ζ_{eff} equal to the isolation damping ratio ζ_b in order to investigate the effects of the hysteresis. Compared with the results of ViscoElastic isolation system, ElastoPlastic behavior tends to reduce the

first mode response, but increase the higher mode response. Lower post-yield stiffness p reduces the 1st mode acceleration response more than higher p value. Higher p value does not reduce the 1st mode acceleration response so much, however, it increases the acceleration responses at the higher mode periods. Comparing the responses between the two systems, in general, overall responses exhibit similar trends.

Chapter 3 Response Comparison with Conventional Structures

In order to examine the efficiency of having the isolation system, the responses of conventional fixed-base structure are investigated through the use of simple shear beam model. The fixed-base structures are designed following the ASCE 7-10 code. Nonlinear behaviors of these structures are studied. Comparing the results with those from Chapter 2 shows that the isolation systems are very efficient, even with tall structures. The drift ratios of the 20-story base-isolated are less than 0.5 times those of the fixed-base structures. They are even less than 0.5 times for shorter buildings. The reduction of floor acceleration is also large, but not as significant as the drift ratio. Comparing the floor response spectra of the base-isolated buildings with the fixed-base buildings show that the component accelerations from the base-isolated buildings are much smaller for the short buildings (3-story), and could be slightly smaller or even higher for tall buildings (20-story) if isolation period T_b is very close to superstructure period T_s.

Chapter 4 Probabilistic and Time-Based Performance Evaluation Methodology

The PEER PBEE framework which is based on probabilistic approach is utilized. From the framework, three types of assessments can be described which are intensity-based, scenario-based, and time-based assessments. In this study, time-based approach is utilized and the performance evaluation methodology is explained in detail. As examples of the evaluation method, nonstructural components of partition wall and suspended ceilings are selected which represent drift-sensitive and acceleration-sensitive components, respectively. It should be

noted that the component acceleration is higher than the floor acceleration, and thus is used in the evaluation process. The result of the performance evaluation is interpreted as a return period in years which indicates how many years the building is expected to be continuously functional considering the damage on the specified nonstructural component. Compared with the fixed-base structures, performances are excellent for short base-isolated structures, and less distinct but still better for taller isolated structures. These performance results are obtained considering a single fragility function of the partition wall and suspended ceiling only. Sensitivity to the fragility functions characterized by the strength x_m and dispersion β is examined. The return period appears to be very sensitive in the short structures, and less sensitive in taller structures.

A new application of the PEER methodology for finding necessary strength x_m and dispersion β to satisfy the target performance level T_R is described. x_m and β are plotted with respect to T_R which is convenient for estimating desired mean strengths and dispersions in order to produce nonstructural components. Moreover, the plot will be useful for selecting and designing particular nonstructural components during the initial design phase and budget planning.

Chapter 5 Simplified Performance Evaluation Methodology

For vibration controlled damped buildings, the so-called performance curve can be constructed which is expressed by a function of few basic parameters that indicate the damping performance, and it can be used to estimate the maximum response, equipment connection, supporting material, and frame response. Therefore, it is also meaningful to construct the seismic isolation performance curve with the same advantages as the vibration control performance curves. This Chapter describes how the performance curve for base-isolated buildings are developed. Several building cases from short to tall buildings are verified with the performance curve. Also additional cases where the building has high damping or the isolation has bilinear behavior are also investigated. Comparing the responses from time history analyses with those obtained from the prediction in the performance curve indicates that the

accuracy of the proposed method is reasonably well and can be used for design of base-isolated buildings.

Chapter 6 Application to an Existing Base-Isolated Building

In previous chapters, only the stick models have been used to represent the base-isolated and fixed-base structures. In this chapter, an existing J2 base-isolated building in Suzukakedai campus, Tokyo Institute of Technology is analyzed by using a 3D nonlinear sophisticated model. The accuracy of the J2 building has been verified by comparing the responses with the recorded data. This complicated model is then simplified to only stick model to capture major responses of the displacement, drift ratio, and acceleration. The results of the stick model are shown to be very accurate. By using this simple shear model, the performance of the J2 base-isolated building is evaluated by using the PEER framework described in Chapter 4. In Japan, clearance distance of the base floor is usually limited. Hence, the framework is extended to evaluate the performance considering this clearance distance. Furthermore, the performance curve proposed in Chapter 5 is also verified with the J2 building. Further application of the performance curve is described.

7.2 Future Study

1. This study describes two performance evaluation methods which are based on probabilistic and deterministic approaches. These two methodologies are combined in such a way that when selecting the desired return period and allowable clearance distance against pounding, combination of building properties can be selected from the performance curve.

REFERENCES

1) J. M. Kelly, “The Role of Damping in Seismic Isolation,” Earthquake Engineering and Structural Dynamics, Vol.28, No.1, pp. 3-20, 1999.

2) N. Makris and S. P. Chang, “Effect of Viscous, Viscoplastic and Friction Damping on the Response of Seismic Isolated Structures,” Earthquake Engineering and Structural Dynamics, Vol.29, No.1, pp. 85-107, 2000.

3) R. S. Jangid and J. M. Kelly, “Base Isolation for Near-Fault Motions,” Earthquake Engineering and Structural Dynamics, Vol.30, No.5, pp. 691-707, 2001.

4) D. Ordoñez, D. Foti, and L. Bozzo, “Comparative Study of the Inelastic Response of Base Isolated Buildings,” Earthquake Engineering and Structural Dynamics, Vol.32, No.1, pp. 151-164, 2003.

5) I. Politopoulos, “A Review of Adverse Effects of Damping in Seismic Isolation,” Earthquake Engineering and Structural Dynamics, Vol.37, No.3, pp. 447-465, 2008.

6) T. Y. Yang, D. Vamvatsikos, J. M. Kelly, “The Influence of Isolator Hysteresis on Equipment Performance in Seismic Isolated Buildings,” Earthquake Spectra, Vol.26, No.1, pp. 275-293, 2010.

7) J. Moehle and G. G. Deierlein, “A Framework Methodology for Performance-Based Earthquake Engineering,” Proceedings of the 13th World Conference on Earthquake Engineering, Vancouver, Canada, 2004.

8) American Society of Civil Engineers (ASCE 7), “Minimum Design Loads for Buildings and Other Structures,” Reston, Virginia, 2010.

9) P. Somerville, D. Anderson, J. Sun, S. Punyamurthula, and N. Smith, “Generation of Ground Motion Time Histories for Performance-Based Seismic Engineering,” Proceedings of the 6th National Conference of Earthquake Engineering, 1998.

10) R. Retamales, R. Davies, G. Mosqueda, and A. Filiatrault, “Experimental Seismic Fragility Assessment of Light Gauge Steel Studded Gypsum Partition Walls,” Proceedings of the 9th US National and 10th Canadian Cnference on Earthquake Engineering, Toronto, Canada, 2010.

11) S. Motoyui, Y. Sato, G. A. Macrae, and R. P. Dhakal, “Ceiling Fragility of Japanese Ceiling Systems,” Proceedings of the 9th Pacific Conference on Earthquake Engineering, Auckland, New Zealand, 2011.

12) Federal Emergency Management Agency (FEMA P-58), “Seismic Performance Assessment of Buildings,” August, 2012.

13) E. H. Field, T. H. Jordan, and C. A. Cornell, “OpenSHA: A Developing Community-Modeling Environment for Seismic Hazard Analysis,” Seismological Research Letters, Vol.74, No.4, pp. 405-419, 2003.

14) K. W. Campbell and Y. Bozorgnia, “NGA Ground Motion Model for the Geometric Mean Horizontal Component of PGA, PGV, PGD and 5% Damped Linear Elastic Response Spectra for Periods Ranging from 0.01 to 10 s,” Earthquake Spectra, Vol.24, No.1, pp. 131-171, 2008.

15) K. Matsuda and K. Kasai, “Study on Dynamic Behavior of High-Rise Base-Isolated Building based on its Responses Recorded during the 2011 Tohoku-Oki Earthquake,” Journal of Structural and Construction Engineering (AIJ), Vol.79, No.704, pp. 1445-1455, 2014.

16) K. Suzuki, E. Saeki, and A. Watanabe, “Development of U-shaped Steel Damper for Seismic Isolation System,” Nippon Steel Technical Report, No.92, pp. 56-61, 2005.

17) R. Sinha and T. Igusa, “CQC and SRSS methods for non-classically damped structures,” Earthquake Engineering and Structural Dynamics, Vol.24, No.4, pp. 615-619, 1995

18) M. Wang and X. Zhou, “On Precise Time Integration Method for Non-Classically Damped MDOF systems,” Earthquake Engineering and Engineering Vibration, Vol.5, No.1, pp. 79-85, 2006

19) B. Chiou, R. Darragh, N. Gregor, and W. Silva, “NGA Project Strong-Motion Database,” Earthquake Spectra, Vol.24, No.1, pp. 23-44, 2008

20) 日本建築学会: 免震構造設計指針 (第 4 版), 丸善出版株式会社, 2013.10

21) 日本免震構造協会, 応答制御建築物調査委員会報告書, 5 免震構造地震応 答評価部会報告書, 2012.1

22) 欄木龍大, 長島一郎, 新居藍子, 篠崎洋三, 木村雄一, 青野英志: 東北地方太平洋沖地震における免震・制振建物の効果, 観測記録の分析に基づく免震・制振効果の検証, 大成建設技術センター報, 第 44 号, pp.05_1-8, 2011

23) 境茂樹, 加藤貴司, 田中靖彦, 片山喜隆: 東北地方太平洋沖地震による超高層免震建物の地震時挙動, ハザマ研究年報, pp.1-6, 2011.12

24) 猿田正明, 山本祥江, 森川和彦, 中西啓二, 飯場正紀, 小豆畑達哉, 井上波彦: 東北地方太平洋沖地震における超高層免震建物の挙動, 日本建築学会技術報告集, 第 19 巻, 第 42 号, pp.477-480, 2013.6

25) 松田和浩, 笠井和彦: 東北地方太平洋沖地震における観測記録を用いた超高層免震建物の動的挙動に関する研究, 日本建築学会構造系論文集, 第 704 号, pp. 1445-1455, 2014.10

26) 笠井和彦, 伊藤浩資: 弾塑性ダンパーの剛性・降伏力・塑性率の調節による制振構造の応答制御手法, 日本建築学会構造系論文集, No.595, pp.45-55, 2005 年 9 月

27) 笠井和彦, 湊直生, 川鍋佳史: 粘弾性ダンパーの等価剛性の調節による制振構造の応答制御手法, 日本建築学会構造系論文集, 第 610 号, pp.75-83, 2006 年 12 月

28) 笠井和彦, 湊直生, 櫻井馨: 粘弾塑性ダンパーの等価剛性調節による制振構造の応答制御手法, 日本建築学会構造系論文集, 第 618 号, pp.23-31, 2007 年 8 月

29) 笠井和彦, 小椋崇之, 鈴木陽: 非線形粘性ダンパーの等価剛性調節による制振構造の応答制御手法, 日本建築学会構造系論文集, 第 618 号, pp.97-104, 2007 年 8 月

30) 笠井和彦, 伊藤浩資, 小椋崇之: オイルダンパーの等価剛性調節による制振構造の応答制御手法, 日本建築学会構造系論文集, 630 号, pp.1281-1288, 2008 年 8 月

31) 秋山宏: エネルギーの釣合に基づく建築物の耐震設計, 技報堂出版, 1999

32) 東野さやか, 北村春幸: 粘性ダンパーを付与した免震構造のエネルギーの釣合に基づく応答評価法, 日本建築学会構造系論文集, 第 588 号, pp.79-86, 2005 年 2 月

33) 石丸辰治: 応答性能に基づく「対震設計」入門, 彰国社, 2004

34) 秦一平, 石丸辰治, 長谷川純: 非線形粘性ダンパーと弾塑性ダンパーを併用した系の応答性能設計手法, 日本建築学会構造系論文集, 第 617 号, pp.47-54, 2007 年 7 月

35) ジェームス・M・ケリー: 免震構造と積層ゴムの基礎理論, 東京電機大学出版局, 2005

36) 山崎久雄、渡邉信也、高山峯夫、笠井和彦：応答スペクトルを用いた免震層の最大応答予測法－その 1 既提案法の精度改善と非線形粘性ダンパーの考慮－、日本建築学会大会学術講演梗概集（北海道）、論文 21440, pp.799-800, 2013.8

37) 渡邉信也、山崎久雄、高山峯夫、笠井和彦：応答スペクトルを用いた免震層の最大応答予測法－その 2 応答予測式と応答予測曲線－、日本建築学会大会学術講演梗概集（北海道）、論文 21441, pp.801-802, 2013.8

38) 笠井和彦, 大熊潔: 振動数に依存する制振構造の等価周期・等価減衰の評価法とその精度－弾性架構と粘弾性ダンパーやオイルダンパーをもつ一質点構造における全体減衰系への置換法－, 日本建築学会構造系論文集, 第 580 号, pp.51-59, 2004.6

39) 笠井和彦, 川鍋佳史: 粘性減衰・履歴減衰を併用する構造における動的特性と地震最大応答の簡易評価法, 日本建築学会構造系論文集, 第 591 号, pp.43-51, 2005 年 5 月

40) 笠井和彦, 山下忠道, 山崎義弘, イグサタケル: 捩れ振動をともなう 1 層高減衰構造のスペクトル応答予測法, 日本建築学会構造系論文集, 636 号, pp.225-234, 2009 年 2 月

41) 笠井和彦, 伊藤浩資, 渡辺厚：等価線形化手法による一質点系弾塑性構造の最大応答予測法, 日本建築学会構造系論文集, 第 571 号, pp.53-62, 2003.9

APPENDIX A

Beam Property Inputs for PC-ANSR (G4)

	Stiffness										
Name	***E***	E_h/E	***A***	***I***	k_{ii}	k_{jj}	k_{ij}	A_{shear}	**Poisson**	**Factor**	**Tor Stiff**
G1 (10-20)	20500	0.01	281.00	355000	4	4	2	160.3	0.03	99999	4.56E+06
G1 (7-9)	20500	0.01	281.00	355000	4	4	2	160.3	0.03	99999	4.56E+06
G1 (3-6)	20500	0.01	305.00	390000	4	4	2	182.4	0.03	99999	6.22E+06
G1 (2-2)	12212	0.01	2568.89	5281590	4	4	2	2134.9	0.025	99999	1.32E+11
G2 (19-20)	20500	0.01	263.00	328000	4	4	2	143.7	0.03	99999	3.57E+06
G2 (13-18)	20500	0.01	281.00	355000	4	4	2	160.3	0.03	99999	4.56E+06
G2 (7-12)	20500	0.01	305.00	390000	4	4	2	182.4	0.03	99999	6.22E+06
G2 (3-6)	20500	0.01	343.26	425115	4	4	2	204.4	0.03	99999	8.32E+06
G2 (2-2)	20500	0.01	853.58	2129751	4	4	2	497.8	0.03	99999	3.57E+07
G3 (19-20)	20500	0.01	263.00	328000	4	4	2	143.7	0.03	99999	3.57E+06
G3 (13-18)	20500	0.01	281.00	355000	4	4	2	160.3	0.03	99999	4.56E+06
G3 (7-12)	20500	0.01	305.00	390000	4	4	2	182.4	0.03	99999	6.22E+06
G3 (3-6)	20500	0.01	343.26	425115	4	4	2	204.4	0.03	99999	8.32E+06
G3 (2-2)	20500	0.01	853.58	2129751	4	4	2	497.8	0.03	99999	3.57E+07
G4 (19-20)	20500	0.01	288.00	370000	4	4	2	164.1	0.03	99999	3.98E+06
G4 (16-18)	20500	0.01	309.00	402000	4	4	2	183.2	0.03	99999	5.14E+06
G4 (13-15)	20500	0.01	337.00	444000	4	4	2	208.6	0.03	99999	7.09E+06
G4 (7-12)	20500	0.01	438.60	556000	4	4	2	267.7	0.03	99999	1.15E+07
G4 (4-6)	20500	0.01	438.60	556000	4	4	2	267.7	0.03	99999	1.15E+07
G4 (3-3)	20500	0.01	469.10	602000	4	4	2	296.6	0.03	99999	1.50E+07
G4 (2-2)	20500	0.01	853.58	2129751	4	4	2	497.8	0.03	99999	3.57E+07
G11 (19-20)	20500	0.01	263.00	328000	4	4	2	143.7	0.03	99999	3.57E+06
G11 (16-18)	20500	0.01	281.00	355000	4	4	2	160.3	0.03	99999	4.56E+06
G11 (13-15)	20500	0.01	321.64	367626	4	4	2	163.9	0.03	99999	5.22E+06
G11 (7-12)	20500	0.01	344.12	402610	4	4	2	186.4	0.03	99999	6.90E+06
G11 (3-6)	20500	0.01	366.60	436888	4	4	2	208.8	0.03	99999	9.01E+06
G11 (2-2)	11750	0.01	2568.89	5281590	4	4	2	2134.9	0.025	99999	1.27E+11
G12 (19-20)	20500	0.01	263.00	328000	4	4	2	143.7	0.03	99999	3.57E+06
G12 (16-18)	20500	0.01	281.00	355000	4	4	2	160.3	0.03	99999	4.56E+06
G12 (13-15)	20500	0.01	281.00	355000	4	4	2	160.3	0.03	99999	4.56E+06
G12 (10-12)	20500	0.01	360.98	428384	4	4	2	203.2	0.03	99999	8.44E+06
G12 (7-9)	20500	0.01	360.98	428384	4	4	2	203.2	0.03	99999	8.44E+06
G12 (3-6)	20500	0.01	366.60	436888	4	4	2	208.8	0.03	99999	9.01E+06
G12 (2-2)	11369	0.01	2478.41	4998610	4	4	2	2031.5	0.025	99999	1.21E+11
G1 (RF-RF)	20500	0.01	325.00	476000	4	4	2	164.2	0.03	0.027	5.40E+06
G2 (RF-RF)	20500	0.01	307.00	442000	4	4	2	147.3	0.03	0.026	4.41E+06
G3 (RF-RF)	20500	0.01	307.00	442000	4	4	2	147.3	0.03	0.026	4.41E+06
G4 (RF-RF)	20500	0.01	349.00	520000	4	4	2	186.7	0.03	0.028	7.08E+06
G11 (RF-RF)	20500	0.01	306.92	407831	4	4	2	130.4	0.03	0.024	3.60E+06
G12 (RF-RF)	20500	0.01	306.92	407831	4	4	2	130.4	0.03	0.024	3.60E+06
G1P (2-PHR)	20500	0.01	120.00	14000	4	4	2	100.0	0.03	1.000	2.71E+06
G1 (PHR-PHR)	20500	0.01	223.50	97600	4	4	2	140.8	0.03	0.116	3.06E+06
G11 (PHR-PHR)	20500	0.01	223.50	97600	4	4	2	140.8	0.03	0.116	3.06E+06
G12 (PHR-PHR)	20500	0.01	206.40	88800	4	4	2	124.3	0.03	0.112	2.29E+06

	Yield Strength								
Name	**Shape Code**	M_{y+}	M_{y-}	P_{yc}	P_{yt}	M_A	P_A	M_B	P_B
G1 (10-20)	2	271375	271375	9133	9133	1	0.15	1	0.15
G1 (7-9)	2	271375	271375	9133	9133	1	0.15	1	0.15
G1 (3-6)	2	298350	298350	9913	9913	1	0.15	1	0.15
G1 (2-2)	2	1397339	1397339	62844	29806	1.25	0.15	1.25	0.15
G2 (19-20)	2	250900	250900	8548	8548	1	0.15	1	0.15
G2 (13-18)	2	271375	271375	9133	9133	1	0.15	1	0.15
G2 (7-12)	2	298350	298350	9913	9913	1	0.15	1	0.15
G2 (3-6)	2	325088	325088	11156	11156	1	0.15	1	0.15
G2 (2-2)	2	1153615	1153615	27741	27741	1	0.15	1	0.15
G3 (19-20)	2	250900	250900	8548	8548	1	0.15	1	0.15
G3 (13-18)	2	271375	271375	9133	9133	1	0.15	1	0.15
G3 (7-12)	2	298350	298350	9913	9913	1	0.15	1	0.15
G3 (3-6)	2	325088	325088	11156	11156	1	0.15	1	0.15
G3 (2-2)	2	1153615	1153615	27741	27741	1	0.15	1	0.15
G4 (19-20)	2	283400	283400	9360	9360	1	0.15	1	0.15
G4 (16-18)	2	307450	307450	10043	10043	1	0.15	1	0.15
G4 (13-15)	2	338000	338000	10953	10953	1	0.15	1	0.15
G4 (7-12)	2	425750	425750	14255	14255	1	0.15	1	0.15
G4 (4-6)	2	425750	425750	14255	14255	1	0.15	1	0.15
G4 (3-3)	2	461500	461500	15246	15246	1	0.15	1	0.15
G4 (2-2)	2	1153615	1153615	27741	27741	1	0.15	1	0.15
G11 (19-20)	2	250900	250900	8548	8548	1	0.15	1	0.15
G11 (16-18)	2	271375	271375	9133	9133	1	0.15	1	0.15
G11 (13-15)	2	281125	281125	10453	10453	1	0.15	1	0.15
G11 (7-12)	2	307878	307878	11184	11184	1	0.15	1	0.15
G11 (3-6)	2	334091	334091	11915	11915	1	0.15	1	0.15
G11 (2-2)	2	1333676	1333676	61876	287758	1.25	0.15	1.25	0.15
G12 (19-20)	2	250900	250900	8548	8548	1	0.15	1	0.15
G12 (16-18)	2	271375	271375	9133	9133	1	0.15	1	0.15
G12 (13-15)	2	271375	271375	9133	9133	1	0.15	1	0.15
G12 (10-12)	2	327588	327588	11732	11732	1	0.15	1	0.15
G12 (7-9)	2	327588	327588	11732	11732	1	0.15	1	0.15
G12 (3-6)	2	334091	334091	11915	11915	1	0.15	1	0.15
G12 (2-2)	2	1211866	1211866	59255	25945	1.25	0.15	1.25	0.15
G1 (RF-RF)	2	325000	325000	10563	10563	1	0.15	1	0.15
G2 (RF-RF)	2	302250	302250	9978	9978	1	0.15	1	0.15
G3 (RF-RF)	2	302250	302250	9978	9978	1	0.15	1	0.15
G4 (RF-RF)	2	357500	357500	11343	11343	1	0.15	1	0.15
G11 (RF-RF)	2	279042	279042	9975	9975	1	0.15	1	0.15
G12 (RF-RF)	2	279042	279042	9975	9975	1	0.15	1	0.15
G1P (2-PHR)	2	26000	26000	3900	3900	1	0.15	1	0.15
G1 (PHR-PHR)	2	126750	126750	7264	7264	1	0.15	1	0.15
G11 (PHR-PHR)	2	126750	126750	7264	7264	1	0.15	1	0.15
G12 (PHR-PHR)	2	115375	115375	6708	6708	1	0.15	1	0.15

APPENDIX B

Column Property Inputs for PC-ANSR (G10)

	Local y and z axes					Torsion				
Name	K_1	K_2	K_3	YS_1	YS_2	K_1	K_2	K_3	YS_1	YS_2
C1 (19-RF)	6.44E+09	6.44E+07	0.01	3.12E+05	1E+15	4.03E+09	4.03E+07	0.01	1E+10	1E+15
C1 (16-18)	6.91E+09	6.91E+07	0.01	3.40E+05	1E+15	4.32E+09	4.32E+07	0.01	1E+10	1E+15
C1 (13-15)	7.46E+09	7.46E+07	0.01	3.75E+05	1E+15	4.66E+09	4.66E+07	0.01	1E+10	1E+15
C1 (10-12)	7.98E+09	7.98E+07	0.01	4.08E+05	1E+15	4.99E+09	4.99E+07	0.01	1E+10	1E+15
C1 (7-9)	8.39E+09	8.39E+07	0.01	4.37E+05	1E+15	5.24E+09	5.24E+07	0.01	1E+10	1E+15
C1 (6-6)	8.43E+09	8.43E+07	0.01	4.37E+05	1E+15	5.27E+09	5.27E+07	0.01	1E+10	1E+15
C1 (3-5)	8.84E+09	8.84E+07	0.01	4.68E+05	1E+15	5.52E+09	5.52E+07	0.01	1E+10	1E+15
C1 (2-2)	9.17E+09	9.17E+07	0.01	4.95E+05	1E+15	5.73E+09	5.73E+07	0.01	1E+10	1E+15
C2 (16-RF)	5.94E+09	5.94E+07	0.01	2.82E+05	1E+15	3.71E+09	3.71E+07	0.01	1E+10	1E+15
C2 (13-15)	6.44E+09	6.44E+07	0.01	3.12E+05	1E+15	4.03E+09	4.03E+07	0.01	1E+10	1E+15
C2 (10-12)	6.95E+09	6.95E+07	0.01	3.41E+05	1E+15	4.35E+09	4.35E+07	0.01	1E+10	1E+15
C2 (7-9)	7.50E+09	7.50E+07	0.01	3.76E+05	1E+15	4.69E+09	4.69E+07	0.01	1E+10	1E+15
C2 (4-6)	8.02E+09	8.02E+07	0.01	4.08E+05	1E+15	5.01E+09	5.01E+07	0.01	1E+10	1E+15
C2 (3-3)	8.43E+09	8.43E+07	0.01	4.37E+05	1E+15	5.27E+09	5.27E+07	0.01	1E+10	1E+15
C2 (2-2)	8.84E+09	8.84E+07	0.01	4.68E+05	1E+15	5.52E+09	5.52E+07	0.01	1E+10	1E+15
C3 (16-RF)	5.94E+09	5.94E+07	0.01	2.82E+05	1E+15	3.71E+09	3.71E+07	0.01	1E+10	1E+15
C3 (13-15)	6.44E+09	6.44E+07	0.01	3.12E+05	1E+15	4.03E+09	4.03E+07	0.01	1E+10	1E+15
C3 (10-12)	6.95E+09	6.95E+07	0.01	3.41E+05	1E+15	4.35E+09	4.35E+07	0.01	1E+10	1E+15
C3 (7-9)	7.50E+09	7.50E+07	0.01	3.76E+05	1E+15	4.69E+09	4.69E+07	0.01	1E+10	1E+15
C3 (4-6)	8.02E+09	8.02E+07	0.01	4.08E+05	1E+15	5.01E+09	5.01E+07	0.01	1E+10	1E+15
C3 (3-3)	8.43E+09	8.43E+07	0.01	4.37E+05	1E+15	5.27E+09	5.27E+07	0.01	1E+10	1E+15
C3 (2-2)	8.84E+09	8.84E+07	0.01	4.68E+05	1E+15	5.52E+09	5.52E+07	0.01	1E+10	1E+15
C4 (13-RF)	6.44E+09	6.44E+07	0.01	3.12E+05	1E+15	4.03E+09	4.03E+07	0.01	1E+10	1E+15
C4 (10-12)	6.95E+09	6.95E+07	0.01	3.41E+05	1E+15	4.35E+09	4.35E+07	0.01	1E+10	1E+15
C4 (7-9)	7.50E+09	7.50E+07	0.01	3.76E+05	1E+15	4.69E+09	4.69E+07	0.01	1E+10	1E+15
C4 (4-6)	8.02E+09	8.02E+07	0.01	4.08E+05	1E+15	5.01E+09	5.01E+07	0.01	1E+10	1E+15
C4 (3-3)	8.43E+09	8.43E+07	0.01	4.37E+05	1E+15	5.27E+09	5.27E+07	0.01	1E+10	1E+15
C4 (2-2)	8.84E+09	8.84E+07	0.01	4.68E+05	1E+15	5.52E+09	5.52E+07	0.01	1E+10	1E+15
C5 (16-RF)	5.94E+09	5.94E+07	0.01	2.82E+05	1E+15	3.71E+09	3.71E+07	0.01	1E+10	1E+15
C5 (13-15)	6.44E+09	6.44E+07	0.01	3.12E+05	1E+15	4.03E+09	4.03E+07	0.01	1E+10	1E+15
C5 (10-12)	6.95E+09	6.95E+07	0.01	3.41E+05	1E+15	4.35E+09	4.35E+07	0.01	1E+10	1E+15
C5 (7-9)	7.50E+09	7.50E+07	0.01	3.76E+05	1E+15	4.69E+09	4.69E+07	0.01	1E+10	1E+15
C5 (4-6)	8.02E+09	8.02E+07	0.01	4.08E+05	1E+15	5.01E+09	5.01E+07	0.01	1E+10	1E+15

	Axial					
Name	K_1	K_2	K_3	YS_1	YS_2	YS_3
C1 (19-RF)	2.00E+07	2.00E+05	0.01	1.76E+04	1E+15	2.98E+04
C1 (16-18)	2.10E+07	2.10E+05	0.01	1.95E+04	1E+15	3.13E+04
C1 (13-15)	2.22E+07	2.22E+05	0.01	2.18E+04	1E+15	3.33E+04
C1 (10-12)	2.41E+07	2.41E+05	0.01	2.41E+04	1E+15	3.66E+04
C1 (7-9)	2.51E+07	2.51E+05	0.01	2.63E+04	1E+15	3.83E+04
C1 (6-6)	2.54E+07	2.54E+05	0.01	2.63E+04	1E+15	3.97E+04
C1 (3-5)	2.67E+07	2.67E+05	0.01	2.89E+04	1E+15	4.16E+04
C1 (2-2)	2.78E+07	2.78E+05	0.01	3.14E+04	1E+15	4.34E+04
C2 (16-RF)	1.91E+07	1.91E+05	0.01	1.57E+04	1E+15	2.82E+04
C2 (13-15)	2.00E+07	2.00E+05	0.01	1.76E+04	1E+15	2.98E+04
C2 (10-12)	2.17E+07	2.17E+05	0.01	1.95E+04	1E+15	3.28E+04
C2 (7-9)	2.29E+07	2.29E+05	0.01	2.18E+04	1E+15	3.48E+04
C2 (4-6)	2.44E+07	2.44E+05	0.01	2.41E+04	1E+15	3.80E+04
C2 (3-3)	2.54E+07	2.54E+05	0.01	2.63E+04	1E+15	3.97E+04
C2 (2-2)	2.67E+07	2.67E+05	0.01	2.89E+04	1E+15	4.16E+04
C3 (16-RF)	1.91E+07	1.91E+05	0.01	1.57E+04	1E+15	2.82E+04
C3 (13-15)	2.00E+07	2.00E+05	0.01	1.76E+04	1E+15	2.98E+04
C3 (10-12)	2.17E+07	2.17E+05	0.01	1.95E+04	1E+15	3.28E+04
C3 (7-9)	2.29E+07	2.29E+05	0.01	2.18E+04	1E+15	3.48E+04
C3 (4-6)	2.44E+07	2.44E+05	0.01	2.41E+04	1E+15	3.80E+04
C3 (3-3)	2.54E+07	2.54E+05	0.01	2.63E+04	1E+15	3.97E+04
C3 (2-2)	2.67E+07	2.67E+05	0.01	2.89E+04	1E+15	4.16E+04
C4 (13-RF)	2.00E+07	2.00E+05	0.01	1.76E+04	1E+15	2.98E+04
C4 (10-12)	2.17E+07	2.17E+05	0.01	1.95E+04	1E+15	3.28E+04
C4 (7-9)	2.29E+07	2.29E+05	0.01	2.18E+04	1E+15	3.48E+04
C4 (4-6)	2.44E+07	2.44E+05	0.01	2.41E+04	1E+15	3.80E+04
C4 (3-3)	2.54E+07	2.54E+05	0.01	2.63E+04	1E+15	3.97E+04
C4 (2-2)	2.67E+07	2.67E+05	0.01	2.89E+04	1E+15	4.16E+04
C5 (16-RF)	1.91E+07	1.91E+05	0.01	1.57E+04	1E+15	2.82E+04
C5 (13-15)	2.00E+07	2.00E+05	0.01	1.76E+04	1E+15	2.98E+04
C5 (10-12)	2.17E+07	2.17E+05	0.01	1.95E+04	1E+15	3.28E+04
C5 (7-9)	2.29E+07	2.29E+05	0.01	2.18E+04	1E+15	3.48E+04
C5 (4-6)	2.44E+07	2.44E+05	0.01	2.41E+04	1E+15	3.80E+04

APPENDIX C

Response Histories of the Ground Motions

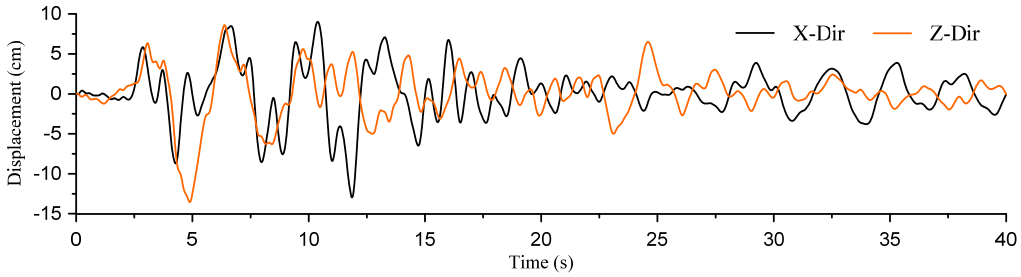

(a) 2nd floor

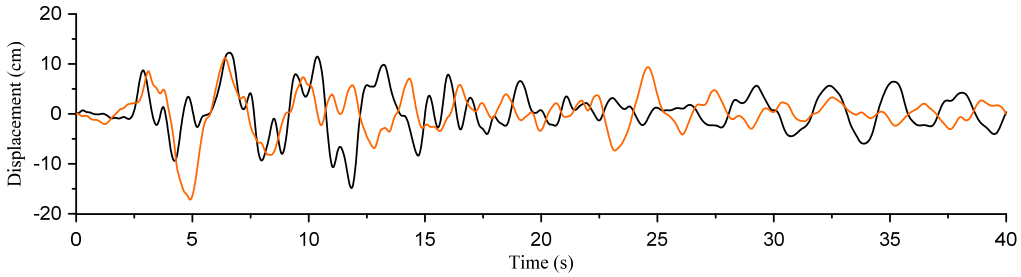

(b) 7th floor

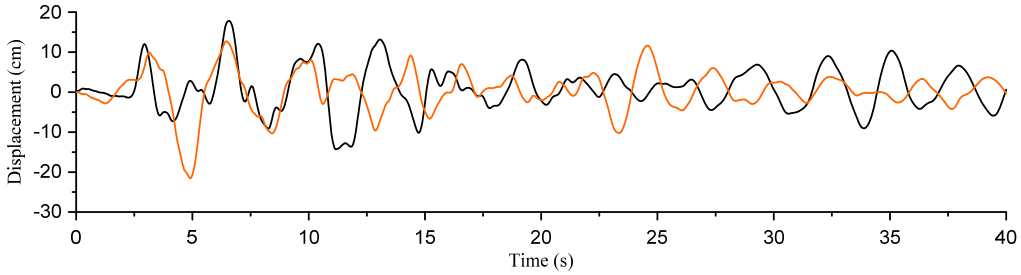

(c) 14th floor

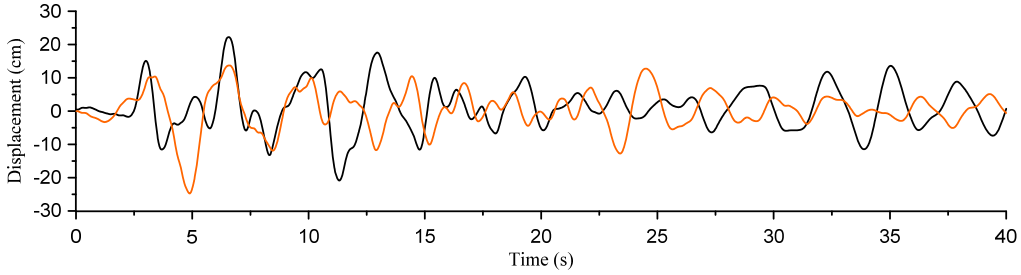

(d) 20th floor

Figure C.1 Floor displacement relative to the isolation floor (Tohoku U – NS(X),EW(Z))

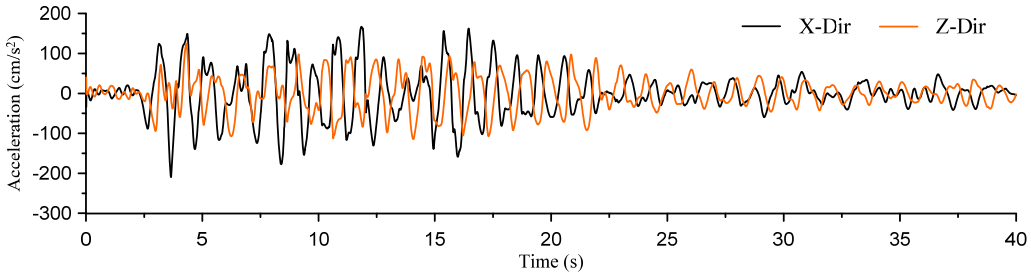

(a) 2nd floor

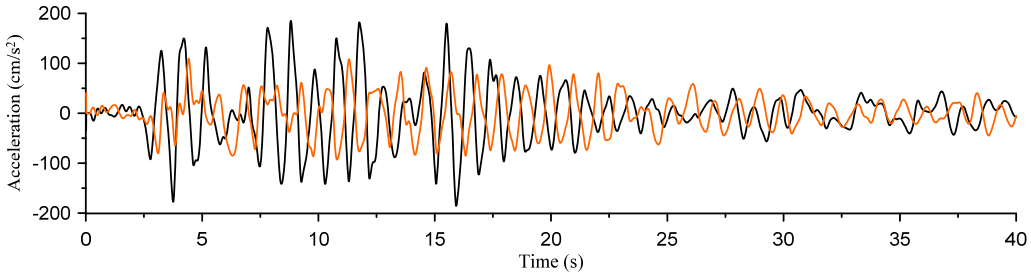

(b) 7th floor

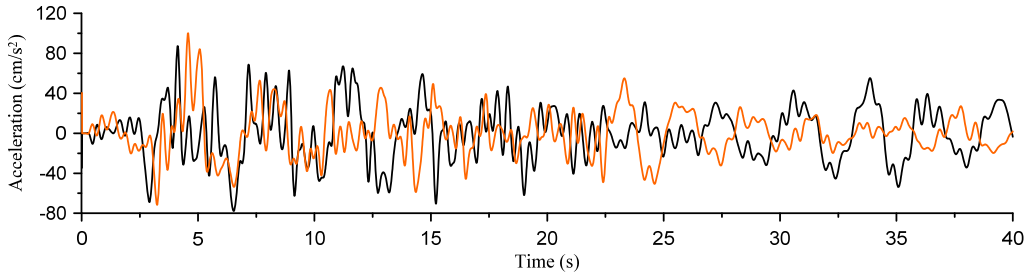

(c) 14th floor

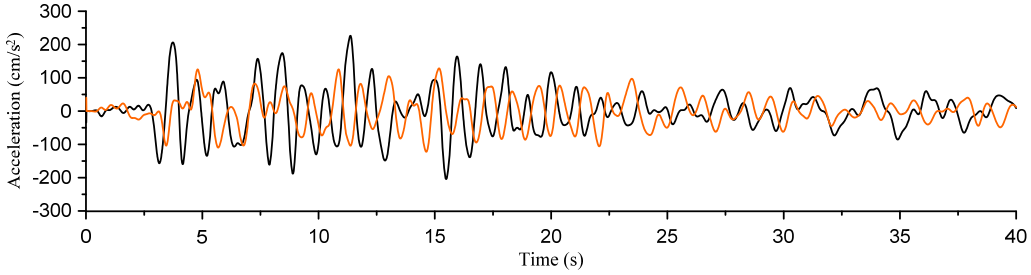

(d) 20th floor

Figure C.2 Absolute floor acceleration (Tohoku U – NS(X),EW(Z))

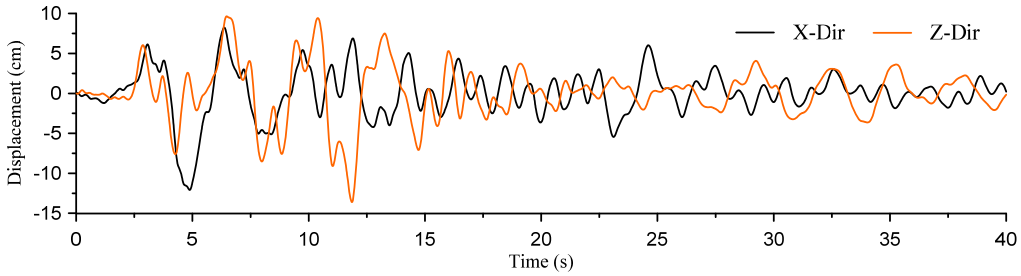

(a) 2nd floor

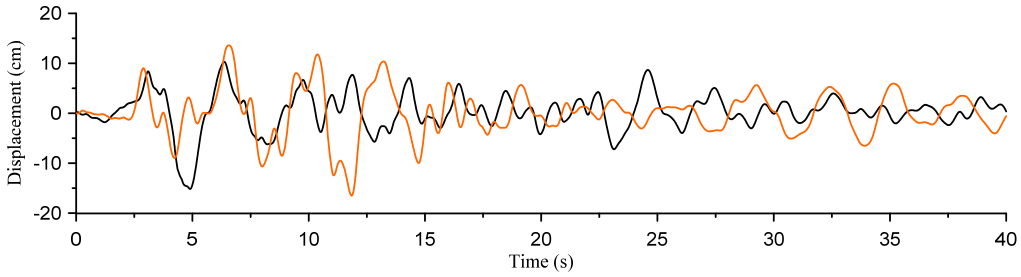

(b) 7th floor

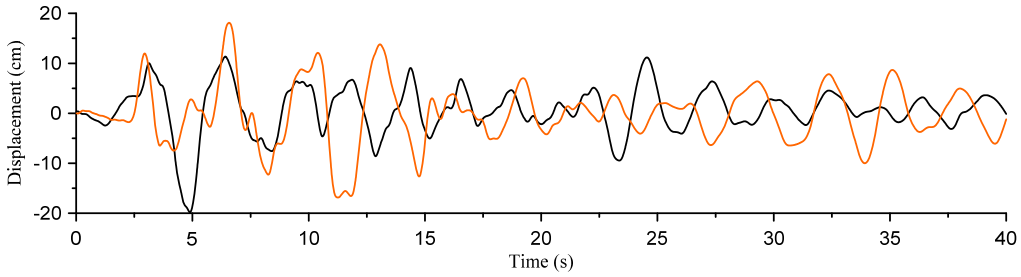

(c) 14th floor

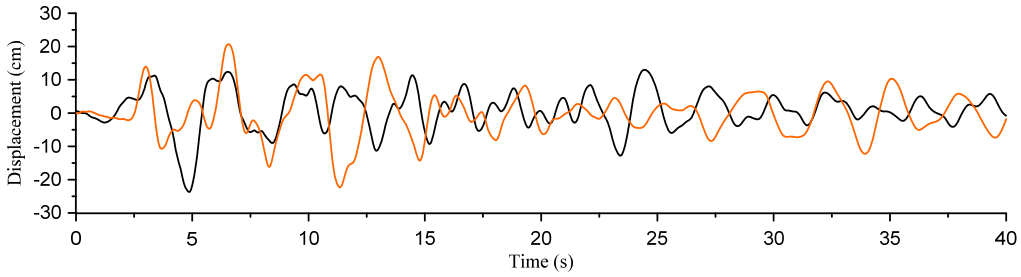

(d) 20th floor

Figure C.3 Floor displacement relative to the isolation floor (Tohoku U – NS(Z),EW(X))

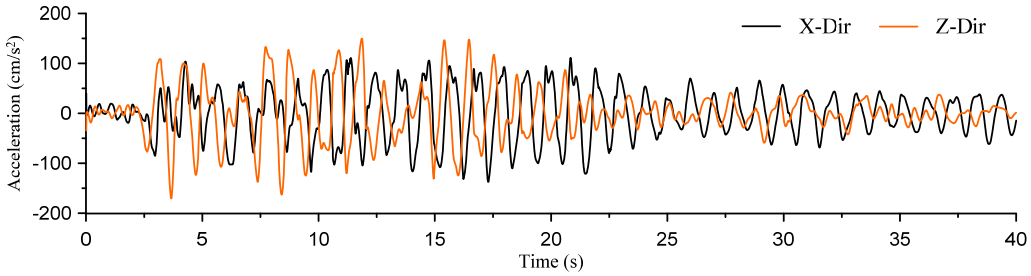

(a) 2nd floor

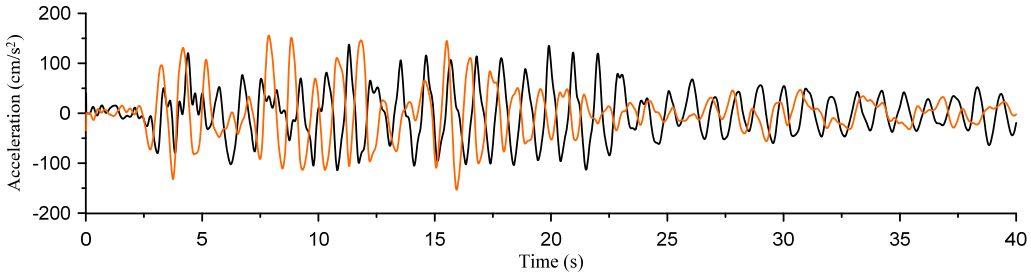

(b) 7th floor

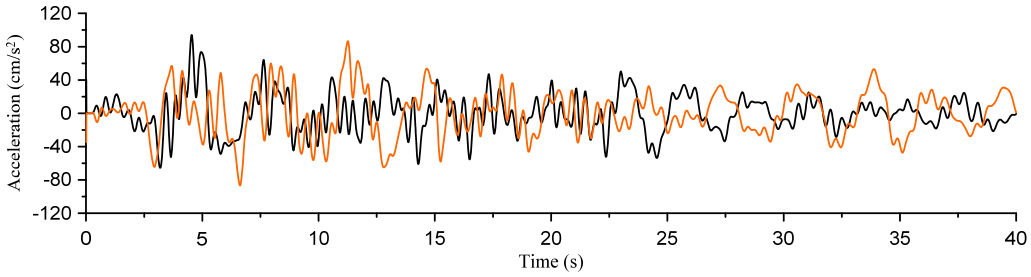

(c) 14th floor

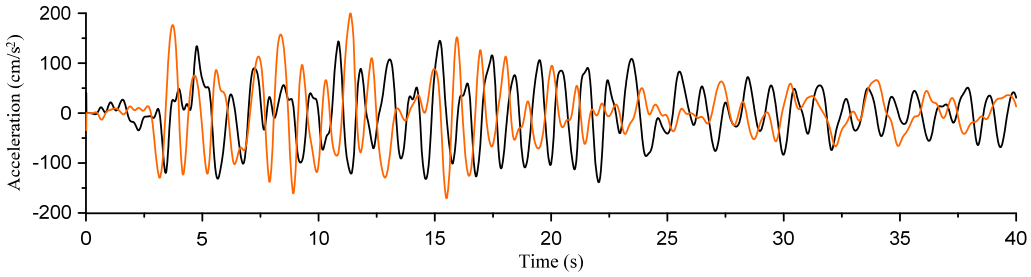

(d) 20th floor

Figure C.4 Absolute floor acceleration (Tohoku U – NS(Z),EW(X))

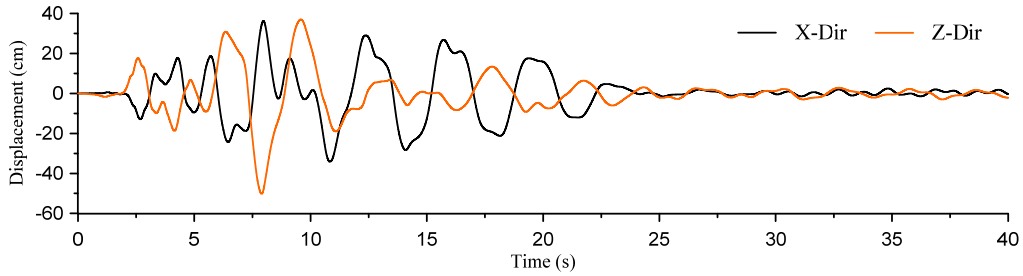

(a) 2nd floor

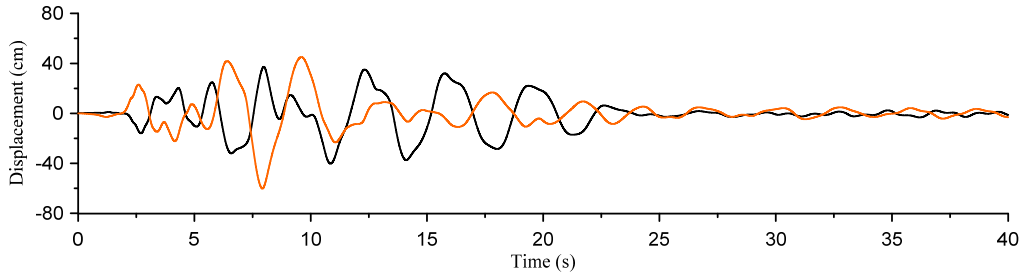

(b) 7th floor

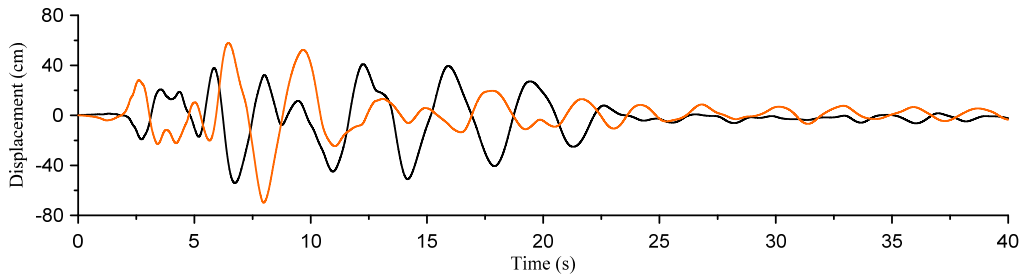

(c) 14th floor

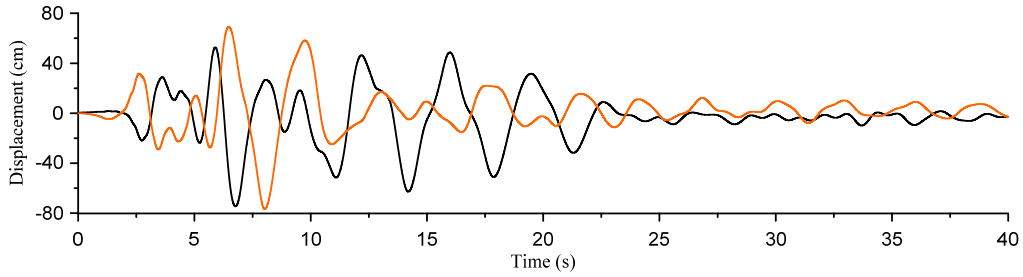

(d) 20th floor

Figure C.5 Floor displacement relative to the isolation floor (Takatori – NS(X),EW(Z))

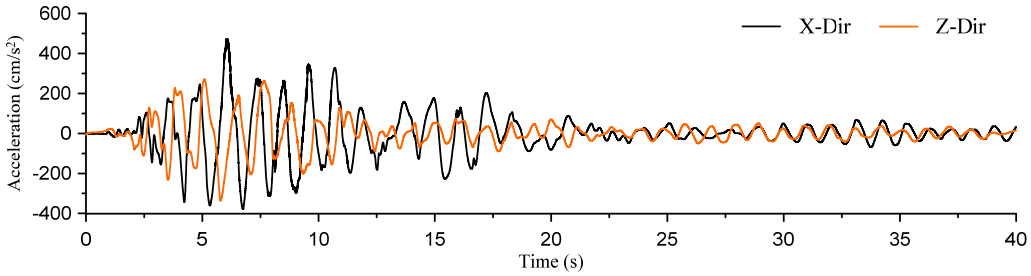

(a) 2nd floor

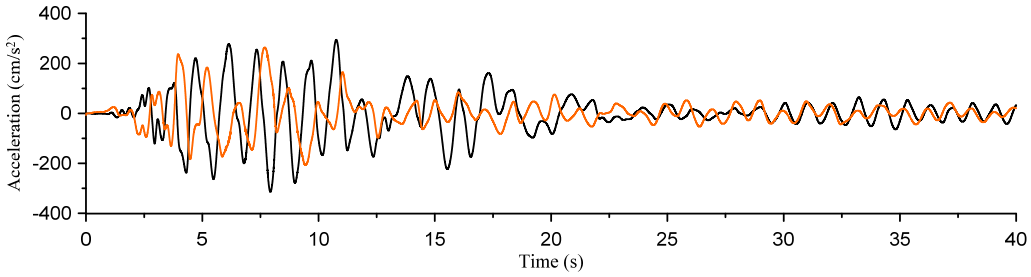

(b) 7th floor

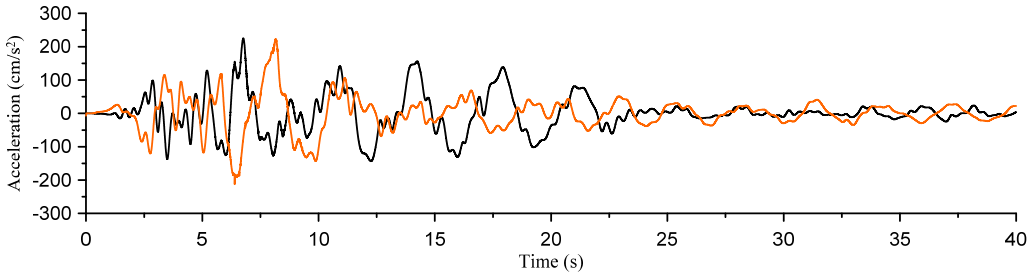

(c) 14th floor

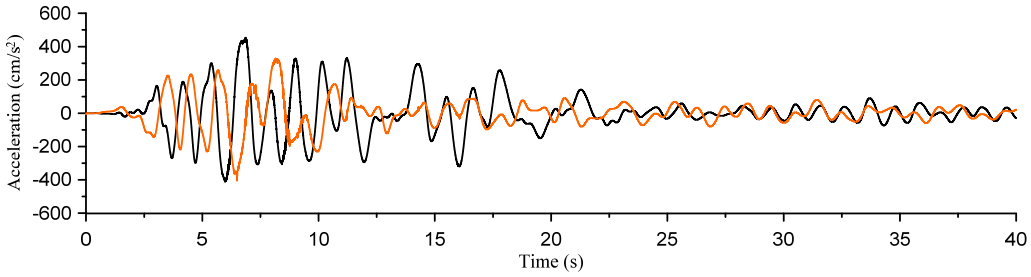

(d) 20th floor

Figure C.6 Absolute floor acceleration (Takatori – NS(X),EW(Z))

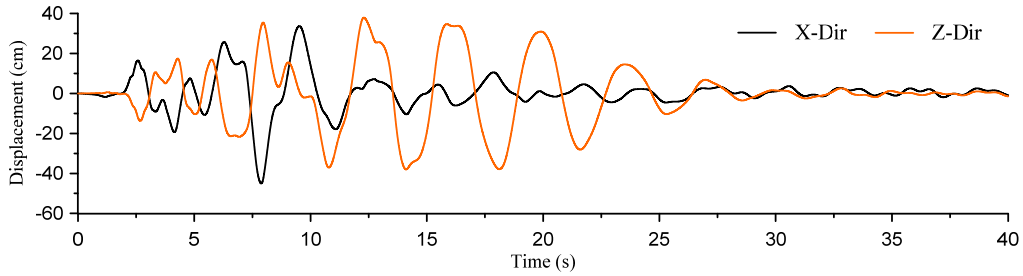

(a) 2nd floor

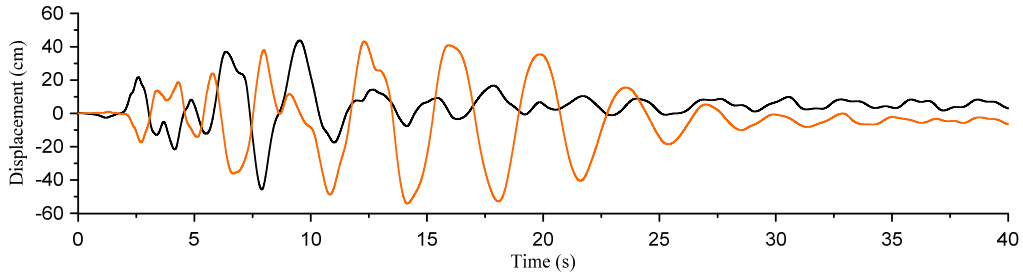

(b) 7th floor

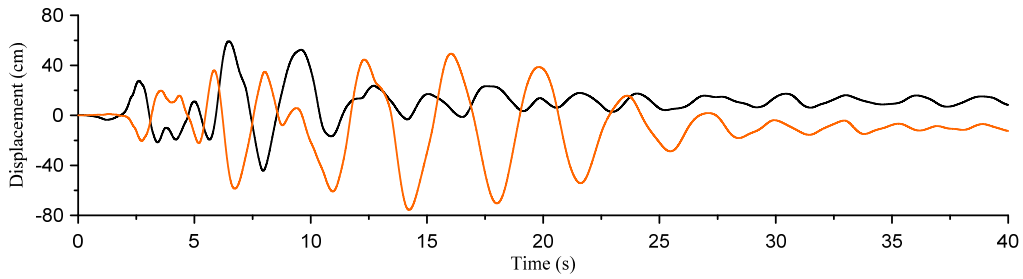

(c) 14th floor

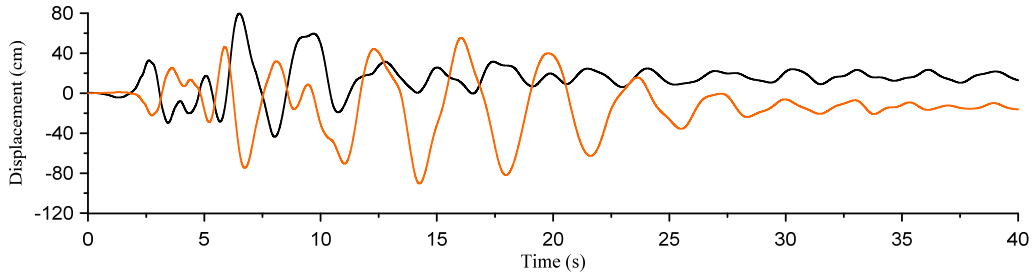

(d) 20th floor

Figure C.7 Floor displacement relative to the isolation floor (Takatori – NS(Z),EW(X))

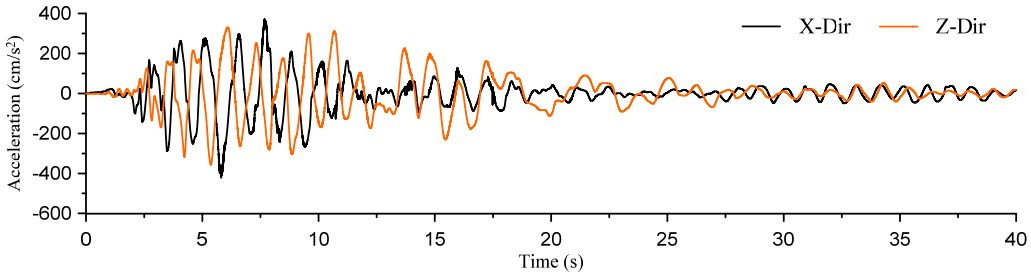

(a) 2nd floor

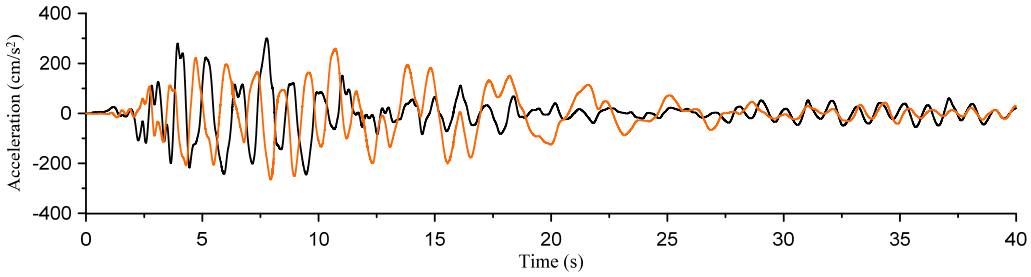

(b) 7th floor

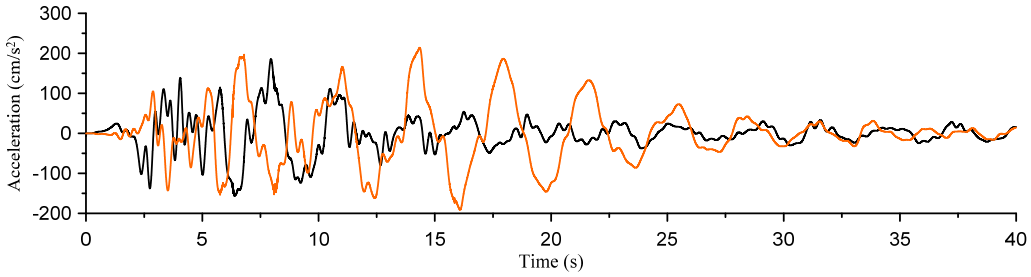

(c) 14th floor

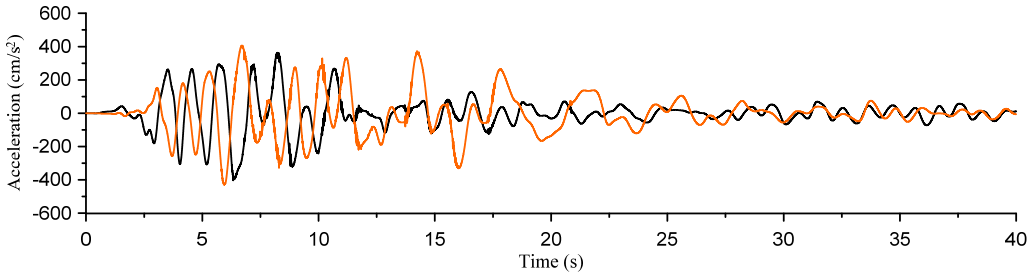

(d) 20th floor

Figure C.8 Absolute floor acceleration (Takatori – NS(Z),EW(X))

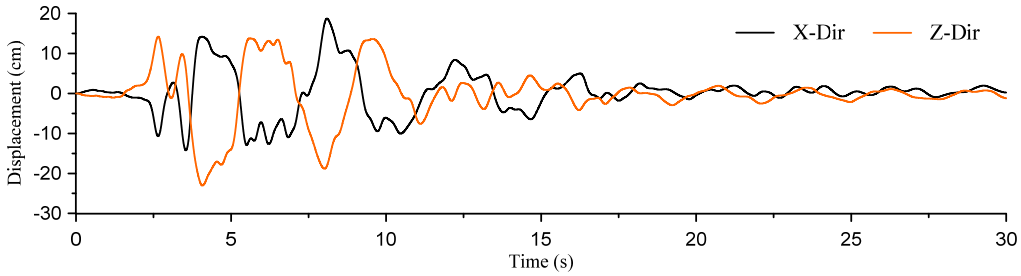

(a) 2nd floor

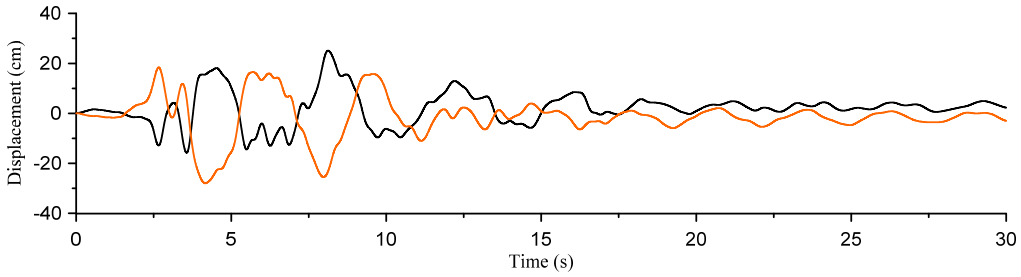

(b) 7th floor

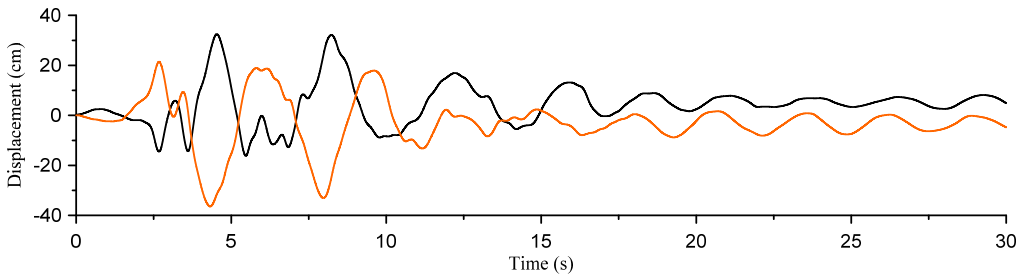

(c) 14th floor

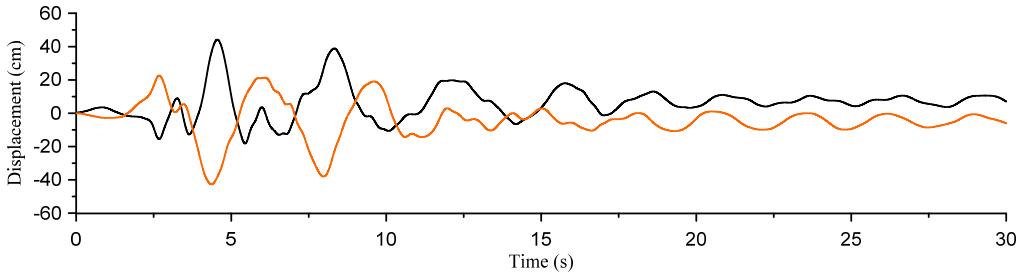

(d) 20th floor

Figure C.9 Floor displacement relative to the isolation floor (JMA Kobe – NS(X),EW(Z))

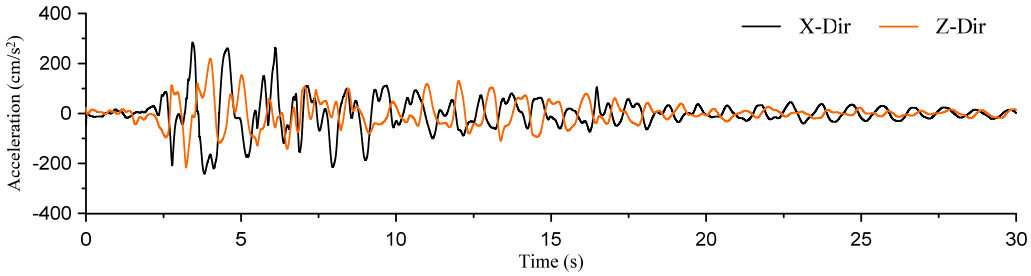

(a) 2nd floor

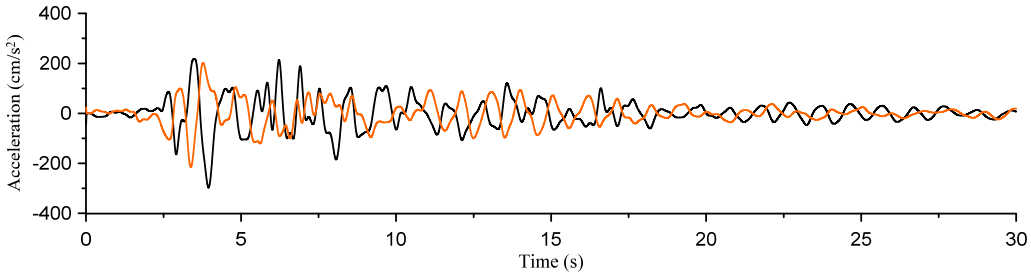

(b) 7th floor

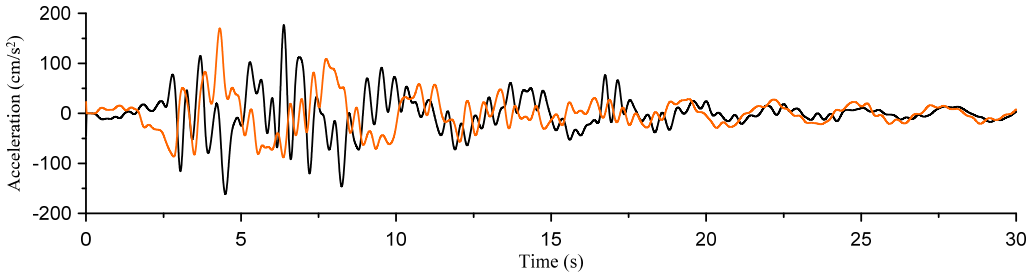

(c) 14th floor

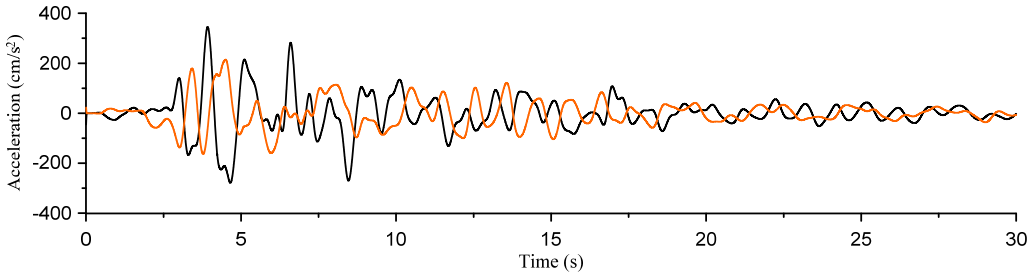

(d) 20th floor

Figure C.10 Absolute floor acceleration (JMA Kobe – NS(X),EW(Z))

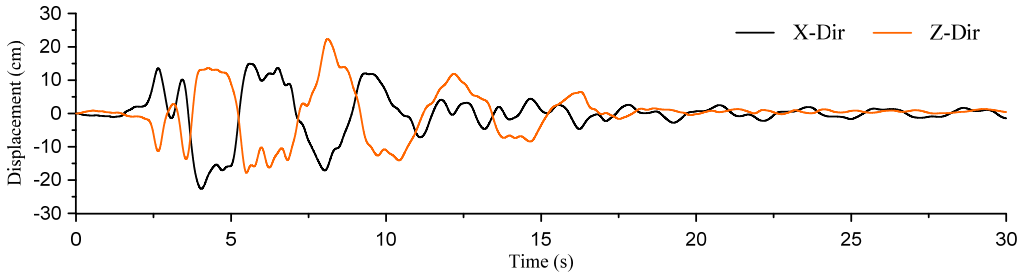

(a) 2nd floor

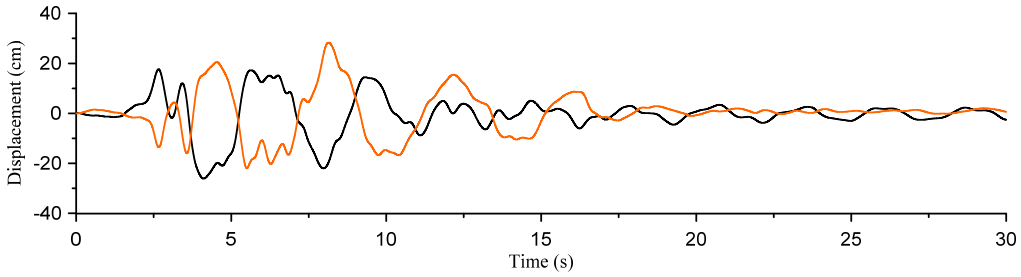

(b) 7th floor

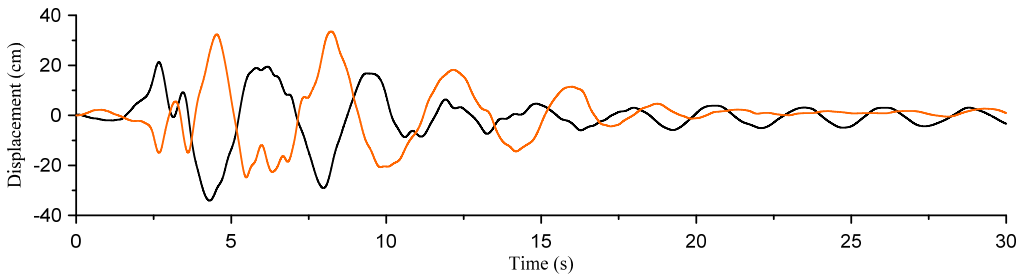

(c) 14th floor

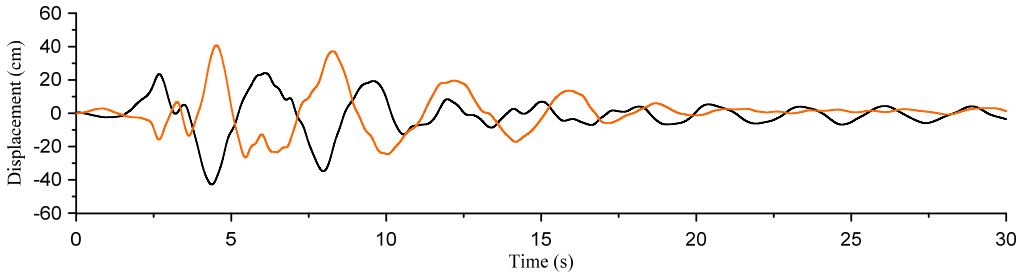

(d) 20th floor

Figure C.11 Floor displacement relative to the isolation floor (JMA Kobe – NS(Z),EW(X))

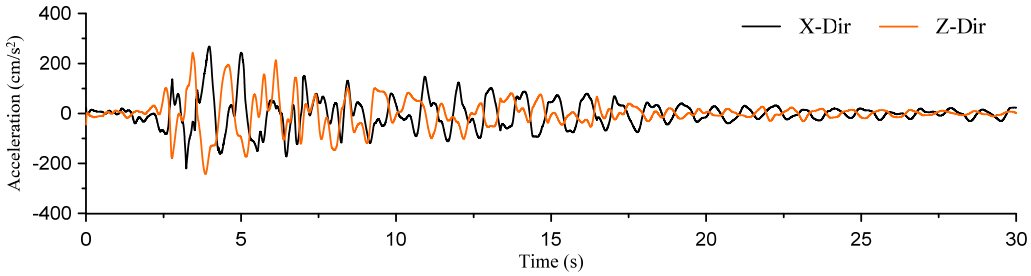

(a) 2nd floor

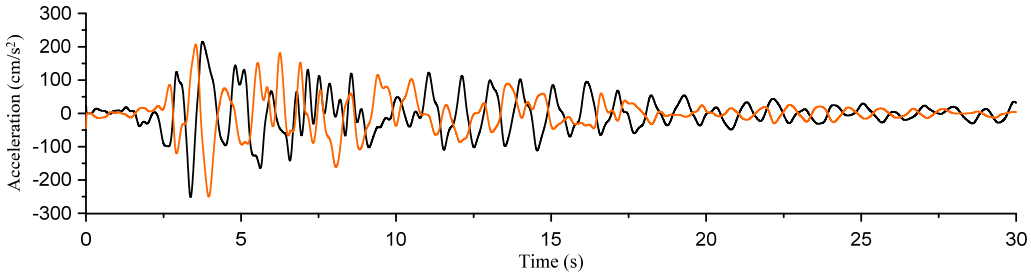

(b) 7th floor

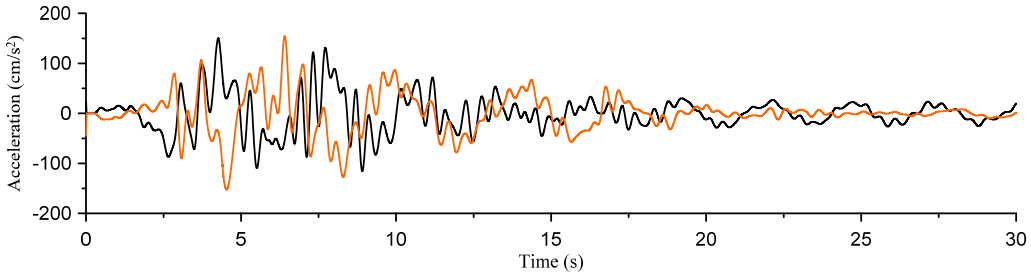

(c) 14th floor

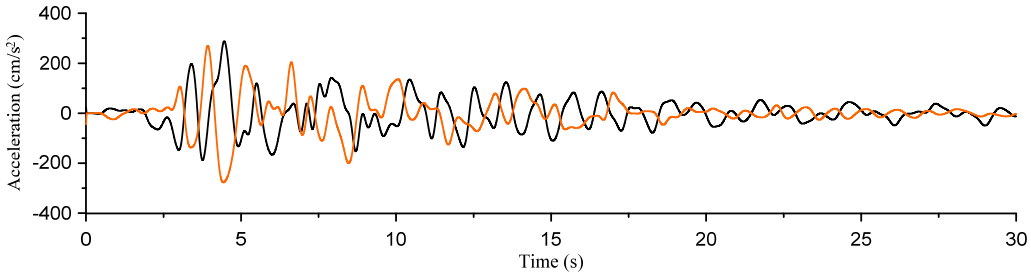

(d) 20th floor

Figure C.12 Absolute floor acceleration (JMA Kobe – NS(Z),EW(X))

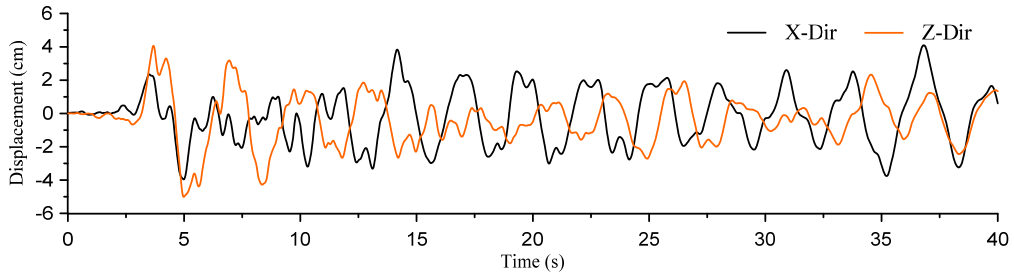

(a) 2nd floor

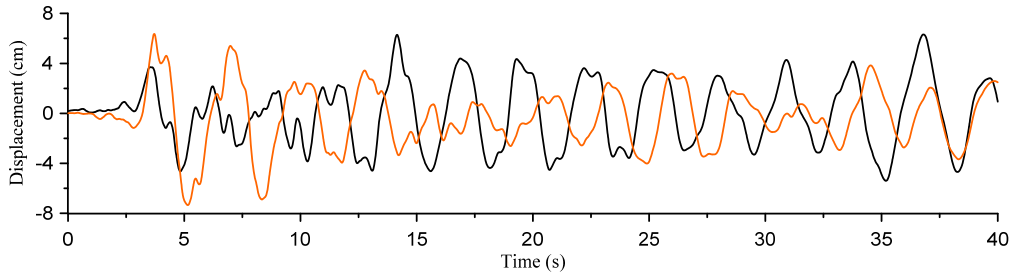

(b) 7th floor

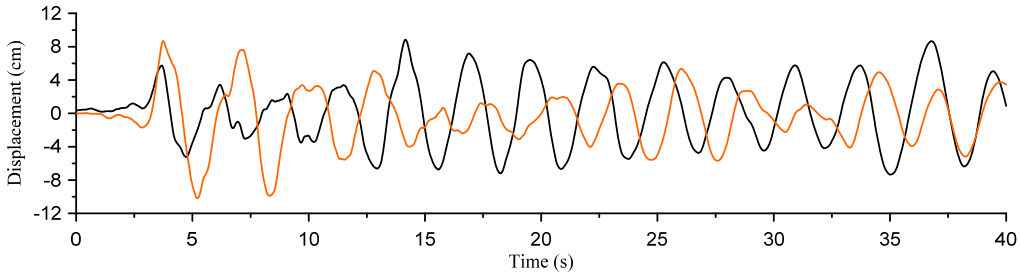

(c) 14th floor

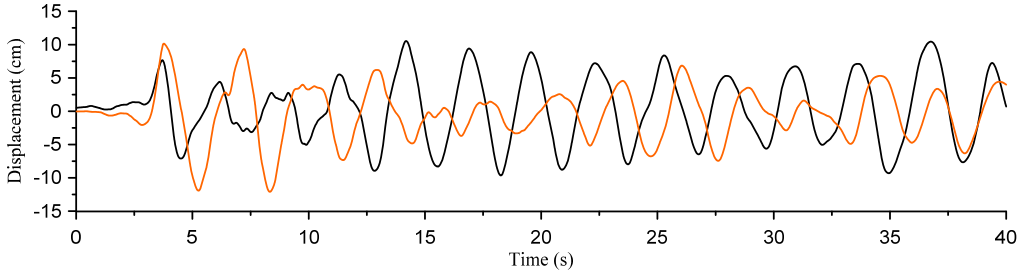

(d) 20th floor

Figure C.13 Floor displacement relative to the isolation floor (Taft – NS(X),EW(Z))

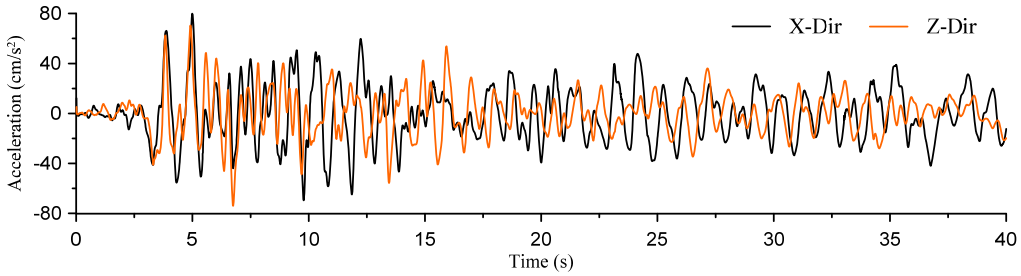

(a) 2nd floor

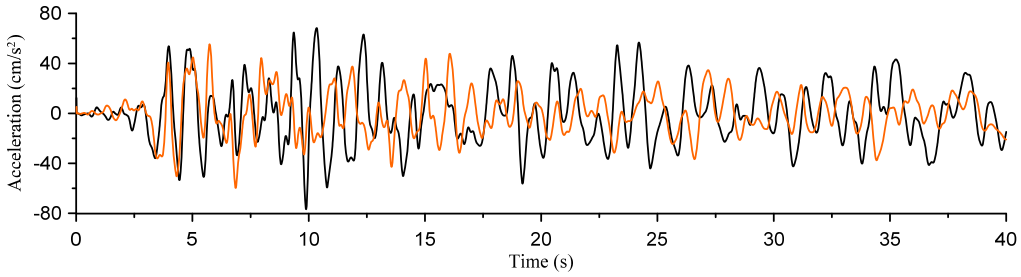

(b) 7th floor

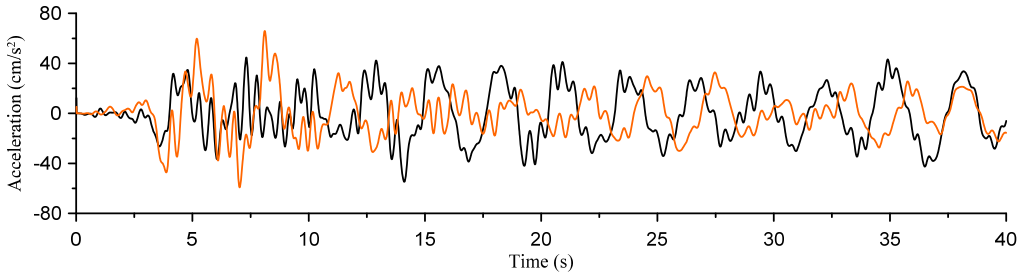

(c) 14th floor

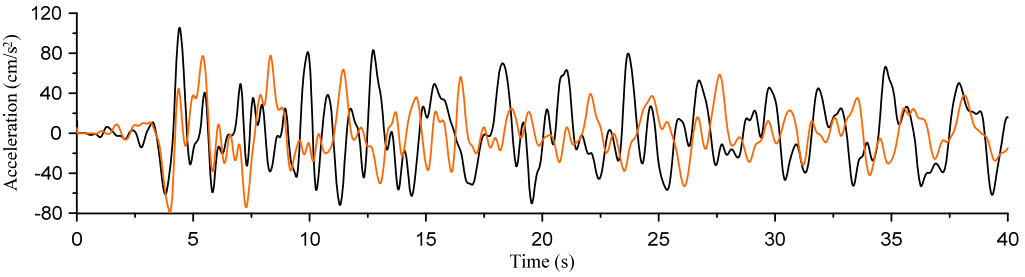

(d) 20th floor

Figure C.14 Absolute floor acceleration (Taft – NS(X),EW(Z))

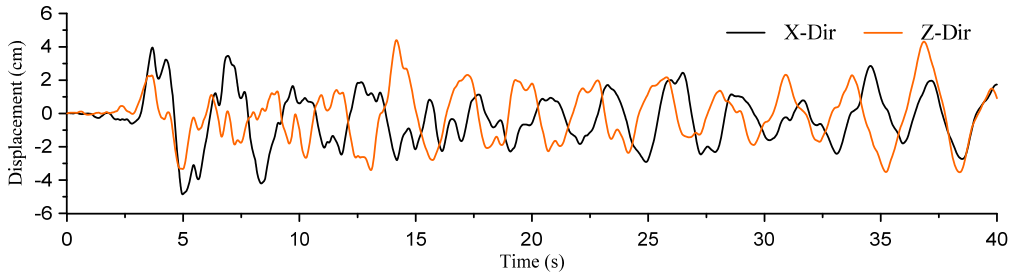

(a) 2nd floor

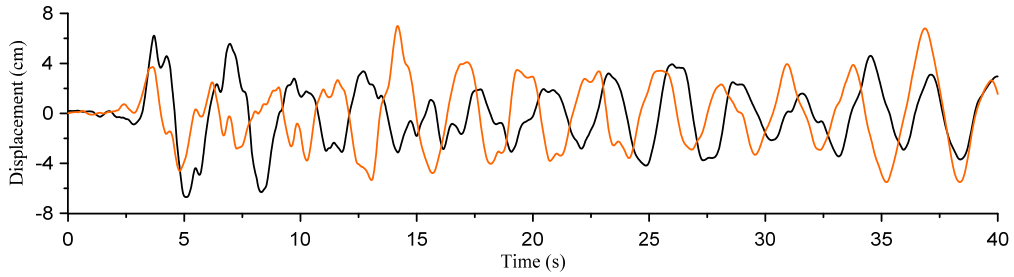

(b) 7th floor

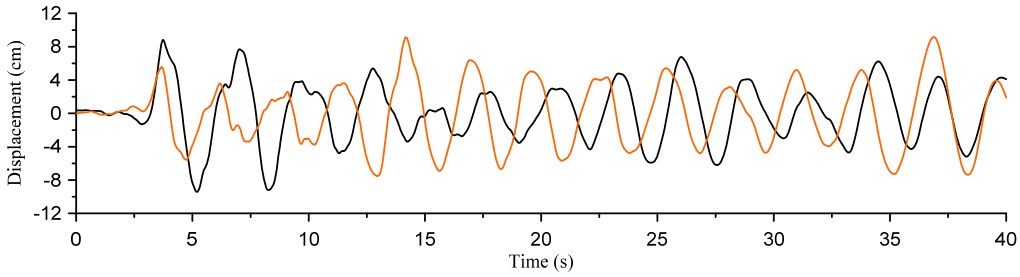

(c) 14th floor

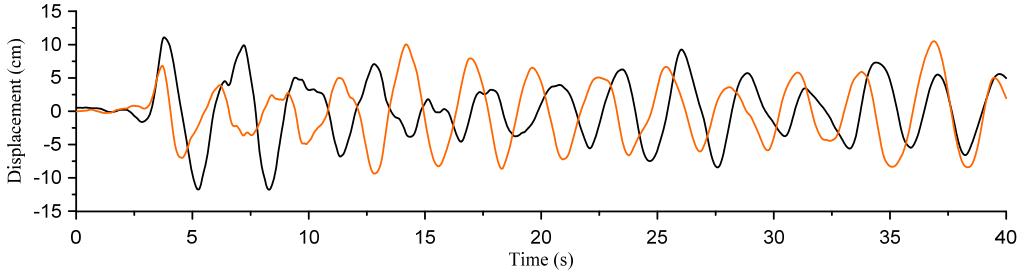

(d) 20th floor

Figure C.15 Floor displacement relative to the isolation floor (Taft – NS(Z),EW(X))

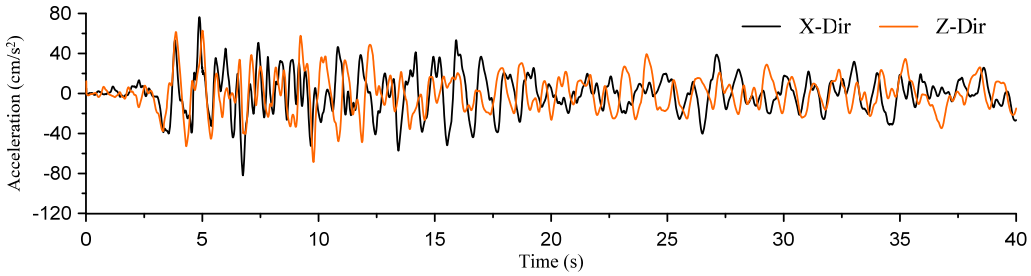

(a) 2nd floor

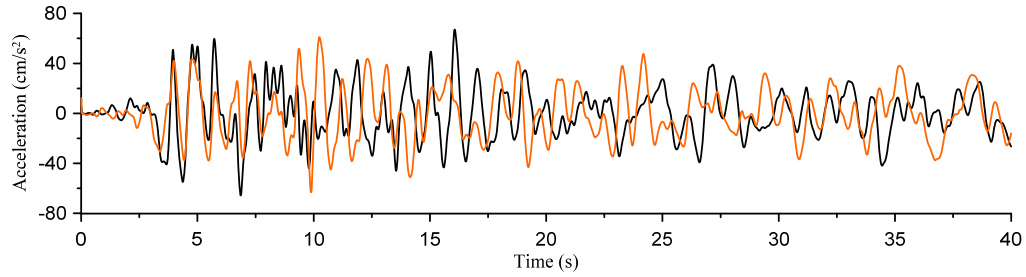

(b) 7th floor

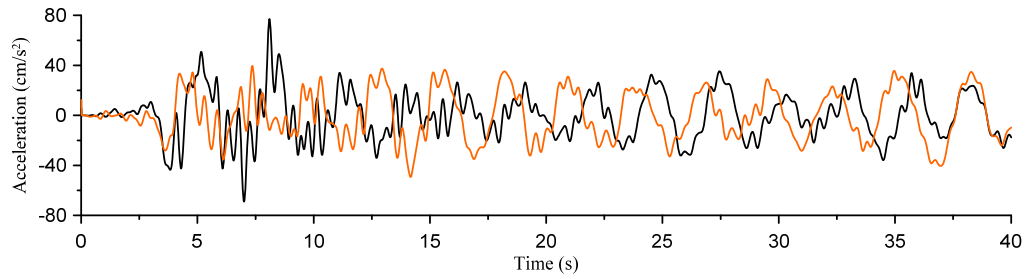

(c) 14th floor

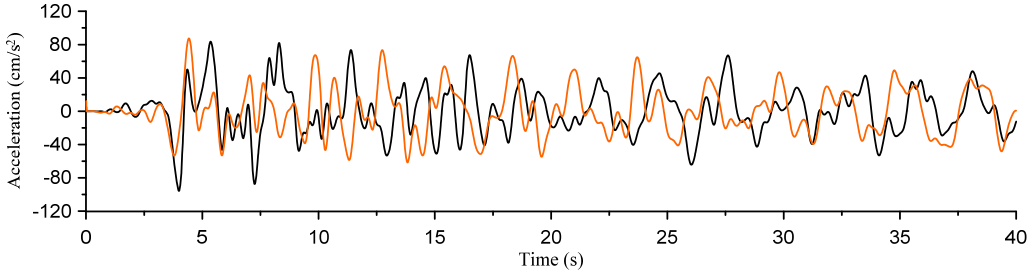

(d) 20th floor

Figure C.16 Absolute floor acceleration (Taft – NS(Z),EW(X))

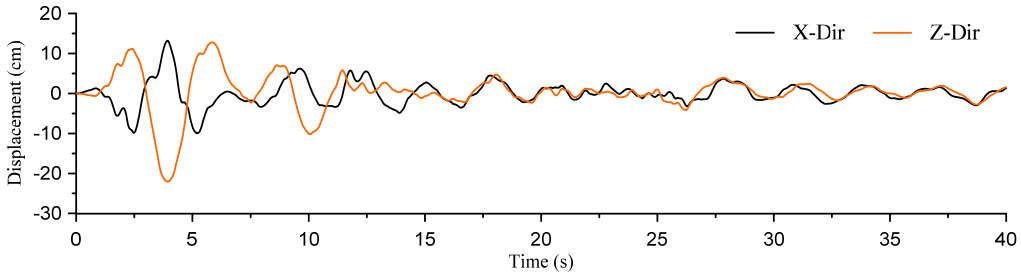

(a) 2nd floor

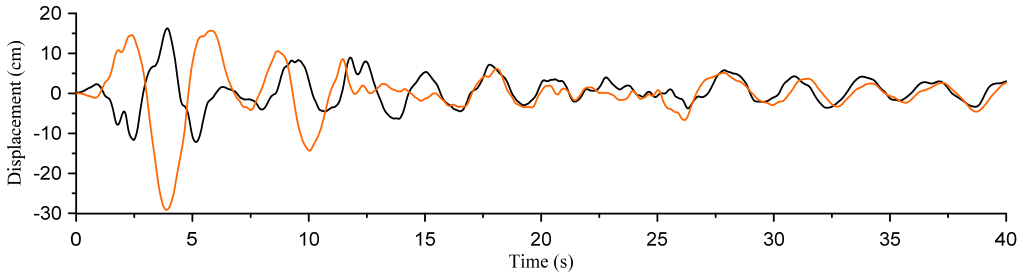

(b) 7th floor

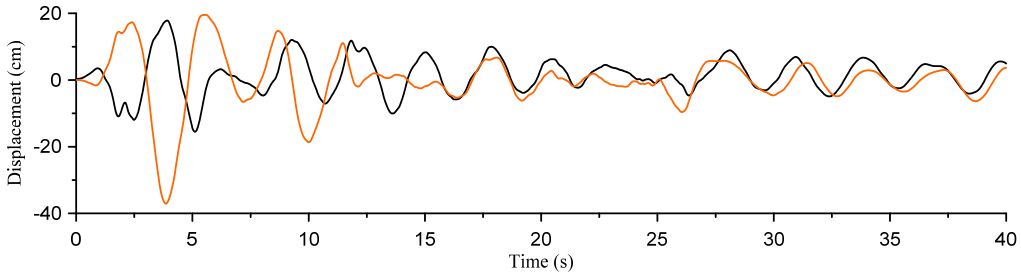

(c) 14th floor

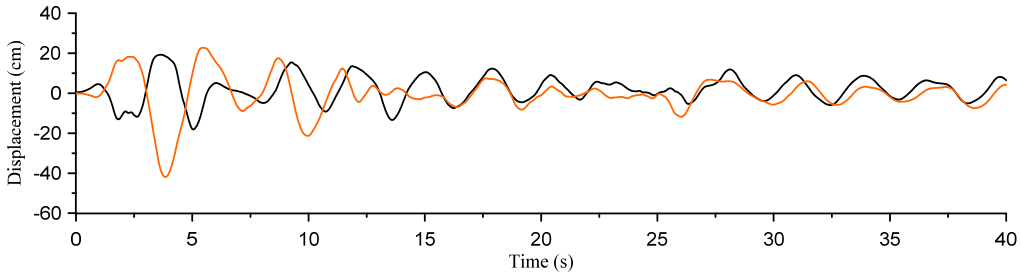

(d) 20th floor

Figure C.17 Floor displacement relative to the isolation floor (El Centro – NS(X),EW(Z))

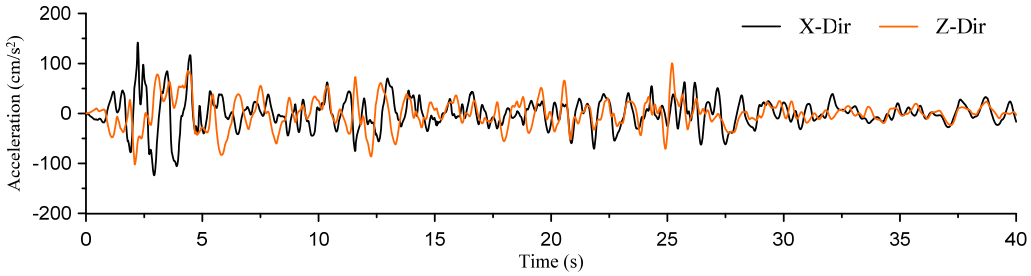

(a) 2nd floor

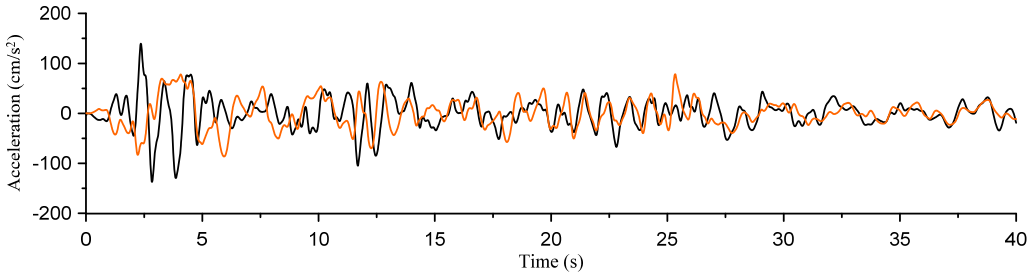

(b) 7th floor

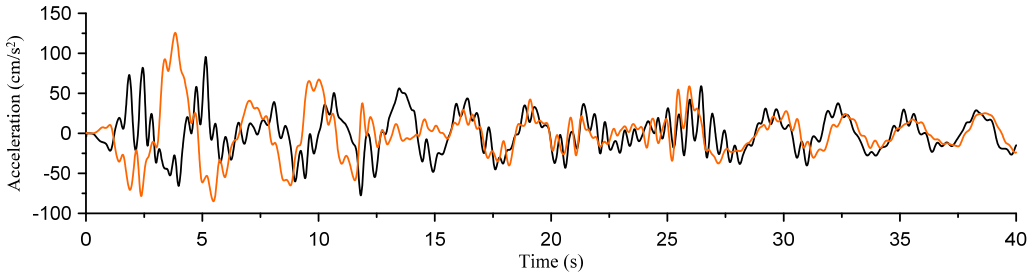

(c) 14th floor

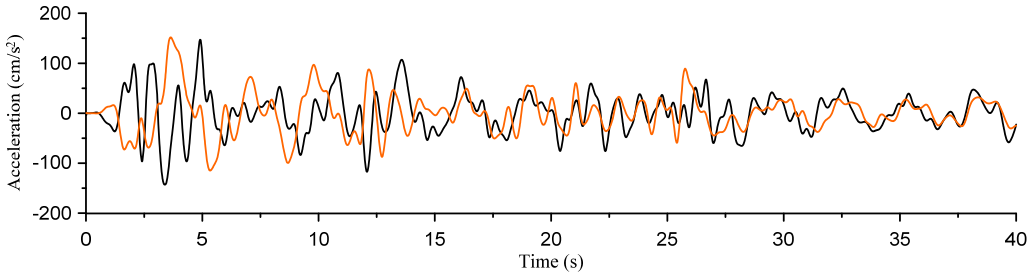

(d) 20th floor

Figure C.18 Absolute floor acceleration (El Centro – NS(X),EW(Z))

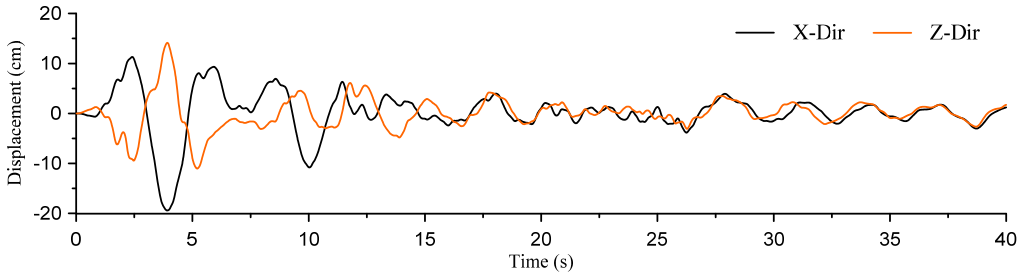

(a) 2nd floor

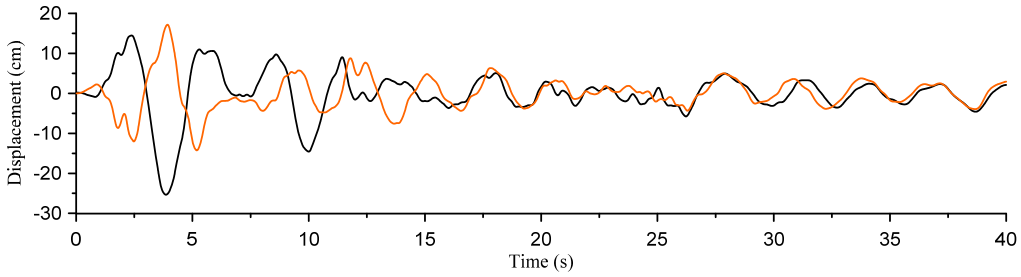

(b) 7th floor

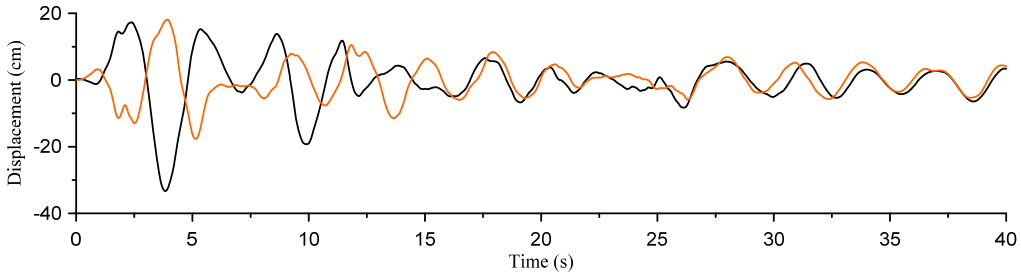

(c) 14th floor

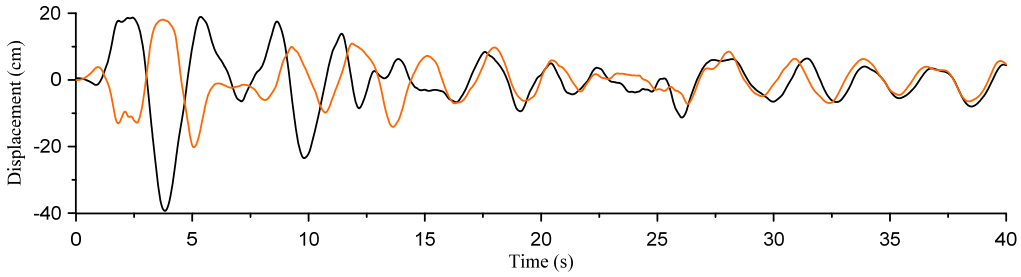

(d) 20th floor

Figure C.19 Floor displacement relative to the isolation floor (El Centro – NS(Z),EW(X))

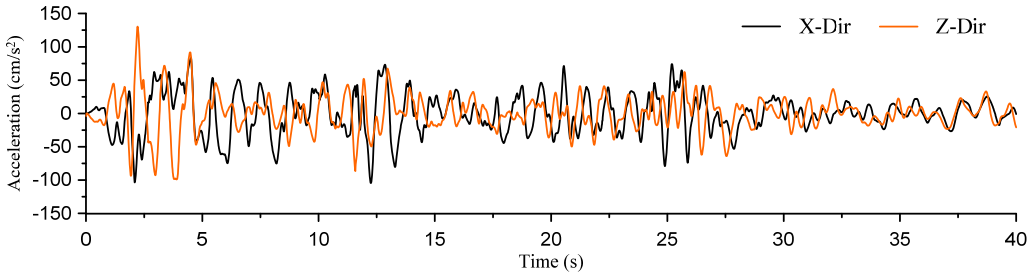

(a) 2nd floor

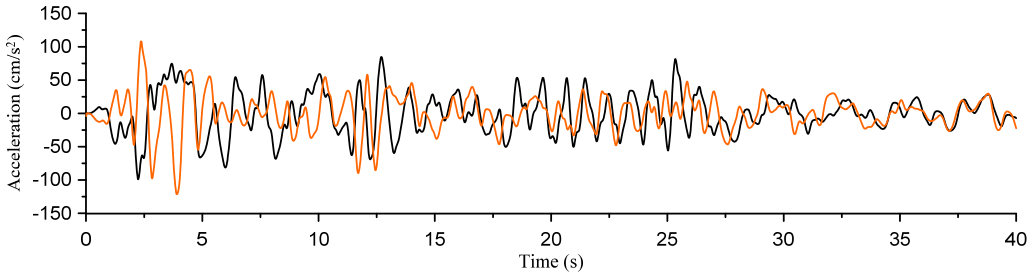

(b) 7th floor

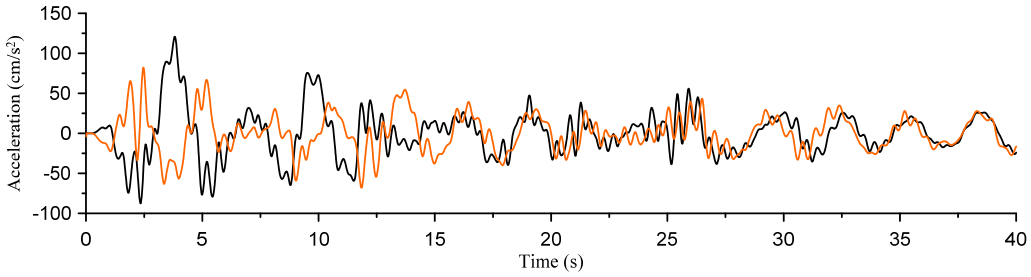

(c) 14th floor

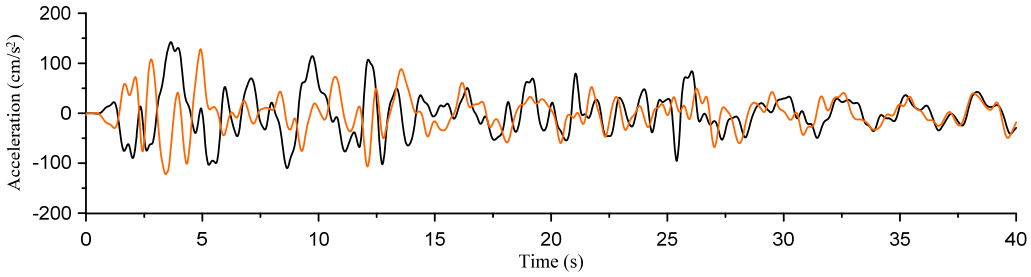

(d) 20th floor

Figure C.20 Absolute floor acceleration (El Centro – NS(Z),EW(X))

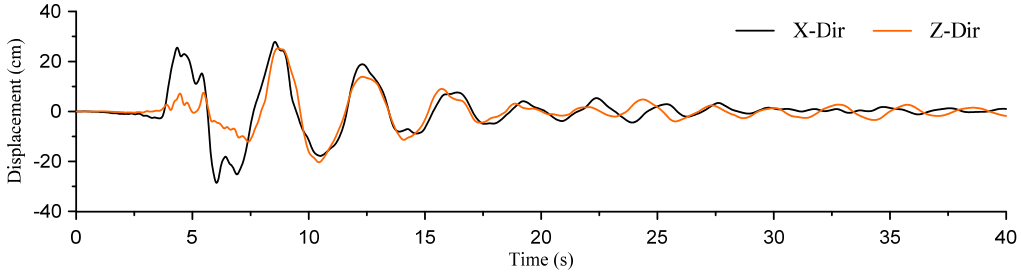

(a) 2nd floor

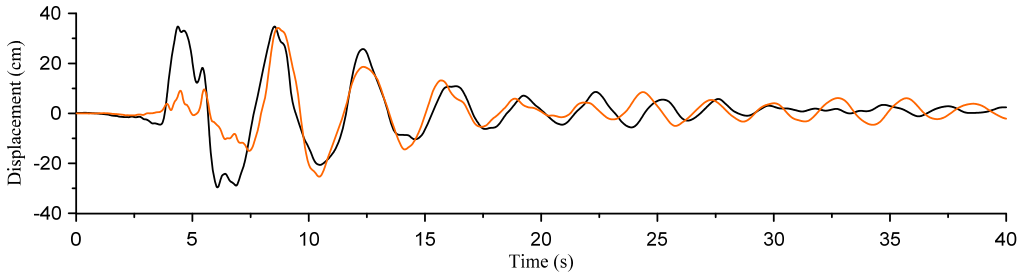

(b) 7th floor

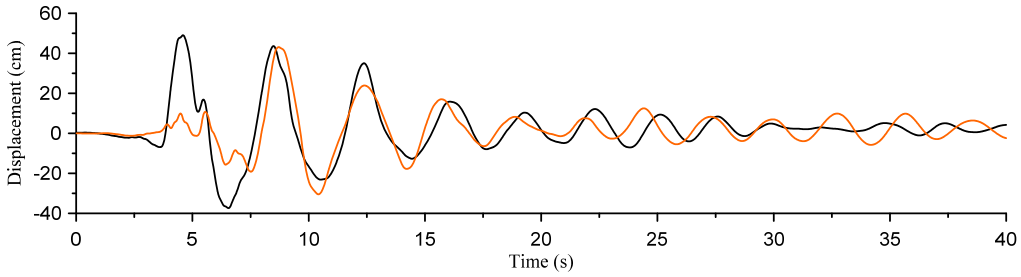

(c) 14th floor

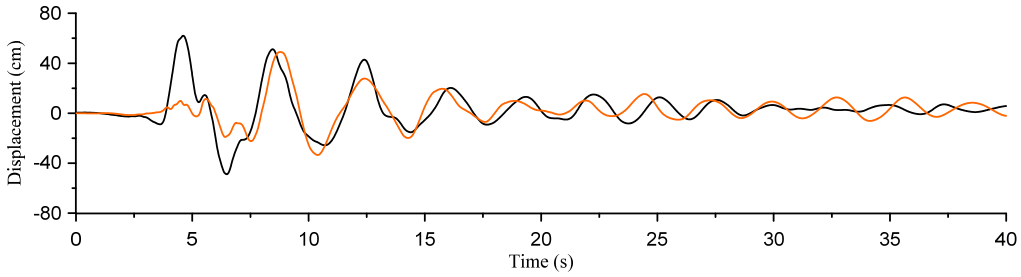

(d) 20th floor

Figure C.21 Floor displacement relative to the isolation floor (New Hall – NS(X),EW(Z))

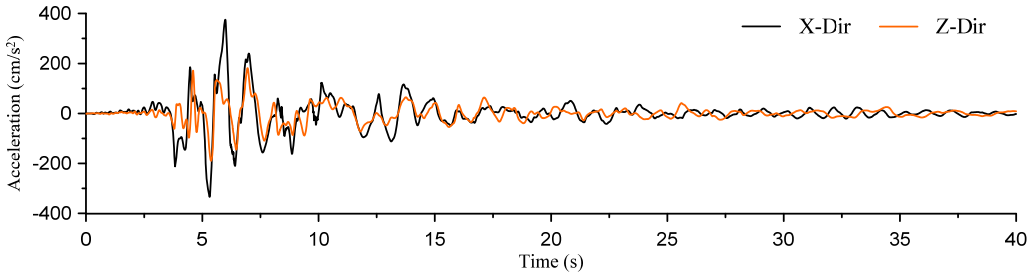

(a) 2nd floor

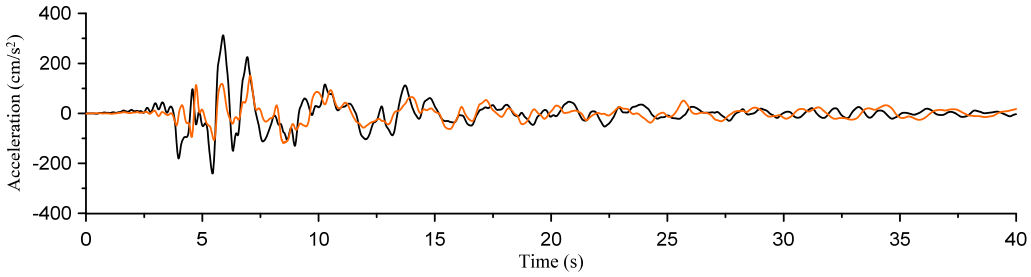

(b) 7th floor

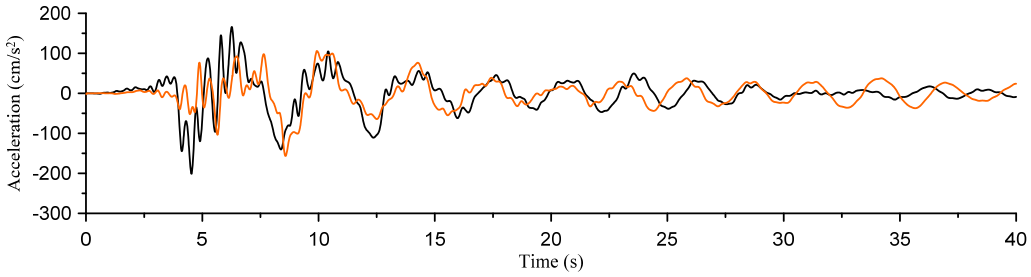

(c) 14th floor

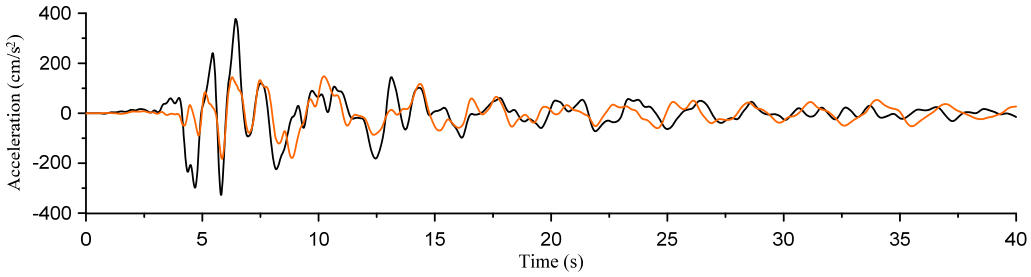

(d) 20th floor

Figure C.22 Absolute floor acceleration (New Hall – NS(X),EW(Z))

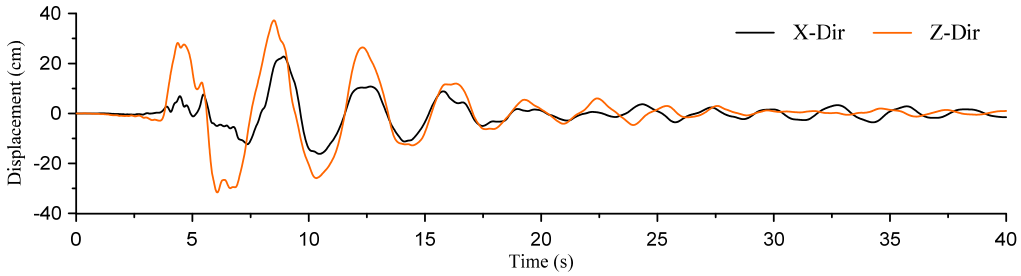

(a) 2nd floor

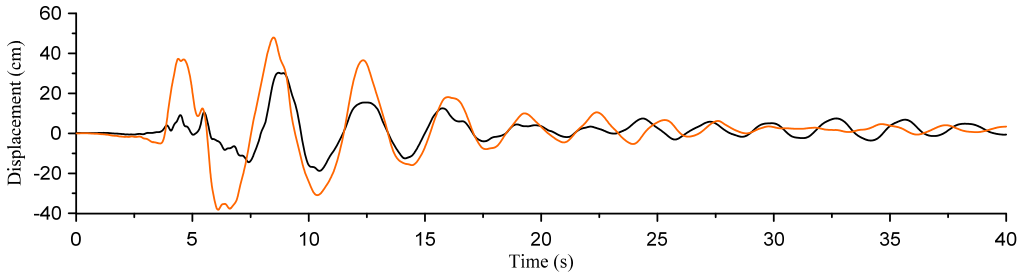

(b) 7th floor

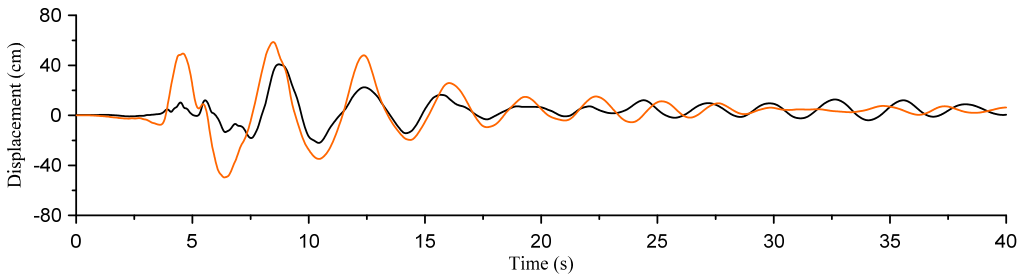

(c) 14th floor

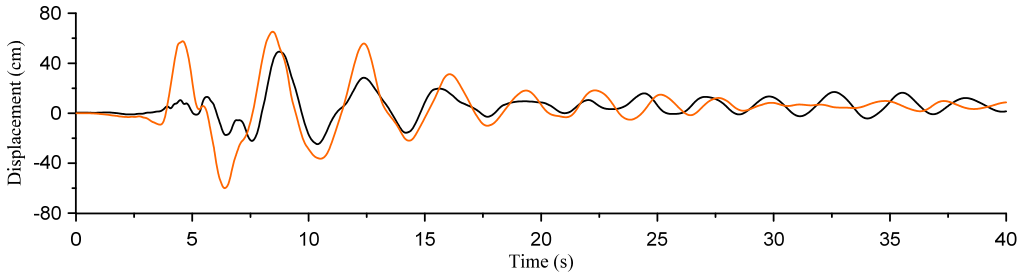

(d) 20th floor

Figure C.23 Floor displacement relative to the isolation floor (New Hall – NS(Z),EW(X))

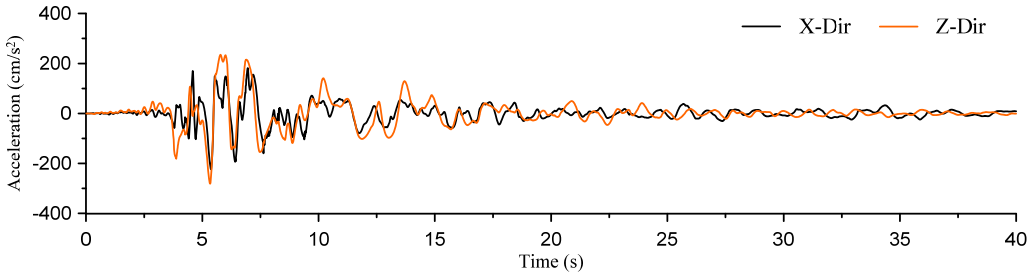

(a) 2nd floor

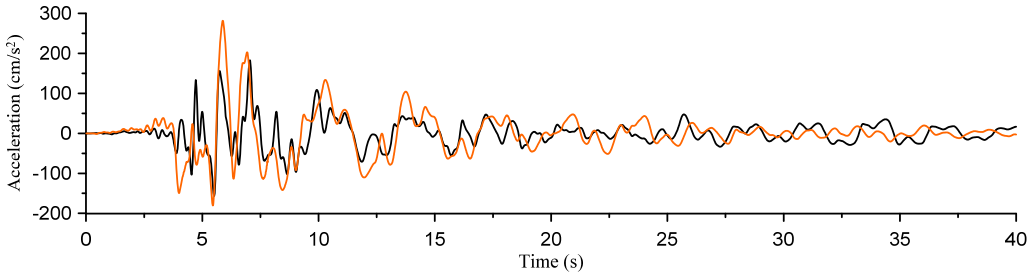

(b) 7th floor

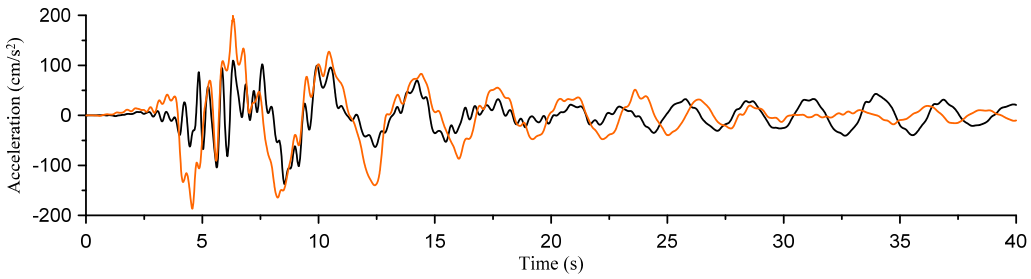

(c) 14th floor

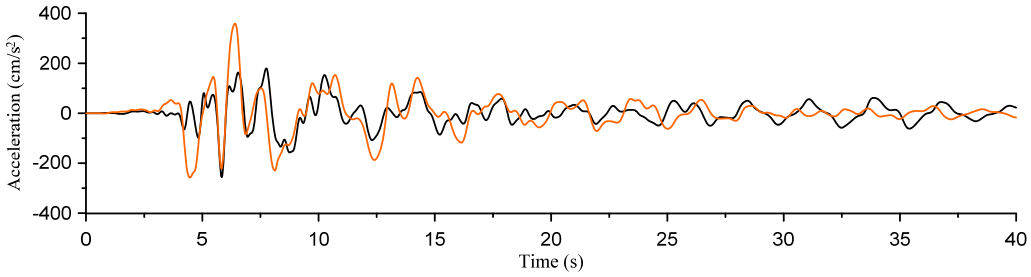

(d) 20th floor

Figure C.24 Absolute floor acceleration (New Hall – NS(Z),EW(X))